AD-A148 080   THE SHOCK AND VIBRATION BULLETIN PART 2 VIBRATION   1/2
               ANALYSIS(U) NAVAL RESEARCH LAB WASHINGTON DC SHOCK AND
UNCLASSIFIED   VIBRATION INFORMATION CENTER   SEP 77 BULL-47-PT-2
                                               F/G 20/11   NL
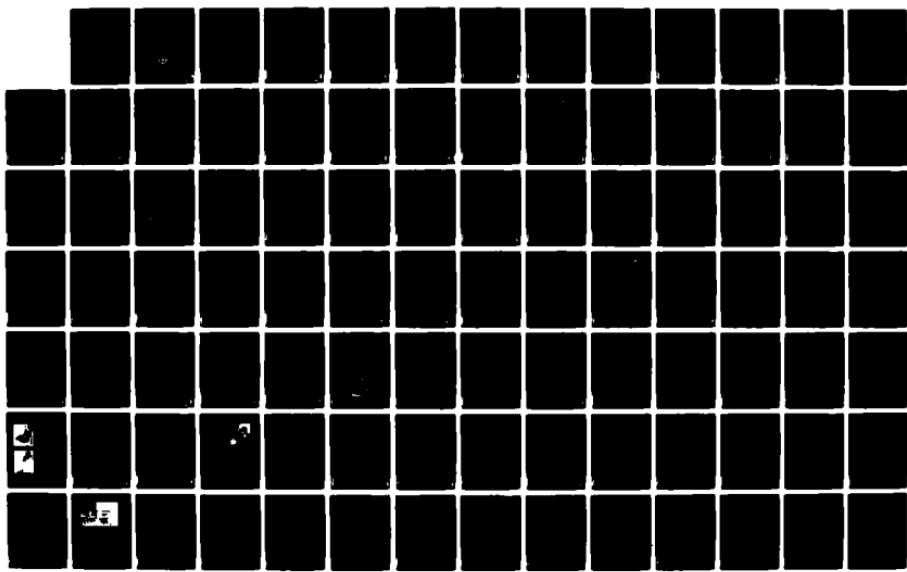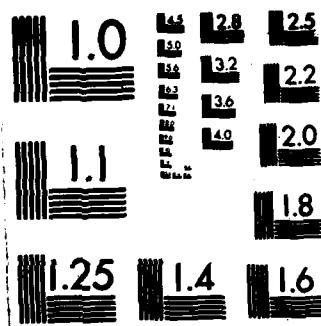
MICROCOPY RESOLUTION TEST CHART

NATIONAL BUREAU OF STANDARDS-1963-A

AD–A148 080

THE
SHOCK AND VIBRATION
BULLETIN

Part 2
Vibration Analysis

SEPTEMBER 1977

A Publication of
THE SHOCK AND VIBRATION
INFORMATION CENTER
Naval Research Laboratory, Washington, D.C.

DTIC
ELECTE
NOV 2 9 1984

A
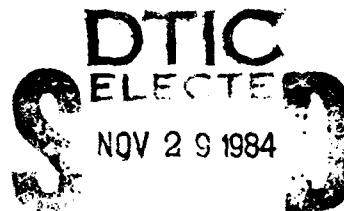
Office of
The Director of Defense
Research and Engineering

84 11 26 19 6

SYMPOSIUM MANAGEMENT

THE SHOCK AND VIBRATION INFORMATION CENTER

Henry C. Pusey, Director
Rudolph H. Volin
J. Gordan Showalter
Barbara Szymanski
Carol Healey

THE
SHOCK AND VIBRATION
BULLETIN

SEPTEMBER 1977

A Publication of
THE SHOCK AND VIBRATION
INFORMATION CENTER
Naval Research Laboratory, Washington, D.C.

The 47th Symposium on Shock and Vibration was held
at the Albuquerque Inn and Convention Center, Albu-
querque, New Mexico on October 19-21, 1976. The
Defense Nuclear Agency, Washington, D.C., the Field
Command Defense Nuclear Agency, and the Air Force
Weapons Laboratory, Kirtland Air Force Base, New
Mexico were the hosts.

Office of
The Director of Defense
Research and Engineering

CONTENTS

PAPERS APPEARING IN PART 2

Vibration Analysis

(over) iii

cont)

PAPERS APPEARING IN PART 1

Keynote Address

IMPACTS OF SHOCK AND VIBRATION CONSIDERATIONS ON WEAPON
DEVELOPMENT
   Dr. Hua Lin, Assistant Director (Offensive Systems) Office Director of
   Defense Research and Engineering, Washington, DC

Invited Paper

NUCLEAR HARDENING IN A MISSILE DEFENSE SYSTEM
   Noah J. Hurst, Ballistic Missile Defense Systems Command, Huntsville, AL

Panel Session

DYNAMICS EFFECTS ON RELIABILITY

Shock Analysis

SCALING OF STRONG SHOCK HUGONIOTS
   W.E. Baker, Southwest Research Institute, San Antonio, TX

SHOCK SPECTRA AND RESPONSES BY POCKET CALCULATOR
   C.T. Morrow, Consultant, Dallas, TX

STUDIES OF THE TERRADYNAMICS OF A PROJECTILE
PENETRATING SAND
   L.E. Malvern, R.L. Sierakowski, University of Florida, Gainesville, FL and
   J.A. Collins, DLYV/Air Force Armament Laboratory, Eglin AFB, FL

HARDENED SYSTEM VULNERABILITY ANALYSIS
   J.D. Collins, J.H. Wiggins Company, Redondo Beach, CA

Shock Testing

Isolation and Damping

PAPERS APPEARING IN PART 3

Vibration Testing

Instrumentation and Data Analysis

PAPERS APPEARING IN SUPPLEMENT

VIBRATION ANALYSIS

SOME ASPECTS OF VIBRATION CONTROL SUPPORT DESIGN*

P. Bezler, J. R. Curreri
Stress Analysis Group
Department of Applied Science
Brookhaven National Laboratory
Upton, NY 11973

Transfer matrix methods were used to investigate the characteristics of vibration control supports for piping systems. Using a spring supported cantilever beam and a spring supported equal span "L" bend as analytical models data were developed to delineate the optimum support placement and effectiveness as a function of support spring rate. Although accurate support placement was found to be imperative, the second mode node point was found to be the best compromise location for all spring rates. Also, near ideal effectiveness was produced with a support having a spring rate equal to that of the second natural frequency of the unsupported system.

Intermediate supports are a common feature in piping systems. They are introduced to provide support against weight loadings and to effect an increase of system natural frequencies above undesired ranges. Support hangers are typically constant force and spring types, liberally dispersed throughout the system and designed to just balance dead weight loads. As such, they produce an average stiffening of the entire system but are not used to control gross system vibrational characteristics. Vibration control supports are specifically designed to be rigid members, fixing a point in space. If properly located, they strongly affect system vibrational characteristics.

Rigid supports are introduced in order to raise the natural frequencies of a system to a range of acceptable values. It is a well understood principle that the introduction of a single constraint in a vibrating system cannot raise the fundamental frequency any higher than the second mode frequency of the system without constraint. Specifically, in beam or pipe structures a rigid pin support placed at the node point for the second mode of motion for the unsupported system will force the system lowest natural frequency from the first to the second natural frequency of the unsupported system. The

support in this case is 100% effective, producing a maximum increase in frequency magnitude. However, in the real world there is no such item as a rigid pin support. Each real support has associated with it a calculable elastic spring constant and a finite attachment width. The elasticity of these supports tends to reduce their effectiveness while the attachment width (rotational constraint is added) tends to increase their effectiveness. The effectiveness of non-rigid pin supports and their optimal placement is the subject of this investigation. Attachment width affects are not considered.

Using transfer matrix methods evaluations were made of the first natural frequency of a spring supported cantilever beam and a spring supported "L" bend. The transfer matrix relations were based on classical beam theory and incorporated a distributed mass representation of the beam element. For the cantilever beam the computations were performed for spring rates ranging from 0 to 400 times the basic beam stiffness (EI/ℓ^3) and locations from the second mode node point (taken as $.785\ell$ in this study) to the free end. For the "L" bend only variations in the spring rate were considered, the placement always being taken at the node point for the second mode.

The cantilever beam served as the model to investigate optimum spring location as a function of spring rate. It is a non-symetric structure and as such, its node point for the second mode motion does not coincide with it's point of maximum motion in the first mode (ℓ). In this regard it is considered typical of a most general structure. For these optimal support placement is a function of support spring rate. For symetric systems the point of maximum motion in the first mode coincides with the second mode node point and optimal support placement is not a function of support spring rate.

The results for the cantilever beam investigations are shown in Figure 1. Two sets of data are depicted, the eigenvalue coefficient (β_1) for the first mode of motion of the spring supported beam and the optimum spring location both as functions of the non-dimensional spring rate. The ordinate scale to the left applies to the eigenvalue data while the ordinate scale to the right applies to the location parameter.

The optimum spring location curve is developed from the computed eigenvalue data. Considering the latter, the graph depicts the variation of the first mode eigenvalue coefficient of a spring supported cantilever beam as a function of spring rate. This is shown for ten values of spring location varying from 0.785ℓ to the free end. For a spring located at the free end ($X/\ell=1$), the eigenvalue coefficient varies from 1.875 for a null spring rate to 3.854 for a spring rate 400 times the basic beam stiffness. As may be seen, the free end location curve is the upper most curve (most effective location) at low spring rates and the lower most curve (least effective) at high spring rates. The location curve which forms the upper envelope of the curves at a given spring rate establishes that location as the optimum support location for the spring rate. Following this interpretation the optimum spring location curve was developed.

An important general conclusion can be drawn from the data. As can be seen, the curve corresponding to a support located at the second mode node point ($.785\ell$) is never far below the upper-most curve. A spring located here will produce almost optimal effect. It may then be concluded that in the absence of detailed analyses, the second mode node point location represents the best compromise location for all spring rates.

Defining support effectiveness as the percentage of frequency increase produced by a spring, 100% being the increase from the first to the second natural frequency of the unsupported system, a measure of relative support efficiency was possible. Figure 2 depicts the variation of support effectiveness versus non-dimensional spring rate for the cantilever beam and for a "L" bend with the support located at the second mode node point for each system. The "L" bend was selected as being typical of a general symetric system. The non-dimensional spring rate is formed by taking the ratio of support stiffness to the stiffness associated with the second natural frequency of the unsupported system ($K=k/m\omega_2^2$), m-system mass, ω_2-system second natural frequency and k-support spring rate). Non-dimensionalized in this way the curves for the two systems are very similar. For each, near ideal "rigid support" effect is produced as the non-dimensional spring rate approaches unity.

Support effectiveness was found to be a function of both spring rate and location. At low spring rates, 0-80 times the basic beam stiffness, the support effectiveness was only weakly dependent on location, provided the spring was placed near the point of expected maximum motion. Conversely, at high spring rates, greater than 300, the effectiveness was strongly dependent on location, a variation of 40% in effectiveness being produced from the poorest ($X/\ell=1$) to the optimal location ($X/\ell=0.785$). Although accurate support placement is imperative, the second mode node point is the best compromise location for all spring rates. Also, near ideal effectiveness is produced with a support having a spring rate equal to the spring constant associated with the second natural frequency of the unsupported system.

2

Figure 1

Figure 2

3
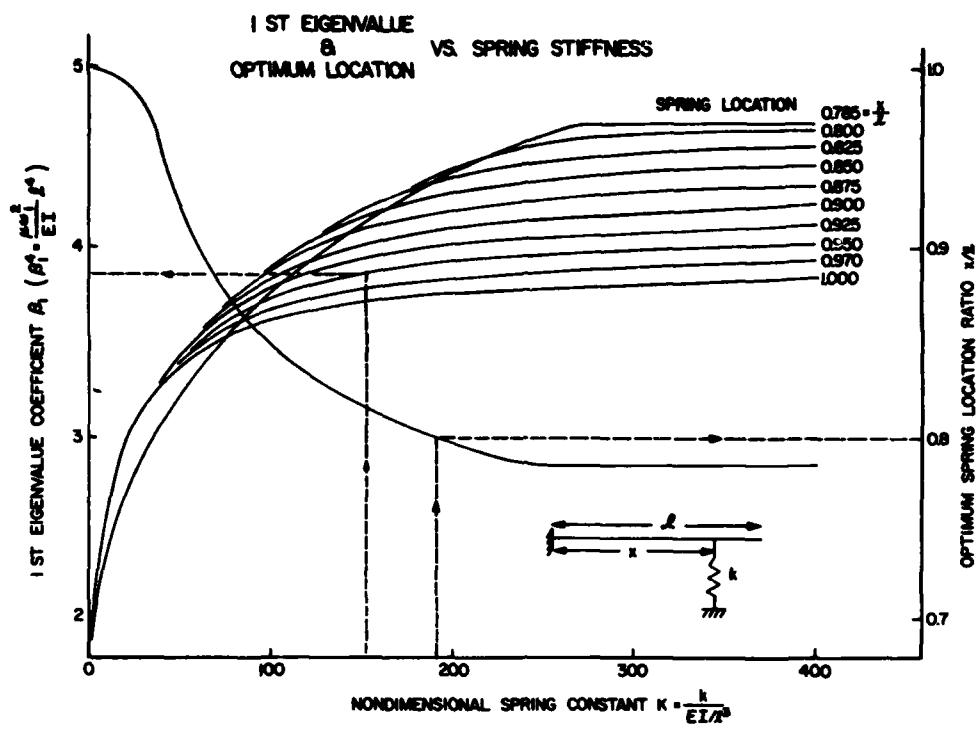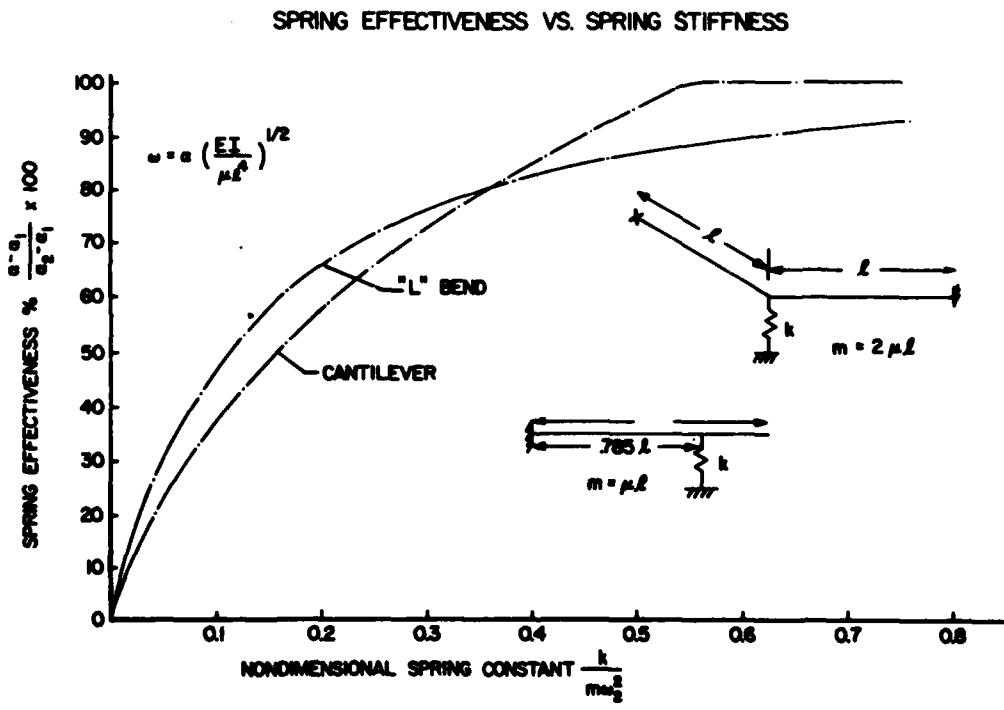
RESPONSE OF A HARDENING SPRING OSCILLATOR TO RANDOM EXCITATION

Joseph T. Kayanickupurathu
Research Fellow

and

John R. Curreri
Professor of M.E., Polytechnic Institute of N.Y.
Consultant - Brookhaven National Laboratory

The mean square response of a hardening spring oscillator with
viscous damping is developed by using a transfer function method,
assuming the non-linear system is linear. The purpose is to
determine the errors incurred in treating the hardening system
as though it were linear. The transfer function solution is
compared with equivalent linearization and a Fokker-Planck solu-
tion. The equivalent linearization solutions are shown to under-
estimate the mean square response while the transfer function
approach overestimates the response.

Many investigators have worked on
the non-linear response of the one de-
gree of freedom system subjected to ran-
dom white excitation. These studies,
in general, developed the equations for
the response either from Fokker-Planck,
equivalent linearization or perturba-
tion methods. It sometimes occurs,
either by design, by assumption, or by
lack of sufficient information, that a
non-linear system is treated as though
it were a linear system. In such cases,
a knowledge of the non-linear response
by itself is not used and the question
might be raised on the magnitude of
error incurred. In particular, suppose
that an unknown system is dynamically
tested to develop an input-output trans-
fer function by sweeping the frequency
of a sinusoidal input. If this transfer
function is used to predict the spectral
response of the system to any random in-
put, as is done in a linear system, an
error is incurred if the system is actu-
ally non-linear. An evaluation of this
error is investigated in this paper.
The size of the error is quantitatively
developed as a function of the non-
linear magnitude.

This paper develops the mean square
response of a hardening spring oscilla-
tor by the transfer function approxima-
tion method. This is accomplished by
deriving the transfer function of a
hardening type mechanical oscillator
with viscous damping. The transfer
function is squared and numerically in-
tegrated over the frequency range to
get the response. The results show the
magnitude of error involved in the mean
square response when it is developed on
the basis of a transfer function that
is obtained from tests for a non-linear
system that is assumed linear. An equi-
valent linearization solution based up-
on less restrictive assumptions than
have appeared in the literature is also
shown.[2][3][7] All results are com-
pared with a Fokker-Planck solution [10]
[11].

A Duffing's type mechanical oscil-
lator, having linear viscous damping
and hardening type spring elements, sub-
jected to random white excitation, is
considered. To develop a transfer func-
tion, an equivalent sinusoidal excita-
tion, is obtained. Using this, a

5

frequency-amplitude relation is developed. For any assumed amplitude the corresponding frequencies are evaluated. Making use of this, a transfer function is obtained. This transfer function exhibits multiple solutions depending upon the non-linearity and the level of the exciting force. The transfer function has two stable paths, one when the frequency is swept upwards and the other when the frequency is swept downwards past the resonance. Using these, the mean square response of the system is approximately evaluated.

The equation of the system investigated is of the form [1]:

$$\ddot{y} + 2\xi\omega_n\dot{y} + \omega_n^2(y+\epsilon^2 y^3) = F\cos(\omega t + \phi) \quad (1)$$

where

$$\dot{y} = \frac{dy}{dt} \qquad \omega_n^2 = \frac{k}{m} \qquad \xi = \frac{c}{c_c}$$

$$\epsilon^2 = \text{non-linearity (in}^{-2})$$

Equation (1) can be rewritten as:

$$\ddot{y} + 2\xi\omega_n\dot{y} + \omega_n^2(y + \epsilon^2 y^3) = B_1\cos\omega t - B_2\sin\omega t \quad (2)$$

where

$$B_1 = F\cos\phi \qquad\qquad B_2 = F\sin\phi$$

$$\phi = \tan^{-1}\frac{B_2}{B_1} \qquad\qquad F^2 = B_1^2 + B_2^2$$

Assume an approximate solution of the form
$$y(t) = A\cos\omega t \quad (3)$$

and substitute back to get:

$$y = \left(\frac{\omega_n^2}{\omega^2}A + \frac{3}{4}\frac{\omega_n^2}{\omega^2}\epsilon^2 A^3 - \frac{B_1}{\omega^2}\right)\cos\omega t +$$

$$\left(-2\xi\frac{\omega_n}{\omega}A + \frac{B_2}{\omega^2}\right)\sin\omega t + \frac{\omega_n^2\epsilon^2 A^3}{36\omega^2}\cos 3\omega t \quad (4)$$

Following the Duffing procedure, the equation relating the frequency, the amplitide, and the excitation becomes

$$\left(\frac{\omega^2}{\omega_n^2}\right)^2 + \left(\frac{\omega^2}{\omega_n^2}\right)[-2 + 4\xi^2 - \frac{3}{2}\epsilon^2 A^2] +$$

$$+ [1 + \frac{3}{2}\epsilon^2 A^2 + \frac{9}{16}\epsilon^4 A^4] = \left(\frac{Fo}{k}\right)^2\frac{1}{A^2} \quad (5)$$

The maximum value of A is obtained by differtiating equation (5) implicitly with respect to ω and setting $dA/d\omega = 0$.

$$\frac{A}{Fo/k} = \frac{1}{2\xi}\cdot\frac{1}{\sqrt{(1 - \xi^2 + \frac{3}{4}\epsilon^2 A^2)}} \quad (6)$$

The maximum amplitude given by equation (6) occurs at a frequency

$$\omega^2 = \omega_n^2 + \frac{3}{4}(\omega_n^2\epsilon^2)A^2 - 2(\xi\omega_n)^2 \quad (7)$$

In obtaining the mean square response of a linear system with random excitation the squared magnitude of the system transfer function is multiplied by the input spectral density and integrated over the input frequency range. This method of solution, in general, is not legitimate for the non-linear system. However, for very small non-linearities it is reasonable to adopt the above procedure to find an approximate result. The error incurred in treating a non-linear system as though it were a linear system is pursued here. Once an approximate solution is obtained by the experimental determination of the transfer function, we can determine its variation from the differential equation solution and hence establish how the experimental results compare with the analytical solution.

The temporal mean square response of a system is given by

$$\langle y^2\rangle = \int_{-\infty}^{\infty}|H(\omega)|^2 G(\omega)d\omega = 4\pi G_0\int_0^{\infty}|H(f)|^2 df \quad (8)$$

$$G(\omega) = G_0$$

where

H = complex frequency response
G = temporal spectral density

In equation (8) a factor of 2 is to account for the change in the limit and 2π for the change of circular frequency in rad./sec. to cps.

The integral in eq. (8) can be viewed as a sum in the following form

$$\langle y^2\rangle = 4\pi G_0\sum_i |H_i|^2(\Delta f)_i \quad (9)$$

where $|H_i|$ and $(\Delta f)_i$ are taken as indicated in Fig. 4. In eq. (9) $(\Delta f)_i$ is chosen in such a way that H is approximately linear in that range. The average value of H in the frequency interval is chosen since H has to be a single valued function at any interval.

The approximate mean square response is evaluated for different non-linearities as shown in Fig. 5. In this figure, the mean square response

6

obtained by the Fokker-Planck method and by the equivalent linearization procedure are also shown for comparison.

To solve eq. (1) by equivalent linearization, the parameter λ is introduced to get

$$\ddot{y} + 2\xi\omega_n\dot{y} + \lambda y - R = F(t) \qquad (10)$$

where

$$R = \lambda y - \omega_n^2(y + \epsilon^2 y^3) \qquad (11)$$

For an ideal white noise input, the mean square response is $E[y^2] = \dfrac{\pi S_o \omega_n^3}{2\xi\lambda}$. Using equivalent linearization, form $E[R^2]$ and then set

$$\frac{\partial E[R^2]}{\partial \lambda} = 2\lambda E[y^2] - 2\omega_n^2(E[y^2] + \epsilon^2 E[y^4])$$

$$= 0 \qquad (12)$$

Therefore

$$\lambda = \omega_n^2\{1 + \epsilon^2 \frac{E[y^4]}{E[y^2]}\} \qquad (13)$$

where the terms in the bracket must be evaluated.

By assuming that ϵ is small, an approximation to $E[y^2]$ has been shown to be

$$E[y^2] = \sigma_o^2[1 - 3\epsilon^2\sigma_o^2 + 9\epsilon^4\sigma_o^4 \pm \ldots]$$

$$\text{for } |3\epsilon^2\sigma_o^2| < 1 \qquad (14)$$

If the assumption is made that the forth moment is approximately linear, an expression for $E[y^2]$ with only the first two terms is obtained. If, however, neither $E[y^2]$ nor $E[y^4]$ are assumed linear but are given by a Gaussian distribution, then

$$E[y^2] = \frac{\sigma_o^2}{1 + 3\epsilon^2 E[y^2]} \qquad (15)$$

which when solved and expanded in a binominal series gives

$$E[y^2] = \sigma_o^2[1 - 3\epsilon^2\sigma_o^2 + 18\epsilon^4\sigma_o^4 - $$

$$- 135\,\epsilon^6\sigma_o^6 +- \ldots] \qquad (16)$$

Eqs. (14) and (16) are plotted in Fig. 5. These are compared with a Fokker-Planck solution. It is seen that this approximation which results

in eq. (16) is closer to the Fokker-Planck solution. However, all three equivalent linearization approximations are below while the transfer function approximation method is above the Fokker-Planck curve. Only for small non-linearities ($\epsilon^2\sigma^2 < 0.01$) are the differences in the curves small. Above this, the differences are appreciable.

REFERENCES

1. Stoker, J. J., Non-linear Vibrations in Mechanical and Electrical Systems, Interscience, New York, 1950.

2. Notes for the MIT Special Summer Program on Random Vibration, edited by Crandall, S. H., 1958.

3. Lyon, R. H., "Equivalent Linearization of Hard Spring Oscillator", Jn. of Acoust. Soc. Am., 32, 1960, pg. 1161-1162.

4. Lyon, R. H., "On the Vibration Statistics of Randomly Excited Hard Spring Oscillator", Jn. of Acoust. Soc. Am., 32, 6, pg. 716-719.

5. Lyon, R. H., "On the Vibration Statistics of a Randomly Excited Hard Spring Oscillator, II", Jn. of Acoust. Soc. Am., 33, 1961, pg. 1395-1403.

6. Lyon, R. H., Heckl, M. and Hazelgrave, C. B., "Response of Hard Spring Oscillator to Narrow Band Excitation", Jn. of Acoust. Soc. Am., 33, 10, 1961, pg. 1404-1411.

7. Caughey, T. K., "Equivalent Linearization Technique", Jn. of Acoust. Soc. Am., Vol. 35, N11, 1963.

8. Crandall, S. H., "Perturbation Techniques for Random Vibration of Non-linear Systems", Jn. of Acoust. Soc. Am., V35, N11, 1963.

9. Subudhi, M., "On the Steady-state Response and Stability of Non-linear Two-Degree-of-Freedom Systems", (Ph.D. Thesis), Polytech. Inst. of New York, New York, 1974.

10. Wasmund, R. H., "Random Vibration of Certain Mechanical Systems", Report for M.S.M.E., Polytechnic Institute of Brooklyn, New York, 1965.

11. Kayanickupurathu, J. T., "Random Vibrations of Discrete Non-Linear Mechanical Systems", (Ph.D. Thesis), Polytech. Inst. of New York, NY, 1975.

7
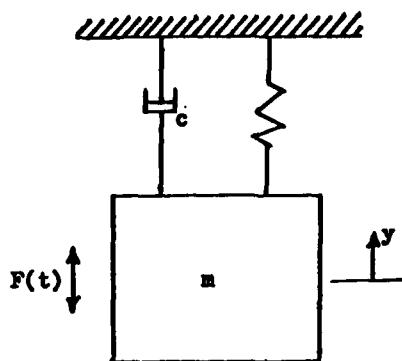
FIG. 1.   SINGLE DEGREE OF FREEDOM SYSTEM

FIG. 2.

FREQUENCY RATIO, $\frac{f}{f_n}$
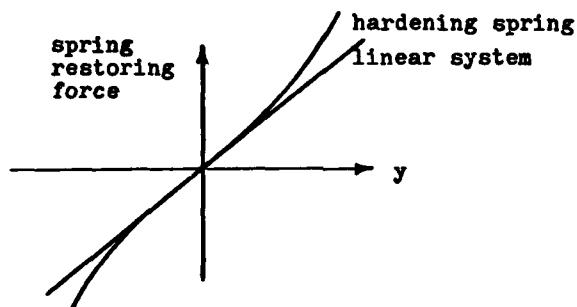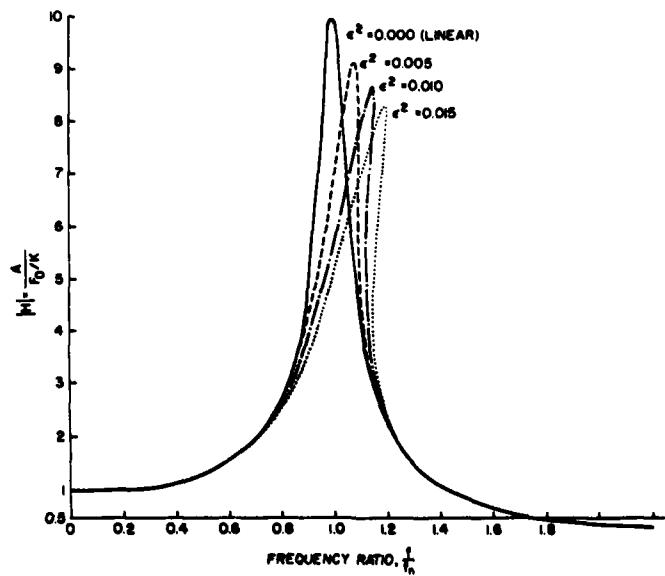
FIG. 3.   RESPONSE OF ONE
DEGREE OF FREEDOM
SYSTEM FOR DIFFERENT
NON-LINEARITIES,
$C/C_c = 0.05$, $F_0/k = 0.7698$ IN.

8
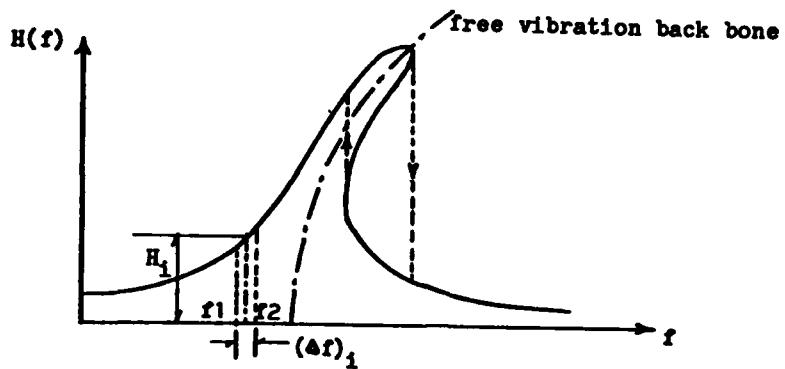
FIG. 4. STEADY STATE RESPONSE OF STIFFENING SYSTEM AS A FUNCTION OF FORCING FREQUENCY

FIG. 5
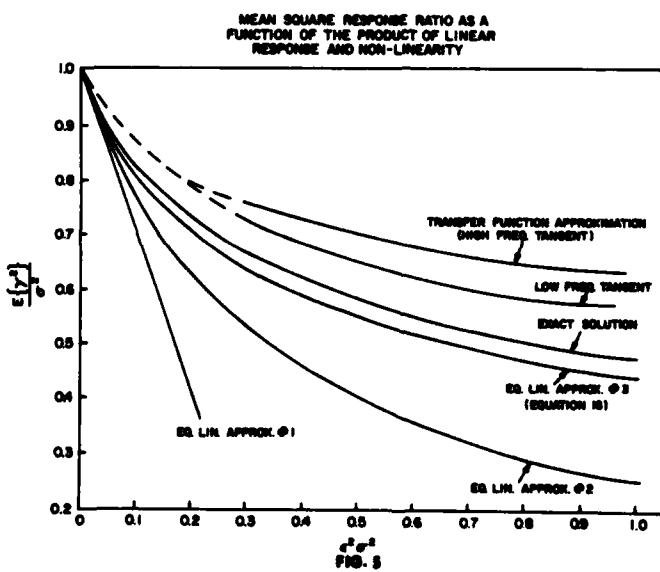
NON-LINEAR DYNAMIC RESPONSE OF A MULTI-MASS SYSTEM WITH GAPS*

Bernard Koplik** and Morris Reich***

Department of Applied Science
Brookhaven National Laboratory
Upton, NY 11973

The dynamic response of a multi-mass system with gaps
is investigated for a sinusoidal input forcing function.
Using a High Temperature Gas-Cooled Reactor core as a
model, results are obtained for the dependence of reso-
nant frequency on total clearance and distribution of
mass. Numerical results using the OSCIL computer pro-
gram show that an increase in total clearance is accom-
panied by a reduction in the peak forces developed
while the initial distribution of clearance between ad-
jacent elements has no effect on the system response.
Further investigation reveals that the non-linear re-
sponse is invariant for reduced mass representations.

The dynamic response of an "N" de-
gree of freedom in-line system of
masses and springs subjected to a sinu-
soidal forcing function has been
thoroughly investigated in the litera-
ture. In addition, the dynamics of a
single mass and spring separated by a
gap has received considerable attention
and the solutions are well documented.
However, there is little information
available on the response of a multi-
mass system in which gaps initially
exist between adjacent masses and
springs and supports. This paper is
concerned with the dynamics of an "N"
degree of freedom in-line system with
non-linearities introduced due to gaps
or clearances between elements of the
system. In particular, the ability to
analyze the response of a complex non-
linear system with gaps by using a model
with a reduced number of masses is de-
monstrated.

Although the dynamic response of
a multi-mass system with gaps is of
general interest for a number of de-
sign applications, this present paper
utilizes a model of a High Temperature
Gas-Cooled Reactor (HTGR) core for the
purpose of obtaining numerical results.
The HTGR core under consideration con-
sists of several thousands of hexagonal
elements arranged in vertical stacks
containing about eight elements per
stack. There are clearance gaps be-
tween adjacent elements, which can
change substantially due to radiation
effects produced during their active
lifetime. Surrounding the outer peri-
phery of the core are reflector blocks
and restraining spring-pack arrange-
ments which bear against the reactor
vessel structure. The impending sinu-
soidal forcing function will result in
multiple impacts between the reflector
blocks and the restraining spring packs.
This leads to a highly complex non-
linear response associated with the
multiple collisions across the clear-
ance gaps and with the spring packs.

To stimulate the response of this
system, a model using a single row, or
slice, of horizontal elements was
adopted for the dynamic investigations.
Actual clearances as well as the total
mass of a typical horizontal slice

were used. A pictorial representation
of the analytical model is shown in
Figure 1, which represents an "N" mass
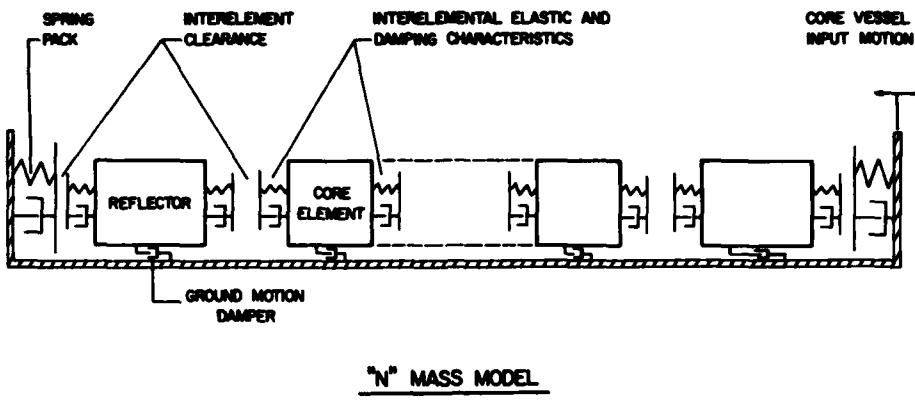
"N" MASS MODEL

Figure 1

model. The input motion is supplied by
the horizontal displacement of the core
vessel. The spring packs include the
actual elastic members in the core
structure as well as the hard elastic
stop of the vessel wall itself. Inter-
elemental elastic and damping coeffi-
cients are derived from the element geo-
metry and material characteristics. Co-
efficient of restitution data was
obtained from a model test using
graphite. The viscous interelemental
damping coefficients in the analytical
model were adjusted to duplicate the
energy dissipated during a collision
in the model test. The viscous damping
coefficients of the ground-motion dam-
pers were evaluated on the basis that
they would dissipate the same energy
per cycle as ground friction.

In order to solve for the response
of the system, a computer program, OSCIL
{1}, was developed which is capable of
handling "N" masses with gaps and in-
cludes the interelemental elastic and
damping characteristics. The program
has the flexibility to handle the in-
puts and outputs in terms of displace-
ments, velocities, or accelerations as
well as forces. For this study, har-
monic displacements were prescribed as
the input by specifying the amplitude
and frequency at the reactor vessel wall
which is the boundary of the system.

Both numerical and graphical outputs
were obtained specifying the displace-
ments and interelemental forces devel-
oped for various mass distributions and
gap sizes.

Using the OSCIL code a lumped mass
system was investigated in which the
total mass, total clearance space, in-
terelemental damping, and forcing fre-
quency and amplitude were all held con-
stant. For these runs the total mass
was distributed into 5, 7, 9, and 30
individual lumped masses. Results of
the analysis are shown in Figure 2,
which presents graphical strip charts
for reactor vessel inputs as well as
core response outputs for the various
lumped mass models. In these plots, the
strip (or long axis) is the time coor-
dinate, while the dimension across the
strip (the short axis) gives the indivi-
dual mass point displacements. Each
mass is represented by a single trace.
Where the clearance between adjacent
mass points goes to zero, a single
trace then shows the path of the clumped
masses. In all the strip chart plots,
the two boundary or outermost traces,
represent the input vessel motions. A
comparison of the displacement time-
histories of the various mass systems
all excited at 11.4 rad/sec, the natural
frequency of the identical system with-
out clearance, reveals different

12
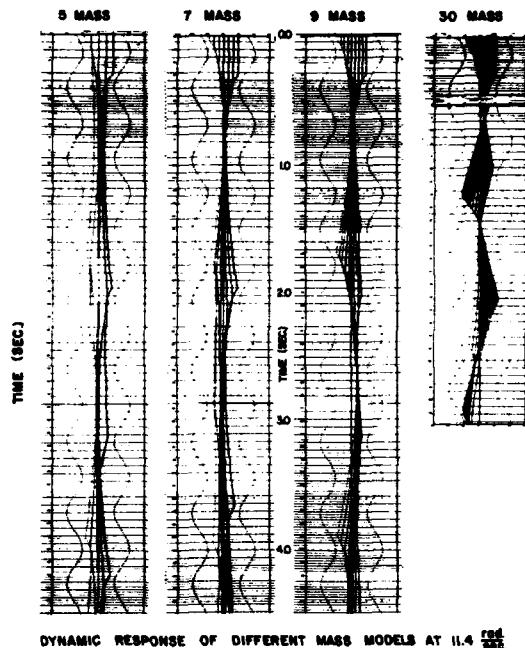
DYNAMIC RESPONSE OF DIFFERENT MASS MODELS AT 11.4 $\frac{rad}{sec}$
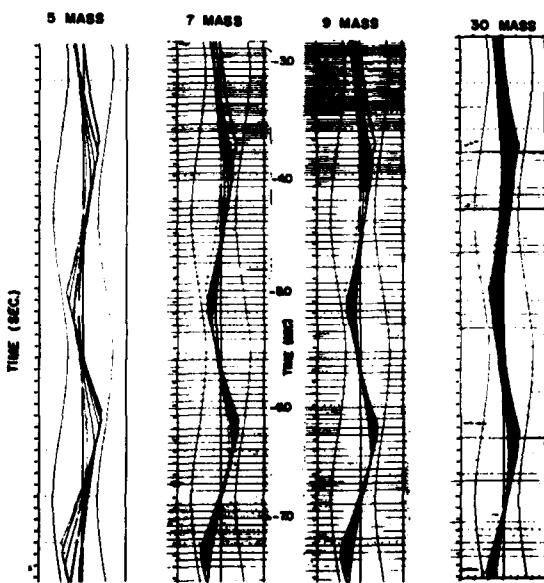
Figure 2

DYNAMIC RESPONSE OF DIFFERENT MASS MODELS AT RESONANCE

Figure 3

13

response characteristics for the four cases considered. Both the displacements as well as the forces developed vary considerably from case to case. Although only the first five seconds of response are shown in Figure 2, runs have been carried out for as long as thirty seconds {2} with no trend towards any similarity in response developing.

In Figure 3 the dynamic responses of the identical lumped mass systems are shown for an excitation at the resonant frequency (or frequency of maximum response) with all other parameters remaining fixed. It shows that, at this frequency, responses of all the mass systems have similar characteristics. Indeed, under the conditions stated above, the five-mass system has the same natural frequency as the thirty-mass system. In addition, an examination of the forces developed at the wall of the vessel shows that the maximum forces are the same for each of the mass representations. Therefore, at resonance, a model using a reduced number of masses is capable of representing the dynamic response of the more complex system. This is found to be true despite the high degree of non-linearity associated with a spring characteristic which represents a stiff structural member adjacent to a free space. The importance of this conclu-

sion is clearly demonstrated by the fact that the requirements for computer time would be prohibitive if a model using a reduced number of masses was not applicable. Further study shows that for extended runs at the resonant frequency, starting with different initial positions of the masses, the initial transients have largely disappeared after only ten seconds and identical steady-state motions are obtained. This is shown to be true for the entire spectrum of initial spacing of masses, from equally spaced to all masses clumped together, as long as the total clearance is held constant. This result, which demonstrates that the resonant frequency of the system is not altered if the total clearance is held constant, is also independent of the mass model chosen.

However, the effect of varying the total clearance has a dramatic effect on the resonant frequency of the non-linear system for a fixed input amplitude. Starting with a linear system without clearance, the resonant frequency was shown to be reduced by a factor of four as the total clearance was increased to 100% of nominal clearance. The results are plotted in Figure 4 with the resonant frequency dropping from 11.4 rad/sec without clearance to 2.52 rad/sec under conditions of nominal clearance. The procedure clearly establishes
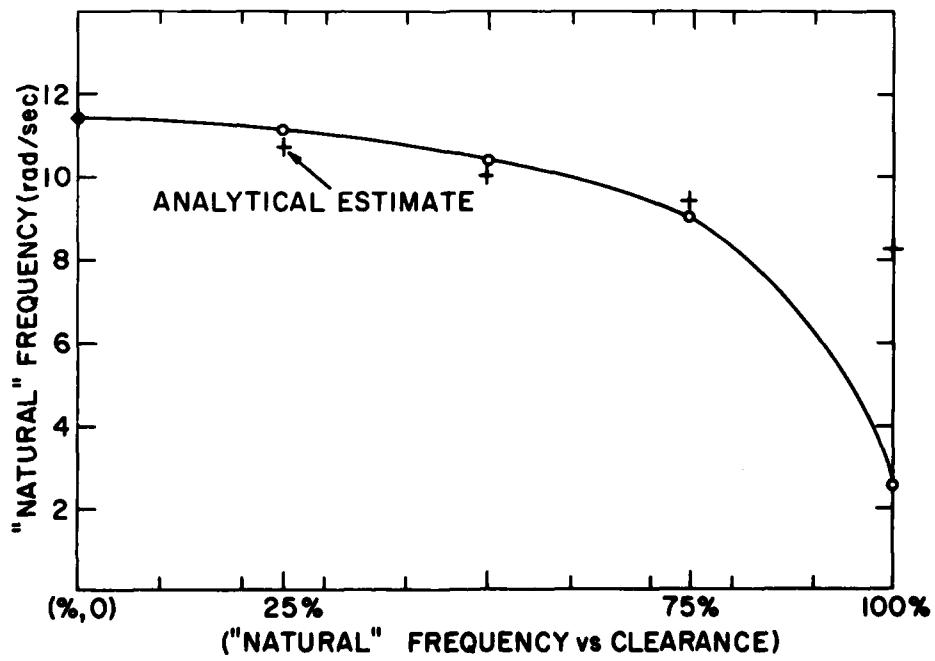
Figure 4

14

the dependence of resonant frequency and the development of peak forces on total clearance. Since during the lifetime of the HTGR core clearances may develop, further runs have been carried our for as much as 130% of nominal clearance {3}. As seen in Figure 4, although a very small clearance induces only slight departures from resonance, as the total clearance increases, the system becomes highly non-linear and the resonant frequency drops off significantly.

In conslusion, the present study demonstrates the successful implementation of an analytical model for the dynamic response of a multi-mass system with gaps such as an HTGR core, by using considerably fewer masses than the actual system, even though the problem is highly non-linear. The reduced mass model is capable of accurately predicting resonant frequencies and maximum induced forces for clearances that vary during the operational lifetime of the system.

References

1. "OSCIL: One-Dimensional Spring-Mass System Simulator for Seismic Analysis of High Temperature Gas-Cooled Reactor Cores", L. Lasker, Ed., BNL 21023, January, 1976.

2. HTGR Safety Evaluation Division, Brookhaven National Laboratory, Quarterly Report, BNL 50460, November, 1975.

3. HTGR Safety Evaluation Division, Brookhaven National Laboratory, Quarterly Report, BNL 50479, January, 1976.

Discussion

Mr. Roggio (Naval Air Engineering Center): How do you generate the stiffness and the damping characteristics at impact?

Mr. Bezler: For our studies so far, we have just modeled the stiffness using the length of the block and the axial stiffness of the material, that is we treat the block as if it were linear spring. To model the damping we ran some collision impact tests to measure the coefficient of restitution and related that back to an equivalent viscous damping.

Mr. Roggio: What was the criteria for the 10^{-10} t timestep?

Mr. Bezler: We use the gear integration scheme. It adopts a timestep consistent with what is happening in the system. As a collision occurs, it will adopt timesteps as small as 10^{-10}. As soon as the collision is over, it will then adopt a very coarse timestep such as 10^{-4} or 10^{-3}. It is actually built into this package and it does it automatically.

Mr. Roggio: Does it base this timestep on the stiffness and mass characteristics?

Mr. Bezler: That is correct.

Mr. Roggio: What ratio of mass to stiffness characteristic did he use?

Mr. Bezler: This is during a numerical time integration.

Mr. Roggio: What ratio of the period of the spring mass blocks does it use to come up with 10^{-10}? Or does it use it in your program?

Mr. Bezler: It doesn't use it at all. There is some sort of error function that you can specify in the beginning. It predicts the solution and then calculates the solution and that is the error involved. You specify how large you will let that error be from timestep to timestep at the outset. This is the criterion that it uses to select the timesteps. That package is available in the gear integration scheme.

AN IMPROVED DERIVATION OF THE DUNKERLEY-MIKHLIN FORMULA

John E. Brock
Professor, Department of Mechanical Engineering
Naval Postgraduate School
Monterey, California

A somewhat more elegant proof is given of the matrix form of the Dunkerley-Mikhlin formula, based upon the idempotency of the filtering matrix F.

It is the purpose of this brief report to provide a modified and somewhat more elegant derivation of the "Dunkerley-Mikhlin" formula which appears as equation (12) in references [1] and [2]. The present proof is self contained; the notation is the same as in references [1] and [2].

We consider and undamped linear vibrating system characterized by $N \times N$ symmetrical matrices K (stiffness) and M (mass). Suppose that there are p rigid body motions which are known (by inspection). If $p > 0$, K has no inverse. It is well known that there exists an $N \times N$ modal matrix U and an $N \times N$ diagonal matrix Ω^2 in which frequency squares are arranged in nondescending order, such that

$$KU = MU\Omega^2; \quad U^TMU = I_N \qquad (1a,b)$$

The first p columns of a valid expression for U may be constructed from the known rigid body modes by the usual Gram-Schmidt orthonormalization process. The first p diagonal positions in Ω^2 contain zeros.

Now conceptually add sufficient constraints so as to prohibit all rigid body modes. Let the stiffness of the modified system be K* with inverse C. Let $k > p$ be given. There exist numbers a_{jk} $(j=1,2,3,\ldots,p)$ such that the displacement vector

$$v_k = u_k + \sum_{j=1}^{p} a_{jk}u_j \qquad (2)$$

does not involve loading any of the new constraints not present in the original system. Thus

$$Kv_k = K^*v_k; \quad CKv_k = CK^*v_k = v_k \qquad (3)$$

The a_{jk} may be found as follows. For $k > p$ and $r \leq p$,

$$u_r^TMv_k = u_r^TMu_k + \sum_{j=1}^{p}a_{jk}u_r^TMu_j = a_{rk} \qquad (4)$$

Thus,

$$v_k = u_k + \sum_{j=1}^{p}u_j^TMv_ku_j = u_k + Av_k \qquad (5)$$

where $k > p$ and

$$A = \sum_{j=1}^{p}u_ju_j^TM \qquad (6)$$

is an idempotent matrix, viz.

$$A^2 = \sum_{j=1}^{p}\sum_{k=1}^{p}u_ju_j^TMu_ku_k^TM$$

$$= \sum_{j=1}^{p}u_ju_j^TM = A \qquad (7)$$

Thus we see that

$$u_k = Fv_k \quad (k > p) \qquad (8)$$

where the filtering matrix

$$F = I - A \qquad (9)$$

is also idempotent, viz.

$$F^2 = (I-a)(I-A) = I - 2A + A^2$$

$$= I - A = F \qquad (10)$$

It is thus clear that

$$Fu_k = 0 \quad (k \leq p) \qquad (11a)$$

$$F_uk = u_k \quad (k > p) \qquad (11b)$$

The truth of equation (10) can be seen immediately by inspection since once the first p components are removed from an arbitrary vector by an initial premultiplication by F, subsequent premultiplications by F leave the result unchanged.

From equation (3) we have

$$v_k = CKv_k = CKu_k + C\sum_{j=1}^{p}a_{jk}Ku_j$$

$$= CMu_k\omega_k^2 + \sum_{j=1}^{p}a_{jk}Mu_j\omega_j^2 = CMu_k\omega_k^2 \qquad (12)$$

17

for k > p. Thus

$$FCMFu_k = 0 \text{ for } k \leq p \qquad (13a)$$

$$FCMFu_k = u_k\omega_k^{-2} \text{ for } k > p \qquad (13b)$$

and these equations may be combined into the single matrix equation

$$FCMFU = U\Lambda \qquad (14)$$

where

$$\Lambda = \text{diag}\{0 \ 0 \ 0 \ \ldots \ \omega_{p+1}^{-2} \ \omega_{p+2}^{-2} \ \ldots \ \omega_N^{-2}\} \qquad (15)$$

Thus we may write

$$\Lambda^n = (U^{-1}FCMFU)^n \qquad (16)$$

where n is any positive integer and by taking traces we have

$$\sum_{k=p+1}^{N} \omega_k^{-2n} = \text{tr}[\Lambda^n] =$$

$$= \text{tr}[U^{-1}F(CMF)^nU] = \text{tr}[(CMF)^n]$$

$$= \text{tr}[Q^n] \qquad (17)$$

where

$$Q = CMF \qquad (18)$$

An explicit formula for v_k, viz.

$$v_k = CKu_k \quad (k > p) \qquad (19)$$

may be obtained from equation (12). Equation (17) above, obtained by noting the idempotency of F and the equality tr[AB] = tr[BA], is the Dunkerley-Mikhlin formula in matrix form, the same as equation (12) in references [1] and [2].

(One should note an error in the F_{23} term on page 8 of reference [1]; this term should be -36 rather than 36. The error is not propagated in subsequent calculations therein.)

It may also be useful to add another example of the application of the general method in a case involving (one) rigid body mode and both lumped and distributed mass. Consider the flexural vibrations of a uniform elastic bar of length L and mass ρM, freely hinged at the left and having a concentrated mass (1-ρ)M at the right. A constraint against rotation at the left is conceptually added, giving the compliance function

$$z(x,y) = (3xyw-w^3)/6EI \qquad (20a)$$

$$w = \text{Min}\{x,y\} \qquad (20b)$$

The mass distribution is

$$m(x) = \rho M/L + (1-\rho)M\delta(x-L) \qquad (21)$$

The rigid body mode is a rotation about the left end, viz.:

$$u_1(x) = \theta x; \quad \theta^{-2} = ML^2(1-2\rho/3) \qquad (22a,b)$$

the value of θ being obtained by normalizing. Straightforward calculations lead to

$$\omega_2^{-2} < \sum_{k=2}^{\infty} \omega_k^{-2} = \frac{\rho ML^3(7-6\rho)}{210EI(3-2\rho)} \qquad (23)$$

A Rayleigh estimate based on the assumed deflection

$$y = x\left[\frac{(12-9\rho)}{(12-8\rho)} - x\right] \qquad (24)$$

gives

$$\omega_2^{-2} > \frac{\rho ML^3(24-37\rho+14\rho^2)}{320EI(3-2\rho)^2} \qquad (25)$$

and a mixture

$$\omega_2^{-2} = \frac{2\times(\text{Formula 24}) + (\text{Formula 25})}{3}$$

$$= \frac{\rho ML^3(1848-2825\rho+1062\rho^2)}{20160EI(3-2\rho)^2} \qquad (26)$$

has a maximum error of 0.44% in the range $0 \leq \rho \leq 1$ when compared to the exact solution

$$\omega_2^{-2} = \rho ML^3/EI\beta^4 \qquad (27)$$

where β is the smallest positive root of the equation

$$\rho[\cot(\beta) - \coth(\beta) + 2\beta] = 2\beta \qquad (28)$$

The mixture indicated in the approximation, equation (26), was obtained by comparing with the readily available elementary solutions for the cases ρ = 0 and ρ = 1.

REFERENCES

1. J. E. Brock, "DM Approximations for the Gravest Frequency of a Vibrating System," Technical Report NPS-59BC75111 Naval Postgraduate School, Monterey, California, November 1975.

2. _____, "Dunkerley-Mikhlin Estimates of Gravest Frequency of a Vibrating System," J. Appl. Mech., Vol. 43, E, No. 2 (Vol. 98 of ASME Trans.) June 1976, p. 345.

RECENT ADVANCES IN

FAILURE ANALYSIS BY STATISTICAL TECHNIQUES (FAST)

W. H. Rowan
TRW Defense and Space Systems Group
Redondo Beach, California

ABSTRACT

The FAST technique has evolved over the past ten years through its application to vulnerability analysis of strategic systems. The technique can be used to assess the hardness of a system at any phase in the system's development, from concept development of new systems to hardness upgrade of existing systems. Recently, the FAST algorithm has been modified to reduce computer time by more than an order of magnitude and to enable much more information to be extracted from the calculation.

The paper reviews the orignal FAST algorithm and then discusses the new development. The basis of the new algorithm is presented and its application to three areas is discussed. These areas comprise:

1) Potential development of a system of all effects target vulnerability descriptors.

2) Automated capability supporting hardness design trade studies.

3) Capability for data base evaluation, by determining the sensitivity of system response to underlying data base inaccuracies.

1.0 Introduction

The growth of strategic weapon systems from 1950 - 1960 brought the need for quantitative techniques for assessing nuclear survivability. Failure Analysis by Statistical Techniques (FAST) was developed for the Air Force's Space And Missile System's Organization (SAMSO) during the last decade to satisfy this need. The evolution of the FAST methodology has been documented in the Shock and Vibration Bulletin [Reference 1] and as a User's Manual sponsored by the Defense Nuclear Agency [Reference 2]. Following a quick review of the present documentation, this report continues with the recent advances in the methodology.

The FAST methodology has been applied to in-place systems to evaluate inherent system hardness or the benefit of hardness improvements. It also has wide applicability to the hardness/ survivability evaluation of any military system and can be applied to civilian systems as well.

In the early development of FAST there was recognition of the need for a statistical approach to account for modeling uncertainties and random variations in geology and construction. The more recent work at TRW has demonstrated that target vulnerability may be adequately modeled by a simplified statistical model that permits accurate calculation of the probability of damage to a target attacked by a nuclear weapon. Because of this finding, it was possible to modify the FAST calculation and achieve three substantial results:

1. Computation costs are significantly reduced by as much as one or two orders of magnitude.

2. Much more information is extracted from a FAST calculation.

3. A multi-environment target vulnerability/survivability assessment system can be developed.

Targets may be classified in various ways. They may be point, line, or area targets. Or they may be single entities or a complex of similar or different entities. Furthermore, a single target entity may be subjected to weapon effects from a single weapon or from multiple weapons; and the case of multiple weapons would further complicate the analysis because in general the probabilities of survival against successive weapons are not independent. The mathematical tools to be discussed apply to all these situations. But the discussion in this

report will be limited to point targets attacked by a single weapon.

Target vulnerability is defined in terms of the damage function, which gives the probability that a specified weapon will cause a specified level of damage as a function of position with respect to the target, including height of burst if appropriate. The damage criterion is defined at any appropriate level. Typical examples of damage criteria include denial of partial mission capability denial of complete mission capability or making the target completely unavailable to the user after the attack.

To define target survivability, we shall assume that a single weapon of specified yield and height of burst is delivered against a target of interest with a random miss distance depending on the weapon impact distribution about the aim point. Target survivability is then defined as the probability the target survives. The next paragraph outlines the report contents.

First, the original FAST calculation as documented in References [1] and [2] is reviewed. Then following the probability of damage accuracy study, which paved the way for the new FAST method of calculation, the new calculation procedure is described, showing the reduction in computer cost that may be expected. The new method is implemented by means of the interactive FAST Data Analysis System, which permits the user to develop the Integrated Nuclear Damage Assessment System (INDAS), a major result of the new method. The report concludes by discussing the second major result of the new method, the calculation and use of sensitivity/correlation coefficients for such purposes as system optimization and data base prioritization.

2.0 Summary and Conclusions

The report first reviews the original Failure Analysis by Statistical Techniques (FAST) methodology (References [1] and [2]) to describe how FAST can assess the hardness of any military or civilian system and provide basis for discussing the recent advances.

A system damage criteria is postulated, such as inability to accomplish the mission or submission during a specified period after an attack. The system is functionally analyzed to determine all of the potential failure mechanisms; and a system network diagram is constructed, showing appropriate series/parallel relationships between the various failure mechanisms. Each failure mechanism is represented by a component in the system diagram from which FAST automatically

constructs a set of system network equations for calculating system failure probabilities.

Three kinds of data are required for each component: component resistances, or fragilities, which are functions giving the probability of component failure as a function of internal response to a hostile environment; transfer functions, which convert hostile free-field environments into internal response; and scaling laws, which relate free-field environments to the position of the detonation with respect to the target. For each of the three classes of data, estimates of random and systematic variations and of correlations are required. The original FAST code assumes a specified position between the detonating weapon and the target.

Environment scaling laws and transfer functions are applied to predict local responses within the facility, which, in turn, are compared with the fragility to establish the probability of failure for each of the components. The probabilities of failure are then combined in system network equations to obtain the system failure probability. At each stage of the calculation, the fragilities, transfer functions, and free-field environments, are drawn from appropriate distributions of random and systematic variation.

The Monte Carlo sampling process is exercised in two stages: an inner loop, in which random variations are sampled and an outer loop in which systematic variations are sampled. In the inner loop an averaging process suppresses the linear effects of random variation. The outer loop serves to determine the distribution of systematic variation of probability of survival induced by systematic variations on the inputs. A damage function is generated by repeating the process at a preselected set of separations between the weapon and the target.

Damage functions are ordinarily input to the calculation of target survivability when the system is attacked by a weapon of specified yield and delivery accuracy. TRW has studied the most commonly used methods for calculating target survivability to determine the effect on their accuracy when assumptions regarding the form of the damage function are not satisfied. To summarize this study one of the major findings is that a normal distribution model of the damage function can provide accurate probability of survival calculation even when the actual damage function is far from being normal. From this, it follows that the FAST calculation can be executed in a new way, estimating only the mean and standard deviation of the damage function since these parameters define the normal distribution, and that this would provide a number of benefits mentioned in the introduction.

The new FAST approach executes the calculation in the inverse mode of the original approach. The new approach randomizes on the random and systematic variations of the fragility distribution to select a local environment, which is converted, by means of an inverse transfer function, to a free-field environment and then to a damage distance by means of environment scaling laws. The Monte Carlo sampling process is used in this fashion to generate the distribution of damage distances. At each iteration, the system damage distance together with other parameters of interest, such as randomized weapon yield and height of burst, are placed into a data vector which is stored in a data matrix. The data matrix is analyzed by the FAST Data Analysis System to obtain regression coefficients relating figures of merit such as the system damage distance to other parameters of interest such as weapon yield and height of burst.

For one application of the new methodology such data are tabulated into a handbook for a variety of strategic and tactical targets useful to targeteers, weapon system designers, and others for conveniently regenerating damage functions for targets of interest. Such a target vulnerability system is called the Integrated Nuclear Damage Assessment System (INDAS). It organizes the regression coefficients for each target into a coded string of alphanumeric characters which enable a user to regenerate damage functions for targets of interest. These damage functions take into account all of the nuclear weapons environment.

For a second application of the new approach, the data matrix can also be analyzed to generate sensitivity data for optimization of the system hardness. The optimization can then be done either on a technical or cost effectiveness basis.

Sensitivity data from the data matrix can also be used to upgrade the data base for a system. In the design of a system, safety factors are needed to compensate for uncertainty in the various phenomenological and system response models. If the uncertainty of key inputs can be reduced, the associated safety factors can be reduced and, thereby, the system cost as well. The discussion shows how the key uncertainty factors can be identified and prioritized to provide a basis for planning test and analysis programs for reducing the key uncertainties.

3.0   FAST Methodology

A brief discussion of the original methodology of the FAST technique is appropriate here to show how it can be used to calculate weapon system damage functions. The vulnerability of a complex system subjected to a hostile environment is evaluated or assessed by calculating the probability of response of each component to the hostile environment, determining the probability of failure of each component to that response,

and combining the component probabilities to obtain the failure probability of the system. The FAST code has been designed to perform this evaluation in such a manner that studies in parametric sensitivity, trade-off, and optimization can be readily accomplished.

The mission of a typical system is identified, and a level of damage sufficient to preclude mission performance is defined as system failure. After all system components are identified, they are cataloged. To facilitate the cataloging, components can be grouped into subsystems. Then the possibility of each component or subsystem directly or indirectly contributing to the system failure is ascertained. The individual failure mechanisms and resistance levels of the components are determined and related to parameters of the hostile environment.

A diagram describing the FAST methodology (Figure 1) illustrates how, for a simplified system, selected parameters of a total hostile environment may be critical to the survivability of a hardened system. The free-field environments are transformed by transfer functions to establish local system responses to the environments, which are in turn used to predict component failure probabilities.

In the FAST code, each component failure probability is modeled by a fragility curve that defines for the component or subsystem the probability of failure as a function of the local system response to the free-field environments. Component probabilities of failure are combined in system network equations to compute system probability of survival. The system network is a functional description, which specifies the series/parallel relationship between components. Components are in series if an essential system function requires the performance of all components, and they are in parallel if the essential function can be performed by any one component.

One of the most valuable features of FAST is its treatment of the underlying uncertainties in predicting system hardness. Of the four system/environment inputs, the system network is the only one which must be known exactly. The coding acknowledges and accommodates finite uncertainty in modeling transfer functions, component fragilities, and environments. Uncertainty in environment estimates is often due to the lack of adequate analytic or empirical models for scaling nuclear weapon effects. This is also true of the uncertainties ascribed to transfer functions. In component fragilities, uncertainties are primarily a consequence of insufficient data on components at levels near and beyond failure.

Two categories of variations are recognized by the FAST code, namely random and systematic variations. The fundamental difference between them is that a systematic variation represents potential errors of a system model and extends uniformly over a population of facilities; whereas random variations extend nonuniformly
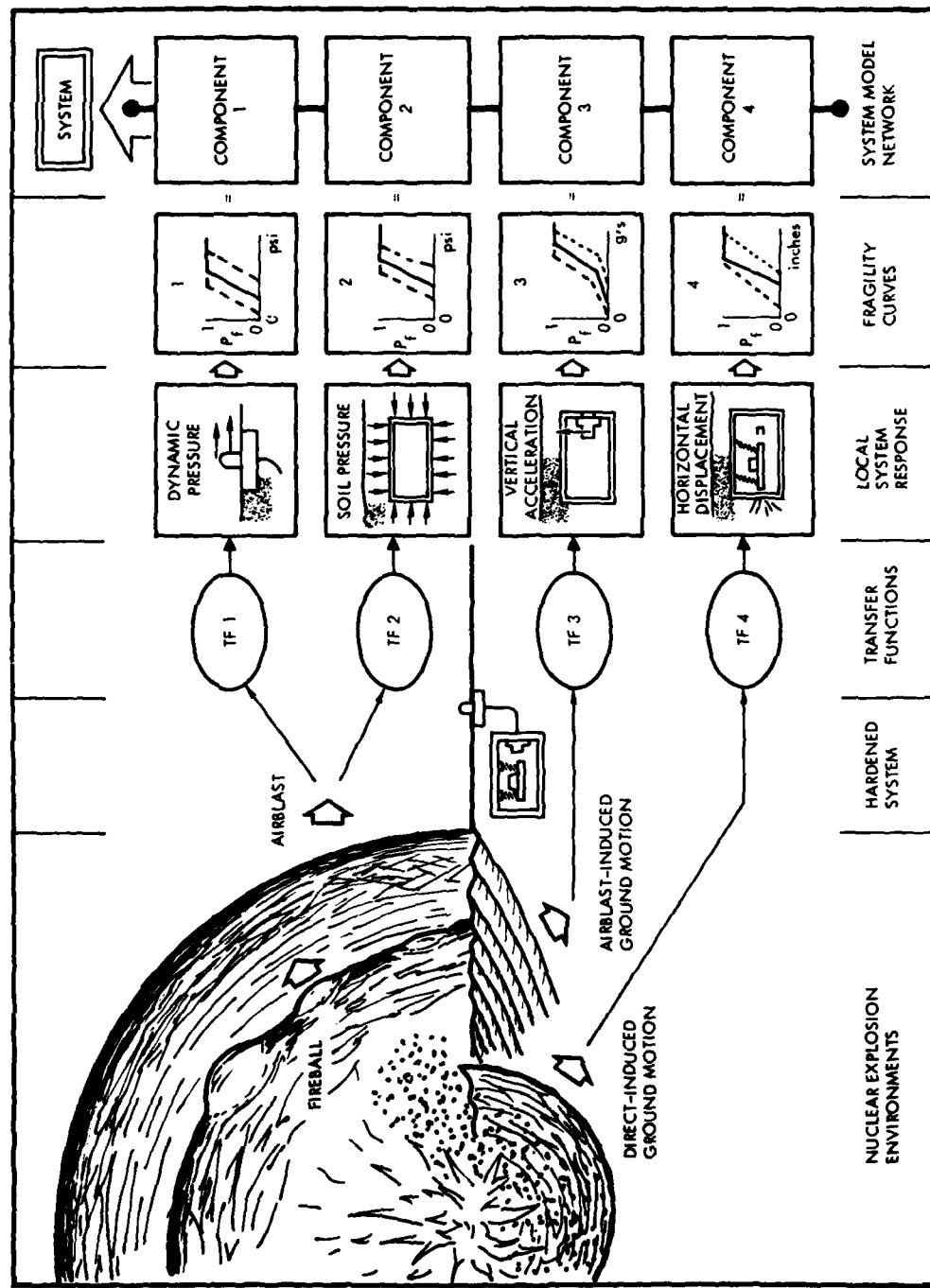
FIGURE 1. OVERVIEW OF THE FAST METHODOLOGY

from one facility to another. Random variations tend to average out over a large population, whereas systematic variations do not. It is noted that systematic variations may usually be reduced by test or analysis programs which improve models of the phenomenology and system behavior. The effects of random variations may also be reduced under some conditions. The FAST code treats both random and systematic variations of fragilities, transfer functions, and environments.

Another important feature of FAST is that the code accounts for correlation or covariance between variables. For example, if two components are affected by strongly correlated environments, both would either tend to fail or tend to survive, with the probability of both surviving being higher than if the environments are uncorrelated. Alternatively, if the environments are negatively correlated (anti-correlated), the probability of system survival can be substantially less than for the uncorrelated case. Relatively strong correlation or anti-correlation between environments is not unusual. For example, a specific system might be vulnerable to a combination of air-induced ground shock, direct-induced ground shock, and debris. Each of these is strongly affected by soil stiffness and, therefore, is anti-correlated, correlated, and anti-correlated, respectively, with soil stiffness.

An overview of the original FAST computation process is diagrammed in Figure 2 for a simplified system of just two components. These components together with their associated fragilities, transfer functions, and environments are denoted by the superscripts 1 and 2. The FAST code accomplishes the sampling process in two stages, to distinguish between random and systematic variations.

The first stage, accomplished in an outer loop of the code, selects bias values from the systematic variation distributions for the fragilities, transfer functions, and environments. This is illustrated by the point (e_1, e_2), selected from the environment systematic variation distribution in the left-hand panel in Figure 2, by the selection of the solid lines labeled TF1 and TF2 from the transfer function systematic variation distributions, and by the selection of the solid lines labeled fragility 1 and fragility 2 from the fragility systematic distributions.

The systematic variations defined in the outer loop are passed to the inner loop where the second stage of the sampling process is accomplished. The middle panel of Figure 2 shows how values are selected from the random variation distributions for the environments and transfer functions. The environment values are chosen from the multivariate distribution defined by the mean (e_1, e_2) and the random covariance matrix. One such selection is indicated by the symbol * in the inner loop distribution

diagram of Figure 2. The component probabilities of failure are calculated by multiplying the appropriate free-field environment value by the corresponding transfer function and comparing the resulting response parameter to the fragility curve. Next, system network equations are used to combine the component probabilities of failure and obtain subsystem and system probabilities of failure.

The inner loop process is repeated until sample size or convergence criteria are satisfied. The mean probability of failure is computed from accumulated inner loop sample statistics for every component, subsystem, and system. These sample means constitute the output from a single outer loop iteration. The process is repeated for many outer loop iterations, accumulating the probability of failure data (inner loop sample means) in histogram format, as shown at the right of Figure 2. This process continues until outer loop sample size criteria are satisfied. The histogram output from the outer loop iterations forms the survivability statistics.

These calculations are described for a single miss distance. To generate the entire damage function the process is repeated for a number, typically 5 or 10, or other miss distances.

Results of FAST calculations can be displayed in various formats as illustrated in Figure 3. One important display is that of system probability of damage, together with associated uncertainty, as a function of overpressure (see upper left of the Figure 3). In the upper right of this figure is plotted the median value of the probability of damage of the system and its subsystems, as functions of overpressure. This output format is valuable for identifying subsystems which are weak-link items, and hence potential candidates for hardening.

The other three diagrams of the figure each show the median probability of damage of a critical subsystem, together with the medians of the components, all as functions of overpressure. This format enables components that are weak links in the subsystem to be identified. Taken together, these displays identify the subsystems and components contributing most to the failure of the system.

The next section reviews the TRW probability of damage accuracy study, which opened the way to the new FAST calculation procedure, subsequently described.

4.0 Probability of Damage Accuracy Study

Frequently, the FAST outputs, or damage functions described in the previous section, are used as an input to the calculation of target survivability, which is the most significant figure of merit. For this reason, TRW undertook a study of the influence of the mathematical form of the damage function on the accuracy of

23
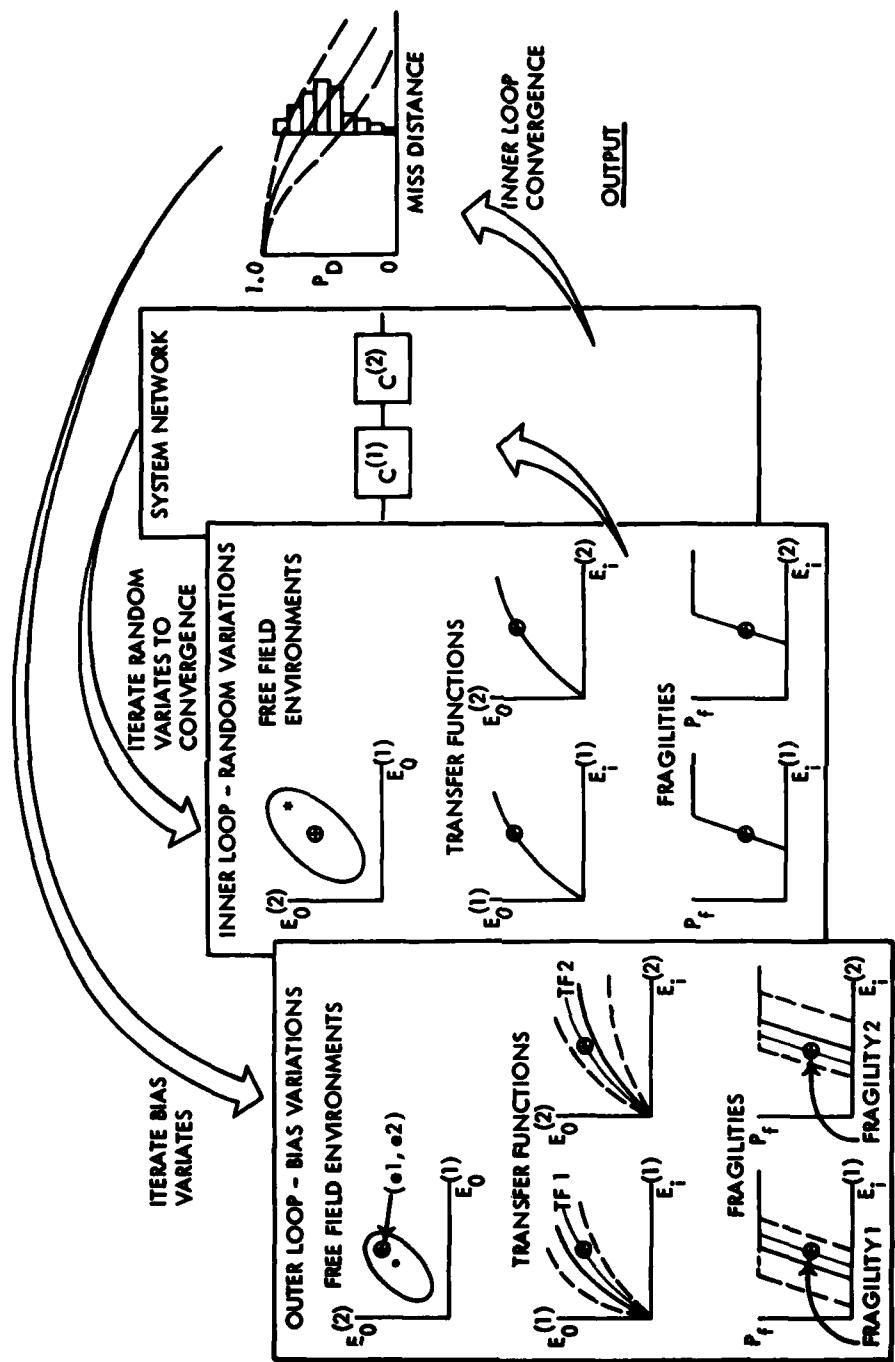
FIGURE 2. ORIGINAL FAST COMPUTATION PROCESS
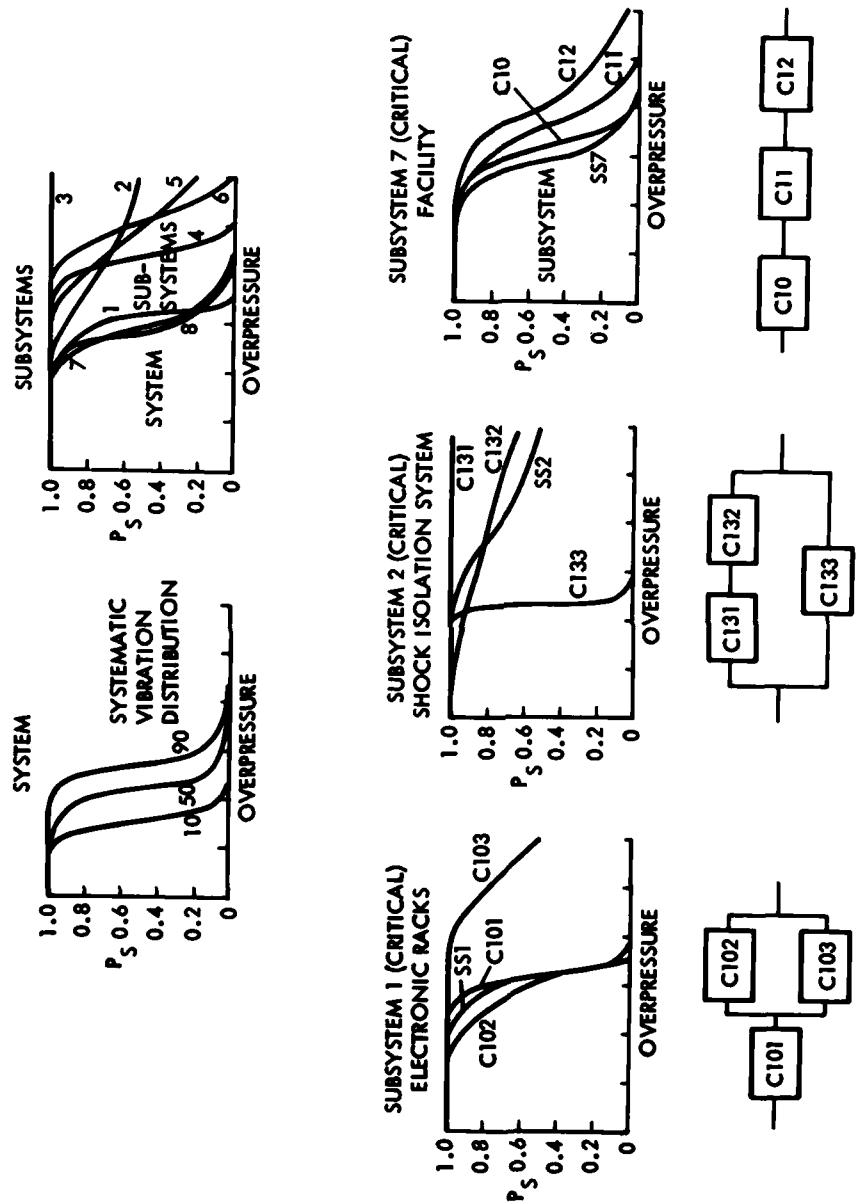
FIGURE 3. TYPICAL FAST OUTPUT DISPLAYS

25

the equations most commonly used for calculating the probability of damage to a target attacked by a nuclear weapon. This section summarizes the most significant results of that study. The discussion is limited to point targets attacked by a single weapon which is subject to delivery (ballistic) errors. The general approach is, however, applicable to any kind of target.

The probability of target survival can be calculated as the integral of the target damage function, which takes into account threat parameters such as weapon yield and height of burst as well as the target damage criterion; and the weapon miss distance distribution, which takes into account weapon delivery data. The calculation can be accomplished by numerical techniques, which will be accurate for any form of the damage function and weapon ballistic miss distance distribution. For tactical and planning applications, however, it is more convenient to postulate specific forms for these functions so that the integration can be accomplished analytically, and yield a closed form solution for the target probability of survival. In the case of the ballistic error miss distance distribution, the usual assumption is that of a bivariate normal distribution.

Two alternative forms are most frequently used for the damage function. The first of these, called the "cookie cutter" damage function, neglects all of the random variation in the damage function and therefore assumes a single value (for a given threat) for the system damage distance. This approach is diagrammed in Figure 4. The postulated bivariate normal weapon-impact density function is shown together with the postulated cookie cutter function at the top left. The miss distance density function is shown at the top center. The probability that the target is damaged is indicated by the shaded fraction of the area under the miss distance density curve which is intercepted by the cookie cutter damage function. The cookie cutter damage function is compared to an alternate damage function in the middle of Figure 4.

The second commonly used form for the damage function makes use of the mean and variance of the system damage distance distribution. This is the approach employed by the Vulnerability Number (VN) System [Reference 3], which describes the blast sensitivity of many targets. The approach is diagramed across the bottom of Figure 4. At the left, the postulated circular bivariate normal weapon-impact density function is shown together with the system damage function, which has the form of a cumulative normal distribution. The density function for the weapon miss distance is shown again at the lower center. The probability that the target is damaged is obtained by multiplying the weapon miss distance density by the damage function to generate the shaded area indicated at the bottom center of the figure. The normal damage function is indicated by the S-shaped curve in the middle of the figure.

A critical question regarding these two approaches for calculating target survivability is the potential error introduced by the forms that are postulated for the damage functions. This is the question to which the TRW study addressed itself.

The study approach was to postulate actual damage functions which departed radically from normal distributions. Damage functions of the following limiting forms were postulated:
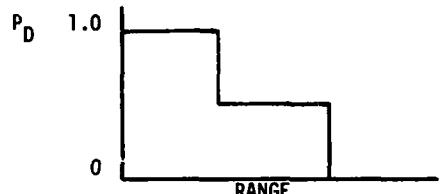
STEP TYPE DAMAGE
FUNCTION
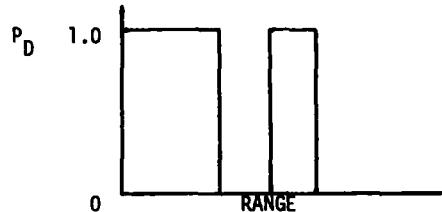
NOTCH TYPE OF DAMAGE
FUNCTION

The step function format of the damage function can occur when the target population consists of two groups of differing hardness, or when strong azimuth sensitivity exists. The notch type of sensitivity can occur when a detection system is employed for protection against some hostile environment and its minimum sensitivity is not low enough to shield an inherent vulnerability. For example, the threshold setting of blast valves might be too high so that the valves do not actuate at low, but lethal, overpressures.

The next step was to calculate with these damage functions the probability of target damage, using the step type damage function. These results were compared with the damage probabilities obtained by the use of approximating cookie cutter and normal damage functions. The discrepancies between the approximate methods and the exact calculations bound the error of the cookie cutter and the normal methods for the class of damage functions which are less pathological than the step or the notch.

An example of the results of this bounding error analysis is shown at the right in Figure 4. At the top, the difference between the cookie cutter and the exact calculation is plotted against the probability of damage for the exact calculation and σ_D, where σ_D is the coefficient
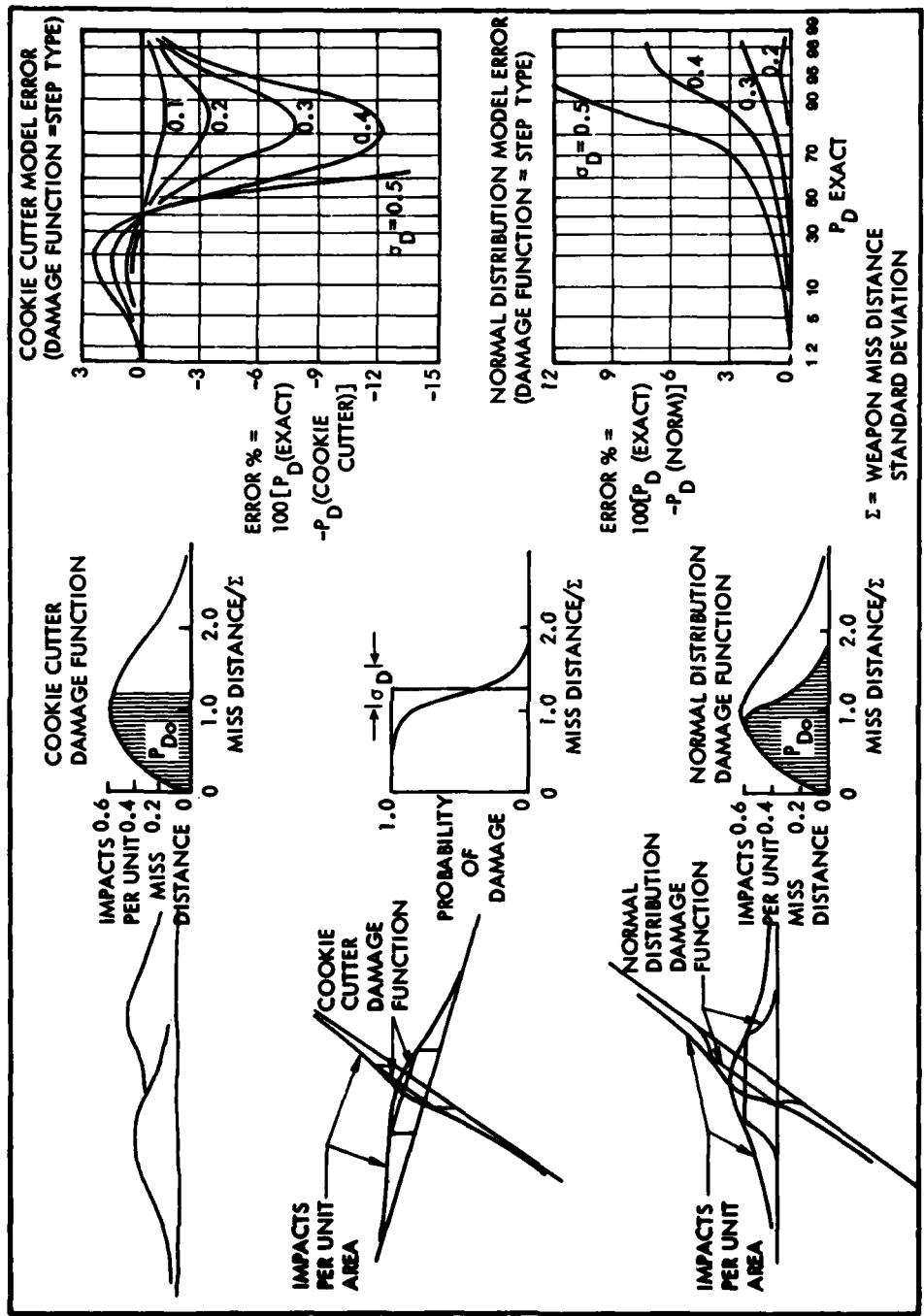
FIGURE 4. TARGET PROBABILITY OF SURVIVAL CALCULATION ACCURACY STUDY

27

of variation for the damage function, i.e., the standard deviation of the damage function divided by its mean. From this plot, it may be concluded that the cookie cutter model can be significantly in error for values of σ_D in the range of 0.2 or higher. Since both tactical and strategic targets may have values of σ_D in the range of 0.2 or higher, this study suggests that the use of the cookie cutter model may introduce significant error.

The results for the normal model, drawn in the same format as for the cookie cutter model, are shown at the lower right of Figure 4. This plot shows that the normal model is reasonably accurate for values of σ_D up to 0.2 and 0.3. Many strategic targets, such as hardened ICBM sites, fall into this range. Therefore, it can be concluded that the use of a normal distribution damage function is sufficiently accurate for many strategic targets. Tactical targets tend to have higher values of σ_D and further experience will be required before it can be concluded with assurance that all these can be adequately represented by a normal distribution damage function.

The conclusion that the normal distribution model for the damage function can provide the basis for accurate target probability of survival calculation has a significant effect on the manner in which FAST calculations can be performed. The next section will describe how the result has led to the improvements in the FAST calculation that were mentioned in the Introduction.

5.0   Recent Advances in the FAST Calculation

The original formulation for the FAST calculation made no assumption regarding the form of the damage function. Therefore, calculations were done at a preselected set of miss distances. The target damage function could then be obtained as a function of systematic error distribution by joining corresponding confidence levels in the distributions of systematic error obtained at each miss distance. As was described, the code operated in a manner to average out or suppress random variations in a damage function, so that this class of information was lost. This was appropriate for weapon systems that employed many sites built almost identically, as was the case for those systems for which FAST was originally developed. For systems which employ only one or a few sites, however, information on random variability becomes important and so it is significant that the new FAST calculation preserves, analyzes, and displays this kind of information.

The finding that, for the purpose of target survivability calculation, the target damage function could be adequately represented by a normal distribution model means that only the mean and standard deviation of the damage function need be estimated (since these parameters completely define the normal distribu-

tion). These two parameters can be obtained by performing the FAST calculation in an inverse mode, and this approach achieves the several advantages mentioned in the Introduction.

A diagram describing the inverse FAST calculation is shown in Figure 5. At the upper left is a panel showing the four classes of input data required for each system. These are the same inputs required for the original FAST calculation.

The panel labeled component 1 in Figure 5 shows the process, starting at the fragility of a typical component. Random numbers are drawn from the fragility distributions of random and systematic variation to establish a random internal environment from the component fragility distribution. This environment is transformed to a free-field environment by the use of the inverse transfer function. At this stage, random numbers are also drawn to establish random and systematic perturbations to the transfer function. In turn, the free-field environments are converted into component damage distances by means of environment scaling laws, while taking into account random and systematic perturbations to these laws determined by random numbers drawn from appropriate distributions. The scaling laws also take into account such threat variables as height of burst and weapon yield. To establish parameters describing the influence of these threat parameters, it is frequently desirable to randomly select threat values from appropriate distributions, for reasons which will be discussed more fully.

The preceding calculation determines a component damage distance for a typical component. This process is repeated for each of the components in the system to obtain a random component damage distance for each component. These component damage distances are then combined in accordance with the system network logic to obtain random subsystem and system damage distances.

This completes a single iteration of the FAST calculation. The results of the calculation are collected into a vector of random variables, as indicated in Figure 5. The vector can contain such elements selected by the analyst as the system damage distance, the randomly selected weapon yield, and the height of burst; frequently the damage distances for each of the components will be included, and possibly selected critical perturbations to the fragilities, transfer functions, and environment scaling laws.

One important aspect of the calculation not shown in Figure 5 is that the perturbations of the fragilities, transfer functions, and environment scaling laws are all drawn from a single multivariate distribution, hence, they take into account the appropriate correlations.

The vector of random variables from a single iteration reflects all the correlations of the inputs. To extract this information,

28
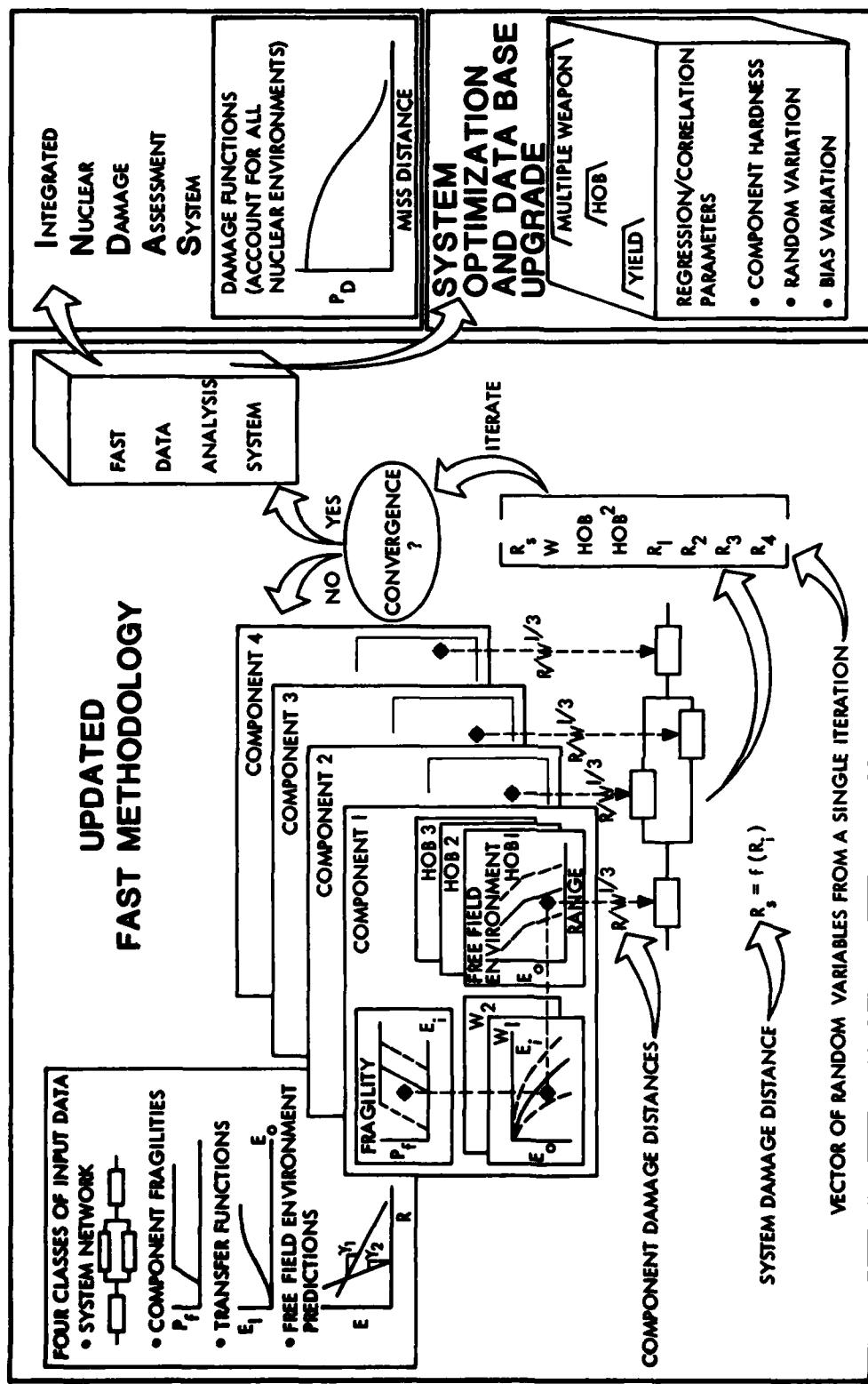
FIGURE 5. INVERSE FAST CALCULATION PROCEDURE

the process just described is taken through many interations until appropriate convergence criteria are satisfied. The result of these calculations is a set of vectors, one from each iteration, which is assembled into a data matrix.

The data matrix is processed by the FAST Data Analysis System to generate a wealth of useful outputs. The outputs may be divided into two classes: (a) data which support the Integrated Nuclear Damage Assessment System (INDAS), and (b) sensitivity data which support system hardness optimization, hardness upgrade programs, or prioritization of data uncertainties for data base upgrade programs. These two outputs will be discussed respectively in the next two sections. Before preceding, however, it is of interest to consider the potential savings in computer costs, that may be achieved by the new approach.

When a system hardness assessment is performed at TRW, it is not unusual for the code to execute 80 iterations on the inner loop and 625 iterations on the outer loop for a total of 50,000 iterations at each miss distance. If calculations are done at ten different miss distances, this means 500,000 iterations will be performed to define one damage function. If this process is repeated for two weapon yields, a million iterations are performed. Some studies may find it desirable to investigate the effect of height of burst, which would further increase the number of iterations.

The inverse FAST calculation requires orders-of-magnitude-fewer iterations. For example, a typical hardened strategic target will frequently have a value of σ_D (damage function coefficient of random variation) of 0.2 or less. The number of iterations required to estimate the mean of the damage function within a one-sigma accuracy of one percent is 400. The conclusion to be drawn here is that the 400 iterations by the inverse FAST approach will provide approximately the same accuracy in the damage function as the one million iterations provided by the previous FAST calculation.

As another example, consider the uncertainty or systematic variation in the damage function, which frequently is larger than the random variation. Our experience is that, for hardened strategic systems, the coefficient of variation for systematic variation is usually less than 0.4. The number of iterations required to estimate the mean within a one-sigma precision of one percent is 1600 iterations.

The number of iterations for the inverse mode in the previous two paragraphs must be increased by the number of degrees of freedom (number of variables placed in the random vector of Figure 5), but the increase in the number of iterations will usually be negligible.

Needless to say, the total computer time is not necessarily directly proportional to the number of iterations; nevertheless, the preceding remarks illustrate that the inverse FAST calculation mode may reduce computer costs by one or two orders of magnitude.

6.0   FAST Data Analysis System

The output of the FAST calculation just described is a set of vectors of random variables from each FAST iteration arranged into a data matrix. The FAST Data Analysis System is an interactive code designed to allow statistical analysis of the data matrix. The operator can perform a number of operations on the raw data matrix. For example, he can take logarithms or he can exponentiate designated columns in the data matrix. He can also perform linear operations such as adding, subtracting, or interchanging columns.

When all the desired operations have been performed, the data analysis system will compute a covariance matrix that will contain information on the variances of all of the variables in the vector of random variables from the FAST calculation, together with the correlations among those variables.

The data analysis system permits the operator to perform selected linear operations on the covariance matrix. The operator can then designate an arbitrary set of variables to be regressed against a second set of arbitrarily selected variables, and the data analysis system will then calculate the matrix of regression coefficients. At the operator's discretion, the data analysis system will test the coefficients within the regression matrix to determine which, if any, of the coefficients are not significantly different from zero. These negligible coefficients will be set equal to zero and the resulting regression matrix will be displayed.

The regression matrix is a powerful tool for the systems analyst, providing easy access to much information which previously was unavailable either because of high computer costs or because of the amount of physical or manual effort that was required to extract the information. Specific applications of this information will be discussed in the next two sections.

7.0   Integrated Nuclear Damage Assessment System (INDAS)

The regression coefficients discussed in the previous section allow one to write an equation predicting the mean of the system damage function as a function of the weapon yield and height of burst, and other pertinent parameters. Indeed, the reason that these parameters were randomized in the FAST calculation and the random values placed in the vectors of random variables was to permit the regression equation to be obtained. The standard deviation for both random and systematic variation for the system damage function can be obtained from the covariance matrix. Thus, all the information necessary for constructing the system damage

30

function is available from the FAST data analysis system output. This information can be coded into strings of alphanumeric characters for each type of target. By performing the analysis for many tactical and strategic types of targets, handbook data are obtained which are useful to strategic and tactical planners.

The damage functions constructed by means of INDAS take into account all of the nuclear environments. Furthermore, the damage functions are obtained explicitly as a function of the distributions of both systematic and random variations. Heretofore, the influence of systematic variations on the probability of target damage has not ordinarily been considered. The FAST approach permits this systematic variation in the probability of survival to be explicitly treated in the analysis. This becomes important to strategic targeteers, who wish to obtain a specified high confidence of damaging targets. In such a situation, it is not proper to combine the systematic variation with the random variation and then to assume that the probability of damage is the same for successive weapons. Instead, it is important to treat the random and systematic variations separately in order to validly calculate the damage expectancy from a given weapon allocation and to evaluate potential errors. Even neglecting the systematic variation, it is not valid to assume that the probability of damage from successive weapons is identical. The reason for this is that certain weapon effects tend to have a cumulative effect; also, the weaker targets tend to be preferentially damaged by the initial weapons. Further discussion of the targeting aspects of systematic and random variations of the damage functions is beyond the scope of this report, but the reader should be aware that the FAST methodology generates data on these two kinds of variations, and therefore, will permit their proper accounting in targeteering calculations.

8.0 System Optimization and Data Base Prioritization

The FAST code, which outputs the data matrix, together with the FAST data analysis system, provides the analyst with a powerful tool for optimizing weapon systems. For example, he can regress the system damage function against the damage distances for each of the components of the system to obtain a regression matrix. He has the option of testing all of the coefficients in the matrix to determine whether they are significantly different from zero. The nonzero regression coefficients identify all the components that contribute to system failure. Indeed, the relative contribution of each component is indicated by the relative size of its regression coefficient. The analyst thus has an automated means of prioritizing the components in terms of their contribution to system failure.

The analyst has the option of operating on the data in the data matrix in various ways.

For example, he might multiply all of the damage distances for a weak-link component by a number less than one and then construct a new regression matrix. This would correspond to strengthening the weak-link component. By proceeding in this fashion, the analyst could quickly determine how much hardening of the component is required in order to remove it from the critical list. In a somewhat similar fashion, certain other components that are not weak-link items might possibly be weakened without contributing to system failure. By proceeding in this interactive mode, the analyst could quickly arrive at a balanced hardness configuration for the system. In accomplishing this end, it will frequently be unnecessary to return to the FAST program to generate a new data matrix.

If sufficient cost information on hardening components is available, this information can be used in the optimization process. Frequently such cost information can be summarized in the form of cost estimating relations, i.e., with polynomials that give the cost for different levels of hardness for each of the components. With cost data in this form, it is a simple matter to prepare a computer code that will quickly find the most cost effective system configuration having a specified level of hardness.

The quality of the data base affects the cost of developing a system. Uncertainties on fragilities, transfer functions, and environment scaling laws, arising from possible errors in mathematical models call for appropriate safety factors in system design. Clearly, the larger the safety factors the higher the system cost. FAST propagates systematic and random variations through the calculations in a correct and balanced way, thereby overcoming the need for the overly conservative approach of accumulating safety factors at each stage of the calculation which results in costly overdesign of the system.

The uncertainties in the data base are not all equally important. If the critical ones could be identified then it might be possible, say by means of test or analysis programs, to reduce them, and thereby reduce the size of the safety factor required. The FAST data analysis system achieves this end by identifying all the potentially critical uncertainty factors. As these random and uncertainty parameters are determined by the drawing of random numbers they are placed in the vector of random variables. When the simulation is complete, the data matrix is processed in the FAST data analysis system to regress the system damage function against the random and systematic parameters. Those parameters that have a significant effect on the system damage function are identified because their regression coefficients are significantly greater than zero. The result is that all the uncertainty factors in the data base are prioritized according to the size of the regression coefficient. The display of the regression matrix then provides the basis for planning possible test or analysis programs to reduce key uncertainties.

There has not yet been time to gain experience applying the new FAST techniques to a variety of system optimization and data base upgrade programs. From the limited experience to date, the advance appears to be much more significant than just an easier and more economical way of accomplishing what was done before. The orders of magnitude improvement in both computer cost and information extractable from the FAST calculation allow a truly significant improvement in the quality and quantity of data available for system analysis. The capability for automated filtering, prioritization, and display of output data by means of the FAST Data Analysis System provides a convenient means for managing the enhanced data flow. In short, it is anticipated that the new FAST technique will have extensive, and even unforeseen, impact on future design and analysis of hardened survivable systems.

REFERENCES

1. Rowan, W. H., "Hardness Evaluation", The Shock and Vibration Bulletin, Naval Research Laboratory, Washington, D. C., December 1970.

2. Rowan, W. H., et al., "Failure Analysis by Statistical Techniques (FAST) User's Manual", (U) Volumes I and II TRW Systems Group, DNA3336F-1 and 2, September 1974.

3. Physical Vulnerability Handbook - Nuclear Weapons (U) Defense Intelligence Agency, AP-550-1-2-69-INT, 1 June 1969 (Confidential)

ON THE MEAN LIFE EVALUATION OF A MATERIAL WITH IDEAL ELASTO-PLASTIC BEHAVIOUR, SUBJECTED

TO A STOCHASTIC LOADING PROGRAMME WITH A FINITE NUMBER OF STRAIN LEVELS

G. A. Philippin, T. H. Topper and H. H. E. Leipholz
Department of Civil Engineering
Solid Mechanics Division
University of Waterloo, Waterloo, Ontario, Canada

In a previous paper presented at the 46th Shock and Vibration Symposium, San Diego, California, October, 1975, the authors confirmed the mathematical soundness of Miner's rule and its applicability to mean life prediction under the assumption that a proper damage parameter and its statistical data are being used in that rule.

If the loading programme is such that the actual damage parameter (quantity related with the area of the hysteresis loops in the loading programme) is proportional to the respective stress (or strain) peak of the programme, the statistical distribution of these peaks may be used in Miner's rule. Such a procedure is in accordance with the classical approach of Wöhler to fatigue. This fact has been used in the paper mentioned above in order to determine the probability densities of prescribed strain peaks for a material remaining in the linearly elastic domain. These densities were then used in Miner's rule.

In this paper, a more realistic situation is being considered. It is assumed that the material is elastic-plastic in the ideal sense and subjected to a loading programme with well defined strain peaks. It is also assumed that the material returns after each reversal to the zero-strain state. Such assumption is not restricting generality in a severe way. Any other strain level could have been chosen as the state of rest in place of the zero-strain level, which has only a normalizing function. Keeping in so far the features of the loading programme very regular, and restricting the stochastic nature of the programme to the irregular way in which the possible strain peaks are distributed over time, makes it possible to rigorously evaluate the probability distribution of hysteresis loops collected in classes of equal damaging events. This is achieved using combinatorics.

The so obtained probability densities are then used in Miner's rule and a mean life evaluation is carried out. During these calculations it comes to light that such a process as simple as it is, is nevertheless nonstationary, a result of great practical importance.

Although the loading programme considered may in itself have already some value, as it may very well be a good model of practical situations of some significance, it has in any case a great value for the development of a sound theory of stochastic fatigue. On the one hand it allows one to calculate probability densities accurately and to predict mean life by means of Miner's rule as safely as this is possible for a stochastic process. On the other hand, the proposed loading programme and the corresponding mean life can easily be reproduced and verified, respectively, in the fatigue laboratory. Thus, one has a reliable means of checking reality against theory, a fact which is certainly basic and important for any progress in the theory of stochastic fatigue.

INTRODUCTION

Consider a material subjected to a stochastic loading programme P consisting of n_1 peaks of amplitude ℓ_1, n_2 peaks of amplitude ℓ_2, etc. For the sake of simplicity, a loading programme shall be said to be of length k if it contains k peaks, or if

$$\sum_i n_i = k.$$

Assume that the amplitudes ℓ_1, ℓ_2, ... are statistically distributed according to some probability law independent of time. Then, the loading programme P is a stationary stochastic process. Under these circumstances, it is clear that the mean values $E\{n_1\}$, $E\{n_2\}$, ... of the numbers of peaks of amplitudes ℓ_1, ℓ_2, ... are proportional to the length k of the given programme P. This fact can be expressed as follows:

$$E\{n_i\} = kE_i, \qquad i = 1, 2, \ldots . \qquad (1)$$

Let N_i denote the number of peaks of amplitude ℓ_i the specimen can resist until fracture. N_i will be called the life time of the specimen under constant load amplitude ℓ_i. This is a random variable whose mean value $E\{N_i\}$ will be denoted by ν_i ($i = 1, 2, \ldots$). Let N denote the maximum number of peaks the specimen can resist under the stochastic loading programme P. N is also a random variable called the life time of the specimen under the stochastic loading programme P. Its mean value $E\{N\}$ will be denoted by ν. Let $1/N_i$ be the damage increment corresponding to every peak of load amplitude ℓ_i. Miner [1] proposed the following rule for the evaluation of the life time N: the sum of all damage increments caused by each individual peak is determined. The fracture of the specimen occurs when this sum reaches the value one. This rule gives the following relationship for N:

$$\sum_i \frac{\dfrac{N n_i}{k}}{N_i} = 1, \qquad (2)$$

from which

$$N = \left(\sum_i \frac{\dfrac{n_i}{k}}{N_i} \right)^{-1} \qquad (3)$$

is obtained, with

$$\sum_i n_i = k.$$

This last expression for the life time N, as plausible as it may appear to be, has nevertheless been without a proper mathematical foundation for a long time. (For $i = 1$, i.e., for a loading programme P_1 of constant amplitude ℓ_1, (2) is trivially true. For $i > 1$, i.e., several load amplitudes, (2) only represents a possible generalization of the case $i = 1$). Only in 1968, Birnbaum and Saunders have found a probabilistic interpretation of Miner's rule [2]. Unfortunately no attention was paid in engineering circles to their results published in a mathematical journal. With the intent of changing this situation, a new version of these results have been published by Philippin, Topper, and Leipholz [3]. Summarizing, the basic statement in [3] reads as follows:

$$\nu = \left(\sum_i \frac{\dfrac{E\{n_i\}}{k}}{\nu_i} \right)^{-1}, \qquad (4)$$

or with the aid of (1):

$$\nu = \left(\sum_i \frac{E_i}{\nu_i} \right)^{-1}. \qquad (5)$$

These two formulas show that Miner's rule is correct if the life times are replaced everywhere by their corresponding mean values.

In writing (2), it has been assumed that any peak of load amplitude ℓ_i is responsible for the *same* damage increment $1/N_i$. This hypothesis is actually without foundation, and cannot survive in the light of arguments, suggested by the following situation: Suppose that the material under consideration does not behave purely elastically. The state of the material will change, even if the loading programme contains only peaks of the same amplitude. For instance, due to an ageing process of the material, the reversals (of constant load amplitude) will be getting more damaging with ongoing time. This clearly shows that the load amplitude as a parameter is unable to correctly partition the peaks of the programme in classes of equally damaging reversals. A parameter T able to perform this task, cannot depend only on local properties associated with just one peak. Such a parameter has to depend on the complete load history to which the material is subjected. The use of Miner's rule in its original form (3) or in its statistical interpretation (5), is only possible if the two following conditions are satisfied:

(a) a suitable damage parameter T (i.e., adequate to collect in classes all equally damaging reversals), has to be chosen,

(b) the stochastic structure of the damage parameter T (correctly chosen) has to be determined from the given stochastic process of which the loading programme P is supposed to be a realization.

The first condition states a physical problem for which no satisfying answer is known. However, Topper, Sandor and Morrow [4], have obtained experimentally very accurate life time evaluations by choosing as a damage parameter $T = \Delta\sigma_M \cdot \Delta\varepsilon$, based on stress and strain at the fatigue crack initiation site, where σ_M is the peak stress and $\Delta\varepsilon$ is the strain range. It is not possible to define a value of the product $T = \Delta\sigma_M \cdot \Delta\varepsilon$ after each reversal of the loading programme. Such a value of T can only be defined after each closed hysteresis loop, as it arises in the realization of the loading programme.

The second condition states the following mathematical problem: for a given loading programme P of known stochastic nature, find the statistical distribution of the closed hysteresis loops with respect to the value of T associated with each loop. This problem has already been presented and solved in [3] for the very simple case of an elastic material subjected to strain peaks randomly chosen from two possible values $\varepsilon_1 < 0 < \varepsilon_2$ with the corresponding probabilities π_1, π_2, $\pi_1 + \pi_2 = 1$. This situation generates only three kinds of hysteresis loops, so that a combinatorial investigation was possible. In the general case for which no restriction is made about the possible strain levels to which the material might be subjected, the set of different

kinds of closed hysteresis loops is no longer countable, and the problem cannot be treated by means of combinatorial methods. In order to preserve the advantages of a combinatorial analysis, one could discretize the problem by choosing m possible strain levels. Such a method is however far from being satisfactory, since the number of different kinds of closed hysteresis loops does not only depend on m, but also on the different values of discretization levels! Yet such discretization process cannot be completely disregarded, because at this time, other approaches may not be easily available. The technique of computer simulation, which might be an alternative, is not supposed to be considered in this context.

In this paper, an example of life time evaluation will be presented for a special case which involves only a small number of strain levels representing the loading programme P.

A DISCRETE MODEL FOR MEAN LIFE EVALUATION

In this section, a solution of the fatigue problem of an ideal elastoplastic material will be presented for the special case in which the loading programme P consists of a sequence of strain peaks, randomly chosen from four possible values $\epsilon_{-2} < \epsilon_{-1} < 0 < \epsilon_1 < \epsilon_2$ with the corresponding probabilities π_i,

$$\sum_{\substack{i=2 \\ i \neq 0}}^{+2} \pi_i = 1 .$$

In this model, the strain level zero is considered to be a certain event occurring after every peak of the loading programme. The material under consideration is supposed to be initially in the state of rest R_o, (see Figure 1). The only condition to be satisfied with respect to the values of the possible strain levels ϵ_i, is that the different kinds of possible closed hysteresis loops registered in a stress-strain diagram of the material are consistent with the map in Figure 1.

In the situation of Figure 1, five states of rest denoted by R_i, i = -2, ..., +2, are observed. The number of different kinds of possible closed hysteresis loops is 16. Among these different kinds 13 are degenerated, i.e., their corresponding surface areas are zero. They will be denoted by h(i,j) or by h(i,j,-j), i,j = -2, ..., +2, where i indicates that they are born from the state of rest R_i, j,-j indicate the strain peaks ϵ_j, ϵ_{-j}, responsible for their creation. The three remaining loops containing a non-zero surface area will be denoted by h(α) α = 0, + 2, the values α = ± 1 will be used to designate the two positive and negative reversals which build the h(0) - loops. If the same kind of loops can be generated in two different ways, what is the case for h(i,i), i = ± 1, one of them will be marked by a star. Figure 2 gives a description of these loops and shows how they arise during the realization of the loading programme

P. An arbitrary enumeration of these different kinds of loops is given in the first column of Figure 2.
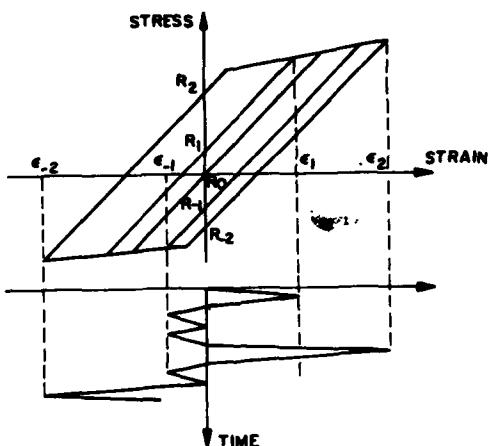
Figure 1

Each point represents the accomplishment of a new closed loop, and the preceding arrow (not *necessarily connected*) indicates which parts of the programme are responsible for the corresponding loop. A location of these loops in a stress-strain diagram is given in Figure 3.

Although Figure 1 need not be symmetric with respect to the origin, it is worthwhile to note that there is a one to one correspondence between the different events occurring during the realization of P, so that the probabilistic problem is symmetric. This fact has been outlined by the introduced indexation in Figures 1, 2, 3, and will be used in the following computation.

35

STRAIN

5 10 15 20 25 30

ϵ_2
ϵ_1
0
ϵ_1
ϵ_2

k

NOTATIONS

h_1	$h(0,1)$
h_2	$\begin{cases} h(0,1,-1) \\ h(0,-1,1) \end{cases}$
h_3	$h(0,-1)$
h_4	$\begin{cases} h(1,1) \\ h^*(1,1) \end{cases}$
h_5	$\begin{cases} h(1,1,-1) \\ h(1,-1,1) \end{cases}$
h_6	$h(1,-1)$
h_7	$h(-1,1)$
h_8	$\begin{cases} h(-1,1,-1) \\ h(-1,-1,1) \end{cases}$
h_9	$\begin{cases} h(-1,-1) \\ h^*(-1,-1) \end{cases}$
h_{10}	$h(-2,1)$
h_{11}	$h(-2,2)$
h_{12}	$h(2,-1)$
h_{13}	$h(2,-2)$
h_{14}	$h(2)$
h_{15}	$h(-2)$
h_{16}	$h(0)$
	$h(1)$
	$h(-1)$

Figure 2

36
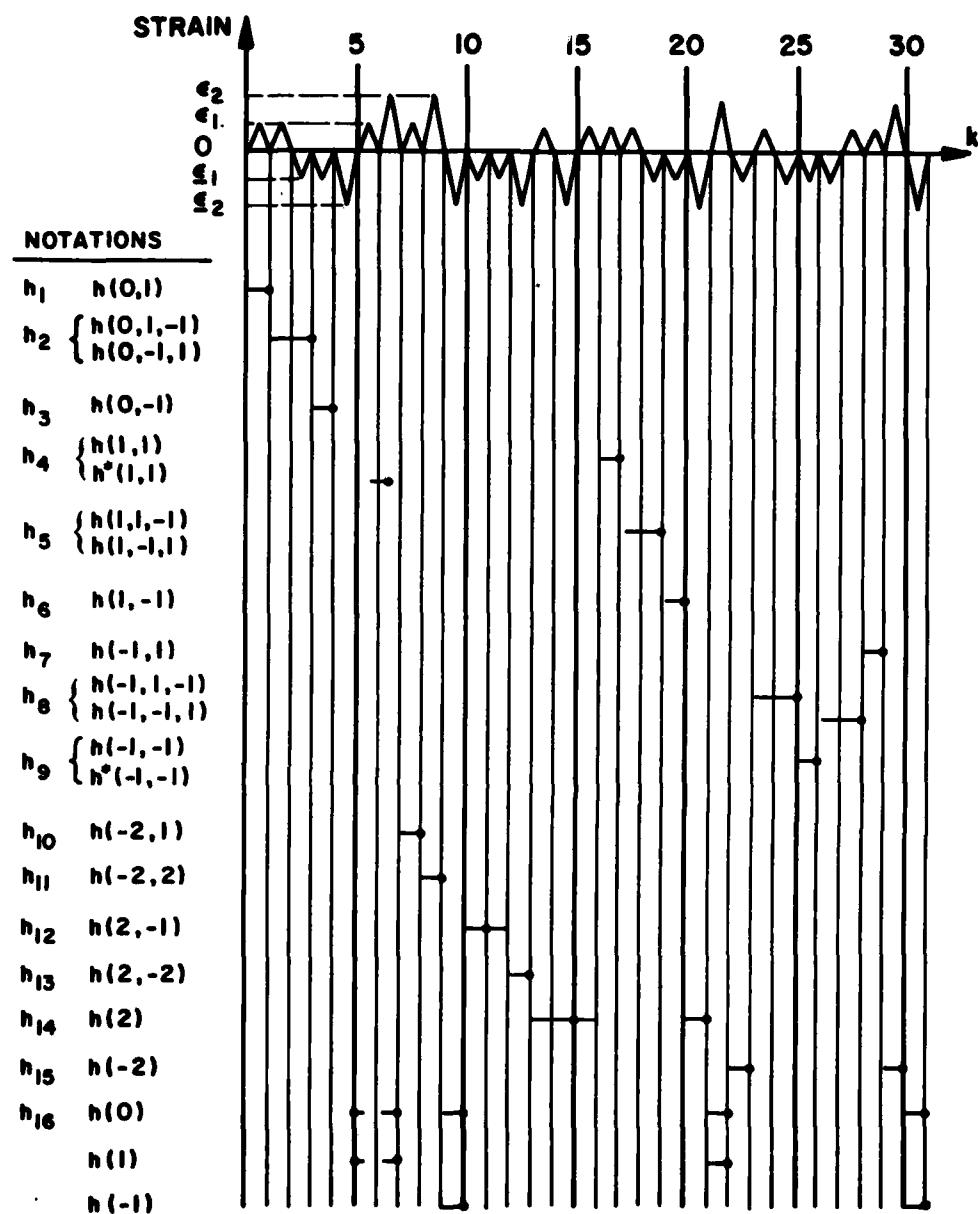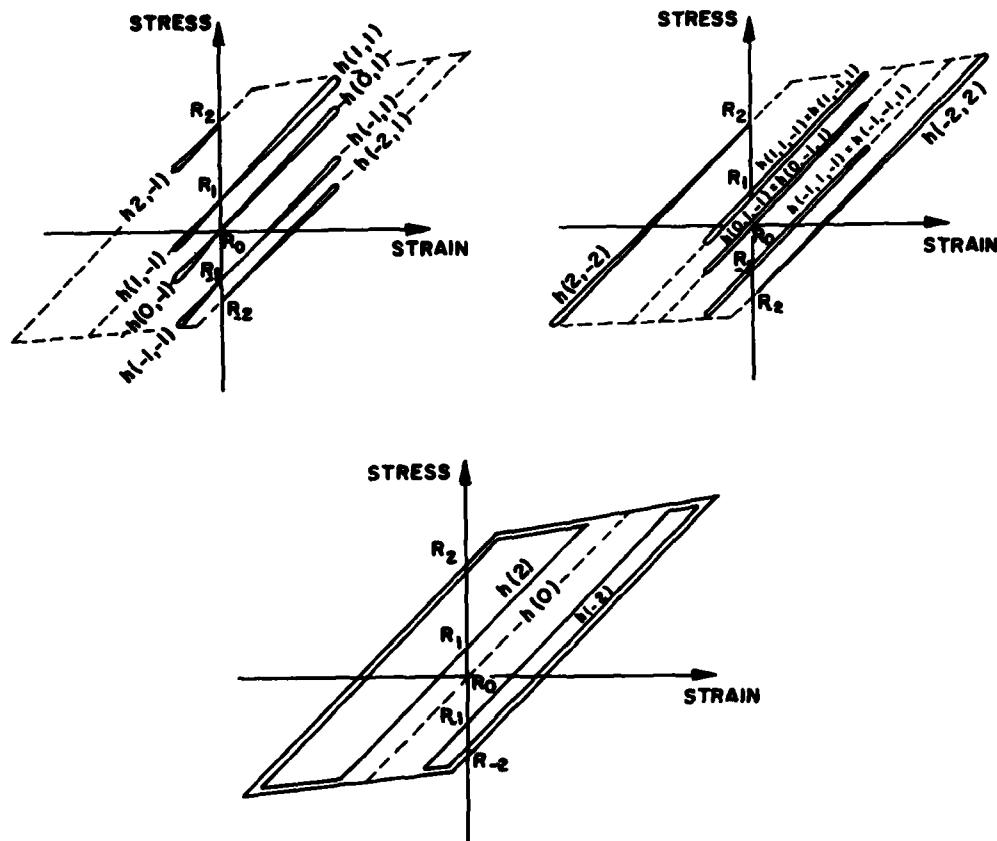
Figure 3

Let $P_k(R_i)$ denote the probabilities that after k strain peaks, the material is left in the rest states R_i, $i = -2, \ldots, +2$. From [5] these probabilities are given by the following formulas:

$$P_k(R_0) = (\pi_{-1}+\pi_1)^k = \pi^k , \qquad (6)$$

$$P_k(R_i) = \frac{\pi_{-2i}\,\pi_i}{(1-\pi_{-i})(1-\pi)} + \frac{\pi_{-2i}}{1-\pi_{-i}}\,\pi_{-i}^k - \frac{\pi_{-2i}}{1-\pi}\,\pi^k,$$

$$i = \pm 1, \quad (7)$$

$$P_k(R_{2i}) = \pi_{-2i}\,\frac{1-\pi_{-i}^k}{1-\pi_{-i}} , \quad i = \pm 1 , \qquad (8)$$

with $\pi = \pi_{-1}+\pi_1$. From (6), (7), (8), let us derive the following formulas to be used later:

$$\sum_{\mu=1}^{k-1} P_\mu(R_0) = \pi\,\frac{1-\pi^{k-1}}{1-\pi} , \qquad (9)$$

$$\sum_{\mu=1}^{k-1} P_\mu(R_i) = (k-1)\,\frac{\pi_i\,\pi_{-2i}}{(1-\pi_{-i})(1-\pi)} + \frac{\pi_{-2i}\,\pi_{-i}}{(1-\pi_{-i})^2}$$

$$(1-\pi_{-i}^{k-1}) - \frac{\pi\,\pi_{-2i}}{(1-\pi)^2}\,(1-\pi^{k-1}) , \; i = \pm 1 , \quad (10)$$

$$\sum_{\mu=1}^{k-1} P_\mu(R_{2i}) = \frac{\pi_{-2i}}{1-\pi_{-i}}\,\{k-1-\pi_{-i}\,\frac{1-\pi_{-i}^{k-1}}{1-\pi_{-i}}\} ,$$

$$i = \pm 1 . \quad (11)$$

From 4^k possible loading programmes of length k, let $N_k(R_i)$ be the expected number of programmes leading the material into the rest state R_i. $N_k(R_i)$ is given by

$$N_k(R_i) = 4^k P_k(R_i), \quad i = -2, \ldots, +2,$$
$$k = 1, 2, 3, \ldots . \tag{12}$$

Let $H_k(\cdots)$ denote the expected number of programmes of length k finishing with a $h(\cdots)$-loop. Between the various quantities $H_k(\cdots)$, the following relationships hold:

$$H_k(i,j) + H_k(i,-j,j) = 4\pi_j N_{k-1}(R_i), \tag{13}$$

$$H_k(i,j,-j) = 4\pi_{-j} H_{k-1}(i,j), \tag{14}$$

$$H_k(i,j) = 4\pi_j \{ H_{k-1}(i,j) + H_{k-1}(i,j,-j) +$$
$$+ H_{k-1}(i,-j,+j) \}, \tag{15}$$

with $i = 0, \pm 1$, $j = \pm 1$, $k = 2,3,4, \ldots$. Furthermore,

$$H_k^*(i,i) = 4\pi_{2i} N_{k-1}(R_i), \tag{16}$$

$$H_k(2i) = 4\pi_{-2i} N_{k-1}(R_i), \tag{17}$$

$$H_k(2i,-ij) = 4\pi_{-ij} N_{k-1}(R_{2i}), \tag{18}$$

with $i = \pm 1$, $j = 1,2$, $k = 2,3,4, \ldots$. A relationship involving $H_k(o)$ is not easily derived. For this reason the $h(o)$-loops will be split into their two positive and negative reversals denoted by $h(i)$, $i = \pm 1$. Instead of counting events corresponding to $h(o)$, this will be done with respect to $h(i)$, $i = \pm 1$:

$$H_k(i) = 4\pi_{2i} \{ N_{k-1}(R_{2i}) + N_{k-1}(R_i) \},$$
$$i = \pm 1, \quad k = 2,3,4, \ldots \tag{19}$$

$H_k = H_k(-1) + H_k(+1)$ is the expected number of programmes of length k finishing with the half of an $h(o)$-loop, and must not be confounded with $H_k(o)$. By inserting (7), (8), (12) into (19),

$$H_k = \frac{2\pi_{-2}\pi_2}{1-\pi} 4^k (1 - P_{k-1}(R_o)), \quad k = 1,2,3, \ldots \tag{20}$$

is obtained. Let N_k be the expected number of half $h(o)$-loops contained in 4^k possible loading programmes of length k. N_k is determined by the following recursion formula:

$$N_k = 4N_{k-1} + H_k, \quad k = 2,3,4, \ldots, \tag{21}$$

with the initial condition

$$N_1 = 0 . \tag{22}$$

The solution of (21), (22) is

$$N_k = \sum_{\mu=2}^{k} 4^{k-\mu} H_\mu , \tag{23}$$

or, with the aid of (20), (6),

$$N_k = \frac{2\pi_2 \pi_{-2}}{1-\pi} 4^k \{ k-1 - \frac{\pi}{1-\pi} (1-\pi^{k-1}) \},$$
$$k = 1,2,3, \ldots . \tag{24}$$

Let n_k be the expected number of half $h(o)$-loops contained in one programme of length k. The expected number $n_k(o)$ of $h(o)$-loops contained in such a programme is then

$$n_k(o) = \frac{n_k}{2} = \frac{\pi_2 \pi_{-2}}{1-\pi} \{ k-1 - \frac{\pi}{1-\pi} (1-\pi^{k-1}) \},$$
$$k = 1,2,3, \ldots . \tag{25}$$

Let $N_k(\cdots)$ be the expected number of $h(\cdots)$-loops contained in 4^k possible loading programmes of length k. All the quantities $N_k^*(i,i)$, $N_k(2i)$, $N_k(2i,-ij)$, $i = \pm 1$, $j = 1,2$, satisfy the same recursion formula already used for the computation of N_k (see (21)),

$$N_k(\cdots) = 4N_{k-1}(\cdots) + H_k(\cdots), \tag{26}$$

with the same initial condition:

$$N_1(\cdots) = 0 . \tag{27}$$

For the degenerated loops created from the states of rest R_i, $i = 0, \pm 1$, the recursion mechanism is more complicated, since an $h(i,j)$-loop, $i = 0, \pm 1$, $j = \pm 1$, born in P during the kth peak, may very well be transformed into an $h(i,j,-j)$-loop by application of the next peak. For these loops, we have

$$N_k(i,j) = 4N_{k-1}(i,j) + H_k(i,j) - H_k(i,j,-j),$$
$$i = 0, \pm 1, \quad j = \pm 1, \tag{28}$$

Table 1

i	E_i	i	E_i
1	0	9	$\dfrac{\pi_{-1}\pi_2}{(1-\pi_1)(1-\pi)}\left\{\pi_{-1}+\pi_{-2}-\dfrac{\pi\pi_1\pi_{-1}}{1-\pi_1\pi_{-1}}\right\}$
2	0	10	$\dfrac{\pi_2\pi_1}{1-\pi_1}$
3	0	11	$\dfrac{\pi_2^2}{1-\pi_1}$
4	$\dfrac{\pi_1\pi_{-2}}{(1-\pi_{-1})(1-\pi)}\left\{\pi_1+\pi_2-\dfrac{\pi\pi_1\pi_{-1}}{1-\pi_1\pi_{-1}}\right\}$	12	$\dfrac{\pi_{-2}\pi_{-1}}{1-\pi_{-1}}$
5	$\dfrac{\pi\pi_1^2\pi_{-1}\pi_{-2}}{(1-\pi_{-1})(1-\pi)(1-\pi_1\pi_{-1})}$	13	$\dfrac{\pi_{-2}^2}{1-\pi_{-1}}$
6	$\dfrac{\pi_1\pi_{-2}}{(1-\pi_{-1})(1-\pi)}\left\{\pi_{-1}-\dfrac{\pi_1\pi_{-1}}{1-\pi_1\pi_{-1}}\right\}$	14	$\dfrac{\pi_1\pi_{-2}^2}{(1-\pi_{-1})(1-\pi)}$
7	$\dfrac{\pi_{-1}\pi_2}{(1-\pi_1)(1-\pi)}\left\{\pi_1-\dfrac{\pi_1\pi_{-1}}{1-\pi_1\pi_{-1}}\right\}$	15	$\dfrac{\pi_{-1}\pi_2^2}{(1-\pi_1)(1-\pi)}$
8	$\dfrac{\pi\pi_1\pi_{-1}^2\pi_2}{(1-\pi_1)(1-\pi)(1-\pi_1\pi_{-1})}$	16	$\dfrac{\pi_2\pi_{-2}}{1-\pi}$

REFERENCES

[1] M. A. Miner, "Cumulative Damage in Fatigue", Journal of Applied Mechanics, Vol. 12, 1945, pp. A159-A164.

[2] Z. W. Birnbaum and S. C. Saunders, "A Probabilistic Interpretation of Miner's Rule", SIAM, Journal of Applied Mathematics, Vol. 6, 1968, pp. 637-652.

[3] G. A. Philippin, T. H. Topper and H. H. E. Leipholz, "Mean Life Evaluation for a Stochastic Loading Programme with a Finite Number of Strain Levels Using Miner's Rule", 46th Symposium on Shock and Vibration, (1975), San Diego, California.

[4] T. H. Topper, B. I. Sandor and JoDean Morrow, "Cumulative Fatigue Damage Under Cyclic Strain Control", ASTM, Vol. 4, No. 1, March, 1969, pp. 189-199.

[5] G. A. Philippin and H. H. E. Leipholz, "On the Distribution of the Stress States of a Material with Ideal Elastoplastic Behaviour, Subjected to a Finite Number of Strain Levels", Mechanics Research Communications, Vol. 2, 1975, pp. 215-220.

FATIGUE ANALYSIS OF MULTI-DEGREE-OF- FREEDOM SYSTEMS
UNDER RANDOM VIBRATION

Ronald G. Lambert
General Electric Company
Aircraft Equipment Division, Utica, New York 13503

Closed form analytical solutions using Miner's cumulative damage hy-
pothesis have previously been derived quantitatively to describe several
areas of interest regarding fatigue under random vibration for single
degree-of-freedom systems. These areas include relating root-mean-
square (rms) stress to cycles and time-to-failure, the probability den-
sity function of cycles-to-failure, and the probability of failure to cycles-
to-failure. It is proposed in this paper that the above developed equa-
tions can be used for either single or multiple degree-of-freedom sys-
tems by adding both the stresses and the frequencies of the multiple
modes in the rms sense rather than the linear sense to include interac-
tion effects between the modes. That is, systems with the same rms
stress σ and the same effective frequency (i.e., one-half the average
number of zero crossings per second) will have the same time to failure.
This proposal is based upon the fact that the actual number of stress
peaks above 1.5σ is the same for the two cases and that most fatigue
damage is done by stress peaks above 2σ for at least the single degree-
of-freedom case. The experimental data of J.T. Broch of Brüell and
Kjaer tend to confirm this proposal. Further analytical and experimen-
tal effort is required before firm conclusions can be made. An alterna-
tive approach which linearly summed the damage cumulated from each
individual mode independently was discarded because of the large dis-
parity with experimental results.

INTRODUCTION

This paper deals primarily with single de-
gree-of-freedom (SDF) and two degree-of-free-
dom (2DF) structural systems subjected to
wideband random vibration but can be extended
to multiple degree-of-freedom by inductive
reasoning. The structural elements respond as
narrow-band random functions at or near their
individual resonant frequencies. The static
stresses are typically much smaller than the
dynamic stresses.

Landgraf [1] has used Miner's linear dam-
age rule for analyzing complex random stress
profiles with good agreement between analytical
and experimental results. Damage was cumu-
lated by linearly summing the damage done by
each stress-strain hysteresis loop in the actual
stress-time profile, a laborious and time-con-
suming procedure. The analytical results were
numerical, not closed-form expressions.

Closed-form fatigue expressions for the
SDF case have been derived in reference [2].
However, similar rigorous expressions for the
2DF case have not been derived and do present
a formidable task, because the probability den-
sity function of the stress-strain hysteresis
loop amplitude is difficult to calculate.

The approach taken in this paper is not to
rigorously derive fatigue expressions for the
2DF case but to extend the application of those
expressions derived in reference [2]. The av-
erage rate of stress zero crossings (i.e.,
twice the effective frequency) can be rigorously
derived and calculated for single or multiple
degree-of-freedom systems. The application
of the fatigue expressions derived in reference
[2] can be extended to 2DF systems, if it can
be shown that systems having the same rms
stress and the same effective frequency also
have the same fatigue life or time to failure.
It is also necessary to show that the form of the

expressions for the probability density and distribution functions of times to failure matches the form of the experimental data.

NARROW-BAND RANDOM FATIGUE

The following expressions were derived in reference [2]. The sinusoidal S-N fatigue curve of a material is as follows:

$$S = AN_s^{-1/\beta} \qquad (1)$$

where

S = stress amplitude (psi, Pa)

A = y-intercept for $N_s = 1$ on a log-log plot

A = true ultimate stress (psi, Pa)

N_s = number of cycles to failure

β = negative reciprocal of the slope of the curve on a log-log plot

A and β are material constants and are always positive values

The corresponding narrow-band random σ-N fatigue curve is as follows:

$$\sigma = C N_T^{-1/\beta} \qquad (2)$$

where

$$C = \left[\frac{A}{\sqrt{2}}\right]\left[\frac{1}{\Gamma\left[\frac{2+\beta}{2}\right]}\right]^{1/\beta} \qquad (3)$$

The constant C is a function only of the true ultimate stress A and β the negative reciprocal of the slope of the sinusoidal S-N fatigue curve. Both are material constants. C can be thought of as the true ultimate rms random stress, since it represents the y-intercept for $N_T = 1$ in equation (2) on a log-log plot

and

σ = rms stress level (psi, Pa)

N_T = average number of stress cycles to failure

Γ = gamma function

Therefore

$$N_T = C^{\beta}\sigma^{-\beta} \qquad (4)$$

Figure 1 illustrates equation (2). Figure 2 compares the curves of equations (1) and (2) for G-10 fiberglass epoxy. The values for the material constants were obtained from reference [3].
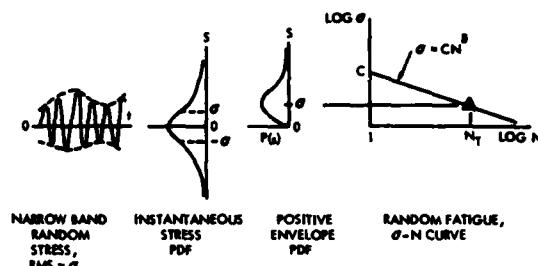
Figure 1. Narrow-Band Random Fatigue
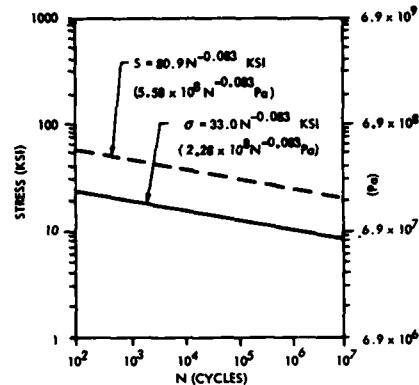
Figure 2. Sinusoidal and Narrow-Band Random Fatigue Curves for G-10 Fiberglass Epoxy

Time to failure, t_F, relates to cycles to failure as follows:

$$t_F = \frac{N_T}{f_{eff}} \quad \text{(seconds)} \qquad (5)$$

where

f_{eff} = effective frequency (Hz)

= one-half the average zero crossings per second

In Appendix A, it is shown that the general expression of f_{eff} for single or multiple degrees of freedom is:

$$f_{eff} = \sqrt{\sum_{j=1}^{k}\left(\frac{\sigma_j^2}{\sigma_T^2}f_j^2\right)} \quad \text{(Hz)} \qquad (6)$$

for k disjoint bandpass processes of center frequency f_j and total rms stress σ_T where

$$\sigma_T = \sqrt{\sum_{j=1}^{k}\sigma_j^2} \qquad (7)$$

$$j = 1, 2, 3, \ldots$$

44

where

j = resonant mode index

k = total number of resonant modes

For a bandpass process of width f_B and center frequency f_0:

$$f_{eff} = f_0 \sqrt{1 + \frac{f_B^2}{12 f_0^2}} \cong f_0 \quad \text{(Hz)} \quad (8)$$

For two disjoint bandpass processes to total rms stress σ_T and center frequencies f_1 and f_2:

$$\sigma_T = \sqrt{\sigma_1^2 + \sigma_2^2} \quad (9)$$

$$f_{eff} \cong \sqrt{\frac{\sigma_1^2}{\sigma_T^2} f_1^2 + \frac{\sigma_2^2}{\sigma_T^2} f_2^2} \quad \text{(Hz)}$$

VARIABLE RMS STRESS

Thus far, A, β, and σ were treated as fixed variables. σ will now be treated as a random variable, which is the typical case. The rms stress usually varies from part to part and subassembly to subassembly even though the applied vibration level may not vary. Stresses vary due to dimensional and geometrical differences between parts, fabrication and assembly, process variability, and structural damping and stiffness variations of adjacent structures.

From equation (4),

$$N_T = C^\beta \sigma^{-\beta}$$

N_T and σ are now random variables.

From reference [2] the probability density function of the average cycles to failure is as follows:

$$p(N_T) = \frac{C}{\beta \delta \sqrt{2\pi} N_T^{(1/\beta)+1}} \quad (10)$$

$$\cdot \exp\left[-\frac{\left\{\frac{C}{N_T^{1/\beta}} - \bar{\sigma}\right\}^2}{2\delta^2}\right]$$

$$\text{for } N_T \geq 0$$

$$p(N_T) = 0 \qquad \text{otherwise}$$

where

$\bar{\sigma}$ = average value of rms stress

δ = standard deviation of rms stress

$F(N)$ = probability of failure in N cycles

$$F(N) = \int_0^N p(N_T) dN_T$$

$$F(N) = 0.5 - erf_p\left[\frac{\frac{C}{N^{1/\beta}} - \bar{\sigma}}{\delta}\right] \quad (11)$$

$$F(0) = 0; \quad F(\infty) = 1$$

$$F(N_{median}) = 0.5$$

for

$$N = C^\beta (\bar{\sigma})^{-\beta} = \text{median of N} \quad (12)$$

where

$$erf_p(\alpha) = \frac{1}{\sqrt{2\pi}} \int_0^\alpha e^{-y^2/2} dy \quad (13)$$

$$erf_p(-\alpha) = -erf_p(\alpha)$$

$$erf_p(\infty) = 0.5; \qquad erf_p(0) = 0$$

EXPERIMENT DESCRIPTION

J.T. Broch of Brüell and Kjaer [4] ran a random fatigue experiment on 200 epoxy paper printed circuit board specimens. There were 100 SDF specimens and 100 2DF specimens. See Figures 3 and 4. Three specimen arrangements of a given type were vibrated simultaneously. The rms stress level was controlled by regulating the output of an accelerometer mounted on the center arrangement of each group of three. (Strain gages were used to initially set the vibration level but their own fatigue life was shorter than those of the specimens.) For the particular resonant frequencies shown in Figure 5, the effective frequency of the 2DF system was adjusted to be equal to that of the SDF system (i.e., 20.5 Hz) by adjusting the ratio

$$\sigma_2^2 / \sigma_1^2 = 0.306$$

The average number of zero crossings was checked with an electronic counter and the upper resonant frequency excitation of the 2DF system was slightly corrected until the desired value was obtained. Then the overall levels of
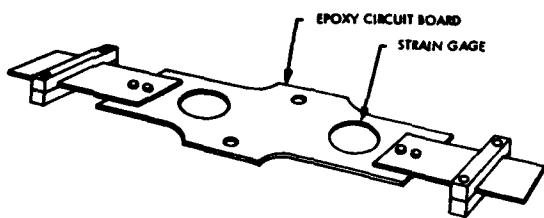
Figure 3. Single Degree-of-Freedom Specimen
Arrangement
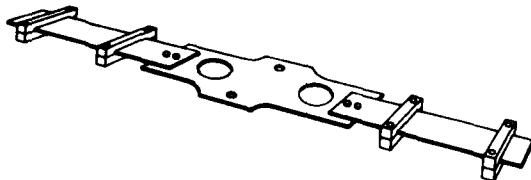
Figure 4. Two Degree-of-Freedom Specimen
Arrangement
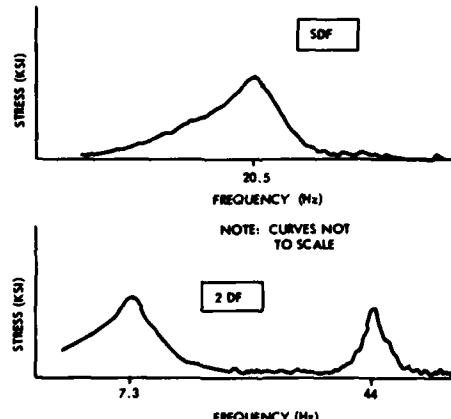
Figure 5. Typical Stress Response
Characteristics

both frequency bands were adjusted within ex-
perimental accuracy to be the same.

RESPONSE RESULTS

The stress-time response profile of a SDF
system is that of a simple oscillator that rings
at its resonant frequency with slowly varying
amplitude in a random fashion (see Figure 6).
The corresponding response profile of the 2DF
system is that of a high frequency riding on top
of a low frequency response (see Figure 7). The
two cases have widely different profiles.

Under the conditions of equal rms stress
and effective frequency, the number of stress
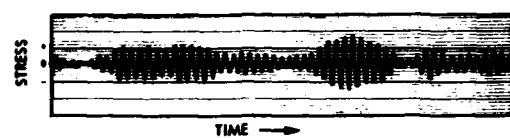
Figure 6. Stress-Time Response Profile of
Single-Degree-of-Freedom System
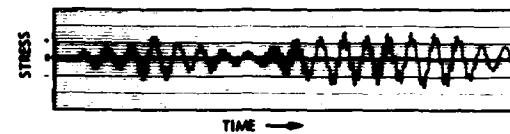
Figure 7. Stress-Time Response Profile of
Two-Degree-of-Freedom System

peaks within stress intervals ΔX wide will be
the same for the two cases. See Figure 8.
Equations in reference [2] were used to calcu-
late the scaled probability density function $G(s)$
of the fatigue damage for a SDF system. As
such, it indicates how the fatigue damage is dis-
tributed as a function of stress.

$$G(s) = \left[\frac{1}{\sigma^2 A^\beta}\right] S^{1+\beta} e^{-S^2/2\sigma^2} \qquad (14)$$

$G(s)$ is a maximum at the statistical mode S_0
where

$$S_0 = \sigma \sqrt{1 + \beta} \qquad (15)$$

$\sigma_{G(s)}$ = standard deviation of $G(s) = 0.7\sigma$
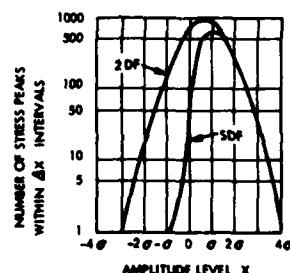
Figure 8. Relative Occurrence of Stress Peaks

Figure 9 shows a plot of $G(s)$ for G-10 ep-
oxy fiberglass, which is the material whose
properties closest match that used in the exper-
iment for which this author has fatigue data.
This figure shows that most fatigue damage is
done by stress peaks between 2σ and 5σ for a
SDF system. Additionally, the fact that the 2DF
and SDF systems have the same number of
stress peaks above 1.5σ (refer to Figure 8) led

46
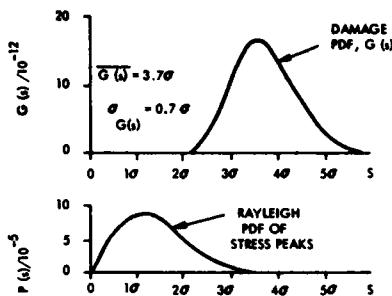
Figure 9. Damage Function for G-10 Glass Epoxy Example

to the hypothesis that the SDF system fatigue equations might also apply to the 2 DF system.

FATIGUE LIFE RESULTS

The time of failure for each specimen is shown sequentially in Table 1. The effective frequency for both systems was 20.5 Hz. The median times to failure (i.e., the time for 50 percent of all failures) were as follows:

t_{median} = 8616 seconds for the SDF system

t_{median} = 14,719 seconds for the 2DF system

The corresponding median cycles to failure were as follows:

N_{median} = 1.77 x 10^5 cycles (SDF)

N_{median} = 3.02 x 10^5 cycles (2DF)

ANALYSIS OF RESULTS

The sinusoidal S-N curve for the particular epoxy printed circuit board material is not known. Reference [3] does have one for a similar material, G-10 glass epoxy, which can be represented as follows:

$$S = 80.9 N_s^{-0.083} \text{ KSI}$$

$$= 5.58 \times 10^8 N_s^{-0.083} \text{ Pa}$$

$$\beta = 12.1$$

$$C = 33.0 \text{ KSI}$$

$$= 2.28 \times 10^8 \text{ Pa (see equation (3))}$$

$$\sigma = 33.0 N_T^{-0.083} \text{ KSI}$$

$$= 2.28 \times 10^8 N_T^{-0.083} \text{ Pa}$$

These curves are plotted in Figure 2.

TABLE 1. Failure Times of Occurrence

	Single Degree-of-Freedom Test				Two Degree-of-Freedom Test		
Rank	Time (s)	Rank	Time (s)	Rank	Time (s)	Rank	Time (s)
1	2085	51	8616	1	2985	51	14993
2	2095	52	8616	2	3075	52	15303
3	2204	53	8665	3	3125	53	15449
4	2239	54	8689	4	3421	54	15545
5	2411	55	8696	5	3720	55	15562
6	2414	56	9016	6	4169	56	15916
7	2811	57	9063	7	4321	57	16062
8	2820	58	9394	8	4353	58	16125
9	2886	59	9397	9	5641	59	16638
10	2996	60	9633	10	5727	60	17008
11	3046	61	9558	11	5756	61	17287
12	3086	62	9688	12	6316	62	17506
13	3124	63	9880	13	6389	63	17674
14	3501	64	10430	14	8014	64	17810
15	3734	65	10490	15	8050	65	18206
16	4078	66	10723	16	8120	66	18229
17	4130	67	10629	17	8145	67	19728
18	4136	68	11206	18	8200	68	20045
19	4177	69	12529	19	8231	69	20170
20	4276	70	12550	20	8265	70	20675
21	4421	71	12806	21	8906	71	21457
22	4426	72	13014	22	9202	72	21879
23	4717	73	13277	23	9718	73	21883
24	4956	74	15915	24	9976	74	22034
25	5223	75	16140	25	10362	75	22329
26	5459	76	16232	26	10390	76	22604
27	5742	77	16418	27	11353	77	23629
28	5807	78	16638	28	11442	78	23663
29	6058	79	17062	29	11516	79	25070
30	6143	80	17787	30	11772	80	25167
31	6194	81	17843	31	12316	81	26022
32	6194	82	17928	32	12339	82	26055
33	6202	83	18003	33	12357	83	26309
34	6640	84	18292	34	12475	84	26425
35	6657	85	19106	35	12570	85	26865
36	6661	86	19133	36	12669	86	26987
37	7566	87	19200	37	13115	87	27620
38	7614	88	20462	38	13160	88	27857
39	7815	89	20796	39	13250	89	27895
40	7984	90	20025	40	13251	90	28000
41	8016	91	21010	41	13330	91	28086
42	8133	92	21333	42	13497	92	28991
43	8190	93	21937	43	13707	93	29159
44	8225	94	22000	44	13795	94	29245
45	8226	95	22220	45	13823	95	29775
46	8355	96	22581	46	13961	96	31003
47	8357	97	23680	47	14014	97	31311
48	8387	98	24281	48	14261	98	32277
49	8493	99	27868	49	14483	99	32541
50	8615	100	30162	50	14719	100	32891

The experimental failure data of Table 1 will be analyzed to estimate the fatigue parameters $\bar{\sigma}$ and δ. These parameters will then be used to calculate the data points of the p(N) and F(N) functions versus N curves and to compare them with the corresponding curves through the experimental data points. It is necessary that the calculated curves match the experimental curves in terms of form and shape in order for the proposed SDF derived equations to be applicable.

<u>SDF:</u>

Refer to the SDF portion of Table 1. Note that time and cycles to failure are related by equation (5) for all cases.

$$\bar{\sigma} = C N_{median}^{-1/\beta} = (33.0)(1.77 \times 10^5)^{-0.083}$$

$$\bar{\sigma} = 12.1 \text{ KSI} = 8.34 \times 10^7 \text{ Pa}$$

$$F(N) = 0.9 \text{ for } t_{0.9} = 20,925 \text{ seconds}$$

$$N_{0.9} = 20.5 t_{0.9} = 4.29 \times 10^5 \text{ cycles}$$

Using equation (11),

$$\text{erf}_p\left[\cfrac{\cfrac{C}{N^{1/\beta}} - \bar{\sigma}}{\delta}\right] = 0.5 - 0.9 = -0.4$$

Therefore,

$$\delta = 0.67 \text{ KSI} = 0.462 \times 10^7 \text{ Pa}$$

and

$$\delta / \bar{\sigma} = 5.5\%$$

From equation (10),

$$p(N) = \frac{1.63}{N^{1.08}} \exp\left[-\cfrac{\left\{\cfrac{33}{N^{0.083}} - 12.1\right\}^2}{0.898}\right]$$

$$N = t_F \times f_{eff} = 20.5\, t_F \text{ cycles}$$

In order to compare this expression with failure data in histogram fashion, it was integrated over small time intervals (e.g., 2000 - 4000 seconds) and the integrated value multiplied by the total number of specimens (100) and plotted at the center of the integration time interval. The calculated and experimental data are compared in Figure 10. The calculated curve is considered to be a good fit to the data, considering the sample size in each of the integration time intervals.
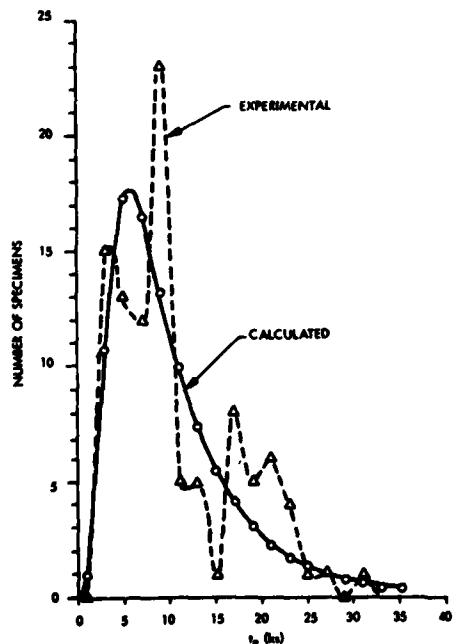
Figure 10. Fatigue Failure Histogram (Single Degree-of-Freedom)

From equation (11),

$$F(N) = 0.5 - \text{erf}_p\left[\cfrac{\cfrac{33}{N^{0.083}} - 12.1}{0.670}\right]$$

$$N = t_F \times f_{eff} = 20.5\, t_F \text{ cycles}$$

This expression is compared with the experimental cumulative failure data in Figure 11. Again, the calculated curve is considered to be a good fit to the data. At present, no attempt has been made to choose the calculated curve parameters by the least squares technique; nor have goodness of fit estimates been made.
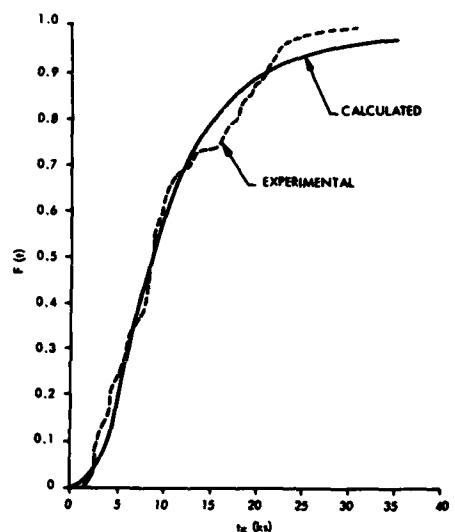
Figure 11. Probability of Failure (Single Degree-of-Freedom)

2DF:

A technique similar to the one used for the SDF system was used for the 2DF system for plotting and comparing equations (10) and (11) with the experimental data in Table 1. The expressions are briefly as follows:

$$\sigma = CN_{median}^{-1/\beta} = \frac{33}{(3.02 \times 10^5)^{0.083}}$$

$$= 11.6 \text{ KSI} = 8.00 \times 10^7 \text{ Pa}$$

$$F(N) = 0.9 \text{ for } t_{0.9} = 28,000 \text{ seconds}$$

$$N_{0.9} = 5.74 \times 10^5 \text{ cycles}$$

Using equation (11),

$$\delta = 0.468 \text{ KSI} = 0.323 \times 10^7 \text{ Pa}$$

$$\frac{\delta}{\overline{\sigma}} = 4\%$$

$$p(N) = \frac{2.33}{N^{1.08}} \exp\left[-\frac{\left\{\frac{33}{N^{0.083}} - 11.6\right\}^2}{0.468}\right]$$

$$F(N) = 0.5 - \text{erf}_p\left[\frac{\frac{33}{N^{0.083}} - 11.6}{0.468}\right]$$

where

$$N = f_{eff} t_F = 20.5 t_F \text{ cycles}$$

These equations are plotted in Figures 12 and 13. The calculated curves are considered to show good agreement with the experimental data.
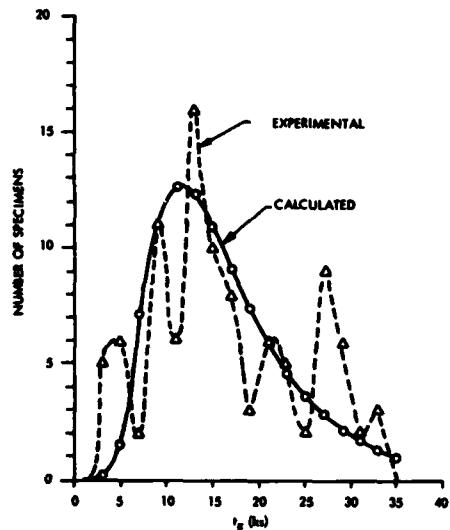
Figure 12. Fatigue Failure Histogram (Two Degrees of Freedom)

The measured median endurance life for the 2DF system is 70 percent greater than for the SDF system. The calculated average value of rms stress for the SDF system is 4 percent (i.e., 0.34 dB) higher than for the 2DF system. The standard deviations, δ, of the rms stress for the two cases are approximately the same. Thus, the slopes of the F(t) versus time curves have approximately the same value. (Refer to Table 2.)
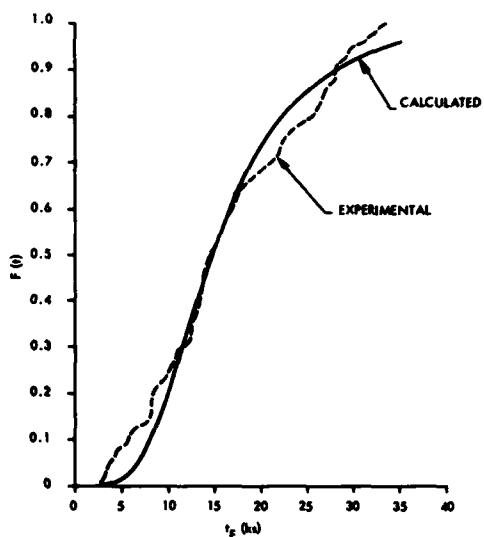
Figure 13. Probability of Failure (Two Degrees of Freedom)

TABLE 2. Experimental Result System Comparison

		SDF	2DF
t_{median}	(seconds)	8616	14,719
N_{median}	(cycles)	1.77×10^5	3.02×10^5
$\overline{\sigma}$	(KSI)	12.1	11.6
	(Pa)	8.34×10^7	8.00×10^7
δ	(KSI)	0.67	0.468
	(Pa)	0.462×10^7	0.323×10^7
$\delta/\overline{\sigma}$	(percent)	5.5	4

The failure points for the two systems are plotted in Figure 14 which shows that the two failure points nearly coincide. The fatigue curve for G-10 epoxy fiberglass is much more sensitive to stress variations than cycles to failure (time) variations.

EXPERIMENTAL ACCURACY

J.T. Broch [4] stated the following three items:

1) The variation in the response of the specimen strain gages from the static strain test was less than 10 percent.

2) The variation in dynamic strain between the specimens when tested on the vibrator was of the order of 1 dB (12%).

49
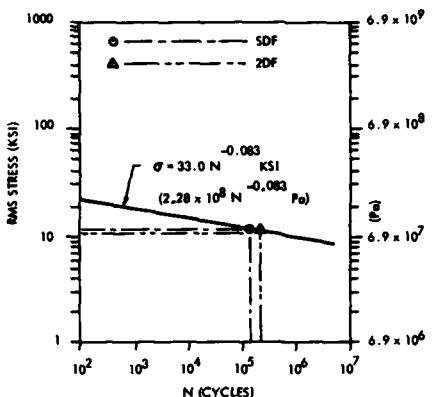
Figure 14. Fatigue Sensitivity

3) The variation in average zero crossing
   frequency between the specimens was less
   than 2 Hz.

No mention is made of an estimation of system-
atic errors. However, this author believes a
systematic error of 0.4 dB is within the bound
of experimental accuracy for this type of ex-
periment.

DISCUSSION OF RESULTS

The expressions for p(N) and F(N) yield re-
sults that closely match the form and shape of
the experimental data for both the SDF and 2DF
systems. The 2DF system had a median fatigue
life 1.7 times that of the SDF system. As such,
both failure points on the fatigue curve nearly
coincided. If the actual average rms stress of
SDF systems was 4 percent (0.34 dB) greater
than that for the 2DF system, the two failure
points would exactly coincide. The actual sys-
tematic error in adjusting the rms stress levels
is unknown. A value of 0.34 dB is believed to
be within the bound of experimental accuracy
for this type of experiment.

By inductive reasoning, it is believed that,
under the same test conditions as above (i.e.,
equal rms stress and equal effective frequency),
multiple degree-of-freedom systems would
have the same fatigue life.

STATIC STRESS ADDITION

The effects of a static stress added to the
random stress can be included by subtracting
the value of the static stress from the value of
A in equations (1) and (3). This is equivalent to
using a Goodman diagram with the engineering

ultimate stress replaced with the true ultimate
stress [2].

In J.T. Broch's experiments, the static
stresses were very small compared with the
random dynamic stresses and hence were not
included in this analysis.

ALTERNATIVE ANALYTICAL APPROACH

An alternative analytical approach was in-
vestigated which also used Miner's rule for
damage cumulation. It differed from the pro-
posed method in that it treated the two resonant
modes for the 2DF system as acting independ-
ently. Their stress responses and frequencies
were added in the linear sense rather than in
the rms sense. Refer to Appendix B. Using
this alternative approach, the time to failure
for the 2DF system was calculated to be ten
times that of the SDF. This factor of 10 does
not come close to agreeing with the factor of
1.7 from Broch's [4] experiment. Therefore,
the alternative analytical approach was con-
sidered invalid.

CONCLUSIONS

The test results cited tend to confirm the
proposal that the fatigue equations developed
for a narrow-band random process can be ap-
plied to multiple degree-of-freedom systems
with reasonable accuracy, given that the stress
responses and frequencies are added in the rms
sense. Further analytical and experimental ef-
fort is required before firm conclusions can be
made.

The fundamental justification for this pro-
posal is that both the SDF and 2DF systems have
the same number of stress peaks above 1.5σ
and these higher peaks are the cause of most
fatigue damage.

SYMBOLS

A	material constant; true ultimate stress
C	constant of random fatigue curve
D_σ	proportion of damage related to stress
erf_p	error function defined by Papoulis [5]
F(N)	probability of failure in N cycles
f_B	bandwidth

f_0 f_1 f_2	bandpass center frequencies	$\bar{\sigma}$	average value of σ
		$G(s)$	standard deviation of $G(s)$
		τ	time difference
		ω	circular frequency

f_{eff}	effective frequency
$G(s)$	scaled damage PDF
j	resonant mode index
k	number of resonant modes
N	number of stress cycles
N_{median}	number of cycles for 50 percent of all failures
$N_{0.9}$	number of cycles for 90 percent of all failures
N_S N_T	number of stress cycles to failure
$p(N)$ $p(N_T)$ PDF	probability density function
$R(\tau)$	autocorrelation function
$R''(\tau)$	second derivative of autocorrelation function
rms	root mean square
S	sinusoidal stress amplitude
S_0	stress at statistical mode of $G(s)$
SDF	single degree-of-freedom system
$S_x(\omega)$	power spectrum
t	time
t_{median}	time for 50 percent of all failures
$t_{0.9}$ t_F t_{2DF} t_{SDF}	time to failure
y	dummy variable
z	power ratio
2DF	two degree-of-freedom system
α	general variable
β	fatigue curve slope parameter
Γ	gamma function
δ	standard deviation of σ
λ	average number of zero crossings per unit time
σ	rms stress level

REFERENCES

1. R.W. Landgraf, "Cumulative Fatigue Damage under Complex Strain Histories," American Society for Testing and Materials, STP 519, p. 213, December 1971

2. R.G. Lambert, "Analysis of Fatigue under Random Vibration," presented at 46th Shock and Vibration Symposium, San Diego, Calif., October, 1975

3. D.S. Steinberg, Vibration Analysis for Electronic Equipment, John Wiley and Sons, 1973

4. J.T. Broch, "Peak Distribution Effects in Random Load Fatigue," Brüell and Kjaer Technical Review 1-1968

5. A. Papoulis, Probability, Random Variables, and Stochastic Processes, McGraw-Hill Book Co., New York, 1965

APPENDIX A

EFFECTIVE FREQUENCY DERIVATION

Refer to pages 485-491 of Papoulis [5].

Consider the bandpass processes as shown in Figure 15. This represents the 2DF case.
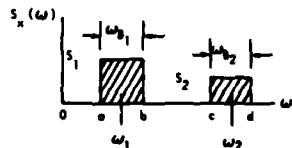
Figure 15. Power Spectrum (2DF)

The average number of zero crossings per unit time of a stress-time function is given by:

$$\lambda = \frac{1}{\pi} \sqrt{-\frac{R''(0)}{R(0)}} \qquad (16)$$

where

$R(\tau)$ = autocorrelation function as a function of time difference

$R''(\tau)$ = second derivative of $R(\tau)$

ω = frequency (radians per second) = $2\pi f$

$S_x(\omega)$ = power spectrum

f = frequency (Hz)

Refer to Figure 15. Energy is additive. Therefore:

$$\lambda^2 = \frac{1}{\pi^2}\left(-\frac{R''(0)}{R(0)}\right) = \frac{1}{\pi^2}\left\{\frac{-R_1''(0) - R_2''(0)}{R_1(0) + R_2(0)}\right\}$$

$$R_1(0) = \sigma_1^2 = \frac{1}{2\pi}\int_{\omega_a}^{\omega_b} S_x(\omega)\, d\omega \tag{17}$$

$$R_2(0) = \sigma_2^2 = \frac{1}{2\pi}\int_{\omega_c}^{\omega_d} S_x(\omega)\, d\omega$$

$$R_1(0) + R_2(0) = \sigma_1^2 + \sigma_2^2 = \sigma_T^2 \tag{18}$$

Therefore

$$\lambda^2 = \frac{1}{3\pi^3\sigma_T^2}\left\{S_1(\omega_b^3 - \omega_a^3) + S_2(\omega_d^3 - \omega_c^3)\right\}$$

Let

$$\omega_a = \omega_1 - \frac{\omega_{B_1}}{2}; \qquad \omega_b = \omega_1 + \frac{\omega_{B_1}}{2}$$

$$\omega_c = \omega_2 - \frac{\omega_{B_2}}{2}; \qquad \omega_d = \omega_2 + \frac{\omega_{B_2}}{2}$$

Then

$$\omega_b^3 - \omega_a^3 = 3\omega_1^2\omega_{B_1} + (\omega_{B_1}^3/4)$$

$$\omega_d^3 - \omega_c^3 = 3\omega_2^2\omega_{B_2} + (\omega_{B_2}^3/4)$$

Therefore

$$\lambda^2 = \frac{4}{\sigma_T^2}\left\{S_1\left(f_1^2 f_{B_1} + \frac{f_{B_1}^3}{12}\right) + S_2\left(f_2^2 f_{B_2} + \frac{f_{B_2}^3}{12}\right)\right\}$$

where

σ = rms stress (psi)

t = time (seconds)

N_T = average number of stress cycles in time t

f_{eff} = effective frequency (Hz)

There will be one stress cycle for every two zero crossings. Therefore:

$$f_{eff} = \lambda/2$$

$$\sigma_1^2 = S_1 f_{B_1}; \quad \sigma_2^2 = S_2 f_{B_2}; \quad N_T = \frac{\lambda}{2}t$$

$$N_T = t\sqrt{\frac{\sigma_1^2}{\sigma_T^2}\left(f_1^2 + \frac{f_{B_1}^2}{12}\right) + \frac{\sigma_2^2}{\sigma_T^2}\left(f_2^2 + \frac{f_{B_2}^2}{12}\right)}$$

For $f_{B_1} \ll f_1$ and $f_{B_2} \ll f_2$

$$N_T \cong t\sqrt{\frac{\sigma_1^2}{\sigma_T^2}f_1^2 + \frac{\sigma_2^2}{\sigma_T^2}f_2^2}$$

$$f_{eff} \cong \sqrt{\frac{\sigma_1^2}{\sigma_T^2}f_1^2 + \frac{\sigma_2^2}{\sigma_T^2}f_2^2} \tag{19}$$

Equation (19) applies for the 2DF system. This derivation can be extended to SDF and other multiple degree-of-freedom systems by the appropriate use of equations (17) and (18).

For the SDF case, $R_2(0)$ and $R_2''(0)$ are eliminated. Equation (19) then becomes:

$$f_{eff} = f_0 \text{ Hz} \tag{20}$$

For k quantity of resonand modes

$$\sigma_T^2 = \sum_{j=1}^{k}\sigma_j^2 \quad \text{stress units squared} \tag{21}$$

where j = resonant mode index and

$$f_{eff} = \sqrt{\sum_{j=1}^{k}\left(\frac{\sigma_j^2}{\sigma_T^2}f_j^2\right)} \quad \text{Hz} \tag{22}$$

INDEPENDENT MODE DAMAGE CUMULATION

Fatigue microcrack initiation usually occurs in the very early portion of the total fatigue life. Many small microcracks undergo two stages of crack growth, then combine into a macrocrack which eventually propagates until the specimen fractures. Fatigue damage is cumulating during the entire fatigue life. Fatigue failure is the catastrophic fracture at the end of fatigue life.

Miner's hypothesis quantitatively expresses damage cumulation and relates it to failure as follows:

$$D_\sigma = \frac{N_\sigma}{N_T} \quad ; \quad \sum D_\sigma = 1 \quad (\text{at failure})$$

where

N_σ = number of stress cycles at stress level σ

N_T = number of stress cycles at stress level σ to cause failure

D_σ = proportion of damage due to stress level

For the SDF case:

From equation (4),

$$N_T = C^\beta \sigma_0^{-\beta}$$

$$N = f_0 t$$

where

f_0 = SDF resonant frequency (Hz)
(f_0 = 20.5 Hz in Broch's experiment)

t = time (seconds)

Therefore

$$D_0 = f_0 \left(\frac{\sigma_0}{C}\right)^\beta t \tag{23}$$

Failure occurs for $D_0 = 1$. Therefore, at failure:

$$t_{SDF} = \left(\frac{1}{f_0}\right)\left(\frac{C}{\sigma_0}\right)^\beta \tag{24}$$

For the 2DF case:

Consider that the damage cumulated for each resonant mode acts independently of all other modes and that the total damage cumulated is the linear sum of each mode's damage cumulation.

$$D_{\text{mode 1}} + D_{\text{mode 2}} = 1 \quad \text{at failure} \tag{25}$$

$$\frac{1}{C^\beta}\left[f_1 \sigma_1^\beta t_{2DF} + f_2 \sigma_2^\beta t_{2DF}\right] = 1$$

$$t_{2DF} = \frac{C^\beta}{f_1 \sigma_1^\beta + f_2 \sigma_2^\beta} \tag{26}$$

For SDF and 2DF cases:

$$\frac{t_{2DF}}{t_{SDF}} = \frac{f_0 \sigma_0^\beta}{f_1 \sigma_1^\beta + f_2 \sigma_2^\beta} \tag{27}$$

$$\sigma_0^2 = \sigma_1^2 + \sigma_2^2 \quad (\text{equal rms stresses})$$

$$f_0^2 = \frac{\sigma_1^2}{\sigma_0^2} f_1 + \frac{\sigma_2^2}{\sigma_0^2} f_2^2 \quad (\text{equal effective frequencies})$$

Define

$$Z = \frac{\sigma_2^2}{\sigma_0^2} = \frac{f_0^2 - f_1^2}{f_2^2 - f_1^2} \tag{28}$$

$$\frac{\sigma_2^2}{\sigma_1^2} = \frac{Z}{1 - Z} \tag{29}$$

Equation (27) becomes

$$\frac{t_{2DF}}{t_{SDF}} = \frac{f_0}{f_1(1 - Z)^{\beta/2} + f_2 Z^{\beta/2}} \tag{30}$$

For Broch's experiment:

f_0 = 20.5 Hz β = 12

f_1 = 7.3 Hz t_{2DF} = 14,719 seconds

f_2 = 44 Hz t_{SDF} = 8616 seconds

Using equation (28),

$$Z = 0.195$$

$$1 - Z = 0.805$$

Using equation (30), the calculated time-to-failure ratio is:

$$\frac{t_{2DF}}{t_{SDF}} = 10$$

This ratio of failure times does not agree at all with the experimental value of 14,719 seconds / 8616 seconds = 1.7. Therefore, the analytical approach of treating the resonant modes independently was discarded.

A MATHEMATICAL MODEL FOR THE STRESS
AND VIBRATIONAL ANALYSIS OF THE HUMAN MITRAL VALVE

J. Mazumdar* and T. C. Hearn

Department of Applied Mathematics

The University of Adelaide, South Australia

Visual inspection of the mitral valve ring shows a degree of asymmetry about the line of contact of the two leaflets. This characteristic has not been taken into account in previous models. In the present paper, a mathematical model, taking this asymmetry into account, has been discussed, together with other models, by considering the mitral valve boundary to be represented by the limacon of Pascal. The limacon is considered in its second mode of vibration, with the nodal line corresponding to the line of contact of the two leaflets and the two vibrating parts of the limacon membrane representing the two leaflets of the mitral valve. The Young's modulus of the leaflets is determined as a function of the fundamental frequency of vibration, forming the basis for non-invasive diagnosis of valve tissue deterioration. Stresses in the valve leaflets are calculated, under adverse physical conditions, in order to obtain structural requirements for a prosthetic valve leaflet.

INTRODUCTION

A detailed account of the role of the mitral valve in cardiac function can be obtained in reference [1]. Very briefly, the function of the mitral valve can be described as follows.

The left side of the heart is divided into two chambers, the left atrium and the left ventricle. The mitral valve consists of a pair of membranous leaflets interposed between these two chambers. Each leaflet is attached along one edge to a fibrous valve ring along the atrio-ventricular junction. The free edge of each leaflet is attached to suspensory ligaments (chordae tendineae) which are anchored to papillary muscles on the inside of the left ventricle. During left ventricular diastole (expansion), the mitral valve opens to permit blood to flow in the direction from the atrium to the ventricle. At the beginning of systole (contraction), blood rushes towards the taut leaflets causing them to vibrate. This vibration is recorded as the first component of the first heart sound. As systole proceeds, the pressure in the left ventricle increases, and the mitral valve closes to prevent any flow of blood back into the atrium. The pressure increases until the aortic valve opens, and the blood is expelled into the arterial system of the body.

As a result of disease, the human mitral valve can become inefficient through the loss of elasticity of the valve leaflets. Ghista and Rao [2,3] have shown how a mathematical model of the leaflets can be used to determine the extent of such deterioration non-traumatically, by measuring the fundamental frequency of vibration of the leaflets. As in these two references, the present paper analyses the valve leaflets in a quasi-static pressure-loaded state combined with a vibrational analysis to yield expressions for the stress in the leaflet and the Young's modulus of the leaflet material, as a function of its fundamental frequency of vibration. This frequency can be measured with the use of a phonocardiographic record, providing an aid in the diagnosis of mitral valve disease when elasticity of the valve leaflets may be affected.

The present study has two main purposes. Firstly, it provides an alternative method for non-invasive determination of the state of the valve tissue, as characterized by the Young's modulus of the tissue material. The Young's modulus is formulated by combining the vibration analysis of the mitral valve leaflets with the spectral analysis of heart-sound frequencies. The in-vivo characteristic will also help to distinguish pathological from normal leaflets. Secondly, it considers the effect on the nature of this relationship by different

* Present Address: Visiting Professor, Department of Metallurgy, Mechanics and Materials Science, Michigan State University, East Lansing, Michigan, U.S.A.

choices of shape parameters of the mitral valve leaflets.

ANALYSIS

It is the object of the mathematical analysis of the mitral valve to yield a method for the determination of the structural state of the valve tissue in terms of the leaflet dimensions, geometry and primary frequency of vibration. This is achieved by a combination of vibrational analysis of the leaflets, together with a quasi-static pressure-loaded stress-deformation analysis of the leaflets at the onset of its vibration.

Consider the mitral valve leaflets at the instant of occurrence of the first heart sound, following the onset of ventricular contraction. At this stage of the cardiac cycle, the mitral valve has just closed. While the leaflets of the mitral are fixed around its curved edge by the fibrous valve ring, the free edges are held in apposition to each other by the suspensory ligaments, the chrodae tendineae.

For the purpose of analysis, it is sufficient to analyse only one of the leaflets (say, the anteromedial one). Each mitral valve leaflet is represented by an homogeneous membrane, which is considered to be held at its boundary (Fig. 1). The membrane is distended due to the pressure loading q, and we denote by C_u, $0 \leq u \leq u^*$, the family of closed curves with the property that the membrane deflection is constant along each curve $u(x,y) \approx$ const. We may view this family of isoamplitude level curves C_u as contours of the function $u(x,y)$, C_0 representing the boundary of the membrane and C_u coinciding with the point(s) at which the maximum $u = u^*$ is attained.

When the membrane vibrates, the dynamic component of the deflection W_d will be superimposed onto the static deflection W_s to give the total deflection of the membrane. Denoting the density per unit area by ρ and tension per unit length by T we have the frequency equation for the normal mode of vibration [see Appendix]
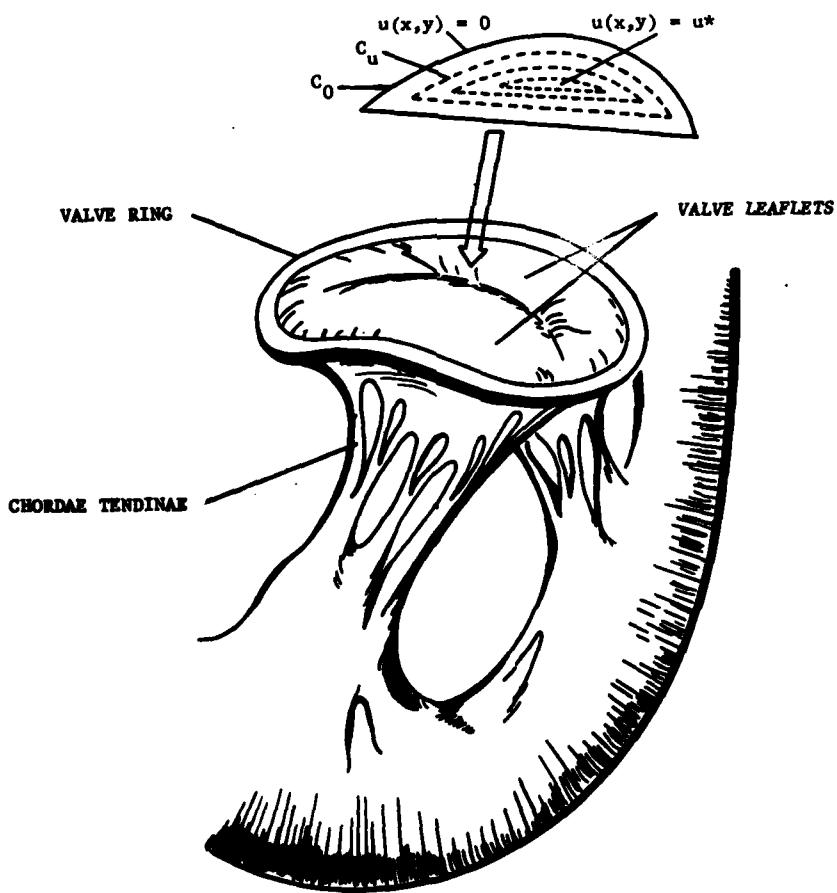
Fig. 1 - Idealised model of the pressure-loaded leaflets

$$\sqrt{2u^*}\ K \ = \ B_i \qquad (1)$$

where B_i is the i-th zero of zeroth order Bessel function and the quantity $\omega\sqrt{\rho/T}$ is denoted by K, ω being the mode frequency. For the fundamental mode of vibration, it is clear that

$$K\left(=\omega\sqrt{\frac{\rho}{T}}\right) \ = \ \frac{2.4048}{\sqrt{2u^*}} \qquad (2)$$

From the above equation it is evident that since u^* can be known and monitorable, T can be obtained when the mode frequency ω is known.

The main objective of this analysis is to express the Young's modulus E of the leaflet material in terms of its fundamental mode frequency and the leaflet size and dimensions. This is achieved by determining the tension T in the membrane, obtained by invoking the physical requirement that the change in membrane surface area due to its taking up its deflected shape, must equal the change in surface area due to its being stretched by the tension T. We thus have [3]

$$\frac{1}{2}\iint_\Omega (\nabla W_s \cdot \nabla W_s)d\Omega \ = \ \iint_\Omega \frac{2T(1-\nu)}{Eh}\, d\Omega \qquad (3)$$

where ν is Poisson's ratio and h is the thickness of the valve leaflet. Using the fact that u is related to W_s by

$$u \ = \ -\frac{2T}{q}\,W_s \qquad (4)$$

we obtain the following expression for the tension

$$T \ = \ \left[\frac{E\,h\,q^2 u^*}{16(1-\nu)}\right]^{1/3} \qquad (5)$$

and then using the equation (1) for the fundamental mode of vibration, we obtain the desired relationship between the Young's modulus E and the frequency f_{11} (cycles/sec.) of the principal mode of vibration of the valve leaflet as follows:

$$E \ = \ \left[\frac{8\pi^2 \rho\, f_{11}^2}{(2.4048)^2}\right]^3 \frac{16(1-\nu)u^{*2}}{hq^2} \qquad (6)$$

The stress σ in the leaflet is given by $\sigma = T/h$; hence, from the expression (5), we get the expression for the stress in the valve-leaflet membrane as follows:

$$\sigma \ = \ \left[\frac{E\,q^2 u^*}{16h^2(1-\nu)}\right]^{1/3} \qquad (7)$$

Thus the stress in the leaflet is obtained as a function of the pressure loading q across the valve leaflet, the thickness h of the valve and the Young's modulus E and the Poisson's ratio ν of the valve-leaflet material.

It is clear that the above equation involves the monitorable quantity u^* which depends on the choice of the shape of the mitral valve leaflet. A number of geometric models for such analysis have been considered in the past. For example, a semi-circular leaflet model was considered in [2]. In [5] a semi-elliptic and a parabolic leaflet model were discussed. However, in none of these models has the effect of the asymmetry of the mitral valve ring been taken into account. It has been observed that the mitral valve ring has a degree of asymmetry about the line of contact of the two leaflets.

We will now take into account the effect of the asymmetry by modelling both leaflets simultaneously, and representing the valve ring geometrically by the limacon of Pascal, given by

$$R(\theta) \ = \ a(1+0.5\,\cos\theta) \qquad (8)$$

The limacon is considered to be a perturbation of a circle of radius a (Fig. 2). We consider the limacon in its second mode of vibration, with the nodal line corresponding to the line of contact of the two leaflets in the pressure loaded state and each vibrating part of the limacon corresponding to a mitral valve leaflet.
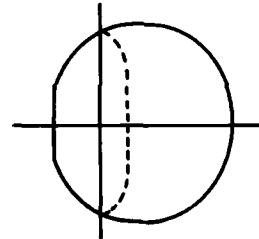
Fig. 2 - The limacon of Pascal, with the nodal line for second mode vibration.

The second mode frequency for the above limacon can be obtained by any of the approximate methods mentioned in [6]. However, using the result given in [7], we have

$$a\omega\sqrt{\frac{\rho}{T}} \ = \ 3.783 \qquad (9)$$

Combining this result with equation (2) yields the value of u^* which when substituted in expression (6) gives the following formula for E:

$$E \ = \ \frac{(8\pi^2 Df_{11}^2)^3\ 16(1-\nu)a^4 h^2}{4(3.783)^4\ (2.4048)^2 q^2} \qquad (10)$$

where D is the mass per unit volume of the leaflet material.

NOMOGRAMS

Expression (7) gives us the Young's modulus-stress relationship for the limacon model as

$$E = \frac{32\,\sigma^3(1-\nu)(3.783)^2}{(2.4048)^2}\,B \qquad (11)$$

where

$$B = \left(\frac{h}{aq}\right)^2 \qquad (12)$$

The parameter a is determined from the maximum valve diameter in accordance with Table 1 for a selected range of values of valve diameter. If we consider adult human mitral valves, for which the maximum diameter varies from 3.5 cm. to 4.0 cm., the corresponding range for a is from 1.5896 cm. to 1.8167 cm. The thickness h varies from 0.05 cm. to 0.1 cm. At the point of cardiac cycle when the mitral valve vibrates, we take the pressure as ranging from 5 mm. to 20.0 mm. of mercury (0.64×10^4 to 2.56×10^4 dyn/cm^2).

TABLE 1

Relationship between the Valve Diameter and the Valve Parameter (a)

Longest valve diam.(cm.)	Corresponding value of a (cm.)
2.0	0.9083
2.2	0.9992
2.4	1.0900
2.6	1.1808
2.8	1.2717
3.0	1.3625
3.2	1.4533
3.4	1.5442
3.5	1.5896
3.6	1.6350
3.8	1.7258
4.0	1.8167
4.2	1.9075
4.4	1.9983
4.5	2.0438

From the expression (12), we then determine the range of the parameter B as being from 4.0×10^{-12} to 3.6×10^{-10}. The relationship (11) is then plotted over this range of B in Fig. 3.

The normal stress-strain data for fresh human mitral valves was obtained by Clark [8]. The equation

$$\sigma = 4083.6(e^{17\epsilon}-1) \qquad (13)$$

where ϵ denotes the strain, provides an excellent fit to the experimental data. The Young's modulus thus obtained is given by

$$E = \frac{d\sigma}{d\epsilon} = 17(\sigma+4083.6) \qquad (14)$$

Equation (14) is also plotted on Fig. 3 representing normal mitral valve leaflets.

Further physiological data has been provided by Ghista [3]. We take the leaflet 'C' in this reference as being pathological. The stress-strain curve takes the form:

$$\sigma = 9714.6(e^{17\epsilon}-1) \qquad (15)$$

The expression for E thus obtained

$$E = 17(\sigma+9714.6) \qquad (16)$$

represents the pathological condition of the valve material. The range of values of E from normal to pathological is shown in Fig. 3.

Now consider the Young's modulus-frequency relationship for the limacon model which is obtained from equation (10) as follows:

$$E = \frac{(8\pi^2 D\,f_{11}^2)\,16(1-\nu)}{4(3.783)^4(2.4048)^2}\,A \qquad (17)$$

where

$$A = \frac{a^4 h^2}{q^2} \qquad (18)$$

Using the same data for a, h and q as before, we find that the range of the parameter is from 9×10^{-11} to 10^{-10}. The relationship (17) is then plotted over this range of A for various values of the frequency f_{11} to provide the nomogram of Fig. 4. Transferring the range of E obtained from Fig. 3 to this monogram yields the frequency range of mitral valve vibration as being between 65 Hz. and 90 Hz. for normal to pathological valve leaflets.

In general, the nomograms can be used to determine the frequency range of vibration of the mitral valve when a, h, q and f_{11} are known. Firstly, with this data the parameter B is determined exactly and the appropriate curve is chosen in Fig. 3. The normal to pathological range of Young's modulus is then obtained from the intersection of this curve with the physiological data. This range is then transferred to Fig. 4 and since the parameter A can be obtained exactly from the values of a, h and q, the corresponding range of frequencies for normal to pathological can be easily determined.

CONCLUSION

The geometry descriptions and material properties of human mitral valve leaflets have been studied with a view towards designing a prosthesis. Typical results obtained from the studies are presented in a form suitable for input into the design process. It is felt that
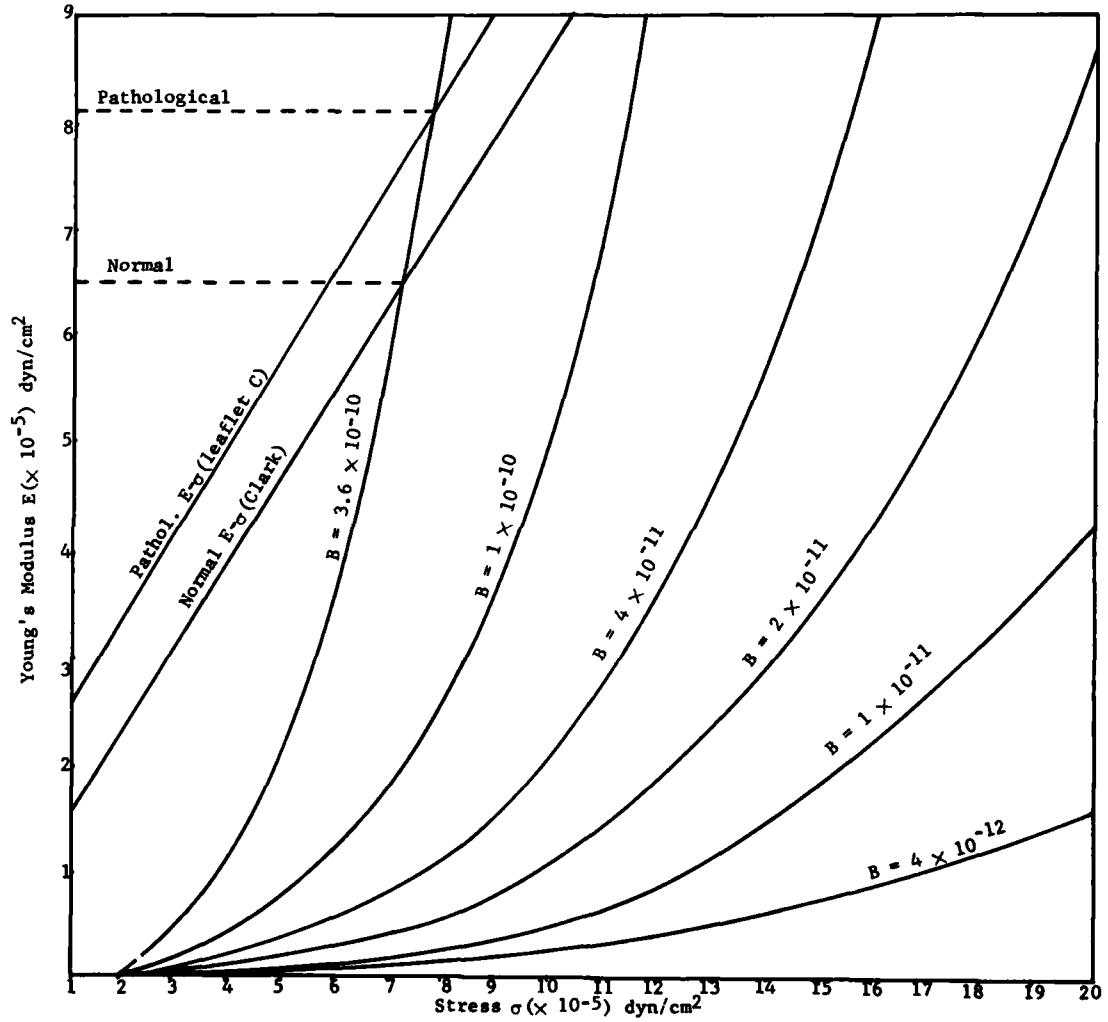
Fig. 3 - E vs σ curves for the range of values of the parameter $B = \left(\dfrac{h}{aq}\right)^2$.

Fig. 4 - Nomogram E vs A for various frequencies f_{11} $A = \dfrac{a^4 h^2}{q^2}$.
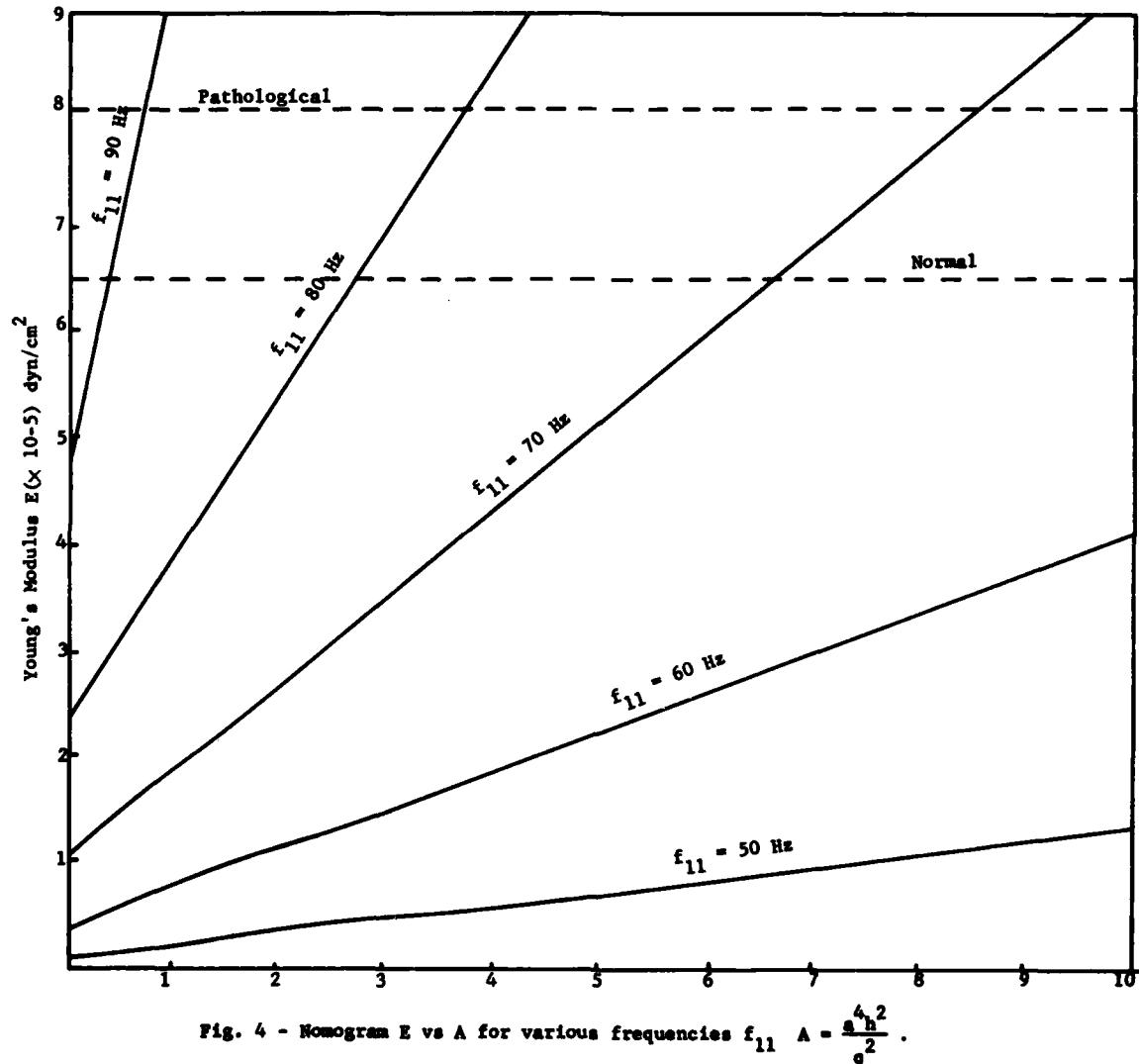
reliable experimental testing as well as significant idealization may be required to produce results useful for design purposes.

In the study we have made a case for possible indirect determination of the Young's modulus of the leaflet material which would help us to characterize its structural deformities. Deformities of the valves produce two main types of functional disturbances: Stenosis and regurgitation. Identifying the affected valve is important, particularly now that palliative surgery for valvular deformities is available.

ACKNOWLEDGEMENTS

APPENDIX

The differential equation of motion of the membrane at any instant of time τ is given by Mazumdar [4] as

$$T \oint_{C_u} \frac{\partial w_d}{\partial n}\, ds - \rho \iint_{\Omega_u} \frac{\partial^2 w_d}{\partial \tau^2}\, d\Omega = 0 \quad (A.1)$$

which, under an assumption of harmonic vibration

$$w_d = W_d\, e^{i\omega\tau} \quad (A.2)$$

leads to the following integro-differential equation

$$T \frac{dW_d}{du} \int_{C_u} \sqrt{t}\, ds + \rho\omega^2 \iint_{\Omega_u} W_d\, d\Omega = 0 \quad (A.3)$$

where ω is the frequency of the mode and W_d is the normal function determining the form of the deflected surface of the vibrating membrane which is a suitable function of u and

$$t = u_x^2 + u_y^2 \quad (A.4)$$

The double integral appearing in equation (A.1) can be simplified to yield

$$\frac{dW_d}{du} \oint_C t\, ds + k^2 \int_{u*}^u W_d\,(u_0) \left[\oint_{C_{u_0}} \frac{1}{\sqrt{t}}\, ds \right] du_0 = 0 \quad (A.5)$$

where the value of k^2 is given by equation (2). Here $u = u_0$ is an arbitrary closed contour. If we differentiate equation (A.5) with respect to u, we obtain:

$$\frac{d^2 W_d}{du^2} \oint_{C_u} \sqrt{t}\, ds - 2 \frac{dW_d}{du} \oint_{C_u} \frac{1}{\sqrt{t}}\, ds + k^2 W_d \oint_{C_u} \frac{ds}{\sqrt{t}} = 0 \quad (A.6)$$

The values of the contour integrals in the above equation can be obtained in the following manner with the help of Green's theorem

$$\oint_{C_u} \sqrt{t}\, ds = - \iint_{\Omega_u} (u_{xx} + u_{yy})\, d\Omega = \frac{2A}{u*}\,(u*-u) \quad (A.7)$$

$$\frac{d}{du} \oint_{C_u} \sqrt{t}\, ds = \oint_{C_u} (u_{xx} + u_{yy}) \frac{ds}{\sqrt{t}} = -2 \oint_{C_u} \frac{ds}{\sqrt{t}} \quad (A.8)$$

where A is the total area of the membrane. Here we have assumed the function $u(x,y)$ to be the Prandtl stress function for the corresponding problem of the torsion of an elastic cylinder, whose shape in cross-section is the same as the membrane boundary. Thus we have

$$u_{xx} + u_{yy} = -2 \text{ in the region } \Omega_0 \quad (A.9)$$

with the values of the above integrals and introducing a new independent variable g given by:

$$g^2 = u* - u \quad (A.10)$$

equation (A.6) finally becomes

$$\frac{d^2 W_d}{dg^2} + \frac{1}{g} \frac{dW_d}{dg} + 2k^2 W_d = 0 \quad (A.11)$$

This is the zeroth order Bessel equation with the general solution

$$W_d = A\, J_0(\sqrt{2}\, kg) + B\, Y_0(\sqrt{2}\, kg) \quad (A.12)$$

where A and B are arbitrary constants.

In order to avoid infinite displacements, we set $B = 0$. Also, since the membrane has zero displacement around the boundary, we have

$$J_0(\sqrt{2u*}\, k) = 0 \quad (A.13)$$

giving

$$\sqrt{2u*}\, k = B_i \quad (A.14)$$

where B_i is the i-th zero of the zeroth order Bessel function, i.e.,

$$\sqrt{2u*}\, k = 2.4048,\ 5.5201,\ 8.6537,\ldots. \quad (A.15)$$

REFERENCES

[1] R. F. Rushmer, Cardiovascular Dynamics. W. B. Saunders Co., 1964.

[2] D. N. Ghista and A. P. Rao, "Structural
Mechanics of the Mitral Valve: Stresses
sustained by the valve; non-traumatic
determination of the stiffness of the in-
vivo valve," J. Biomechanics, Vol. 5, pp.
295-307 (1972).

[3] D. N. Ghista and A. P. Rao, "Mitral Valve
Mechanics - Stress/Strain Characteristics
of excised leaflets, analysis of its func-
tional mechanics and its medical applica-
tion," Medical and Biological Engineering,
pp. 691-702 (1973).

[4] J. Mazumdar, "Transverse vibration of mem-
branes of arbitrary shape by the method of
constant deflection contours," J. Sound and
Vibration 27(1), pp. 47-57 (1973).

[5] J. Mazumdar and T. C. Hearn, "Mathematical
analysis of human mitral valve leaflets,"
sent for publication, J. Biomechanics.

[6] J. Mazumdar, "A review of approximate
methods for determining the vibrational
modes of membranes," The Shock and Vibra-
tion Digest, Vol. 7, No. 6, pp. 75-88
(1975).

[7] P. J. Torvik and F. E. Eastep, "A method
for improving the estimation of membrane
frequencies," J. Sound and Vibration,
21(3), pp. 285-294 (1972).

[8] R. E. Clark, "Stress-strain characteristics
of fresh and frozen human aortic and mitral
leaflets and chordae tendineae," J. Thora-
cic and Cardiovascular Surgery, 66(2),
August (1973).

THE DECREMENT IN VISUAL ACUITY RELATED TO VIBRATION
OF SHAKER, SEAT, AND OBSERVER'S HEAD

Owen F. Hackett
David W. Taylor Naval Ship Research and Development Center
Bethesda, Maryland

Warren G. Lewis
Naval Electronics Laboratory Center
San Diego, California

Robert Langland and Theodore Harder
Pacific Missile Test Center
Point Mugu, California

Subjects wearing flight clothing were strapped into an aircraft ejection seat. During steady vertical vibration of the seat at several discrete frequencies from 3 to 33.6 hertz acceleration was measured on the shaker platform, seat, and a biteboard. Visual acuity was measured with and without vibration and with and without use of a helmet-mounted 3-power binocular. Visual performance was related to vertical seat motion and to skull motion in each of the degrees of freedom of the vertical plane. A single relation between the decrement of unaided vision and the amplitude of apparent angular acceleration of the image was demonstrated when eye response characteristics are taken into account. It was found that above a limiting value of head pitching acceleration, the binocular degrades visual acuity.

BACKGROUND

Visual detection and recognition of distant targets is hampered when observers are vibrated by their vehicles. This was suspected to be the pimrary reason that detection of ground target detail was not enhanced as much as hoped when pilots of A4 aircraft used helmet-mounted binoculars in flight tests at the Pacific Missile Test Center (PMTC). Therefore, a series of tests was performed at PMTC to help determine the extent optical magnification or vibration reduction can improve the visual acuity of pilots subjected to vibration. The laboratory tests were sufficiently fundamental that the results should be applicable to vibrating visual observers in land and sea vehicles, as well as in aircraft.

A literature search at the time of this work uncovered many relevant studies[1-33] of the effect of vibration on vision and of transmission of vibration through the body to the head.

Visual performance during observer vibration has been measured using minimum perceptable acuity (black target on white background)[12], character or dial reading (speed or error rate)[14,15,17,19,25,26,31], perception of horizontal gap[21], minimum separable acuity (Ronchi ruling[9,10], Ives grid[11]), detection of O's in field of C's and O's[3], Landolt "C" acuity[7,16,18,19,24,32], Kholina acuity[33], and Snellen acuity[8]. Some of these measures of visual acuity, though useful in a static environment, may not be appropriate when there is apparent vibration of the visual presentation. For instance, during vertical vibration, a Landolt "C" gap presented at the 12 o'clock or 6 o'clock position will not be smeared by the C, while the C will tend to be smeared across a gap presented at the 3 o'clock and 9 o'clock positions. Because of the relative dwell of the image at two extreme positions during steady vibration, two images can often be seen, and acuity measured by the least discernable separation of two horizontal lines may thus be confounded during vertical vibration. More recently, visual acuity decrements were systematically measured by O'Brient and Ohlbaum[37].

Coermann[14] reported large decrement in visual acuity in two or three frequency bands between 20 and 80 hz, and concluded that eyeball deformation was not responsible. Thomas[27] reported accentuated response of the eye at about 30 and 65 hz when the head was vibrated, and Oshima[12] reported eye resonance with respect to seat vibration at 7 and 16.5 hz.

Previous investigators had often reported information on shaker motion and body attitude and restraint in relation to the associated decrement in visual acuity. None had related the rotation of the eye or head, although in one instance[12] a point of light was placed on the eye and the length of standing wave on the vibrating eye was measured, in another[30] a movie was made of a marked contact lens, and in others 1,3,7,14,17,23,32 a single accelerometer was mounted on the head via biteboard, tape, strap, rubber bathing cap, helmet, or oxygen mask. One study[27] used an accelerometer attached to a contact lens. Another[16] employed three accelerometers oriented orthogonally and attached to the helmet. Guignard and Irving[20] showed that eyes lose visual-feedback stabilization of their sightline at 3 hz or more.

More recently, Lee and King[34] reported data on responses to vertical, while-body vibration of the point of regard and of a single accelerometer mounted on a biteboard. Magdaleno and Allen[35] interpreted that data and recent *transmissability* results, including those of Griffin[36].

Head resonance of seated subjects vibrated vertically has been noted at several frequencies between 4 and 20 hz, and sometimes at higher frequencies (none, reported by Coermann using a biteboard; resonance, reported by Coermann using an accelerometer taped to the top of the subject's head). Significant variability of head response with changes in posture, muscle tone, and restraint system has been demonstrated 1,6,8,14,36.

Hornick, Boettcher and Simons[7] reported that transmissability of fore-aft seat vibration, though less than unity in their tests, was greatest at the highest frequency (5.5 hz) they employed. Dieckman[5] noted head resonance at 4 hz during sideways seat vibration and found that in the range from 1 to 40 hz, head motion was predominantly vertical above 5 hz. He reported vertical vibration transmitted to the head from a seat to be attenuated at least 50 percent above about 30 hz. Goldman and von Gierke[6] indicate that attenuation of horizontal seat excitation at the head is much greater yet. Sideways vibration is apparently attenuated more than 50 percent above 2-1/2 to 3 hz, while fore-aft vibration is apparently at least halved above 8 to 10 hz. Hence, attention was focused on spinewise vibration in this study.

PRELIMINARY TESTS

Preliminary tests were performed in which several seated subjects of a very wide range of sizes, builds, and weights, with varying body-to-seat restraints, muscle tone and posture were vibrated up and down by an electromagnetic shaker operated under conditions of slowly and continuous changing frequency, and approximately constant acceleration. The frequencies at which helmet displacement was appreciable were found to be between 3 and 8 hz. In earlier tests performed at the Pacific Missile Test Center, a

helmet was fastened to a shaker and vibrated in the heads up-down direction with binoculars attached. The binoculars (Figure 1) resonated at about 21 hz. When worn, the helmet slid over the skull noticeably at 6 to 8 hz.
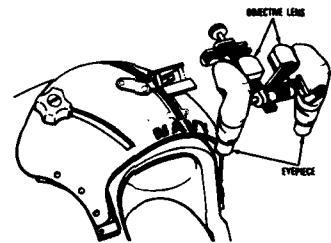
MAGNIFICATION POWER 3x
EXIT PUPIL 6mm x 6mm
FIELD OF VIEW 11 DEGREES
DEFLECTION DOWNWARD OF EXITING OPTICAL AXIS FROM ENTRANCE
OPTICAL AXIS 15°
NO IMAGE STABILIZATION
BINOCULAR DESIGN FOR MARTIN CO (ORLANDO) BY BAUSCH AND LOMB CO

Figure 1 Helmet-Mounted Binocular

When the helmet and subject were strapped-in in the manner used during the later test series, we measured the angular response of the helmet-mounted binoculars relative to the skull and the vertical displacement of the image projected by the binocular onto the eye, using motion pictures. The test setup is shown in Figures 2 and 3, and results are plotted in Figure 4. Measurements at 33.6 hz were too small for accurate reduction, but showed the trend indicated by the dashed lines. Figure 4 shows that vignetting should not have occurred often during the tests, since before each test the binoculars were adjusted so that the spots of light projected from them were concentric with the subjects pupils, and overlapping them.

To aid in interpreting flight test data of vibration of an A4E and its seat, which showed significant power in the region from one to seventeen hertz and some power in the higher range up to 100 hz, preliminary tests were conducted in which an accelerometer was located at the front of the cantilevered seat and oriented for measuring near-vertical motion, as in flight tests. The ratio of seat front to shaker acceleration is shown for a typical subject in Figure 5, *which demonstrates significant magnification between 12 and at least 60 hz.* A survey showed that within the ranges of vibration parameters selected for the main tests, the response of the base of the seat was essentially equal to the shaker motion.

Because of the above information on vibration transmissability and observed decrement in visual acuity, attention was focused on vertical, or spinewise vibration in the range of 3 to 33.6 hz. *The upper limit of frequency was verified*

Figure 2. Test Setup for Transmissability or Visual Acuity Tests.
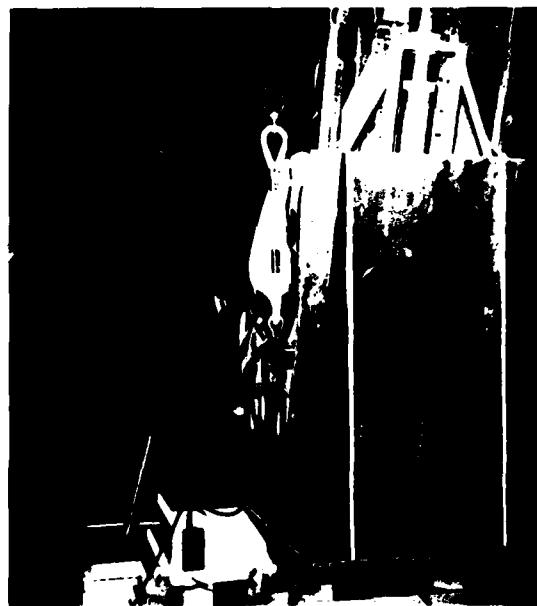
Figure 3. Setup for Presentation of Visual Stimuli and Front View Camera Positioned for Transmissability Testing
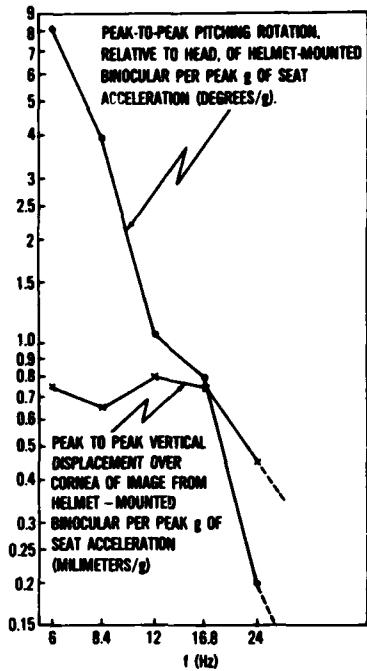

Figure 4 Mechanical Responses of Helmet -Mounted Binocular (Relative to the Head) to Vertical Seat Vibration.
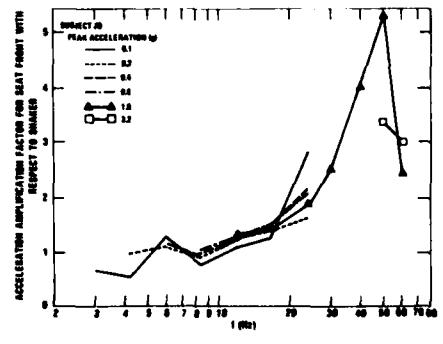

Figure 5

Ratio of Amplitude of Acceleration at Front of Raypack Seat to Amplitude to Acceleration of Shaker Table

by testing of three subjects. Two were subjected to shaker vibrations of 30, 40, 50 and 60 hz at 1.6 and 3.2g peak sinusoidal acceleration, and one also experienced 70, 80, 90 and 100 hz at the same acceleration levels (see Figure 6). These subjects all exhibited their greatest decrement in visual acuity below 40 hz, and head motion diminished roughly as predicted in the literature.
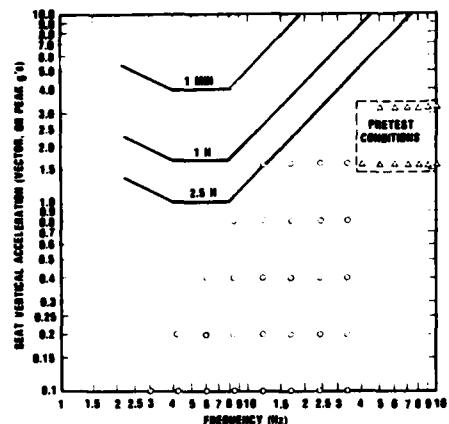
Figure 6.

The Experimental Conditions of Vibration, and Various "Fatigue/Decreased Proficiency Boundaries" for Spinewise Vibration, Taken from Reference 36.

All conditions of vibration, including those to be used in the main tests, were found to be physically and psychologically tolerable, although the higher g-levels were found to be unpleasant at low frequencies, and rapid changing of vibration was also quite unpleasant. Results of daily before- and after-test urinalysis showed no measurable physiological damage due to vibration.

TEST CONDITIONS

The main tests were conducted at the values of shaker frequency and peak acceleration indicated in Table 1 and Figure 6. Tolerance limits from Reference 38 are also shown in Figure 6. Visual acuity was also measured before and after vibration at a particular frequency with subjects at rest. The visual conditions and test schedule are indicated in Table 1.

EQUIPMENT

Biteboards shown in Figure 7 were used to measure skull vibration in the vertical plane. Endevco model 2221C accelerometers were mounted as shown so as to completely define rigid-body motion in the vertical, fore-aft or medial plane. Moisture occasionally caused shorting of the leads and the biteboard caused some subjects excessive discomfort (mainly an inability to swallow) over protracted periods of use. Despite these disadvantages, the biteboard accelerometer installation provided useful data. The effects of swallowing, clenching teeth, and changing head orientation did not confound the data. Resonance of the jaw and of the clamped biteboard was not found to be a problem. The roll-off of the Endevco signal conditioning system was calculated to be 2 percent at 2 hz.

An Escapac ejection seat and mounting rails, furnished by the McDonnell-Douglas Corporation were installed on a Calidyne Model 58 shaker as shown in Figures 2 and 3. The subject's feet rested on a stationary platform. Subjects wore a fitted torso harness by which they were attached to the seat just as a pilot is attached in an A4 aircraft. The subjects wore an APH-5 helmet and an A-13A oxygen mask fitted to be snug but comfortable.

DESCRIPTION OF VISUAL ACUITY TEST

The binoculars were prefocused and preset to the observer's interpupilary distance and adjusted horizontally and vertically so that the projections of the binocular exit pupils, two discs of light, were concentric with the subject's eye pupils.

The subject was located near one end of a vision alley 30 feet long, 8 feet high and 10 feet wide, which can be seen in Figure 3. Opposite the subject a wall of neutral gray (36 percent reflectance) was illuminated by 6 photoflood lamps at the sides of the alley and concealed from the view of the subject. The light level was adjusted before each session as necessary to produce an illuminance at the center hole of 250 foot-candles, and then monitored during testing. Three 4x4 inch beveled holes were cut in the wall. The visual stimuli were presented at the center of one of these holes (the other holes were used as "standbys" and were maintained at the nearly uniform luminance of the general background when not in use). Duration of presentation was limited to six seconds by the use of a flap shutter.

The visual stimuli were circular discs of neutral gray paper of 46 percent reflectance. Their areas formed an approximate geometrical sequence of range 0.53 to 19.6 square millimeters and average ratio of 1.24. The stimuli were bonded to long strips of neutral gray paper (reflectance 36 percent). The setup is shown in Figure 2, wherein photographic processing emphasizes the contrast of the holes and flap.

The frequency of vibration of the seat was established by comparison with a reference, then the acceleration was adjusted to the prescribed level. Presentation of visual stimuli was not

66

TABLE 1

Experimental Conditions of Visual Acuity Tests

Vertical, sinusoidal motion of the seat:

    frequencies 3, 4.2, 6, 8.4, 12, 16.8, 24, 33.6 hz

    displacement* $\pm$ 0.0035, 0.0069, 0.0138, 0.0277, 0.554, 0.111,
                0.222, 0.443 mm

    acceleration $\pm$ 0.1, 0.2, 0.4, 0.8, 1.6g

Visual conditions:

    distance from eye to stimulus - 7.62 m (25 ft.)

    area of lighted background - 7.43 sq. m. (80 sq. ft.)

    luminance of lighted background - 90 millilamberts

    range of areas of stimuli - 0.53 to 19.6 square millimeters

    contrast of stimuli with background - 0.28

Average or nominal test schedule:	Time duration: (minutes)
adaptation to illumination and completion of test preparations	10 min
static acuities (aided, unaided) measured	5 min
first vibration session	40 min**
adaptation to illumination and completion of test preparations	10 min
second vibration session	40 min**
static acuities (aided, unaided) measured	5 min
	2 hours

---

* $\underline{\text{Applied}}$ peak acceleration divided by $(f/2\ )^2$. Values accurate to
within $\pm$ 1%.

** Vibration occurred only during presentation of visual stimuli and
during intervals between presentations at a particular frequency when
the acceleration was no greater than 0.4g.

made until steady-state vibration had been achieved.

Subjects used a hand-held buzzer to respond positively (one buzz) or negatively (two buzzes) for each target presentation (a forced choice). They used more buzzes to signal for a consultation. A switch located on the right arm of the seat was available for stopping the shaker in the event of excessive subject discomfort. By way of a sound-powered communications system to the earphones of his APH-5 helmet, the subject was instructed whether to use aided or unaided vision and to which hole he should direct his attention. Visual stimuli were presented in random order, using a range of sizes determined during the training sessions. A sufficient number of presentations was made

to satisfy the criterion that the two smallest target sizes shown have negative responses and that the two largest target sizes shown have positive responses.

The vision test data for a subject were collected in nine sessions which provided three replications of the experiment. In each three-session replication 5 individual thresholds were determined. Therefore, there were 15 threshold determinations for each condition of interest (aided or unaided at a particular frequency and peak acceleration of the seat). Subjects completed one session per day. The sessions were counterbalanced to cancel effects of order of presentation (aided or unaided first, high or low frequency first, and high or low seat acceleration first). Each subject began

67

the tests with a different type of session. The
conditions of vibration were distributed so as to
make the sessions approximately equal in severity
as determined from pretests.

The subjects were one female (M L) and two
males (R S and J W) in the 20 to 35 age bracket.
All met the vision requirements for pilots in the
U.S. Navy and were in good physical condition.
The males weighed 180 pounds and 175 pounds and
the female weighed 125 pounds. Each subject
was fitted with flight equipment by aircrew
equipment specialists. All subjects used
medium size helmets and oxygen masks. In their
briefing the subjects were informed on the
objectives of the experiment, and that blanks
would be presented randomly among the real targets.
They were cautioned not to cock their heads to
the side or lean forward or back.

DESCRIPTION OF TRANSMISSABILITY TESTS

It was not feasible to collect vision and
transmissability data simultaneously. This was
not considered a serious drawback because each
of the subjects was given a lengthy period
(several preliminary sessions) of learning and
adaptation, so that each had developed character-
istic posture by the time data were collected.

There was insufficient time after the
vision tests to carry out a systematic experi-
ment concerning vibration transmission to the
head, as both subjects and equipment became
unavailable. However, some data were obtained
for each subject and a nearly complete set was
obtained for ML.

The biteboards and associated equipment
of the pretests were used. Distances parallel
and perpendicular to the biteboards were
measured to establish the relative position of
accelerometer axes, and of a point midway
between the subject's eyes, as indicated in
Figure 7.

In a test, a frequency of vibration was
established and increasing levels of accelera-
tion were applied. At each level of accelera-
tion the subject was instructed to look for a
stimulus and respond as in the vision experi-
ment, while he/she alternately used aided and
unaided vision. While the subject was thus
engaged (after steady-state conditions had been
established), one recording of approximately
20 seconds duration was made of the five
accelerometer outputs and of buzzer and voice
annotations.

DATA REDUCTION

Vision Data

The threshold area for one series of
responses has been taken as just larger than the
largest pair of consecutive stimuli for which
there were negative responses. The value of the
log threshold stimulus area was then calculated
as the arithmetic average of the log areas just

a. The Measurement
of Distances for
Computation of
Head Motion from
Accelerometer Data.

b. Attachment of Three
Accelerometers to
Biteboard.

c. Leads Fed Through Oxygen
Mask; Ready to be Bitten.
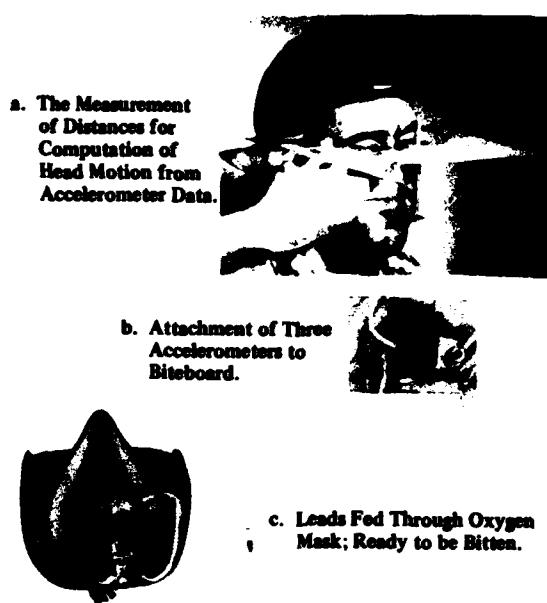
Figure 7. Biteboard Mounted Installation for
Measuring Head Motion.

above and below threshold. Thus for an hypo-
thetical and rare series of response (stimuli
ordered in increasing sizes):

Stimulus:	A	B	C	D	E	F	G	H	I
Responses:	−	−	+	+	−	−	+	+	+

the log threshold area is the average of log
area F and log area G.

The threshold values of area were averaged
arithmetically for the five exposure sequences
(unaided or aided) of each trial of each con-
dition of vibration for each subject.

To assess whether correction for variation
of control conditions was necessary, the aided
and unaided averages were both compared for
each subject's replication. It was found that
all subjects were reasonably consistent in
response, although each one showed increased
variability at the two greatest levels of
acceleration. A comparison was also made of
static acuities measured before and after
vibration of a subject. The "control" or
static acuities were found to vary somewhat but
not to such an extent that corrections to the
remaining data were necessary. The trends of
the corrections were observed to improve the
consistency of the data, which was deemed
adequate without correction, so control correc-
tions were not made in the results presented in
this report.

Averages for each trial were themselves averaged and these pairs (aided or unaided) of values were taken as representing the performance of a particular subject exposed to a particular condition of vibration. Representative variability of trial average is shown in Figure 8, where threshold visual angle is defined in terms of average threshold stimulus area A as n

$$= 1.73 \times 10^{-6} \text{ A steradians.} \quad (1)$$

Visual acuity is taken to be measured by the reciprocal of average threshold stimulus area, but "Effective Magnification" is used for ease of comparison of results. It is defined in this report as the ratio of visual acuity under some circumstances of interest (e.g., when an optical aid is used) to an appropriate reference (e.g., when an aid is not used, other things being equal) value of visual acuity. Disregarding the loss of image
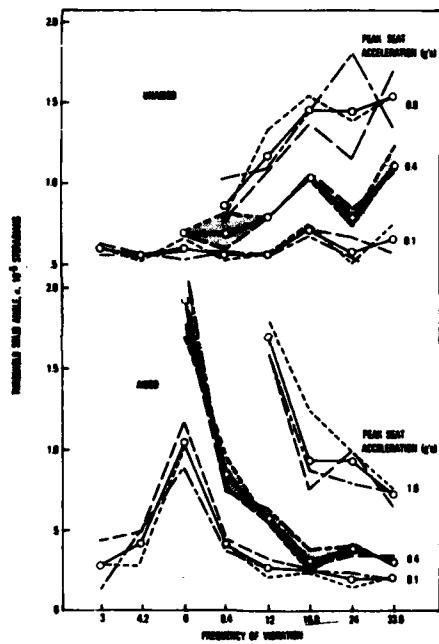
Figure 8 Intratrial Variability of Data on Threshold Visual Acuity. Subject ML

Visual acuity is taken to be measured by the reciprocal of average threshold stimulus area, but "Effective Magnification" is used for ease of comparison of results. It is defined in this report as the ratio of visual acuity under some circumstances of interest (e.g., when an optical aid is used) to an appropriate reference (e.g., when an aid is not used, other things being equal) value of visual acuity. Disregarding the loss of image clarity due to transmission between the target and eye, the effective magnification would be the ratio of the distance at which that observer can just resolve a detail under prescribed conditions, to the distance for just resolving the detail under reference conditions. Thus

$$E M_{uv}^{av} = \frac{A_{uv}}{A_{av}} \quad (2)$$

$$E M_{us}^{uv} = \frac{A_{us}}{A_{uv}} \quad (3)$$

where

A is the average threshold area indicated by the subscripts, in square cm

EM is the effective magnification for superscript conditions referenced to subscript conditions

a indicates use of aided vision

u indicates use of unaided vision

v indicates the presence of vibration

s indicates the absence of vibration, i.e., the static condition

VIBRATION TRANSMISSABILITY DATA

Motion records were analyzed in intervals of time during which the three biteboard and shaker table accelerometer outputs had a steady rhythm preceding buzzes. Since sinusoidal seat motion produced approximately sinusoidal responses, the accelerometer outputs A_1 (t), A_2 (t), and A_3 (t) were processed to calculate the response of the head parallel to the medial plane at the point between the centers of the orbital cavities using the following equations:

Angular (nodding) acceleration:

$$\theta = \frac{1}{L_1} (\gamma_c \sin \omega t - \gamma_s \cos \omega t) \quad (4)$$

Head up-down acceleration (perpendicular to plane of biteboard):

$$Z = (A_3 \cos\phi_3 - \frac{L_2}{L_1} \gamma_c) \sin \omega t +$$
$$+ (A_3 \sin\phi_3 + \frac{L_2}{L_1} \gamma_s) \cos \omega t -$$
$$- \frac{L_3}{\omega^2 L_1^2} (\gamma_c \cos \omega t + \gamma_s \sin \omega t)^2 \quad (5)$$

Head fore-aft acceleration (parallel to plane of biteboard):

$$X = (A_2 \cos\phi_2 - \frac{L_3}{L_1} \gamma_c) \sin \omega t +$$
$$+ (A_2 \sin\phi_2 + \frac{L_3}{L_1} \gamma_s) \cos \omega t -$$
$$- \frac{L_4}{\omega^2 L_1^2} (\gamma_c \cos \omega t + \gamma_s \sin \omega t)^2 \quad (6)$$

where

$$\gamma_c = A_3 \cos\phi_3 - A_1 \cos\phi_1$$

$$\gamma_s = A_1 \sin\phi_1 - A_3 \sin\phi_3$$

$A_1(t) = A_1 \sin(\omega t + \phi_1) =$ the acceleration along the inside vertical accelerometer axis

$A_2(t) = A_2 \sin(\omega t + \phi_2) =$ the acceleration along the horizontal accelerometer axis

$A_3(t) = A_3 \sin(\omega t + \phi_3) =$ the acceleration along the outside vertical accelerometer axis

$\omega = 2\pi f$, $f =$ frequency (hz)

$t =$ time (seconds)

ϕ_1, ϕ_2, ϕ_3 are phase angles with respect to shaker excitation

L_1, L_2, L_3, and L_4 are lengths shown in Figure 9a.

The sign conventions are shown in Figure 9b.
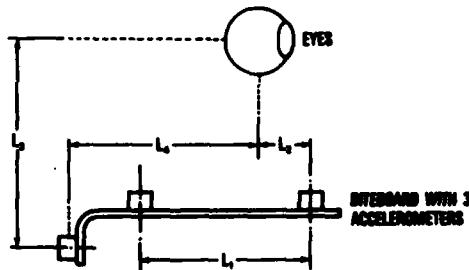
Figure 9a. Lengths Used in Computations of Head Motion
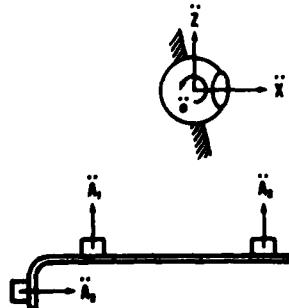
Figure 9b. Sign Conventions Used for Measured and Computed Accelerations

RESULTS AND DISCUSSIONS

Transmissability

The response of the orbital cavities to vertical seat vibration is shown in Figures 10 through 12. In these figures T_{zz}, $T_{\theta z}$, and T_{xz} are respectively the ratios of the amplitude of up-down, nodding, and fore-aft acceleration of the skull (at the point midway between the eyes) to the amplitude of acceleration of the shaker platform.

All the spinewise response data is plotted together with curves from the existing literature representing the same type of response in Figure 10d. This figure indicates a general agreement, but a great degree of variability among results of these various experiments which is probably due in part to the differences of measuring body posture and restraint, head-mounted equipment, etc., as mentioned above. However, data of the present experiment (in which these latter factors were relatively standardized) show a great degree of variability among subjects.

All subjects tended toward nonlinear mechanical behavior, giving lower ratios of response per excitation as the vibration becomes more intense. This effect could account for some of the variability between experiments which is apparent in Figure 10d.

There are data pertaining to the use of binoculars for only one subject (ML). These data (Figures 10a, 11a, and 12 a) show considerably less variation between aided and unaided (vision) mechanical response of the head than exists between subjects that are unaided. Subject ML had generally lower response in both translation and rotation during use of the binoculars than during unaided viewing, a tendency which is most apparent at 8.4, 16.8, 24 and 33.6 hz.

A resonant condition amplifying the motion of the orbital cavities is apparent at a low frequency of about 6 to 8 hz for two subjects (ML and RS) and less for the other (JW). Only one subject (ML) exhibits a discernable second resonance in the frequency range covered; it exists at about 30 hz. A suggestion of a second resonant frequency is given by RS's response.

Head rotation response results of Griffin[36] and of Magdaleno and Allen[35] (sinusoidal excitation) are plotted in Figure 11 for comparison with our results. It appears that the absence of a back support and visual task in Griffin's experiment contributed to a low head rotational response.

The head rotational response of RS was about one-fifth that of ML and JW. RS had correspondingly better unaided visual acuity during vibration, suggesting that he found an efficient posture for unaided vision. Indeed his calculated Lissajous figures for the point between the eyes was nearly circular, while those for the other subjects were much flatter in general.
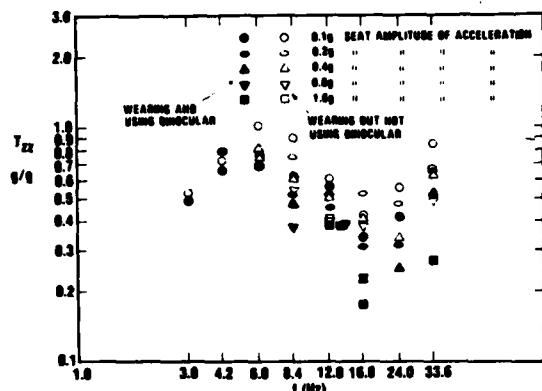
Figure 10a. Subject ML
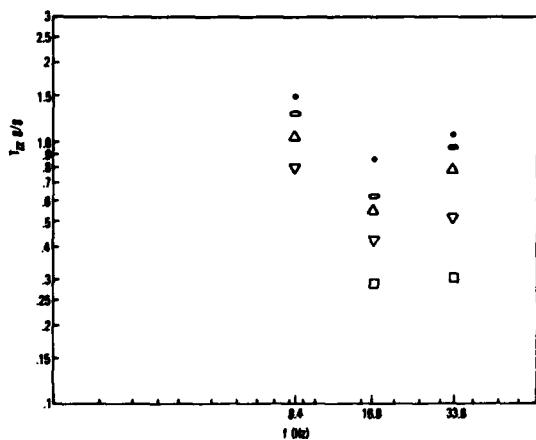
Figure 10b. Subject RS
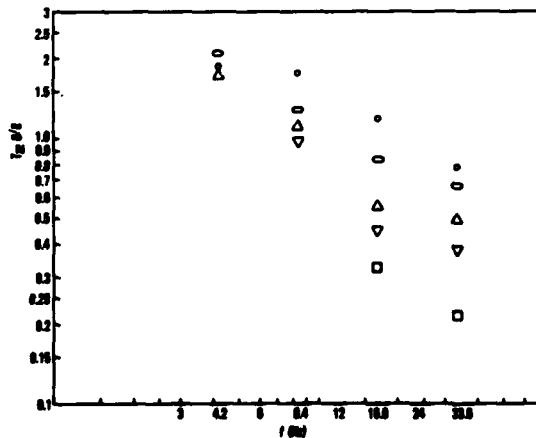
Figure 10c. Subject JW

The response of RS is similar in magnitude
to the Griffin results for fore-aft and nodding
head response.

The equivalent magnification of the bino-
cular during vibration, referenced to the con-
dition of unaided vision under vibration, is
shown for each of the 3 subjects in Figures 13a,
b,c. This same equivalent magnification is
averaged for the three subjects in Figure 13d.
It is seen that use of the binocular actually
tended to degrade what unaided visual acuity is
possible during whole-body vibration at low
frequency where head motion is largest.

The effective magnification of each subject's
unaided vision during whole-body vibration is
shown in Figure 15. Averages for all the sub-
jects are shown in the bottom set of curves of
Figure 14, upon wihich data from the literature
are plotted for comparison. The latter data
do not include results of experiments in which
Ronchi rulings or horizontal gaps were used to
measure acuity, and only the distant-viewing
results of Reference 37 are shown.

Figure 14 shows that in this experiment,
the effect of vertical seat vibration on unaided
visual acuity is largely a monatonic function of
the acceleration of the seat, in agreement with
Oshima[12]. However, Figure 8 shows a frequency-
dependence of unaided visual acuity which
develops as the vibration intensity increases.
Much of the variability of results seen at the
bottom of Figure 14 is probably due to diff-
erences in the vibration transmitted to the
head, which seems to be borne out by Figure 15.

To obtain an estimate of the log effective
magnification for use of a binocular during
vibration at a frequency (f) and peak accelera-
tion (n_z) referenced to static unaided vision,

Figure 10d.
Data of all Subjects (Aided or Unaided)
Transmissability, and Results from the
Literature.

Figure 10   Ratio, T_{zz}, of Heads Up-Down Acceleration Amplitude
at a Point Midway Between Eyes to (Vertical) Seat
Acceleration Amplitude

71
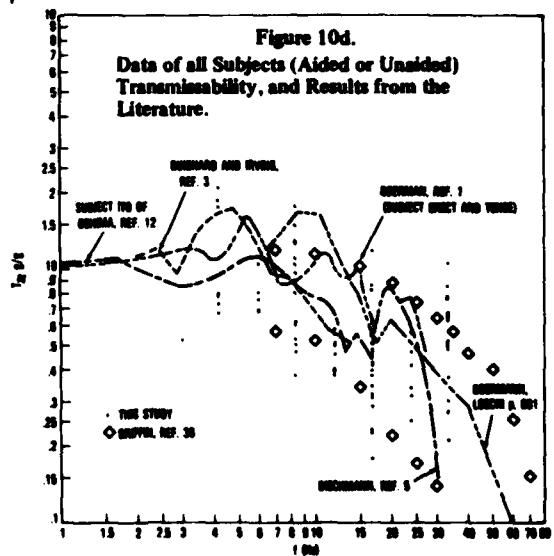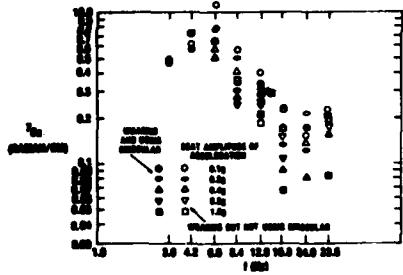
Figure 11a.   Subject ML
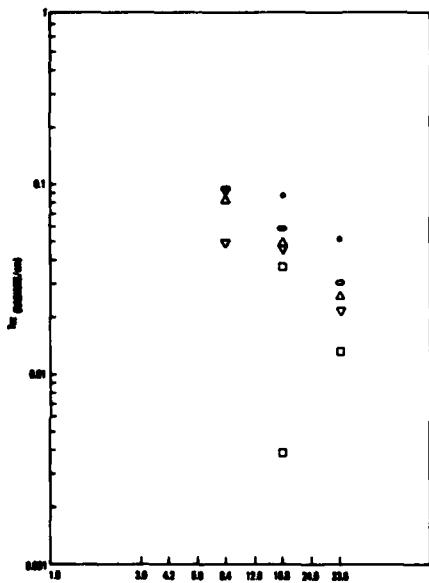
Figure 11b. Subject RS
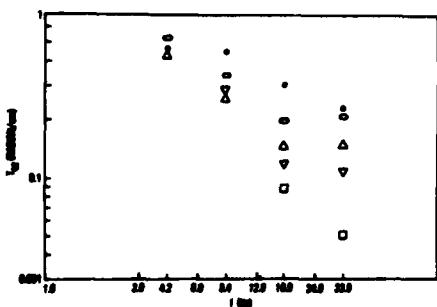
Figure 11c. Subject JW

Figure 11   Angular (Pitching) Acceleration Response of the
Head Per Unit Amplitude of Seat (Vertical)
Acceleration, $T_{\theta z}$ vs Frequency of Seat
Vibration, Subject ML.
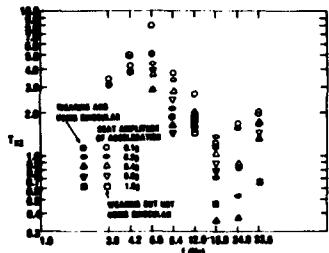
Figure 12a.   Subject ML
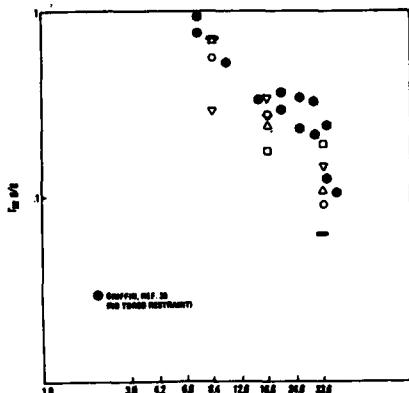
Figure 12b. Subject RS
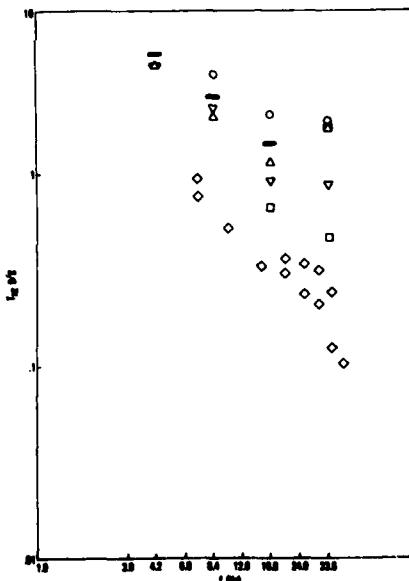
Figure 12c. Subject JW

Figure 12   Response of the Midpoint Between the Eyes
in the Fore-aft Direction to Vertical Vibration
of the Seat, Subject ML.

72
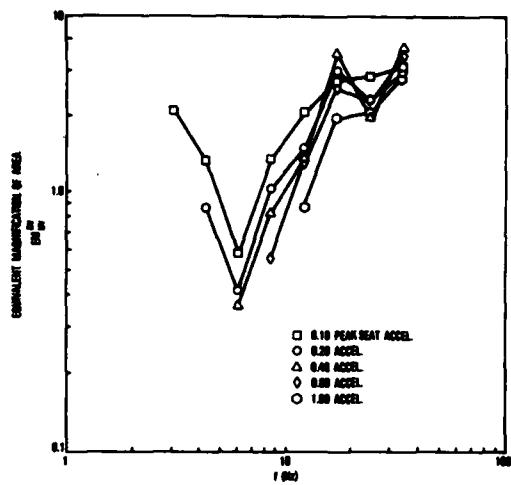
Figure 13a. Subject ML
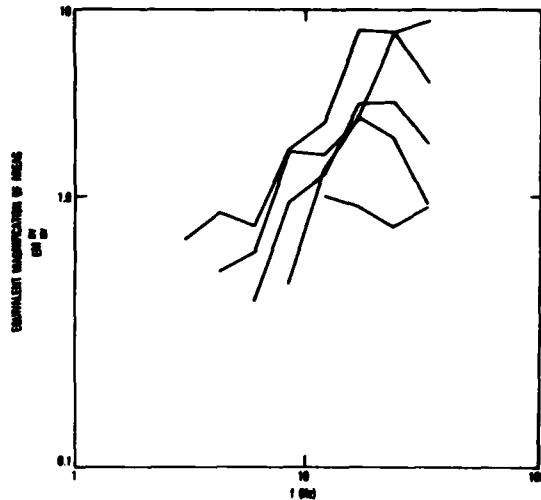
Figure 13c. Subject JW
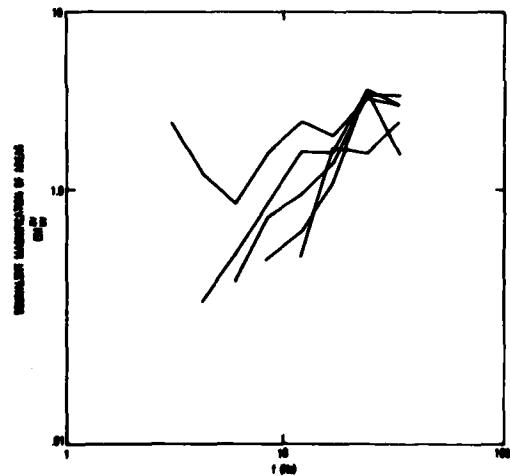
Figure 13b. Subject RS
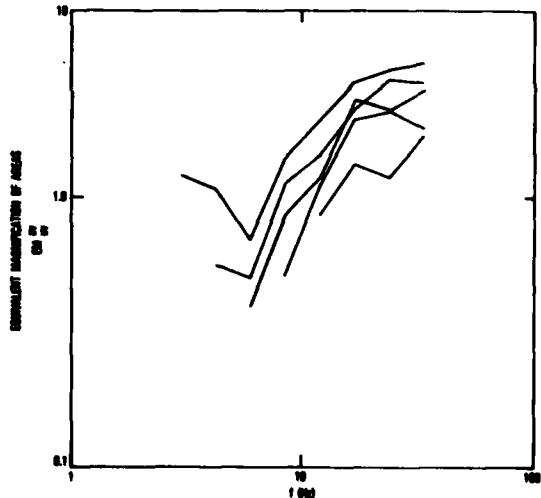
Figure 13d. Same Average of all Subjects.

Figure 13   The Effective Magnification of the Helmet-
Mounted Binocular when the Wearer was
Subjected to Vertical Seat Vibration.
Subject ML

the log effective magnification for f in
Figure 13 may be added to the log effective
magnification for f and n_z in Figure 14.

In Figure 15a the effective magnification
for unaided and aided vision of subject ML
during vibration (referenced to static unaided
and aided vision, respectively) is plotted
against head nodding acceleration.

A rough comparison of aided and unaided
visual performances indicates that when
amplitude of eye nodding acceleration is 40 to
400 radians/sec^2 (depending on frequency) or
more, three power helmet-mounted binoculars do
not improve performance of the visual task of
this experiment, e.g., discrimination of con-
trast detail viewed at a distance. This issue
will be more completely settled (for various
magnifying powers and mountings of optical aids,
restraint of viewers, motions of object viewed,
and viewing distances) through the use of models
of mechanical response adapted from models such
as those described in References 35, 39 and 40,
and the use of visual performance data, including
that given in Figure 15. Though insufficient
data was available for RS and JW, the trend of
their performance generally confirmed the trend
of the unaided performance of ML.

In Figure 15a, a marked frequency effect
can be seen in ML's performance. The gain[*]
for the amplification of head rotation required
to unify her unaided visual response into one
curve (the curve for 3 hz and 12 hz), shown in
Figure 15b, is indicated in that figure. The
gain of eye nodding response with respect to head
nodding response estimated[**] from Figure 10 of
Reference 35 is shown also. The latter was based
on one set of data for eye motion and other
data for head motion, so that the values of gain
may be inaccurate, though a zero (cross-over)
at about 15 hz was obtained by Lee[39].

The frequency effect in Figure 15 may thus
be due to the fact that visual performance was
plotted against rotational acceleration of the
head rather than of the eyes. If so, it appears
from Figure 15b that unaided visual acuity is
not degraded by sinusoidal head rotation at peak
acceleration values below 40 rad/sec^2.

The above trend in gain is in qualitative
agreement with the range of frequency in which
the vestibular system can sense head rotation
inertially[40] and hence tend to compensate or
stabilize eye orientation. The frequency
effect in ML's performance does not agree
especially well with the hypothesis of resonance
of the eye and its supporting tissue as discussed

---

[*] "Gain" is defined as 20 times the log (of the
ratio of amplitudes of angular acceleration, here).
[**] Data on phase difference between head and eye
rotation were incomplete, and the difference
was assumed to drop smoothly from its 10 hz value
to a negligible value at 20 hz.

by Shoenberger[40] considering that the eye has
been shown to resonate in rotation at about
35 hz with a damping factor of 0.5[39]. Coermann's
analysis[14] presumably rules out eyeball de-
formation as a mechanism to explain the
frequency effect, and it seems unlikely that
the eye vergence system[39] caused involuntary
defocussing due to a symmetric rotational
response of the eyes about the head-up axes
(vergence).
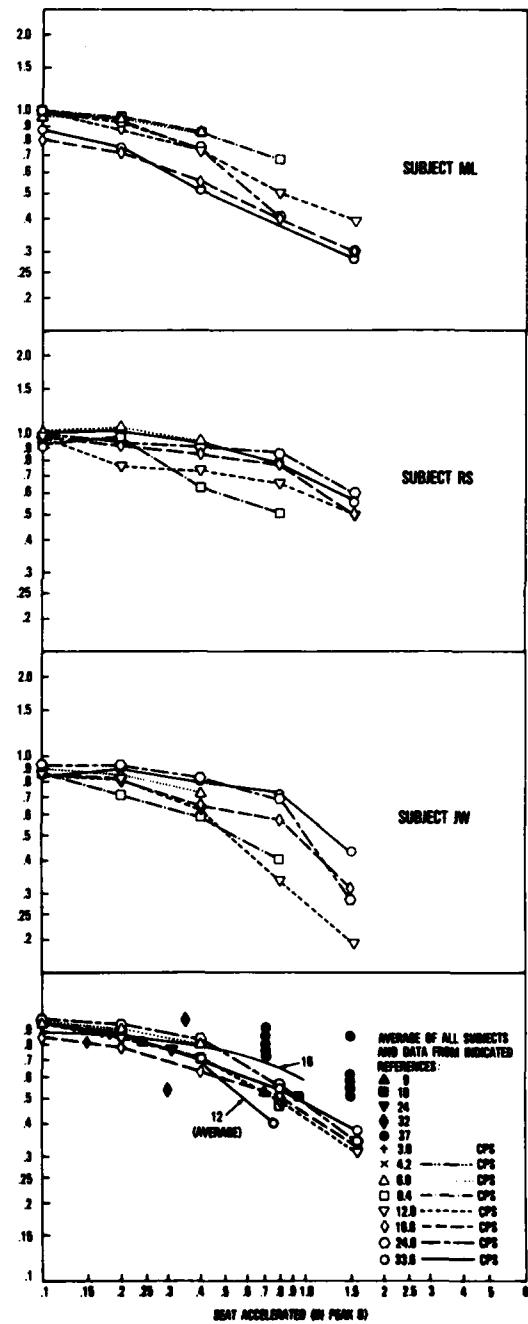
Figure 14. The Effective Magnification of Unaided Visual Acuity
Due to Vertical Seat Vibration of the Observer.

74
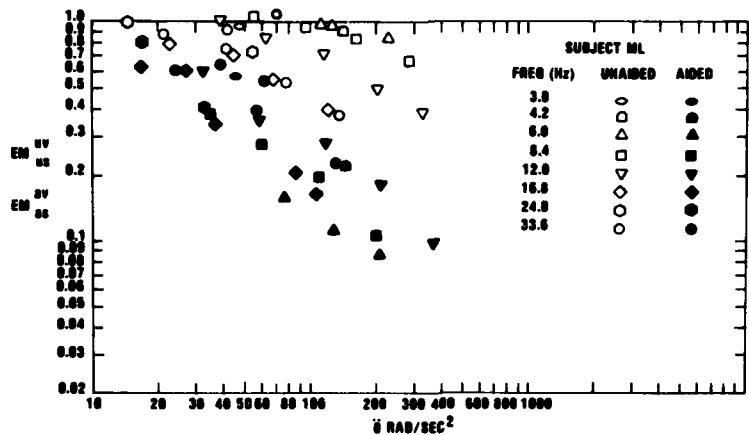
Figure 15a. Visual Performance vs Heand Nodding Ac-
celeration, with and without a Helmet-
Mounted Binocular. Subject ML
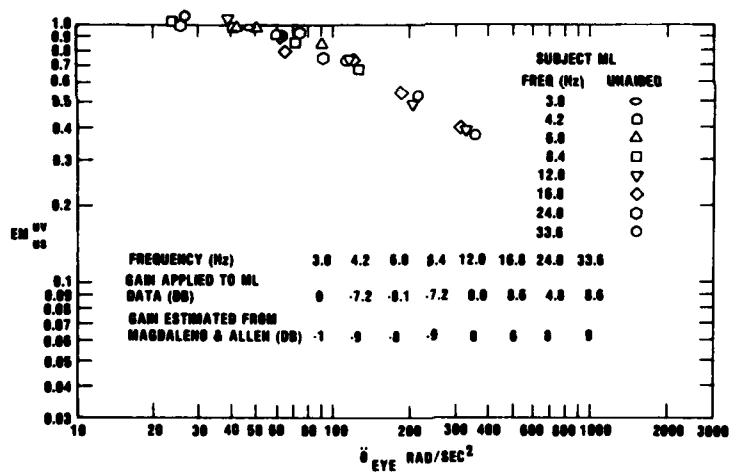
Figure 15b. Unaided Visual performances vs Eye
nodding Acceleration, Subject ML

REFERENCES

1. R.R. Coermann, "The Mechanical Impedance of the Human Body in Sitting and Standing Position at Low Frequencies," ASD Tech. Rept. 61-491, Sep 1961.

2. J.C. Guignard, "The Physical Response of Seated Man to Low-Frequency Vertical Vibration," RAF Inst. of Av. Med. Rept. FPDC 1062, Apr 1959.

3. J.C. Guignard and A. Irving, "Effects of Low-Frequency Vibration on Man," Engineering, pp. 364-367, 9 Sep 1960.

4. A.K. Simons, "Mechanical Response of the Human Body to Wheeled Vehicle Vibration, 1-6 cps," Bostrum Research Labs Report No. 121, 1956.

5. D. Dieckmann, "A Study of the Influence of Vibration on Man," Ergonomics, Vol. 1, No. 4, pp. 347-355, Aug 1958.

6. D.F. Goldman and H.E. Von Gierke, "The Effects of Shock and Vibration on Man," Naval Medical Research Institute Lecture and Review Series No. 60-3, 8 Jan 1960.

7. R.J. Hornick, C.A. Boettcher, and A.K. Simons, "The Effect of Low Frequency, High Amplitude, Whole Body, Longitudinal and Transverse Vibration Upon Human Performance," Bostrum Research Lab Final Report, Ordnance Project No. TE1-1000, Jul 1961.

8. G.J. Hurt, Jr., "Rough-Air Effect on Crew Performance During a Simulated Low-Altitude High-Speed Surveillance Mission," NASA TN D-1924, Aug 1963.

9. M. Loeb, T.A. Barron, and E.S. Burda, "A Preliminary Investigation of the Effects of Whole-Body Vibration and Noise," AMRL Rept. No. 145, Apr 1954.

10. M. Loeb, W.M. Bass, E.E. Roberts, and M.L. Samuelson, "A Further Investigation of the Influence of Whole-Body Vibration and Noise on Tremor and Visual Acuity," AMRL Rept. No. 165, Jan 1955.

11. S.S. Stevens, "The Effects of Noise and Vibration on Psychomotor Efficiency - Report of Present Status," Harvard U. Psycho-Acoustic Lab, Mar 1941.

12. M. Oshima, "Vibration and Human Body," trans. from Hygiene for the Steel Workers Vol. 2-1, 2,3,4, 1953, Technical Documents Liaison Office MCL-803/1+2, 25 Apr 1961.

13. J. Krauskopf, "The Effects of Retinal Image Motion on Contrast Thresholds," AMRL Rept. No. 221, Jan 1956.

14. R. Coermann, "Effect of Vibration and Noise on the Human Organism," RAE Library Translation No. 121, Oct 1946.

15. M.N. Crook, G.S. Harker, A.C. Hoffman, and J.L. Kennedy, "Effect of Amplitude of Apparent Vibration, Brightness, and Type Size on Numeral Reading," Wright-Patterson AFB Tech. Rept. No. 6246, Sep 1950.

16. J.P. Dennis and M.A. Elwood, "The Effect of Vibration Experienced in Different Seating Positions," Ministry of Supply C.S.E.E. Rept. No. 78 M.O.S., Feb 1958.

17. J.P. Dennis, "The Effect of Whole Body Vibration on a Visual Performance Task," C.E.P.R.E. Rept. No. 104, Aug 1960.

18. D.H. Drazin, "Effects of Low-Frequency High-Amplitude Whole-Body Vibration on Visual Acuity," Air Ministry FPEC Memo 128, 1959.

19. D.H. Drazin, "Factors Affecting Vision During Vibration," Research, Vol. 15, No. 275, pp. 275-280, Jul 1962.

20. J.C. Guignard and A. Irving," Measurements of Eye Movements During Low Frequency Vibration," Aero. Med. Vol. 33, No. 10, pp. 1230-1238, Oct 1962.

21. K.O. Lange and R.R. Coermann, "Visual Acuity Under Vibration," Human Factors, Oct 1962.

22. German Aviation Medicine in World War II, Vol. 2, Chapt. 7, Part C, The Physiological Effects of Mechanical Vibrations, p. 717, by W.E. Loeckle and Chapt. 9, Part A, Visual Acuity and Refraction, p. 891, by H.W. Rose, Department of the Air Force, School of Aviation Medicine, 1950.

23. T.J. Matthews, G.R. Allen, and C. Short, "The Transmission of Aircraft Vibration to Man-Mounted Equipment," Ministry of Aviation Tech. Note No. Mech. Eng. 334, Jun 1961.

24. A.K. Simons, and M.A. Schmitz, "The Effect of Low Frequency, High Amplitude Whole Body Vibration on Human Performance," Bostrum Research Labs Progress Rept. No. 1, April 1, 1957 to Jan 31, 1958.

25. H.A. Taub, "The Effects of Vibration on Dial Reading Performance," AMRL-TDR-64-70, Jul 1964.

26. R.J. Teare and D.L. Parks, "Visual Performance During Whole-Body Vibration," Boeing (Wichita) Rept. D3-3512-4, Nov 1963.

27. J.G. Thomas, "Use of a Piezo-Accelerometer in Studying Eye Dynamics," J. Opt. Soc. Am., Vol. 55, No. 5, pp. 534-537, May 1965.

28. A.M. Volkov and V. Chirkov, "Oscillations of the Human Body Under the Effect of Vibration," Gigiena truda i professional eye zabolevaniia (Moskva), Vol. 4, No. 5, pp. 8-12, May 1960.

29. J.W. Wulfeck, A. Weisz, M.W. Raben, "Vision in Military Aviation," WADC TR 58-399, Nov 1950.

30. P. Webb, ed., "Bioastronautics Data Book," NASA SP-3006, 1964.

31. M.M. Mozell. and D.C. White, "Behavorial Effects of Body Vibration," Aviation Medicine, Vol. 29, No. 10, pp. 716-724, Oct 1958.

32. M.A. Schmitz, "The Effect of Low Frequency High Amplitude Whole Body Vertical Vibration on Human Performance," Bostrom Research Labs Rept. No. 128, 1959.

33. I.Y. Borshchevskiy, et al., "The Effect of Vibrations ofCertain Types of Modern Helicopters and Airplanes," Voyenno Meditsinsky Zhurnal, 1958, 1, JPRS/NY-406/CSO-1374/7.

34. R.A. Lee and A.I. King, "Visual Vibration Response," J. Appl. Physio., Vol. 30, No.2, pp. 281-285, Feb 1971.

35. R.E. Magdaleno and R.W. Allen, "Modeling Biodynamic Effects of Vibration," Systems Technology Inc. Interim Scientific Rept. No. 1037-2, Jul 1975.

36. M.J. Griffin, "Vertical Vibration of Seated Subjects: Effects of Posture, Vibration Level, and Frequency," Aviation, Space and Environmental Medicine, pp. 269-276, Mar 1975.

37. C.R. O'Briant and M.K. Ohlbaum, "Visual Acuity Decrements Associated with Whole Body $\pm$ GZ Vibration Stress," Aerospace Medicine, pp. 79-82, Jan 1970.

38. International Standards Organization, "Guide for the Evaluation of Human Exposure to Whole-Body Vibration," ISO/DIS 2631, 1972.

39. R.A. Lee, private communication of 24 Sep 1976, Scientific Computer Division, U.S. Army Tank Automotive Command, Warren Michigan.

40. D.A. Robinson, "Eye Movement Control in Primates," Science, Vol. 160, pp. 1219-1224, 20 Sep 1968.

41. R.W. Shoenberger, "Human Response to Whole-Body Vibration," Perceptual and Motor Skills, Vol. 34, pp. 127-160, 1972.

FREE VIBRATIONS OF UNSYMMETRICALLY LAMINATED

CANTILEVERED COMPOSITE PANELS

Earl A. Thornton

Old Dominion University
Norfolk, Virginia 23508

Experimental and analytical data for the vibration
characteristics of cantilevered, unsymmetrically
laminated, boron-epoxy panels are presented. Vibra-
tion tests were conducted to determine the natural
frequencies, nodal patterns, and damping coefficients
of panels with a progressively increasing amount of
asymmetry. Analytical data is based on the finite
element method and three different modeling tech-
niques are investigated. Comparisons of experimental
and analytical data are made to evaluate the modeling
techniques. The effect of panel asymmetry on vibra-
tion characteristics is studied.

INTRODUCTION

Current applications of laminated
advanced composite panels are customar-
ily made with lamina filament orienta-
tions symmetrical about the middle
surface. However, applications exist
where it may be advantageous to design
unsymmetrically laminated panels. An
example of a potential application con-
cerns minimizing or avoiding flutter in
airfoil designs. Characteristic defor-
mations of symmetrically and unsymmet-
rically laminated panels are compared
in Fig. 1.

Considerable advances [1-7] have
been made in the last decade in under-
standing the vibration behavior of sym-
metrically laminated composite panels.
During the same period analytical
studies [8-11] of the vibration behav-
ior of unsymmetrically laminated panels
were initiated and a small amount of
experimental data [12-14] were obtained.
Recently, a combined analytical and
experimental study [15] was made of
unsymmetrically laminated cantilevered
panels similar to the panels considered
in this study. Vibration data on unsym-
metrically laminated composites are
generally lacking. Further, there is
need for evaluation of available
methods for analyzing unsymmetrically
laminated panels.

This paper presents both experi-
mental and analytical data from the
finite element method on vibration
characteristics of cantileverd, unsym-
metrically laminated, boron-epoxy
panels. To investigate different ana-
lytical techniques three NASTRAN model-
ing of the panels were conducted. The
first neglected the bending-extension
coupling, the second approximately
accounted for the coupling, and the
third fully accounted for the coupling
by use of a newly developed plate bend-
ing element.

FABRICATION OF PANELS

Six composite panels of overall
dimensions of 8 in. by 11 in. were fab-
ricated from eight laminations of boron-
epoxy (Table 1). Two specimens were
symmetrically laminated, and the remain-
ing four specimens were designed to
give a progressively increasing amount
of symmetry. The two symmetrically
laminated panels were unidirectional
layups with a filament orientation of
0 degrees for one specimen and 45
degrees for the other specimen. All of
the unsymmetrically laminated panels
had a bottom layer of four plies orien-
ted at 0 degrees and a top layer of
four plies with equal filament angles

which varied from specimen to specimen. The filament angle of the top layer had values of 22.5, 45, 67.5, and 90 degrees for the four unsymmetrically laminated specimens. A control specimen of aluminum with the same planform was also tested and analyzed.

For tests to determine material properties, three beam models (Table 2) were cut from the layup for panel 6 before it was trimmed to its final dimensions.

EXPERIMENTAL PROCEDURE

Vibration tests were conducted to determine the natural frequencies and nodal patterns of the first six modes and the damping coefficients associated with the first three modes of the panels. Each panel (Fig. 2) was supported to simulate a clamped boundary condition by bolting the panel between two heavy steel supports. The supports-panel assembly was clamped to a massive steel-concrete backstop.

| EXTENSION | BENDING |

| EXTENSION AND BENDING | EXTENSION AND BENDING |
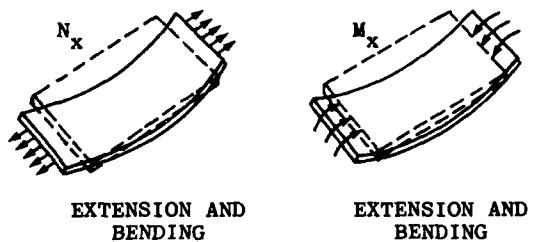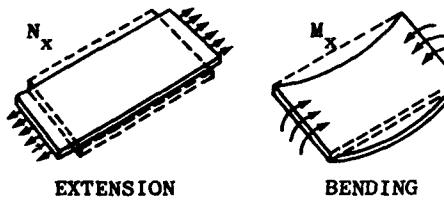
(a) Panels with Symmetrical Laminations   (b) Panels with Unsymmetrical Laminations

Fig. 1 - Characteristic Deformations of Laminated Panels

TABLE 1
Physical Characteristics of
Composite Panels

TABLE 2
Physical Characteristics of
Composite Beam Specimens
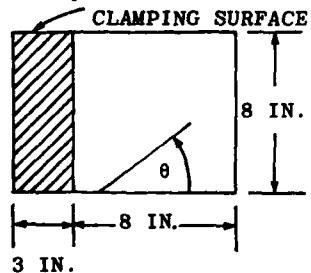
	θ (deg.)		h
Panel	Bottom Layer	Top Layer	Panel Thickness (in.)
1 (0/0)	0.	0.	0.0452
2 (0/22.5)	0.	22.5	0.0492
3 (0/45.)	0.	45.	0.0460
4 (0/67.5)	0.	67.5	0.0470
5 (0/90.0)	0.	90.	0.0490
6 (45./45.)	45.	45.	0.0442
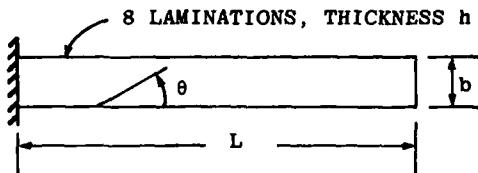
Specimen	θ (deg.)	L (in.)	b (in.)	h (in.)
1	0.	6.	0.55	0.045
2	45.	6.	0.61	0.045
3	90.	5.	0.56	0.045
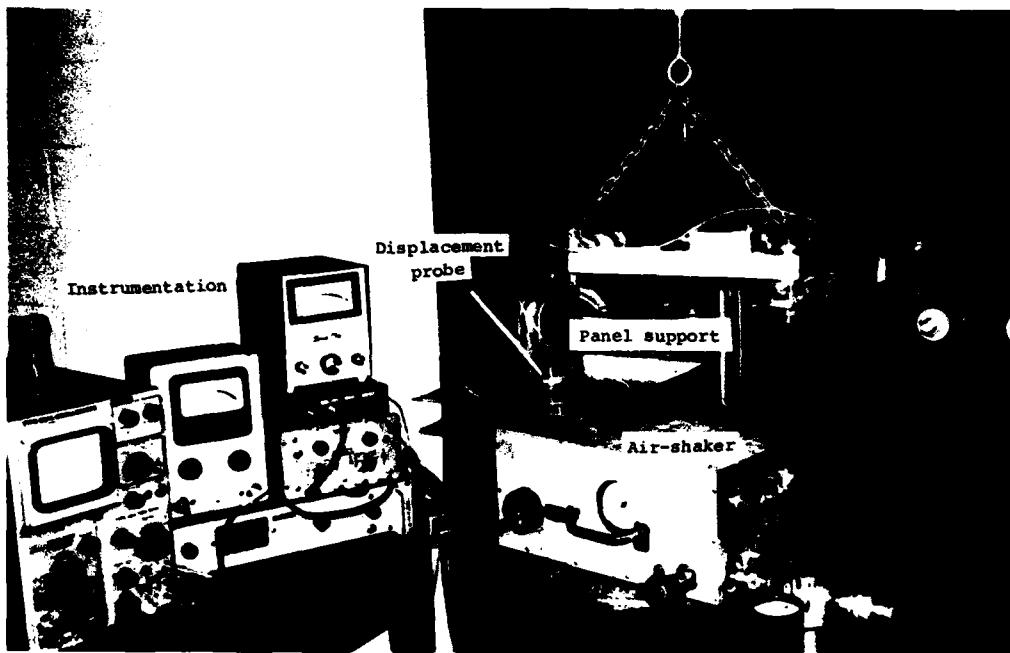
Fig. 2 - Vibration Test System

Natural frequencies were obtained by exciting the panels with an air-jet shaker. The response of the panels was measured using a non-contact displacement probe. Use of the non-contacting air shaker and displacement probe eliminated effects of mass and stiffness associated with electromagnetic shakers and/or accelerometers. The excitation frequency and position of the air-jet were varied until a panel resonant response was obtained. Nodal patterns were determined by sprinkling fine sand on a panel while exciting it at a resonant frequency. After the sand had accumulated at nodal lines the air shaker was cut off and the nodal pattern photographed. Damping coefficients were obtained by exciting a panel at a natural frequency, abruptly shutting off the air and recording the decaying displacement with an oscillograph. The logarithmic decrement method was then used to compute the percent critical damping.

Vibration tests were conducted on aluminum and symmetrical boron-epoxy beam specimens (Table 2) to determine material properties for analysis of the panels. Measured frequencies (Table 3) were used with flexural vibration theory to obtain elastic modulii (Table 4) for the aluminum and boron-epoxy panels.

The elastic moduli, E_ℓ and E_t, were calculated using Bernoulli-Euler beam theory. For a cantilever beam vibrating in its first mode the frequency is given by

$$f_1 = \frac{0.560}{L^2} \sqrt{\frac{gEh^2}{12\gamma}} , \text{ HZ} \qquad (1)$$

where E is the elastic modulus, h is the beam thickness, L is the length, γ is the specific weight of the material, and g is the acceleration of gravity. The natural frequencies for specimens 1 and 3 were substituted into this equation for each test to obtain values for E_ℓ and E_t, respectively.

The dimensions of the specimens given in Table 2 and a measured specific weight γ of 0.069 lb/in.^{3} were used in these calculations. The values of the elastic moduli in Table 4 are the average of the results computed from the two tests.

The value of the shearing modulus was computed from the equation [16]

$$G_{\ell t} = \frac{1}{\dfrac{4}{E_{45}} - \dfrac{1}{E_t} - \dfrac{(1 - \nu_{\ell t})}{E_\ell}} \qquad (2)$$

81

where E_{45} is the value of the elastic modulus for a specimen with filaments 45 degrees to the longitudinal axis. In this case E_{45} was calculated from the vibration tests of specimen 2. A major Poisson's ratio, $\nu_{\ell t} = 0.22$, was assumed and $G_{\ell t}$ was computed from

the last equation. It has been noted (see [7]) that $G_{\ell t}$ is insensitive to the value of $\nu_{\ell t}$ so that the assumed value of $\nu_{\ell t}$ from the literature is satisfactory. The minor Poisson's ratio was then computed using E_ℓ, E_t, and $\nu_{\ell t}$.

TABLE 3
Natural Frequencies of Beam Specimens

Specimen	Test	Frequencies, Hz	
		Mode 1	Mode 2
1 (θ = 0. deg.)	1	72.5	453
	2	73.3	450
2 (θ = 45 deg.)	1	23.4	145
	2	24.3	153
2 (θ = 90 deg.)	1	29.3	190
	2	--	-

TABLE 4
Material Properties

Material Parameter	Aluminum	Boron-epoxy
Young's Modulus		
E_ℓ	9.40×10^6 psi	23.3×10^6 psi
E_t	9.40×10^6 psi	1.81×10^6 psi
Shear Modulus		
$G_{\ell t}$	3.74×10^6 psi	0.976×10^6 psi
Poisson Ratio		
$\nu_{\ell t}$	0.25	0.22
$\nu_{t\ell}$	0.25	0.017

ANALYTICAL PROCEDURE

Three finite element analyses of the panels were made using the NASTRAN program. The first was an approximate uncoupled analysis made using the NASTRAN CQDPLT bending finite element. This element does not permit a coupling between bending and extension. Thus in the first analysis using this element the coupling effects were neglected. A second analysis with the uncoupled CQDPLT element used a reduced set of

bending stiffnesses which approximately takes into account the coupled bending-extension. The approximation [17] consists of replacing the actual bending stiffnesses, D_{ij}, by a reduced set of stiffnesses given by

$$[\bar{D}] = [D] - [B] [A]^{-1} [B] \qquad (3)$$

where [A], [B], and [D] are defined by the stress resultant, mid-plane strain and curvature relationship given by

$$\begin{Bmatrix} N \\ M \end{Bmatrix} = \begin{bmatrix} A & B \\ B & D \end{bmatrix} \begin{Bmatrix} \varepsilon \\ \kappa \end{Bmatrix} \qquad (4)$$

where $\{N\}$ denotes the midplane forces, $\{M\}$ denotes the bending and twisting moments, $\{\varepsilon\}$ represents the mid-plane strains, and $\{\kappa\}$ denotes the plane curvatures. Bending stiffnesses of the test panels were computed external to NASTRAN from lamina properties using standard orthotropic, laminated plate theory.

The third analysis was performed using a new 20-degree of freedom, coupled rectangular plate bending element developed for this study (Fig. 3). The element uses as input data the thickness and elastic constants of each lamina. The matrix equations for the

element were derived from finite element theory using the formula manipulation computer language, FORMAC. FORTRAN subroutines were developed from these equations and the element was incorporated into NASTRAN using the NASTRAN dummy element capability.

All analyses utilized the same finite element mesh of 81 nodes (Fig. 4). The two analyses performed with the NASTRAN CQDPLT element had 3 degrees of freedom per node; the analysis performed with the coupled element had 5 degrees of freedom per node. For the CQDPLT plate element NASTRAN solved an eigenvalue problem of size 216 and for the coupled element an eigenvalue problem of size 360 was solved. All eigenvalue problems were solved by the Givens method (see [18]).
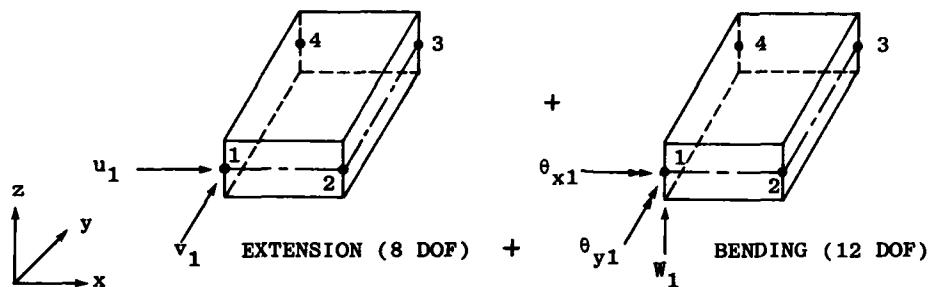
$$u = [1, x, y, xy]\ [\alpha_i]\ (i = 1, 4)$$
$$v = [1, x, y, xy]\ [\alpha_j]\ (j = 5, 8)$$

$$w = [1, x, y, x^2, xy, y^2, x^3, x^2y,$$
$$xy^2, y^3, x^3y, xy^3]\ [\alpha_k](k = 9, 20)$$

Fig. 3 - Displacement Fields for Coupled Rectangular Plate Element
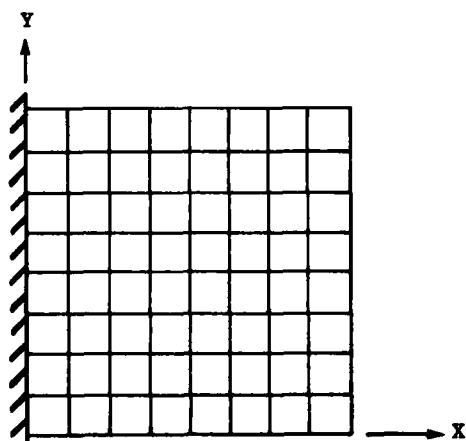
(a) Finite Element Representation for Panel
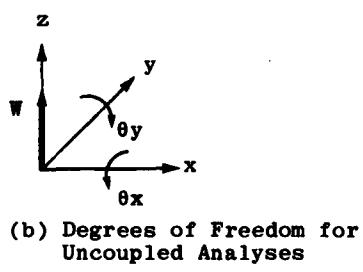
(b) Degrees of Freedom for Uncoupled Analyses
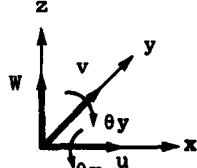
(c) Degrees of Freedom for Coupled Analysis

Fig. 4 - Finite Element Models for Panels

RESULTS AND DISCUSSION

Measured frequencies are compared with frequencies computed using the two types of finite elements in Table 5. The data for the aluminum panel indicate that the measured and finite element calculated frequencies are in good agreement. The average error of the finite element computed frequencies using either element is less than 4 per cent. The frequencies were also computed using the Rayleigh-Ritz approach [19]; the agreement was excellent. These correlations established that the test conditions accurately simulated a fixed boundary and that the finite element model was adequate to accurately predict the vibration characteristics of the composite panels.

TABLE 5
Measured and Calculated Natural Frequencies

Panel No.	Method	Frequency, Hz						Average % Difference
		1	2	3	4	5	6	
Aluminum Panel								
	Experimental	25.2	61.0	154	208	227	–	
	CQDPLT Element	25.0	62.2	152	190	222	–	3.1
	Coupled Element	24.6	60.1	149	186	224		3.8
	Rayleigh-Ritz [19]	25.2	61.6	154	198	225	–	1.2
Boron-Epoxy Panels								
1 (0/0)	Experimental	41.2	48.7	117	–	262	273	–
	CQDPLT Element	41.4	53.2	105	219	252	265	5.3
	Coupled Element	41.5	53.0	103	211	256	267	5.0
2 (0/22.5)	Experimental	34.3	59.4	143	216	264	309	–
	CQDPLT Element							
	No coupling	40.4	64.0	129	248	255	288	10.0
	Approx. coupling	35.0	56.6	121	216	241	259	7.8
	Coupled Element	34.4	56.1	119	214	235	253	8.8
3 (0/45)	Experimental	24.4	55.1	141	157	208	281	–
	CQDPLT Element							
	No coupling	33.4	60.9	140	205	255	283	15.6
	Approx. coupling	23.7	48.1	116	148	190	242	11.1
	Coupled Element	24.3	48.5	118	151	193	242	9.0
4 (0/67.5)	Experimental	21.8	43.3	132	149	184	177	–
	CQDPLT Element							
	No coupling	32.0	52.0	172	198	247	313	29.5
	Approx. coupling	23.5	47.1	141	148	192	276	4.6
	Coupled Element	21.8	43.4	130	138	177	254	1.4
5 (0/90)	Experimental	21.4	34.3	134	157	169	283	–
	CQDPLT Element							
	No coupling	29.7	44.3	183	202	194	305	26.0
	Approx. coupling	21.7	40.9	134	163	148	260	3.0
	Coupled element	20.4	38.4	127	153	140	244	9.2
6 (45/45)	Experimental	17.4	56.1	107	143	209	238	–
	CQDPLT Element	17.3	51.4	107	126	201	244	4.5
	Coupled Element	17.1	50.7	103	124	193	237	6.0

For the symmetrically laminated composite panels (specimens 1 and 6) both elements predicted results which agreed well with the experimental results with an average difference of about 5 percent. For the unsymmetrically laminated panels (specimens 2-5) both the approximate method (reduced bending stiffness) and the coupled finite element satisfactorily predicted the frequencies. However, neglecting the coupling gave very poor predictions with differences up to 50 percent.

It appears from the correlation of the predicted and measured frequencies that the reduced bending *stiffness* method is a good approximation for cantilevered, unsymmetrically laminated panels. The approximation [17] is based upon the assumption that coupling between the inplane forces, (N) and the plate curvatures, (κ) can be neglected in the strain energy equation if the reduced stiffness, Eq. (1), is used. A possible explanation for the good results of this approximation for cantilever panels is that the inplane forces are zero on the three free edges of the panel. Thus, the inplane forces never become large and their effect upon the strain energy is not appreciable. For certain other boundary conditions, [20], it has been found that the reduced stiffness approximation did not give satisfactory results.

The variation of the first four vibration frequencies with increasing asymmetry is presented in Fig. 5. For all four modes frequencies decreased as the asymmetry increased. The maximum reduction in frequency occurred in the first mode and is about 30 percent.

A comparison of experimental and predicted nodal lines is made in Fig. 6. Photographs of the experimental nodal patterns are presented in ref. [21]. Agreement between experiment and analysis is generally good with some exceptions. For example, for panel 1, mode four was not found experimentally.

The percent critical damping for the first three modes are presented in Table 6. The composite panels generally had three or four times more damping than the aluminum control specimen. There was no correlation between filament angle and the amount of damping.

CONCLUDING REMARKS

Vibration characteristics of cantilevered, unsymmetrically laminated boron-epoxy panels have been determined experimentally and analytically using

$\theta = 0$ FOR BOTTOM LAYER

θ VARIES FOR TOP LAYER

(a) First Mode

(b) Second Mode

(c) Third Mode

(d) Fourth Mode
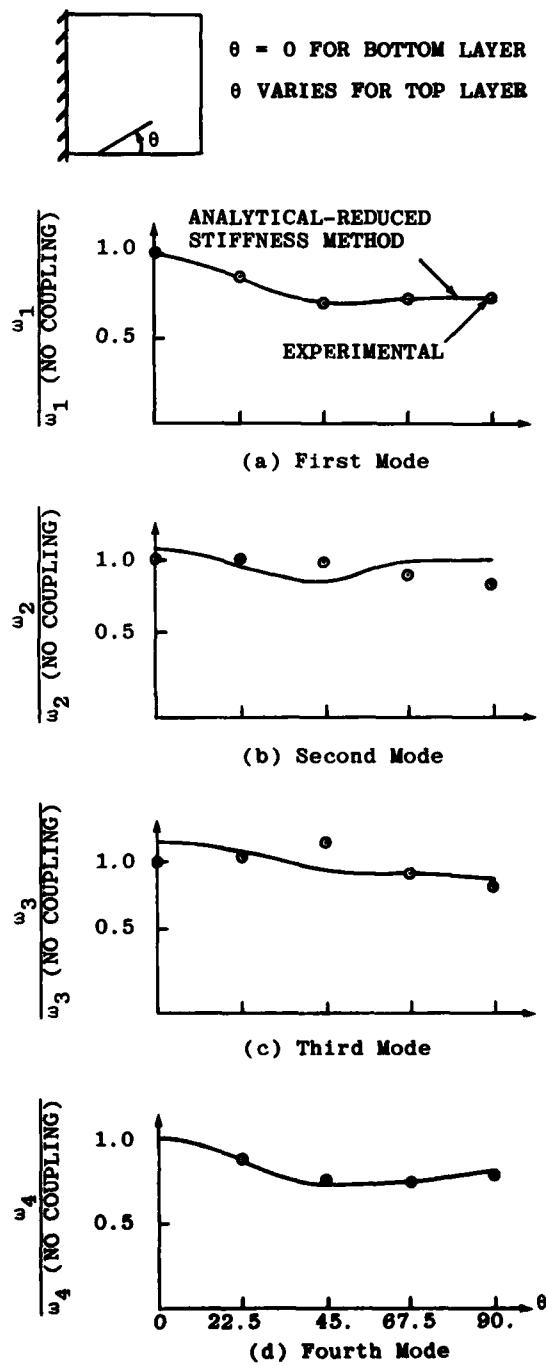
Fig. 5 – Variation of First Four Frequencies for Unsymmetrically Laminated Panels
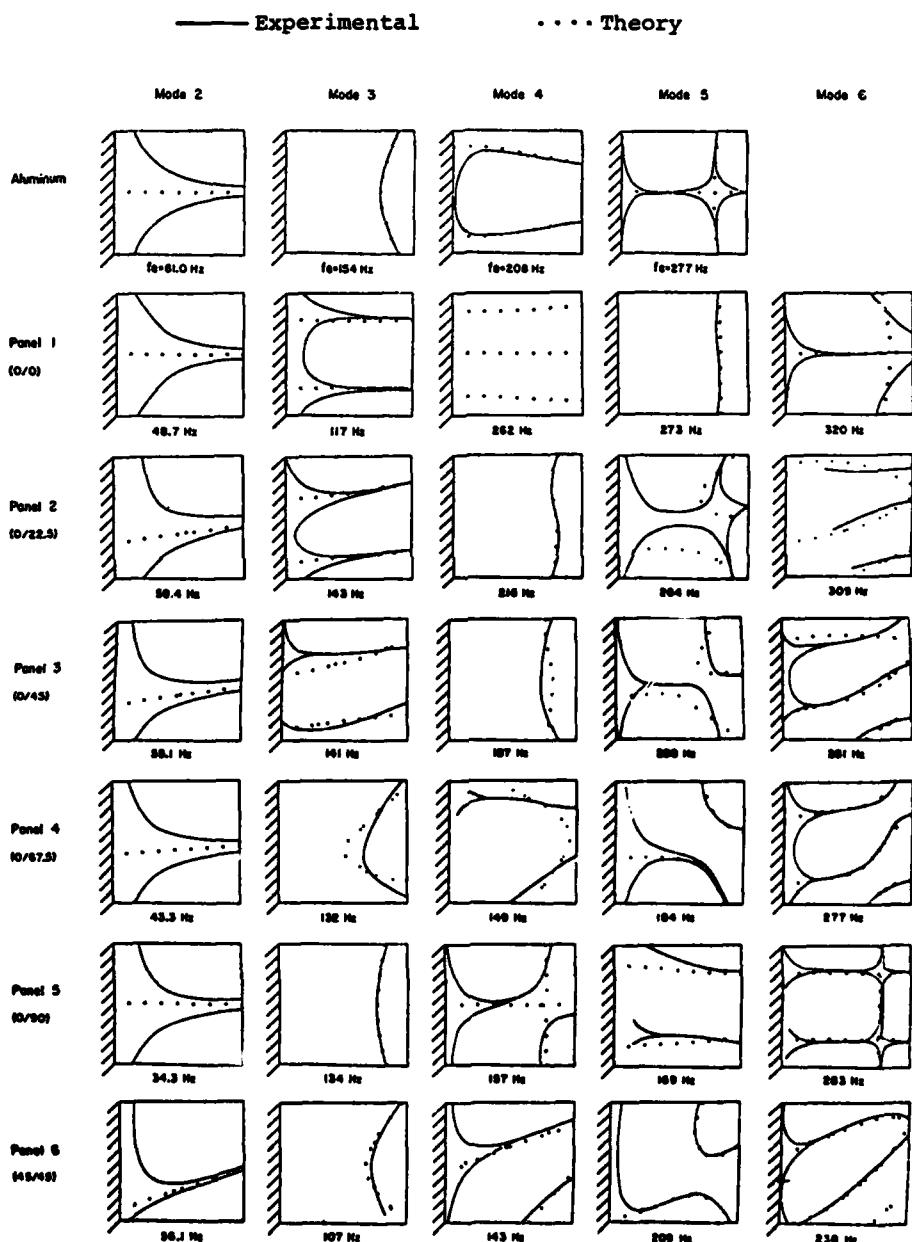
Fig. 6 - Comparison Between Measured and Calculated Nodal Patterns

TABLE 6
Damping Coefficients
(Percent of Critical Damping)

Panel	Mode		
	1 (%)	2 (%)	3 (%)
Aluminum	0.2	0.1	0.3
1 (0/0)	-	0.6	0.9
2 (0/22.5)	0.7	0.8	0.9
3 (0/45.)	0.6	0.7	0.7
4 (0/67.5)	0.7	0.6	0.8
5 (0/90.)	0.8	0.4	1.2
6 (45./45.)	0.7	0.6	1.0

the finite element method. Three NASTRAN finite element analyses of the panel were conducted to investigate different analytical representations of the panels' asymmetry.

Comparisons between experimental and analytical results indicate that filamentary unsymmetrically laminated composites can be satisfactorily represented using orthotropic laminate theory which includes coupling effects. For the boundary conditions considered the approximate reduced bending stiffness method gave satisfactory results and is an attractive alternative to fully coupled plate theory since it can be used in uncoupled plate bending elements available in most finite element programs.

Vibration frequencies tended to decrease with increasing asymmetry. The largest decrease of 30 percent occurred in the first mode. The composite panels had considerably more damping than a comparable aluminum panel but there was no discernible trend between panel assymetry and damping.

REFERENCES

1. J.E. Ashton and J.D. Anderson, "The Natural Modes of Vibration of Boron-Epoxy Plates," Shock and Vibration Bulletin, Vol. 39, Part 4, pp. 81-91, Apr. 1969

2. J.E. Ashton and M.E. Waddoups, "Analysis of Anisotropic Plates," Journal of Composite Materials, Vol. 3, No. 1, pp. 148-165, Jan. 1969

3. "Dynamic Characteristics of Advanced Filamentary Composite Structures," Second Interim Technical Report, General Dynamics Corporation, Jan. 1972

4. "Dynamic Characteristics of Advanced Filamentary Composite Structures," Supplement to Second Interim Technical Report, General Dynamics Corporation, Jan. 1972

5. R.R. Clary, "Practical Analysis of Plate Vibrations Using NASTRAN," NASTRAN Users' Experiences, NASA TM X-2378, Sept. 1971

6. R.R. Clary, "Vibration Characteristics of Unidirectional Filamentary Composite Material Panels," Composite Materials: Testing and Design (Second Conference), ASTM STP 497, American Society for Testing and Materials, pp. 415-438, 1971

7. R.R. Clary and P.A. Cooper, "Vibration Characteristics of Aluminum Plates Reinforced with Boron-Epoxy Composite Material," Journal of Composite Materials, Vol. 7, pp. 348-365, Jul. 1973

8. J.M. Whitney, "A Study of the Effect of Coupling Between Bending and Stretching on the Mechanical Behavior of Layered Anisotropic Composite Materials," Ph.D. Dissertation, The Ohio State University, 1968

9. R.M. Jones, "Buckling and Vibration of Unsymmetrically Laminated Cross-Ply Rectangular Plates," AIAA Journal, Vol. 11, No. 12, pp. 1616-1632, Dec. 1973

10. R.M. Jones, H.S. Morgan, and J.M. Whitney, "Buckling and Vibration of Antisymmetrically Laminated Angle-Ply Rectangular Plates," Journal of Applied Mechanics, Vol. 40, No. 4, pp. 1143-1144, Dec. 1973

11. C.C. Lin and W.W. King, "Free Transverse Vibrations of Rectangular Unsymmetrically Laminated Plates," Journal of Sound and Vibration, Vol. 36, No. 1, pp. 91-103, Sept. 8, 1974

12. C.W. Bert and B.L. Mayberry, "Free Vibrations of Unsymmetrical Laminated Anisotropic Plates with Clamped Edges," Journal of Composite Materials, Vol. 3, pp. 282-293, 1969

13. Y. Hikami, "Transverse Vibration of Laminated Orthotropic Plates," M.S. Thesis, Case Western Reserve University, Apr. 1969

14. E.A. Thornton and R.R. Clary, "A Correlation Study of Finite Element Modeling for Vibrations of Composite Material Panels," Composite Materials: Testing and Design (Third Conference), ASTM STP 546, Williamsburg, VA, pp. 111-129, Mar. 1973

15. Marlin D. Minich and Christos C. Chamis, "Cantilevered Unsymmetric Fiber Composite Laminated Plates," AIAA Journal, Vol. 14, pp. 299-300, Mar. 1976

16. L.R. Calcote, "The Analysis of Laminated Composite Structures," Van Nostrand Reinhold Company, 1969

17. J.E. Ashton, "Approximate Solutions for Unsymmetrically Laminated Panels," Journal of Composite Materials, Vol. 3, pp. 189-191, Jan 1969

18. R.H. MacNeal, editor, "The NASTRAN Theoretical Manual," NASA SP-221, 1969

19. A.W. Leissa, "Vibration of Plates," NASA SP-160, 1969

20. J.M. Whitney, "The Effect of Boundary Conditions on the Response of Laminated Composite," Journal of Composite Materials, Vol. 4, No. 2, pp. 192-203, Apr. 1970

21. E.A. Thornton, "Vibration Characteristics of Unsymmetrically Laminated Advanced Composite Panels," Old Dominion University School of Engineering Technical Report 75-M4, prepared for NASA under Master Contract Agreement NAS1-9434, Task 46, Sept. 1975.

FUNDAMENTAL FREQUENCIES OF ORTHOTROPIC PLATES

WITH VARIOUS PLANFORMS AND EDGE CONDITIONS

Charles W. Bert
School of Aerospace, Mechanical and Nuclear Engineering
The University of Oklahoma
Norman, Oklahoma

In contrast to the considerable information abailable on free vibration of
isotropic plates, there is only a very limited amount of analogous informa-
tion for composite-material plates. To help satisfy this need, this paper
introduces a simple reduction method from which results of existing free-
vibrational analyses for isotropic plates of various planforms and edge
conditions can be converted to analogous results for the important class
of composite-material plates known as orthotropic plates. The method is
applied to obtain fundamental frequency data for rectangular plates with
fifteen different combinations of edge conditions, simply supported and
clamped right triangular plates, clamped isoceles plates and clamped el-
liptic plates. Also, an approximate rational design technique is intro-
duced and applied to illustrate how the orthotropic data may be used to
design a lamination arrangement to maximize the fundamental frequency of
a many-layer plate.

INTRODUCTION

With the increasing use of laminated fila-
mentary composite materials in aerospace struc-
tural panels, there is a need for simple equa-
tions or curves for use by designers. Copious
amounts of such design information are already
available for isotropic-material plates; for
free-vibration information, Leissa's monograph
[1]* is very useful. However, the free-vibration
characteristics of composite-material plates
depend upon the lamination arrangement as well
as four material properties rather than just two.
Thus, none of the information on free vibration
of isotropic plates is directly applicable to
composite-material plates.

The simplest kind of composite-material be-
havior is known as orthotropic and has two axes
of material symmetry with different stiffnesses
along each of these axes and shear stiffness
which is independent of the other elastic prop-
erties. The three basic lamination arrangements
exhibiting orthotropic behavior are:

1. A single aligned layer (one with the
major-symmetry axis, the fiber direction, aligned
with an axis of geometric symmetry of the plate).

2. An aligned parallel-ply laminate with
the layers arranged symmetrically about the mid-
plane of the plate

_____
*A number in brackets indicates a reference
at the end of the text.

3. A symmetrically-laminated cross-ply
plate, in which all plies are oriented at either
0 or 90 degrees to the major geometric axis of
the plate.

Laminated composite-material plates may have
more complicated behavior, depending upon the
lamination arrangement. For example, an unsym-
metrically-laminated cross-ply plate exhibits
an elastic coupling known as bending-stretching
coupling, in which the in-plane (plane stress)
behavior is coupled with the flexural behavior.
However, this coupling is undesirable from the
standpoint of structural rigidity, static stress,
and thermal distortion, so such a layup is gen-
erally avoided.

Another kind of elastic coupling found in
certain laminates is known as shear coupling.
In plates this coupling manifests itself as a
coupling between bending and twisting action.
This coupling is strongest in off-axis parallel-
ply laminates, somewhat weaker in various kinds
of angle-ply laminates with only a few layers
and decreasing rapidly as the number of layers
is increased.

Due to the importance of orthotropic plates,
it is indeed unfortunate that there is only a
limited amount of vibration information avail-
able which is directly useful to composite-
material structural designers. To remedy this
situation, a simple reduction method is intro-
duced in the present paper. It may be considered
to be an extension of the work of Wittrick [2]

and Shuleshko [3] for plate buckling and of Rajappa [4] for plate free vibration.

ANALYSIS

Warburton [5] conducted Rayleigh-type analyses of the free vibration of isotropic rectangular plates with fifteen most common combinations of natural boundary conditions (simple, clamped or free). For the modal functions, he used appropriate combinations of the characteristic beam functions. Hearmon [6] presented similar analyses for orthotropic rectangular plates with all combinations of simple and clamped supports (six cases). Lekhnitskii [7] gave results of Rayleigh analyses for clamped and simply supported right triangular plates and for a clamped isosceles triangular plate. McNitt [8] analyzed free vibration of clamped elliptic plates of isotropic material. He used the Galerkin method in conjunction with a two-term deflection function. Lekhnitskii [7] gave a Rayleigh-type solution for a clamped orthotropic plate.

The present investigator studied the results of [5-8] and found that all of them can be expressed in the following generalized form:

$$\omega^2 = (\pi/a)^4 (\rho h)^{-1} [C_{11}D_{11} + 2(C_{12}D_{12} + 2C_{66}D_{66})R^2$$

$$+ C_{22}D_{22}R^4] \tag{1}$$

where a, b are the major plate dimensions in the x and y directions, $R \equiv a/b$, $\rho \equiv$ mean density of the plate and C_{ij} are coefficients that depend upon the plate planform and boundary conditions. The coefficients C_{ij} are introduced in equation (1) in such a way that they all take on a value of unity for the case of a rectangular plate with all edges simply supported.

Table 1, taken from [5-8], lists the values of the C_{ij} for the fundamental plate-type modes of vibration for nineteen different cases. For Cases 3, 8-11, 14 and 15, there are some rigid-body and beam-type modes which do not depend upon aspect ratio and these are not included in Table 1 but could be deduced from [5] if desired. It is interesting to note that even though Warburton's work was carried out for isotropic plates, his results were presented in such a form that the C_{ij} for orthotropic plates can be deduced. The present C_{ij} are related to Warburton's coefficients as follows:

$$C_{11} = G^4_x \ ; \ C_{12} = H_xH_y \ ; \ C_{22} = G^4_y \ ;$$

$$C_{66} = J_xJ_y \tag{2}$$

In certain cases, results from Hearmon [6] as well as Warburton [5] are available. In Cases 1, 5 and 7, their results coincided, while in Cases 2, 4 and 6, Hearmon's values are slightly lower and thus more accurate. It is cautioned

that the cases involving free edges (Cases 3, 8-15) are especially approximate since the functions used satisfy the free-edge boundary conditions only approximately, as was noted by Warburton [5].

Lekhnitskii [7] presented a Rayleigh-type result for a clamped elliptic plate of orthotropic material. However, when the results of McNitt's two-term Galerkin analysis for a plate of isotropic material are converted to the orthotropic form, lower and thus more accurate, values are obtained for the coefficients.

APPLICATION TO LAMINATE OPTIMIZATION

One of the major advantages claimed for composite materials is their capability to be tailored by appropriate orientation of the filaments in the various layers to obtain desired structural performance characteristics. The difficulty encountered by the designer of such structures is selection of the appropriate orientation scheme. Although there are numerous papers and some books [9-11] covering the analysis of laminated composite-material plates, very little information directly useful to a designer is available. Hayashi [12] and Chen and Bert [13-14] presented syntheses for maximizing the buckling load of simply supported rectangular plates for uniaxial and biaxial compression, respectively.

A rationale to synthesize for maximum fundamental frequency was recently developed by the present investigator and applied to simply supported rectangular plates [15]. The present work extends this synthesis to many-layer plates of arbitrary planform and edge conditions.

Previous work [15] indicated that a symmetric angle-ply (SAP) lamination arrangement is the stiffest one possible from a vibrational standpoint for a laminate consisting of many layers of equal-thickness composite material. Here the term "symmetric" means that the layers are arranged symmetrically with respect to the midplane of the laminate; thus, there can be no coupling between bending or twisting on one hand and inplane stretching or shearing on the other.

The plate stiffnesses $D_{ij}(i,j = 1,2,6)$ are defined as follows:

$$D_{ij} \equiv \int_{-h/2}^{h/2} z^2 Q_{ij} dz \tag{3}$$

Here $h \equiv$ plate thickness, $z \equiv$ thickness-direction coordinate measured from the laminate midplane, and the Q_{ij} are the plane-stress reduced stiffness coefficients defined as follows:

$$\{\sigma_i\} = [Q_{ij}]\{\epsilon_j\} \quad (i,j = 1,2,6) \tag{4}$$

where σ_i are stress components and ϵ_j are the

strain components. The contracted notation, common in composite-material mechanics [11], is used. Here 1 and 2 refer to normal stresses (or strains) and 6 refers to shear stress (or strain).

Assuming uniform macroscopic properties through the thickness of each typical layer (denoted by the index k), one can rewrite equation (3) as follows:

$$D_{ij} = \frac{1}{3} \sum_{k=1}^{n} (z_k^3 - z_{k-1}^3) Q_{ij}^{(k)} \qquad (5)$$

where z_k and z_{k-1} are the z-coordinates of the top and bottom surfaces of typical layer "k", and n is the total number of layers.

From equation (5) and the transformation relations for the Q_{ij} as a function of orientation angle θ, it is noted that for a SAP laminate, all of the D_{ij} except D_{16} and D_{26} can be expressed by the following simple expression:

$$D_{ij} = (h^3/12) Q_{ij}(\theta) \qquad (ij = 11,12,22,66) \qquad (6)$$

where $Q_{ij}(\theta)$ are the stiffnesses associated with orientation θ.

Since $Q_{16}(-\theta) = - Q_{16}(\theta)$ and $Q_{26}(-\theta) = - Q_{26}(\theta)$, the expressions for D_{16} and D_{26} are more complicated than equation (6). Expressions are derived in Appendix A for the SAP laminates with either an odd or an even number of layers. They are the bases for Table 2, which shows that the values for the dimensionless ratios $12D_{16}/h^3 Q_{16}(\theta)$ and $12D_{26}/h^3 Q_{26}(\theta)$ diminish rather rapidly as the number of layers is increased. Furthermore, in practice, the quantities $Q_{16}(\theta)$ and $Q_{26}(\theta)$ are always small compared to the other Q_{ij}. Thus, it can be concluded that as a first approximation certainly adequate for preliminary design purposes, the bending-twisting stiffnesses D_{16} and D_{26} of SAP laminates can be neglected. Then the form of the plate equations simplify to those of a symmetrically laminated orthotropic plate and equation (1) can be used as the basis for an approximate optimization technique for SAP laminated plates.

It can be shown that the plate stiffnesses for the SAP lamination arrangement can be expressed in terms of the layup angle θ as follows:

$$
\begin{aligned}
D_{11} &= C(U_1 + U_2 \cos 2\theta + U_3 \cos 4\theta) \\
D_{12} &= C(U_4 - U_3 \cos 4\theta) \\
D_{22} &= C(U_1 - U_2 \cos 2\theta + U_3 \cos 4\theta) \\
D_{66} &= C(U_5 - U_3 \cos 4\theta)
\end{aligned}
\qquad (7)
$$

where

$$C = h^3/12\lambda \qquad (8)$$

The U_i appearing in equation (7) are the invariants originated by Tsai and Pagano [16]. Expressions relating the U_i and λ to the usual engineering elastic properties of an individual orthotropic layer are presented in Appendix B.

To determine the optimal angle θ_m to maximize the fundamental plate-type frequency, one must substitute equations (7) into equation (1) and set the derivative with respect to θ equal to zero. This determines the following condition for which ω^2 is an extreme (maximum or minimum):

$$(K - \cos 2\theta_m) \sin 2\theta_m = 0 \qquad (9)$$

where

$$K \equiv \frac{-C_{11}+C_{22}R^4}{C_{11}-(2C_{12}+4C_{66})R^2+C_{22}R^4} \frac{U_2}{4U_3} \qquad (10)$$

This leads to three different expressions for the optimal angle θ_m associated with a maximum value of ω^2:

$$\theta_m = 0^\circ \text{ when } K \geq 1$$

$$\theta_m = 1/2 \text{ arc cos } K \text{ when } 1 > K > -1 \qquad (11)$$

$$\theta_m = 90^\circ \text{ when } K \leq -1$$

For Case 1, all $C_{ij} = 1$ and the present results reduce to those of [15].

SPECIFIC EXAMPLE

As a specific example, an elliptic shaped plate with clamped edges and an aspect ratio of 1.25 is to be designed to maximize its fundamental frequency. For economic reasons, the plate is to laminated of unidirectional E-glass fiber/epoxy matrix composite material having the following properties:

Young's modulus in fiber direction	7.8×10^6 lbf/in^2 (53.8 GPa)
Young's modulus perpendicular to fibers	2.6×10^6 lbf/in^2 (17.9 GPa)
Poisson's ratio associated with loading along fibers	0.25
Shear modulus	1.3×10^6 lbf/in^2 (8.8 GPa)
Specific weight	0.072 lbf/in^3 (0.195 N/cm^3)

Using these properties in equations (B-1), one can calculate the following parameters:

$$U_1 = 4.699 \times 10^6 \text{ lbf/in}^2 (32.4 \text{ GPa})$$

$$U_2 = 2.60 \times 10^6 \text{ lbf/in}^2 (17.9 \text{ GPa})$$

$U_3 = 0.501 \times 10^6 \, \text{lbf/in}^2 (3.45 \text{ GPa})$

$U_4 = 1.151 \times 10^6 \, \text{lbf/in}^2 (7.94 \text{ GPa})$

$U_5 = 1.774 \times 10^6 \, \text{lbf/in}^2 (12.2 \text{ GPa})$

$\lambda = 0.9792$

Using the above values of U_2 and U_3 and the values of the C_{ij} from Table 1 for a clamped elliptic plate (Case 16) in equation (10), one obtains a value of 5.928 for K. Thus, from conditions (11), it is clear that the optimal orientation is $\theta_m = 0^\circ$. Using equations (7) and (8) in conjunction with equation (1), it is found that the frequency (rad/sec) is given by:

$$\omega = 2.237 \times 10^6 \, h/a^2$$

where h and a have units of inches.

REFERENCES

1. A.W. Leissa, "Vibration of Plates", NASA SP-160, 1969.

2. W.H. Wittrick, "Correlation Between Some Stability Problems for Orthotropic and Isotropic Plates Under Bi-axial and Uni-axial Direct Stress", Aeronautical Quarterly, Vol. 4, No. 1, pp. 83-92, Aug. 1952.

3. P. Shuleshko, "A Reduction Method for Buckling Problems of Orthotropic Plates", Aeronautical Quarterly, Vol. 8, No. 2, pp. 145-156, May 1957.

4. N.R. Rajappa, "On the Exact Solutions of Vibration Problems of Rectangular Orthotropic Plates", Zeitschrift für angewandte Mathematik and Physik, Vol. 15, pp. 201-205, 1964.

5. G.B. Warburton, "The Vibration of Rectangular Plates", Proc. Instn. of Mech. Engrs., London, Vol. 168, pp. 371-384, 1954.

6. R.F.S. Hearmon, "The Frequency of Flexural Vibration of Rectangular Orthotropic Plates with Clamped or Supported Edges", Journal of Applied Mechanics, Vol. 26, No. 4, pp. 537-540, Dec. 1959.

7. S.G. Lekhnitskii, Anisotropic Plates, 2ud ed., Engl. translation, Gordon and Breach, New York, 1968, section 94.

8. R.P. McNitt, "Free Vibration of a Clamped Elliptical Plate", Journal of the Aerospace Sciences, Vol. 29, No. 9, pp. 1124-1125, Sept. 1962.

9. J.E. Ashton and J.M. Whitney, Theory of Laminated Plates, Technomic Publishing Co., Inc., Stamford, CT, 1970.

10. R.M. Jones, Mechanics of Composite Materials, McGraw-Hill Book Co., New York, 1975, chap. 5.

11. C.W. Bert, Analysis of Plates, chap. 4 in Structural Design and Analysis, Part I, C.C. Chamis, ed., Vol. 7 in Composite Materials, L.J. Broutman and R.H. Krock, eds., Academic Press, New York, 1975.

12. Hayashi, T., "Optimum Design of Cross-and Angle-Plied Laminated Composite Plates Under Compression", Fukugo Zairyo Kenko, Japan, Vol. 3, No. 2, pp. 18-20, 1974.

13. T.L.C. Chen and C.W. Bert, "Design of Composite-Material Plates for Maximum Uniaxial Compressive Buckling Load", Proc. Oklahoma Academy of Science, Vol. 56, pp. 104-197, 1976.

14. C.W. Bert and T.L.C. Chen, "Optimal Design of Composite-Material Plates to Resist Buckling Under Biaxial Compression", Trans. Japan Society for Composite Materials, Vol. 2, No. 1, pp. 7-10, July 1976.

15. C.W. Bert, "Optimal Design of a Composite-Material Plate to Maximize Its Fundamental Frequency", Journal of Sound & Vibr., Vol. 50, 1977 (to appear).

16. S.W. Tsai and N.J. Pagano, "Invariant Properties of Composite Materials", Composite Materials Workshop, S.W. Tsai, J.C. Halpin and N.J. Pagano, eds., Technomic Publishing Co., Inc., Stamford, CT, pp. 233-263, 1968.

17. S.W. Tsai, "Structural Behavior of Composite Materials", NASA CR-71, July 1964.

APPENDIX A

DERIVATION OF EXPRESSIONS FOR D_{16} AND D_{26} OF

SYMMETRIC ANGLE-PLY LAMINATES

Odd Number of Plies

Here we consider an odd number of layers of alternating orientation beginning with θ. Applying equation (5), one obtains the following expression for D_{16}:

$$D_{16} = (1/3)[(h/2)^3 - (h/2-h/n)^3]Q_{16}(\theta)$$

$$+ (1/3)[(h/2-h/n)^3 - (h/2-2h/n)^3]Q_{16}(-\theta)$$

$$+ (1/3)[(h/2-2h/n)^3 - (h/2-3h/n)^3]Q_{16}(\theta)+\ldots$$

$$(A-1)$$

From the angular transformation relations for Q_{16}, it is noted that

$$Q_{16}(-\theta) = - Q_{16}(\theta) \qquad (A-2)$$

Using equation (A-2), one can write equation (A-1) in more compact series form as follows:

$$D_{16} = (2/3)h^3 Q_{16}(\theta)[(1/2)^3$$

$$+ 2 \sum_{k=1,2\ldots}^{\frac{1}{2}(n-1)} (\frac{1}{2} - \frac{k}{n})^3(-1)^k] \quad (A-3)$$

or in dimensionless form

$$12D_{16}/h^3 Q_{16}(\theta) =$$

$$1 + 2 \sum_{k=1,2\ldots}^{\frac{1}{2}(n-1)} (1 - 2k/n)^3(-1)^k \quad (A-4)$$

where index k refers to a typical layer.

The series expression (A-4) is exactly equal to the following simple formula, which is equivalent to that presented without derivation by Tsai [17]:

$$12D_{16}/h^3 Q_{16}(\theta) = (3n^2 - 2)/n^3 \quad (A-5)$$

A similar expression for D_{26} can be obtained by replacing $Q_{16}(\theta)$ by $Q_{26}(\theta)$.

It should be mentioned that an SAP laminate with an odd number of plies is identical to what was referred to by Tsai [17] simply as angle ply with n odd and by Jones [10] as symmetric angle ply.

Even Number of Plies

Taking advantage of the midplane symmetry, one may rewrite equations (3) and (5) as follows:

$$D_{ij} = 2 \int_o^{h/2} z^2 Q_{ij} dz$$

$$= \frac{2}{3} \sum_{k=1}^{n/2} (z_k^3 - z_{k-1}^3) Q_{ij}^{(k)} \quad (A-6)$$

Applying equations (A-2) and (A-6), we obtain:

$$D_{16} = (2/3)[(h/2)^3 - (h/2 - h/n)^3]Q_{16}(\theta)$$

$$- (2/3)[(h/2 - h/n)^3 - (h/2 - 2h/n)^3]Q_{16}(\theta) + \ldots \quad (A-7)$$

In summation form, equation (A-7) may be written as:

$$D_{16} = (2/3)h^3 Q_{16}(\theta)[(1/2)^3$$

$$+ 2 \sum_{k=1,2,\ldots}^{\frac{1}{2}n-1} (1/2 - k/n)^3(-1)^k] \quad (A-8)$$

or in dimensionless form:

$$12D_{16}/h^3 Q_{16}(\theta) =$$

$$1 + 2 \sum_{k=1,2,\ldots}^{\frac{1}{2}n-1} (1 - 2k/n)^3(-1)^k \quad (A-9)$$

The series expression (A-9) can be written in the following more convenient form:

$$12D_{16}/h^3 Q_{16}(\theta) = (3n^2 - 4F)/n^3 \quad (A-10)$$

where

$$F \equiv \begin{cases} 0 & \text{if } n/2 \text{ is even} \\ 1 & \text{if } n/2 \text{ is odd} \end{cases} \quad (A\cdot11)$$

A similar expression for D_{26} can be obtained by replacing $Q_{16}(\theta)$ by $Q_{26}(\theta)$.

It should be emphasized that an SAP laminate with an even number of plies is entirely different than what Tsai [17] referred to simply as angle ply with n even and Jones [10] called antisymmetric angle ply. This latter type of laminate has D_{16} and D_{26} identically equal to zero, but is unsymmetric since it has non-zero twisting-stretching coupling stiffnesses B_{16} and B_{26}. The SAP laminate with n even has all B_{ij} identically equal to zero.

APPENDIX B

EXPRESSIONS FOR U_i AND λ IN TERMS OF

USUAL ELASTIC PROPERTIES

The quantities U_i and λ appearing in equation (7) and (8) can be expressed in terms of the usual engineering elastic properties for an individual orthotropic layer as follows:

$$U_1 = (3/8)(E_L + E_T) + (1/4)E_T \nu_{LT} + (1/2)\lambda G_{LT}$$

$$U_2 = (1/2)(E_L - E_T)$$

$$U_3 = (1/8)(E_L + E_T) - (1/4)E_T \nu_{LT} - (1/2)\lambda G_{LT}$$

$$U_4 = (1/8)(E_L + E_T) + (3/4)E_T \nu_{LT} - (1/2)\lambda G_{LT}$$

$$U_5 = (1/8)(E_L + E_T) - (1/4)E_T \nu_{LT} + (1/2)\lambda G_{LT}$$

$$\lambda = 1 - \nu_{LT} \nu_{TL} \quad ; \quad \nu_{TL} = (\nu_{LT})(E_T/E_L)$$

$$(B-1)$$

Here E_L and E_T are the major and minor Young's moduli (L and T directions respectively parallel and perpendicular to the fiber direction), ν_{LT} is the major Poisson's ratio (ratio of transverse contraction to longitudinal extension when loaded uniaxially in the L direction), and G_{LT} is the shear modulus associated with the L,T axes.
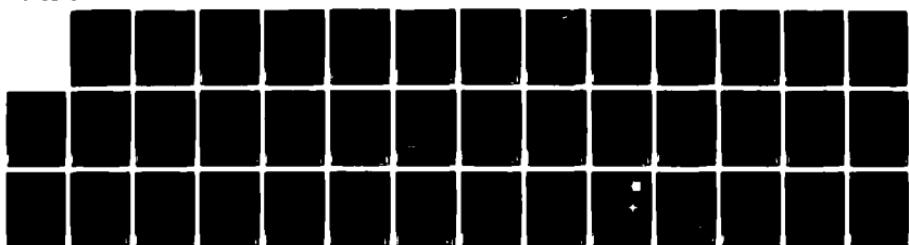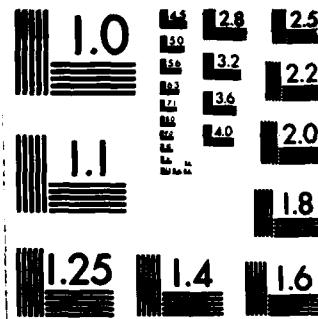
MICROCOPY RESOLUTION TEST CHART
NATIONAL BUREAU OF STANDARDS-1963-A

TABLE 1 Boundary-condition coefficients for lowest plate-type modes

LEGEND

========= SIMPLE SUPPORT /////// CLAMPED ———— FREE

CASE	PLANFORM AND EDGE CONDITIONS	C_{11}	C_{12}	C_{66}	C_{22}	REF.
1		1	1	1	1	5,6
2		5.139 (5.144)	1.553 (1.557)	1.553 (1.557)	5.139 (5.144)	6 5
3		5.144	1.557	25.17	5.144	5
4		2.441 2.441	1.451 (1.453)	1.451 (1.453)	5.139 (5.144)	6 5
5		2.441	1.356	1.356	2.441	5,6
6		5.139 (5.144)	1.246 (1.248)	1.246 (1.248)	1	6 5
7		2.441	1.165	1.165	1	5,6
8		2.441	1.453	13.83	5.144	5
9		2.441	1.356	7.596	2.441	5
10		5.144	1.248	5.017	1	5
11		2.441	1.164	2.756	1	5
12		0.1270	-0.1086	0.5878	5.144	5
13		0.1270	0.00757	0.2218	0.1270	5
14		5.144	1.557	6.261	5.144	5
15		0.1270	-0.1086	2.363	5.144	5
16		6.442 (6.581)	2.148 (2.195)	2.148 (2.195)	6.442 (6.581)	8 7
17		17.24	2.845	2.845	17.24	7
18		41.11	20.56	20.56	41.11	7
19		$\dfrac{2.569}{\sin^4\theta}$	$\dfrac{2.569}{\sin^2\theta\cos^2\theta}$	$\dfrac{2.569}{\sin^2\theta\cos^2\theta}$	$\dfrac{23.12}{\cos^4\theta}$	7

Table 2 Effect of number of plies on the dimensionless bending-twisting coupling stiffnesses of symmetric angle-ply laminates.

No. of layers (n)	$12D_{16}/h^3Q_{16}(\theta) = 12D_{26}/h^3Q_{26}(\theta)$	
	Exact fraction	Approx. %
1	1	100
*		
3	25/27	92.6
4	3/4	75
5	73/125	58.4
6	13/27	48.1
7	145/343	42.3
8	3/8	37.5
9	241/729	33.1
10	37/125	29.6
11	361/1331	27.1
12	1/4	25
13	505/2197	23.0
14	73/343	21.3

*It is impossible to have a two-layer angle-ply laminate that is symmetric.

94

DYNAMIC RESPONSE OF LAMINATED COMPOSITE PLATES

UNDER RESIDUAL THERMAL STRESSES

C. T. Sun
Department of Engineering Science and Mechanics
Iowa State University, Ames, Iowa

In this paper, the classical method of separation of variables, combined with the Mindlin-Goodman procedure, is employed to investigate the effects of residual thermal stresses to dynamic responses of a simply-supported composite plate in plane strain. Numerical results are presented in terms of a ratio of maximum flexural stress (with the presence of the residual stresses) to the same quantity when the plate suffers no temperature change. Numerical results show that in general the residual thermal stresses will increase the dynamic responses.

INTRODUCTION

Composite materials are currently used in a wide variety of applications. Important examples include composite materials for aircraft structural components, composite ablative materials for ABM and re-entry vehicles, filament-wound solid-propellant motor cases and nozzles, fiber-reinforced rotor blades for helicopters, composite turbine blades for jet engines, and fiber-reinforced gun tubes.

Most composite materials are fabricated at an elevated temperature by a hot working process. If the service temperature of the composite materials is at room temperature, then it suffers a temperature drop of about 200°F. In view of the difference of the thermal expansion coefficients between the fiber and the matrix materials, this temperature drop will introduce residual thermal stresses to the composites. It is, therefore, important for structural designers and materials engineers to take these residual thermal stresses into consideration in their theoretical analyses. The objective of this paper is to investigate the effects of residual thermal stresses on the dynamic response of laminated composite plates.

The dynamic problem is solved by using a method previously developed by the author [1]. This method was first developed by Mindlin and Goodman [2] and was subsequently used by Yu [3].

Numerical results for natural frequencies of free vibrations, maximum deflection, and maximum normal stress for simply-supported glass-epoxy plates are evaluated. The maximum dynamic response is then compared with the corresponding response obtained when the plates suffer no temperature change.

Based on the preliminary investigation, it is observed that the effects of residual thermal stresses depend upon the materials involved (in particular, the difference of the thermal expansion coefficients and the degree of anisotropy of the composites), the stacking sequences, geometry, and the type of dynamic loadings. In general, the residual thermal stresses, more often than not, adversely affect the performance of the composites under dynamic loadings.

ANALYSIS

Recently, a dynamic theory, which includes the effects of transverse shear deformation and rotary inertia, was developed for laminated composite plates [1]. By the application of the classical method of separation of variables, combined with the Mindlin-Goodman procedure [1-3] for treating time-dependent boundary conditions and/or dynamic external loadings, a solution for the five displacement variables under plane strain is assumed to be in the form

$$r_i(x,t) = \sum_{n=1}^{\infty} R_{in}(x) T_n(t)$$

$$+ \sum_{j=1}^{10} g_{ij}(x) f_j(t) \qquad (1)$$

where r_i ($i = 1, 2, 3, 4, 5$) stands for five displacement variables u^o, v^o, w, Ψ_x, and Ψ_y, respectively. In Eq. (1) $R_{in}(x)$ represents the nth principal mode of r_i associated with the nth natural frequency ω_n of free vibration; $f_j(t)$ ($j = 1, 2 \text{ --- } 10$) represents the applied forcing function at the boundaries and $T_n(t)$ and $g_{ij}(x)$ are unknown functions of time t and the coordinate x, respectively. Physically, the first term in Eq. (1) represents the solution due to surface traction under homogeneous boundary conditions, while the second term represents the solution generated by the forcing functions $f_j(t)$ prescribed at the boundary. The functions $g_{ij}(x)$ are determined from the Mindlin-Goodman procedure and vanished identically when all $f_j(t) = 0$ at the boundary [1-3].

If the plate suffers a constant temperature drop due to a difference of fabrication and service temperatures, the following thermal resultants will be introduced

$$N_x^T = \int_{-h/2}^{h/2} \left(Q_{11}^{(k)} \alpha_1^{(k)} + Q_{12}^{(k)} \alpha_2^{(k)} \right.$$
$$\left. + Q_{16}^{(k)} \alpha_6^{(k)} \right) \Delta T \, dz$$

$$\qquad (2)$$

$$M_x^T = \int_{-h/2}^{h/2} \left(Q_{11}^{(k)} \alpha_1^{(k)} + Q_{12}^{(k)} \alpha_2^{(k)} \right.$$
$$\left. + Q_{16}^{(k)} \alpha_6^{(k)} \right) z \Delta T \, dz$$

where ΔT represents the temperature drop, α_i represent the coefficients of thermal expansion, and the superscript (k) represents the kth layer. For symmetric lamination M_x^T vanishes identically. It is very easy to show that for a constant temperature change N_x^T will not enter the equations of motion: it will, however, change the constitutive equations of the plate. With the presence of temperature change, the constitutive equations become

$$\sigma_i^{(k)} = C_{ij}^{(k)} \left(\varepsilon_j - \alpha_j^{(k)} T \right) \qquad (3)$$

where C_{ij} are the components of the stiffness matrix. Expressing the strain tensor ε_{j_o} in terms of the inplane strain

tensor ε_j and the curvature tensor η_j, we have

$$\varepsilon_j = \varepsilon_j^o + z \eta_j. \qquad (4)$$

Using Eqs. (3) and (4) and the definitions of the force resultant, N_i, and the moment resultant, M_i, in plate theory, one obtains

$$\bar{N}_i = N_i + N_i^T = A_{ij} \varepsilon_j^o + B_{ij} \eta_j$$
$$\bar{M}_i = M_i + M_i^T = B_{ij} \varepsilon_j^o + D_{ij} \eta_j$$

$$\qquad (5)$$

where A_{ij}, B_{ij}, and D_{ij} are defined in [1], and

$$\left(N_i^T, M_i^T \right) = \int_h C_{ij}^{(k)} \alpha_j^{(k)} T(1, z) \, dz. \qquad (6)$$

In order to calculate the stress components in Eq. (3), we have to express ε_j^o and η_j in terms of $\bar{N}_i$ and $\bar{M}_i$. This can be accomplished by inverting the expressions of Eq. (5) with the result in matrix form

$$\begin{Bmatrix} \varepsilon^o \\ \eta \end{Bmatrix} = \begin{bmatrix} A' & B' \\ H' & D' \end{bmatrix} \begin{Bmatrix} \bar{N} \\ \bar{M} \end{Bmatrix} \qquad (7)$$

where A', B', H' and D' are matrices which can be expressed in terms of $[A]$, $[B]$ and $[D]$ matrices. They are omitted here, but they can be easily derived. For symmetric lamination, M_i^T and $[B]'$ vanish identically. In this case, we have

$$\{\varepsilon^o\} = [A]^{-1}\{\bar{N}\},$$
$$\{\eta\} = [D]^{-1}\{M\}. \qquad (8)$$

Substituting Eq. (8) into Eq. (3), we have the formula for $\sigma_i^{(k)}$ for plates with symmetric lamination

$$\sigma_i^{(k)} = C_{ij}^{(k)} \left[A_{jm}^{-1} \left(N_m + N_m^T \right) + z D_{jm}^{-1} M_m \right.$$
$$\left. - \alpha_j^{(k)} T \right]. \qquad (9)$$

With the absence of the initial external loading

$$\sigma_i^{(k)} = C_{ij}^{(k)} \left[A_{jm}^{-1} N_m^T - \alpha_j^{(k)} T \right]. \qquad (10)$$

When the plate is subjected to dynamic loadings, dynamic stress components will be produced. The total

stress components can be determined from Eq. (9) by solving N_k and M_k from equations of motion or by solving the dynamic problem directly as shown in [1]. The total stress will be equal to the superposition of the dynamic stress plus the initial thermal stresses as given in Eq. (10). The detailed solution of the dynamic problem can be found in [1], and the numerical results of a particular example are shown in the next section.

NUMERICAL RESULTS AND DISCUSSION

Numerical results for maximum flexural in-plane stress, σ_x, are evaluated for glass filament-epoxy resin composites with the following stacking sequences:

(1) Cross-ply composites. Laminate consists of constituent layers oriented alternately at 0° and 90°. All odd layers have one thickness h_1, and all even layers have one thickness h_2, but they are, in general, different from the odd layers. The lamination parameters include the total number of layers n and the cross-ply ratio m, which represents the ratio of the total thickness of the odd layers over that of the even layers. For the present work, only the case of symmetric lamination, i.e., n = odd will be presented. 0° lamination corresponds to the case when fibers are parallel to the x-direction. We also assume that the odd layers are oriented at 0°.

(2) Angle-ply composites. The angle-ply composite consists of n constituent layers oriented alternately at θ° and $-\theta^\circ$, where θ° represents the angle between the direction of fiber orientation and the x-axis. The odd layers are oriented with an angle $-\theta^\circ$ from the x-axis and the even layers at an angle θ°. The total thickness of the odd layers is equal to that of the even layers. The lamination parameters are the total number of layers n and the lamination angle θ°. The mechanical and physical properties of 0° glass-epoxy composite are

$$C_{11} = 7.97 \times 10^6 \text{ psi,}$$
$$C_{22} = 2.66 \times 10^6 \text{ psi,}$$
$$C_{12} = 0.66 \times 10^6 \text{ psi,}$$
$$C_{66} = 1.25 \times 10^6 \text{ psi,}$$
$$\alpha_1 = 3.5 \times 10^{-6}/^\circ\text{F,}$$
$$\alpha_2 = 11.4 \times 10^{-6}/^\circ\text{F,}$$
$$\alpha_6 = 0.$$

The values of C_{ij} and α_i corresponding to other orientations can be determined from the transformation equations. The ratio between L, the span length, and h, the thickness of the plate, is assumed to be 20.

Numerical results are presented in terms of a ratio between $\sigma_{x \text{ max}}$ (due to p (x,t) = 100 H(t) psi and a temperature change $\Delta T = -200^\circ$F) and $\sigma_{x \text{ max}}^0$ (due to the same p (x,t) with $\Delta T = 0$) as a function of lamination parameters. Figure 1 shows the ratio $\sigma_{x \text{ max}}/\sigma_{x \text{ max}}^0$ as a function of m for n = 3. The maximum ratio of $\sigma_{x \text{ max}}/\sigma_{x \text{ max}}^0$ is about 1.9, which occurs when m = 1. The next example is to express the ratio of $\sigma_{x \text{ max}}/\sigma_{x \text{ max}}^0$ as a function of n = odd for m = 1 as shown in Fig. 2. Figure 2 shows that the ratio of $\sigma_{x \text{ max}}/\sigma_{x \text{ max}}^0$ decreases as the value of n increases. This is attributed to the fact that as n increases the composite behaves similarly to an isotropic medium in which the temperature change introduces no thermal stresses. In the third example, we plot $\sigma_{x \text{ max}}/\sigma_{x \text{ max}}^0$ as a function of the lamination angle θ for n = 3, as shown in Fig. 3. Figure 3 shows that the ratio of $\sigma_{x \text{ max}}/\sigma_{x \text{ max}}^0$ is close to unity for the $\theta = 0^\circ$ and 90° cases and reaches a maximum value of about 1.7 when θ is close to 45°. The last example shows the ratio $\sigma_{x \text{ max}}/\sigma_{x \text{ max}}^0$ as a function of n for $\theta = 45^\circ$ in Fig. 4. A similar result is observed in Fig. 2 for cross-ply lamination.

In conclusion, we observe that, more often than not, residual thermal stresses produce adverse effects under dynamic loading.

REFERENCES

1. C. T. Sun and J. M. Whitney, "Forced Vibrations of Laminated Composite Plates in Cylindrical Bending," J. Acoust. Soc. Am., Vol. 37, No. 8, pp. 1003-1008, May 1974.

2. R. D. Mindlin and L. E. Goodman, "Beam Vibrations with Time-dependent Boundary Conditions," J. Appl. Mech. Vol. 17, pp. 377-380, 1950.

3. Y. Y. Yu, "Forced Flexural Vibrations of Sandwich Plates in Plain Strain," J. Appl. Mech., Vol. 27, pp. 535-540, 1960.
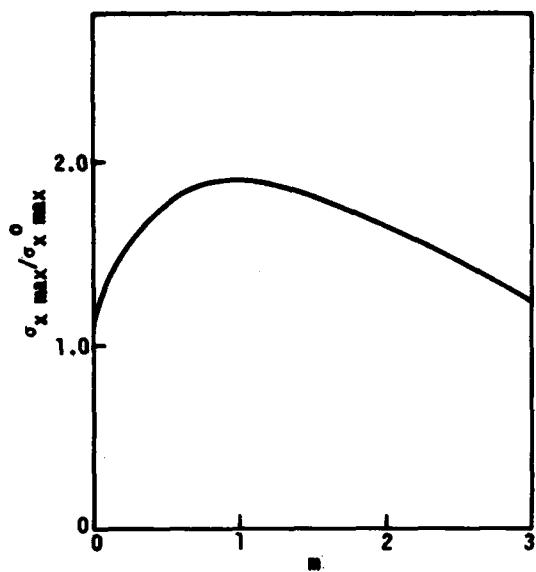
Figure 1. Plot of $\sigma_{x\,max}/\sigma_{x\,max}^{0}$ as a function of the thickness ratio m
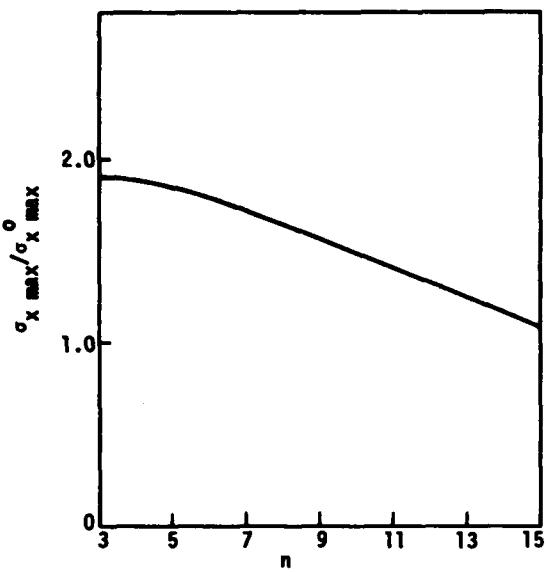
Figure 2. Plot of $\sigma_{x\,max}/\sigma_{x\,max}^{0}$ as a function of number of layers n (cross-ply)
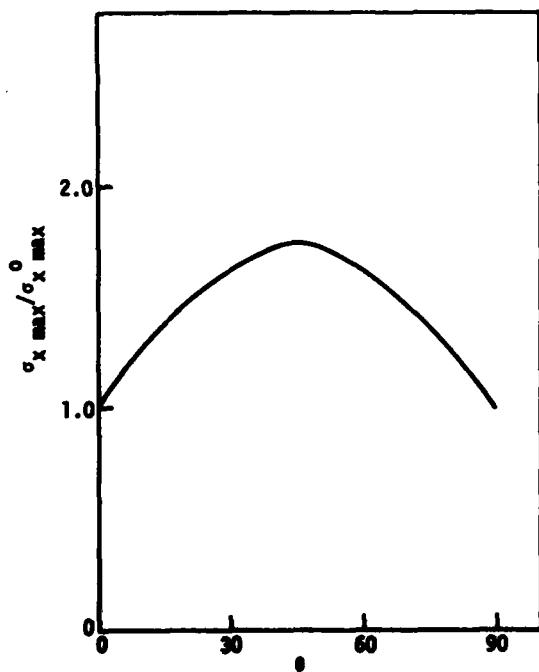
Figure 3. Plot of $\sigma_{x\,max}/\sigma_{x\,max}^{0}$ as a function of lamination angle θ
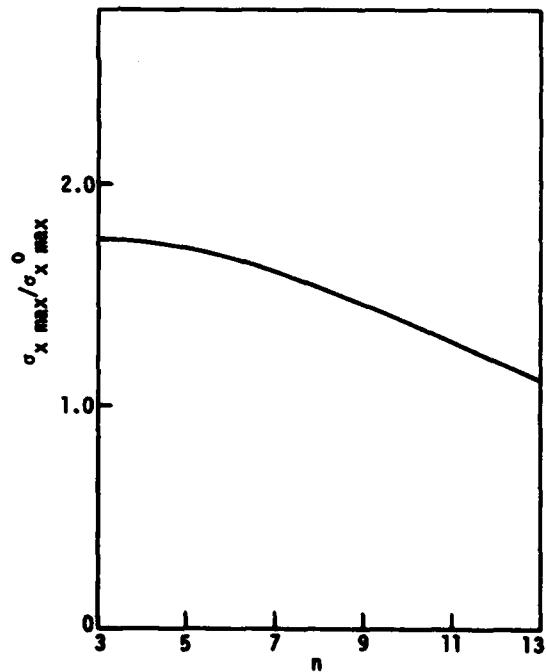
Figure 4. Plot of $\sigma_{x\,max}/\sigma_{x\,max}^{0}$ as a function of number of layers n (angle-ply)

VIBRATION OF COMPOSITE PLATES OF ARBITRARY SHAPE BY

THE METHOD OF CONSTANT DEFLECTION LINES

S. Dharmarajan

Fang Hui Chou
School of Engineering
San Diego State University
San Diego, CA 92182

Although problems of vibrations of composite plates have received
considerable attention in recent years, there are relatively few
exact solutions known. Most of the solutions available to compute
natural frequencies of composite plates are of Rayleigh-Ritz type
analysis and mostly computer oriented. The present paper pre-
sents a convenient method for the treatment of transverse vibra-
tion of composite plates and for approximate computation of the
fundamental frequency of composite plates of arbitrary shape.
It is shown that the method of constant deflection lines appears
to be a powerful tool for the investigation of those vibration
problems which could not be solved by conventional methods. As an
illustration of the method, the problem of the clamped and simply
supported elliptical composite plate is discussed. For various
composite materials the fundamental frequency of vibration is com-
puted.

INTRODUCTION

More and more composite materials are
used for structural components on which the
primary loading may be dynamic in nature. In
such cases, it is imperative that the natural
frequencies of the components be computed.
One of the common structural applications of
composite materials is in constructing plate
elements. Although problems of vibrations of
thin composite plates have received consider-
able attention in recent years, there are
relatively few exact solutions known. The
general methods of finding fundamental fre-
quencies are well developed. However, there
is considerable labor involved in carrying
out the details of the solution for any given
problem. An approximate method which has
found wide application recently is based on
Rayleigh-Ritz type analysis utilizing beam
function [1]. This analysis is computer
oriented.

THEORY

Derivation of Governing Differential Equation

Recently the authors presented a general
method of solving buckling of composite plates
by the method of deflection [2]. The
problem is approached through consider-
ations of determining the correct equa-
tion of lines of equal deflection under
various boundary conditions. This
approach makes it easy to arrive at a
general method as applied to plates of
any given geometric shape. Mazumdar [3]
has utilized the concept of lines of
equal deflection for solving vibration
problems of isotropic plates of arbi-
trary shape. When an elastic plate is
bent under time dependent external load,
the deflection surface of the plate may
be described by a family of curves called
lines of equal deflection. It is pos-
sible to determine equation of such lines
of equal deflection.

In this paper the constant deflection
method is generalized to compute the fun-
damental frequency of composite plates
of arbitrary shape. When a plate vibrates
in a normal mode, the deflected form of
the plate at any instant, τ, may be des-
cribed by a family of lines of equal
deflection and may be written as

$$w(x,y,\tau) = W \cos(\omega\tau + \epsilon) \qquad (1)$$

where ω is the circular frequency and W is the normal function determining the form of the deflected surface of the vibrating plate which is a suitable function of u, where $u(x,y) = $ constant is the equation of the of equal deflection.

The application of D'Alembert's principle and the summing of forces in the vertical direction of a portion of the plate bounded by a closed contour $u(x,y) = $ constant at any instant τ yield the following dynamical equation:

$$\oint \left[Qn - \frac{\partial Mnt}{\partial s} \right] ds + \iint_\Omega \rho h \frac{\partial^2 w}{\partial \tau^2}\, d\Omega = 0 \qquad (2)$$

In equation (2), the contour integral is taken around the closed path $u = $ constant and the double integral is over the region bounded by the closed contour. Substituting the expressions for Qn and Mnt in terms of w and making use of equation (1), one obtains the dynamical equation for the free lateral vibration of the composite plate in the form

$$\frac{d^3 W}{du^3} \oint Rds + \frac{d^2 W}{du^2} \oint Fds + \frac{dW}{du} \oint$$

$$Gds - \rho h \omega^2 \iint_\Omega Wd\Omega = 0 \qquad (3)$$

where R, F, and G are functions of u, and are functions of the elastic constants of the composite plate. These quantities are given in Ref. [2] as well as listed in Appendix. Now the problem of finding the fundamental frequency of a composite plate reduces to solving the integro-differential equation (3).

BOUNDARY CONDITIONS

Clamped Edge

Along a clamped edge the deflection and slope normal to the boundary are zero, so that

$$W \Big|_{u=0} = 0 \quad \frac{\partial W}{\partial n}\Big|_{u=0} = 0 \qquad (4)$$

Simply Supported Edge

Along a simply supported edge the deflection and moment, M_n, are zero, that is

$$W \Big|_{u=0} = 0, \quad P \frac{d^2 W}{du^2} + Q\frac{dW}{du}\Big|_{u=0} = 0 \qquad (5)$$

where P and Q are elastic constants in the Appendix.

SOLUTION TECHNIQUE

We can see now that the lines of deflection method to composite vibration problems reduces to the third order differential equation in W given by equation (3), subject to the boundary conditions given by equations (4) and (5). If the exact equation of the line of equal deflection is not known, a reasonable approximate expression for $u(x,y)$ may be assumed in the form

$$u(x,y) = \Phi(x,y) \sum_{\substack{m=0 \\ n=0}}^{m,n} A_{mn}x^m y^n \qquad (6)$$

Where m and n are integers, the coefficients A_{mn} can be interpreted as coordinates which determine the form of the deflection surface, and $\Phi(x,y) = 0$ represents the boundary of the plate. The function is different from zero within the region of the plate.

FUNDAMENTAL FREQUENCY OF ELLIPTICAL PLATES

Figure 1 shows an elliptical composite plate of major and minor axes of $2a$ and $2b$, respectively. The equation of the boundary of the plate is

$$1 - \frac{x^2}{a^2} - \frac{y^2}{b^2} = 0$$
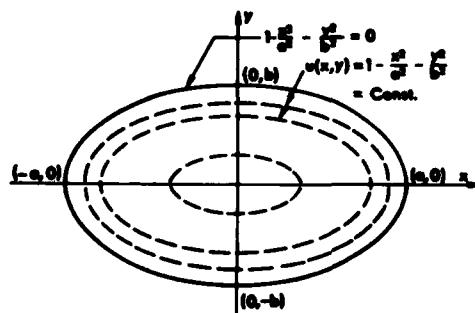
FIG. 1 ELLIPTICAL PLATE AND LINES OF EQUAL DEFLECTION

If we are interested in computing the fundamental frequency of this plate, the equation of lines of equal deflection may be taken as

$$u(x,y) = 1 - \frac{x^2}{a^2} - \frac{y^2}{b^2} \tag{7}$$

Substituting equation (7) into equation (A1) - (A3), R, F, and G are computed as

$$R = \frac{-8}{P}\left[\frac{D_{11}}{a^8}x^4 + D_{22}\frac{y^4}{b^8}\right.$$

$$\left. + 2(D_{12} + 2D_{66})\frac{x^2y^2}{a^4b^4}\right] \tag{8}$$

$$F = 4p^5\left\{\frac{D_{11}}{a^6}\left[\frac{3x^6}{a^8} + \frac{6x^2y^4}{b^8} + \frac{7x^4y^2}{a^4b^4}\right.\right.$$

$$\left. - \frac{x^6}{a^6b^2} + \frac{x^2y^2}{a^2b^6}\right] + \frac{D_{22}}{b^6}\left[\frac{6x^4y^2}{a^8}\right.$$

$$\left. + \frac{3y^6}{b^8} + \frac{7x^2y^4}{a^4b^4} - \frac{y^6}{a^2b^6} + \frac{x^2y^4}{a^6b^2}\right]$$

$$+ 2\frac{(D_{12} + 2D_{66})}{a^2b^2}\left[\frac{x^6}{a^{10}} + \frac{y^6}{b^{10}}\right.$$

$$\left.\left. - \frac{x^4y^2}{a^4b^6} - \frac{x^2y^4}{a^6b^4}\right]\right\} \tag{9}$$

$$G = \frac{-2p^5}{a^2b^2}\left\{\frac{D_{11}}{a^2}\left[\frac{y^4}{b^6} - \frac{x^4}{a^6} - \frac{x^2y^2}{a^4b^2}\right.\right.$$

$$\left. + \frac{x^2y^2}{a^2b^4}\right] + \frac{D_{22}}{b^2}\left[\frac{x^4}{a^6} - \frac{y^4}{b^6} + \frac{x^2y^2}{a^4b^2}\right.$$

$$\left. - \frac{x^2y^2}{a^2b^4}\right] + D_{12}\left[x^4\left(\frac{1}{a^8} - \frac{1}{a^6b^2}\right)\right.$$

$$\left.\left. + y^4\left(\frac{1}{b^8} - \frac{1}{a^2b^6}\right) + \frac{x^2y^2}{a^2b^2}\left(\frac{1}{a^2} - \frac{1}{b^2}\right)\right]\right\} \tag{10}$$

$$p^2 = \frac{1}{\frac{x^2}{a^4} + \frac{y^2}{b^4}} \tag{11}$$

where D_{ij}'s are composite plate stiffnesses and are defined in the Appendix substituting equations (8), (9), (10), and (11) into equation (3) and carrying out the integrations one obtains

$$(1-u)^2\frac{d^3W}{du^3} - 2(1-u)\frac{d^2W}{du^2} +$$

$$\frac{ph\omega^2a^3b^3}{2\pi\left[3D_{11}b^4 + 3D_{22}a^4 + 2(D_{12} + 2D_{66})a^2b^2\right]}\iint_\Omega W d\Omega$$

$$= 0 \tag{12}$$

The double integral in equation (12) may be simplified in a manner similar to that given in Reference [3] by taking a differential area between two curves at u_0 and $u_0 - du_0$. This results in

$$\iint_\Omega W(u)d\Omega = -\pi ab\int_1^u W(u_0)du_0 \tag{13}$$

Substituting equation (13) into (12) and differentiating with respect to u, a fourth order ordinary differential equation is obtained.

$$(1-u)^2\frac{d^4W}{du^4} - 4(1-u)\frac{d^3W}{du^3} + 2\frac{d^2W}{du^2} - \lambda^2W = 0 \tag{14}$$

where

$$\lambda^2 = \frac{a^4b^4ph\omega^2}{2\left[3D_{11}b^4 + 3D_{22}a^4 + 2(D_{12} + 2D_{66})a^2b^2\right]} \tag{15}$$

In order to facilitate the solution, the equation (14) may be written as

$$\left[(1-u)\frac{d^2}{du^2} - \frac{d}{du}\right]\left[(1-u)\frac{d^2}{du^2} - \frac{d}{du}\right]W - \lambda^2W = 0 \tag{16}$$

Introducing an operator

$$L \equiv (1-u)\frac{d^2}{du^2} - \frac{d}{du} \tag{17}$$

and a new independent variable, f,

$$1-u = f^2 \tag{18}$$

and assuming the general solution to be

$$W = w_1 + w_2 \tag{19}$$

equation (16) may be written as

$$f\frac{d^2w_1}{df^2} + \frac{dw_1}{df} + 4\lambda fw_1 = 0 \tag{20}$$

$$f\frac{d^2w_2}{df^2} + \frac{dw_2}{df} - 4\lambda fw_2 = 0 \tag{21}$$

The solutions of equations (20) and (21) are

$$w_1 = A\, J_0(kf) + B\, Y_0(kf) \tag{22}$$

$$w_2 = C\, I_0(kf) + D\, K_0(kf) \tag{23}$$

where J_0 and Y_0 are Bessell functions of the first and second kinds, respectively, I_0 and K_0 are modified Bessel functions of the first and second kinds, and

$$k^2 = 4\lambda \tag{24}$$

Therefore,

$$W = A\, J_0(kf) + B\, Y_0(kf) + C\, I_0(kf) + D\, K_0(kf) \tag{25}$$

Case L Clamped Elliptical Plate

For the clamped edges the boundary conditions are given by,

$$W\Big|_{u=0} = W\Big|_{f=1} = 0 \quad \frac{dW}{du}\Big|_{u=0} = \frac{dW}{df}\Big|_{f=1} = 0 \tag{26}$$

For finite deflection at the center of the plate,

$$B = D = 0 \tag{27}$$

Substitution of equations (26) and (27) into equation (25) results in homogeneous equations and nontrivial solution is obtained by setting the determinant of the coefficients of A and C equal to zero. That is

$$\begin{vmatrix} J_0(k) & I_0(k) \\ J_0'(k) & I_0'(k) \end{vmatrix} = 0 \tag{28}$$

where the prime denotes derivative with respect to the argument.

From equation (28) the frequency equation is obtained as

$$J_0(k)\ I_0'(k) - I_0(k)\ J_0'(k) = 0 \tag{29}$$

Now using

$$I_0'(k) = I_1(k)$$
$$J_0'(k) = -J_1(k) \tag{30}$$

equation (29) becomes

$$J_0(k)\ I_1(k) + I_0(k)\ J_1(k) = 0 \tag{31}$$

the first root of equation (31) is obtained as

$$k = 3.1961$$

Now defining a frequency parameter,

$$\Omega = \omega a^2 \left(\frac{\rho h}{D_{11}}\right)^{1/2}$$

$$= k^2 \left[\frac{3}{8} + \frac{3\delta^4 D_{22}}{8\, D_{11}} + \frac{2\delta^2(D_{12} + 2D_{66})}{8\, D_{11}}\right]^{1/2} \tag{32}$$

where

$$\delta = {}^a/_b$$

numerical values of the frequency are obtained for Boron-Aluminum composite plates for various values of δ and plate thickness as shown in Table 1.

Table 1

Frequency parameters $\Omega = \omega a^2 (\rho h/d_{11})^{1/2}$ for a clamped Boron-Aluminum plate having semi-axes a and b.

δ	1	1.1	1.2	1.3	1.5	2	3	5
25% Boron	8.711	9.488	10.396	11.433	13.890	22.125	46.801	126.990
50% Boron	8.564	9.302	10.165	11.156	13.508	21.430	45.240	122.710

and the stiffnesses D_{ij}'s for several Boron Aluminum composite plates are given in Table 1-a.

Table 1-a

Stiffness for Boron-Aluminum composite plates

	D_{11}	D_{22}	D_{12}	D_{66}
25% Boron, h=0.019 in.	12.785	8.261	2.301	3.321
25% Boron, h=0.025 in.	29.126	18.819	5.243	7.565
50% Boron, h=0.019 in.	19.300	11.646	2.895	4.950
50% Boron, h=0.025 in.	43.967	26.525	6.595	11.272

Case 2 Simply Supported Elliptical Plate

For simply supported edges the boundary conditions become

$$W\Big|_{u=0} = W\Big|_{f=1} = 0 \tag{33}$$

$$Mn = P\frac{d^2W}{du^2} + Q\frac{dW}{du}\Big|_{u=0} = 0 \tag{34}$$

for elliptical plate P and Q are functions of elastic constants, x and y. The boundary condition given by equation (34) may be satisfied only approximately by taking the average values of P and Q at $(\pm a\sqrt{1-u}, o)$ and $(0, \pm b\sqrt{1-u})$. These values are

$$P_{ave.} = -2(1-u) \left(\frac{D_{11}}{a^2} + \frac{D_{22}}{b^2}\right) \tag{35}$$

$$Q_{ave.} = \frac{D_{11}}{a^2} + \frac{D_{22}}{b^2} + D_{12} \left(\frac{1}{a^2} + \frac{1}{b^2}\right) \tag{36}$$

If we let

$$\mu = \frac{D_{12}(1 + \delta^2)}{D_{11} + D_{22}\delta^2} \tag{37}$$

then equation (34) reduces to

$$(1-u) \frac{d^2W}{du^2} - \frac{1 + \mu}{2} \frac{dW}{du}\Big|_{u=0} = 0 \tag{38}$$

or

$$\frac{d^2W}{df^2} + \frac{\mu}{f} \frac{dW}{df}\Big|_{f=1} = 0 \tag{39}$$

Substituting equations (33) and (39) and requiring the deflection is finite at the

center, one obtains two homogeneous equations. The condition of nontrivial solution leads to the following frequency equation.

$$\frac{J_1(k)}{J_0(k)} + \frac{I_1(k)}{I_0(k)} = \frac{2k}{1-\mu} \qquad (40)$$

Numerical values of the frequency are obtained for Boron-Aluminum plates of same properties as Case 1 and are listed in Table 2.

Table 2

Frequency parameter $\Omega = \omega a^2 (\rho h/D_{11})^{1/2}$ for a simply-supported Boron-Aluminum plate having semi-axes a and b

δ	1	1.1	1.2	1.3	1.5	2	3	5
25% Boron	4.092	4.474	4.910	5.410	6.605	10.511	22.376	60.719
50% Boron	3.990	4.329	4.770	5.231	6.342	10.016	21.435	58.142

and the stiffnesses for Boron-Aluminum composite plates are given in Table 1-a.

CONCLUSION

An approximate method to determine the fundamental frequency of vibration of composite plates of arbitrary shape has been outlined by generalizing the lines of equal deflection method of Reference [3]. As far as the authors know, no closed form solutions to determine the fundamental frequency of composite elliptical plates are available. The simplicity of the general method is shown in solving clamped and simply supported elliptical plates.

REFERENCES

1. J.E. Ashton, and J.M. Whitney. "Theory of Laminated Plates," Technomic Publishing Co., Westport, Conn., 1970.

2. S. Dharmarajan, F.H. Chou, and N.A. Hussian. "Buckling of Composite Plates of Arbitrary Shape," Proceedings of 21st National Sampe Meeting at Los Angeles, 1976.

3. J. Mazumbar. "Transverse Vibration of Elastic Plates by the Method of Constant Deflection Lines," Journal of Sound and Vibration, Vol. 18, pp. 147-155, 1971.

APPENDIX

In order not to clutter the central body of the paper with too many equations, some of them are listed in the Appendix.

$$R = -\frac{1}{t^{1/2}} \left\{ D_{11} u_{,x}^5 + D_{22} u_{,y}^5 \right.$$

$$\left. + 2(D_{12} + 2D_{66})\ u_{,x}^2 u_{,y}^3 \right\} \tag{A1}$$

$$F = -\frac{1}{t^{5/2}} \left\{ D_{11}\ [3u_{,x}^5 u_{,xx} \right.$$

$$+ 6u_{,x}^2 u_{,xx}^5 + 7u_{,x}^4 u_{,y}^2 u_{,xx}$$

$$- u_{,x}^6 u_{,yy} - 4u_{,x}^3 u_{,y}^3 u_{,xy}$$

$$+ u_{,x}^4 u_{,y}^2 u_{,yy}] + D_{22} [6u_{,y}^2 u_{,x}^4 u_{,yy}$$

$$+ 3u_{,y}^6 u_{,yy} + 7u_{,x}^2 u_{,y}^4 u_{,yy} - u_{,y}^6 u_{,xx}$$

$$- 4u_{,x}^3 u_{,y}^3 u_{,xy} + u_{,x}^2 u_{,y}^4 u_{,xx}]$$

$$+ (D_{12} + 2D_{66})\ [2u_{,x}^6 u_{,yy} + 4u_{,x}^5 u_{,y} u_{,xy}$$

$$+ 4u_{,x} u_{,y}^5 u_{,xy} + 16u_{,x}^3 u_{,y}^3 u_{,xy}$$

$$+ 2u_{,xx} u_{,y}^6 - 2u_{,x}^2 u_{,y}^4 u_{,xx}$$

$$- 2u_{,x}^4 u_{,y}^2 u_{,yy}] \right\} \tag{A2}$$

$$G = -\frac{1}{t^{5/2}} \left\{ D_{11}\ [u_{,x}^5 u_{,xxx} \right.$$

$$+ 2u_{,x} u_{,y}^4 u_{,xxx} + 3u_{,x}^3 u_{,y}^2 u_{,xxx}$$

$$+ u_{,y}^4 u_{,xx}^2 - u_{,x}^4 u_{,yy} u_{,xx}$$

$$- u_{,x}^4 u_{,y} u_{,xxy}$$

$$- u_{,x}^2 u_{,y}^3 u_{,xxy} - u_{,x}^2 u_{,y}^2 u_{,xx}^2$$

$$- 2u_{,x} u_{,y}^3 u_{,xx} u_{,xy} + 2u_{,x}^3 u_{,y} u_{,xx} u_{,xy}$$

$$+ u_{,x}^2 u_{,y}^2 u_{,xx} u_{,yy}] + D_{22}\ [u_{,y}^5 u_{,yyy}$$

$$+ 2u_{,x}^4 u_{,y} u_{,yyy} + 3u_{,x}^2 u_{,y}^3 u_{,yyy}$$

$$- u_{,y}^4 u_{,xx} u_{,yy} - u_{,x}^2 u_{,y}^2 u_{,xyy}$$

$$- u_{,x} u_{,y}^4 u_{,xyy} + u_{,x}^4 u_{,yy}^2$$

$$+ u_{,x}^2 u_{,y}^2 u_{,xx} u_{,yy} + 2u_{,x} u_{,y}^3 u_{,yy} u_{,xy}$$

$$- 2u_{,x}^3 u_{,y} u_{,yy} u_{,xy} - u_{,x}^2 u_{,y}^2 u_{,yy}^2]$$

$$+ 2D_{66}\ [2u_{,x}^5 u_{,xyy}\qquad + u_{,x} u_{,y}^4 u_{,xyy}$$

$$+ 2u_{,x}^3 u_{,y}^2 u_{,xyy} + 2u_{,y}^5 u_{,xxy}$$

$$+ 2u_{,x}^2 u_{,y}^3 u_{,xxy} - 4u_{,x} u_{,y}^3 u_{,xx} u_{,xy}$$

$$+ 8u_{,x}^2 u_{,y}^2 u_{,xy}^2 - 4u_{,x}^3 u_{,y} u_{,xy} u_{,yy}$$

$$- u_{,x} u_{,y}^4 u_{,xyy}] + D_{12}\ [u_{,x}^5 u_{,xyy}$$

$$+ u_{,x} u_{,y}^4 u_{,xyy} + 2u_{,x}^3 u_{,y}^2 u_{,xyy}$$

$$+ 2u_{,x}^4 u_{,y} u_{,xxy} + u_{,y}^5 u_{,xyy}$$

$$+ 3u_{,x}^2 u_{,y}^3 u_{,xyy} - u_{,y}^4 u_{,xx}^2$$

$$- u_{,x}^3 u_{,y}^2 u_{,xxx} - u_{,x} u_{,y}^4 u_{,xxx}$$

$$+ u_{,yy} u_{,xx} (u_{,x}^4 + u_{,y}^4) + u_{,x}^3 u_{,y}^2 u_{,xyy}$$

$$- u_{,x}^4 u_{,y} u_{,yyy} - u_{,x}^2 u_{,y}^3 u_{,yyy}$$

$$+ u_{,x}^2 u_{,y}^2 (u_{,xx} - u_{,yy})^2$$

$$+ 2u_{,x} u_{,y}^3 u_{,xy}(u_{,xx} - u_{,yy})$$

$$+ 2u_{,x}^3 u_{,y} u_{,xy}(u_{,yy} - u_{,xx}) \right\} \tag{A3}$$

$$P = -\frac{1}{t}\ [D_{11} u_{,x}^4 + 2(D_{12} + 2D_{66}) u_{,x}^2 u_{,y}^2$$

$$+ D_{22} u_{,y}^4] \tag{A4}$$

$$Q = -\frac{1}{t}\ [D_{11} u_{,x}^2 u_{,xx} + D_{12}(u_{,x}^2 u_{,yy} + u_{,y}^2 u_{,xx})$$

$$+ D_{22}u^2_{,y}u_{,yy} + 4D_{66}u_{,x}u_{,y}u_{,xy}] \qquad (A5)$$

The stiffness quantities are defined with reference to Fig. 2 as,

$$D_{ij} = \frac{1}{3}\sum_{k=1}^{N} (Q_{ij})_k \; (Z^3_k - Z^3_{k-1}) \qquad (A6)$$

where,

$$(Q_{11})k = \left[\frac{\dot{E}_\ell}{1-\nu_\ell\, \nu_{t\ell}}\right]_k$$

$$(Q_{12})_k = \left[\frac{\nu_{12}E_t}{1-\nu_{\ell t}\nu_{t\ell}}\right]_k$$

$$(Q_{22})_k = \left[\frac{E_t}{1-\nu_{\ell t}\nu_{t\ell}}\right]_k$$

$$(Q_{66})_k = \left[G_{\ell t}\right]_k \qquad (A7)$$

The subscript in equations A6 and A7 denotes layer number.
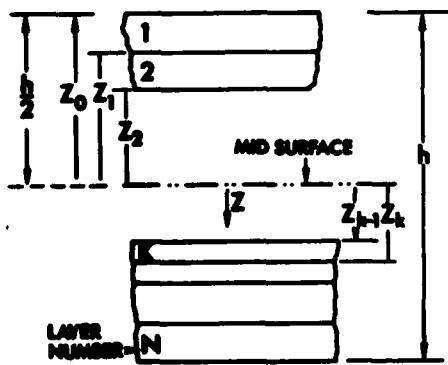
FIG. 2 GEOMETRY OF N-LAYERED LAMINATE

COUPLED VIBRATIONS OF TURBOMACHINE BLADES

J. S. Rao
Indian Institute of Technology
New Delhi-110029

Turbomachine blades are generally pre-twisted with asymmetric cross-section and mounted on a rotating disc at a stagger angle. The three coupled equations of the system in bending-bending torsion are solved by the use of Galerkin's method and the results obtained by a computer program are presented in graphical form with non-dimensional parameters. These nondimensional design charts will help in the design of turbomachine blades. The results obtained are checked with theoretical and experimental results available

INTRODUCTION

Turbomachines are commonly employed in electric power generating stations, marine drives, aircraft propulsion systems etc. Turbines used in electric utility industries may produce powers of the order of 1000 MW at fairly low speeds and those used in aircraft may produce relatively low powers but running at very high speeds of the order of 20,000 rpm.

From experience the failure of turbomachine blading is generally attributed to the fatigue that takes place at or near resonant conditions. In some of the big turbomachines 20,000 or more stationary and moving flexible blades may be employed and failure of any one of them will force a shut down which is very expensive. In the case of aircraft engines, the failure in addition to being expensive, will be catastrophic in nature. Hence determination of natural frequencies of turbomachine blades is an important process in the design of a turbomachine.

A turbomachine blade can be considered as a cantilever blade fixed at its base with an asymmetric aerofoil cross-section and pre-twisted from the fixed end to the free end. This blade is mounted on a rotating disc at a stagger angle. The pre-twist of the blade causes coupling in both the bending directions and the asymmetry of the cross-section makes the coupling further with the torsional motion of the blade. When the blade rotates the stagger angle also accounts for coupling between the two bending motions. The disc rotation causes centrifugal forces and the bending modes are stiffened.

Sometimes the blades are grouped together by a shroud at the end of the blades. Also sometimes the blades are laced at one or two intermediate locations of the blades. These effects are not considered in the present analysis. Higher order effects are also not considered in this analysis as the problem becomes more complex in nature.

For a single turbomachine blade, several researchers applied different methods to determine the natural frequencies and to obtain general information on this fairly vast subject a survey paper by the author [1] may be referred. A historic reference chart containing some important contributions is included in the work Banerji and Rao [2], who considered rotating blades with asymmetry in one plane and compared the theoretical results with experimental values. For small aspect ratio blades, plate or shell theories are to be used and reference may be

made to the work of Lalanne and others [3]. For laced and packeted blades, one may refer to the work of Stuwing [4] and Cottney and Ewins [5] who accounted the disc flexibility also.

This paper considers the coupled bending torsion vibration of pre-twisted blades with asymmetric cross-section mounted at a stagger angle on a rotating disc. The three coupled differential equations of motion are solved by using Galerkin's method and the results obtained are presented in graphical form with nondimensional parameters. Where possible, the results obtained from this program are compared with available theoretical and experimental values.

ANALYSIS

The governing differential equations of motion of a uniform pre-twisted cantilever with asymmetric cross-section mounted on a rotating disc at a stagger angle, neglecting higher order-effects such as shear deflections, rotary inertia, fibre bending, Cariolis accelerations, can be obtained from Cargnegie [6] and Rao and Rao [7]. These differential equations are three in number, and coupled in the two bending displacements x and y and torsional displacement θ and contain integral terms due to rotation effects.

To solve these equations, the well known Galerkin procedure is used. The shape functions for both bending displacements and torsional displacements are assumed according to those given in reference [2]. Differentiating these shape functions with respect to the coordinate distance measured along the length of the blade Z, substituting them in the differential equations and performing the required integrations, the errors in the differential equations can be found. These errors are orthogonalised with respect to the corresponding mode shapes, which leads to three sets of simultaneous algebraic equations, which in turn give the familiar eigen value problem.

The nondimensional eigen values of this problem are obtained from a computer program developed in Fortran IV, using QR transformation. A five term solution for each bending, bending and torsion modes, is found to give converged accurate values for the first three uncoupled modes of each motion. This five term solution is used to study the various effects such as, pre-twist, rotation, disc radius etc., on the nondimensional eigen values.

COMPARISON OF RESULTS

The results obtained from the program are compared with theoretical and experimental results available in the literature for the three cases given below, which account for all the parameters considered in the present work.

Case 1: Stationary pre-twisted blades

The following data is chosen to compare the coupled bending-bending modes and torsion modes of stationary pre-twisted blades with the results of Dawson [8] and Carnegie [10].

I_{xx} = 0.0000262027 in^4

I_{yy} = 0.00566667 in^4

A = 0.068 in^2

L = 6.0 in

ρ = 0.284 lb/in^3

E = 30.0 X 10^6 lb/in^2

G = 12.0 X 10^6 lb/in^2

γ = 45 deg.

The results are compared in Table 1. The bending frequencies are from the work of Dawson [8]. However, the first coupled mode value is taken from Carnegie [10] as Dawson's chart ignores the slight increase in this mode. The torsional frequencies are from Carnegie [10] without correction for fibre bending. The experimental values are reported by Carnegie [10].

Case 2: Stationary blades with asymmetric cross-section

The following data is chosen for comparison with existing results as shown in Table 2.

I_{xx} = 0.000084 in^4

I_{yy} = 0.006710 in^4

L = 6.0 in

A = 0.0914 in^2

ρ = 0.284 lb/in^3

r_x = 0.0076 in

r_y = 0.0470 in

Table 1
Comparison of pre-twisted blade natural frequencies, Hz.

S.No.	Present Results Bending Modes	Torsion Modes	Bending Modes [8]	Torsion modes [10]	Experimental Results [10]
1	61.9		62.0		59.0
2	305.0		301.0		290.0
3	949.0		953.0		920.0
4	1220.0		1230.0		1110.0
5		760.0		757.0	760.0
6		2279.0		2270.0	2300.0
7		3804.0		3750.0	3902.0

$E = 31.0 \times 10^6$ lb/in^2

$C = 0.3180168 \times 10^4$ lb in^2/rad

The analytical and experimental results are both from the work of Carnegie and Dawson [11].

Table 2
Comparison of asymmetric cross-section blade natural frequencies - Hz

Mode No.	Present Results	Analytical Process [11]	Experimental results [11]
1	96.5	96.9	97.0
2	604.9	606.5	610.0
3	842.0	841.2	790.0
4	1089.4	1072.9	1102.0
5	1694.9	1699.0	1693.0

Case 3: Rotating blades with asymmetric cross-section with 90 deg. stagger.

The following data is chosen to compare the results obtained by this program with the existing results as shown in Table 3.

$L = 8$ in

$A = 0.360$ in^2

$R = 6.0$ in

$r_x = 0.117$ in

$r_y = 0.0$ in

$\rho = 0.283$ lb/in^3

$I_{xx} = 0.002408$ in^4

$I_{yy} = 0.04887$ in^4

$E = 30 \times 10^6$ lb/in^2

$C = 1.1084 \times 10^5$ lb in^2/rad

$\omega = 3500$ rpm

$\phi = 90$ deg.

The analytical and experimental results are both from Banerji and Rao [2].

Table 3
Comparison of rotating blade natural frequencies - Hz

S.No.	Present results	Theoretical results [2]	Experimental results [2]
	Bending modes		
1.	169.9	170.0	165.0
2.	926.3	928.0	914.0
3.	2545.1	2550.0	2475.0
	Torsion modes		
4.	1695.4	1695.0	--
5.	5109.6	5108.0	--
6.	8510.2	8518.0	--

The results presented in Tables 1, 2 and 3 above show a good comparison with the existing results.

General nondimensional results:

With the help of the program developed, the effects of different parameters viz., speed of rotation, disc radius, pre-twist, asymmetry of the cross-section, and stagger angle, on the natural frequencies of a single turbomachine blade are studied and the results obtained in the nondimensional form are presented in Figs. 1 to 14. The results are discussed below.

Effect of rotation

The effect of nondimensional rotation parameter α^2 on the frequency parameter ratio λ_i/λ_3 for flapwise as well as chordwise modes in bending (i.e. y-z and x-z planes of bending respectively) are given in Figs. 1 and 2. The effect of rotation is pre-

dominant on the fundamental mode and more so on the flapwise modes. For all the modes, the frequency parameter ratio increases linearly with α^2. For chordwise modes, the effect of rotation on the frequency parameter ratio is less than that compared with the corresponding flapwise modes. There is no effect of rotation on the natural frequencies in torsional modes.
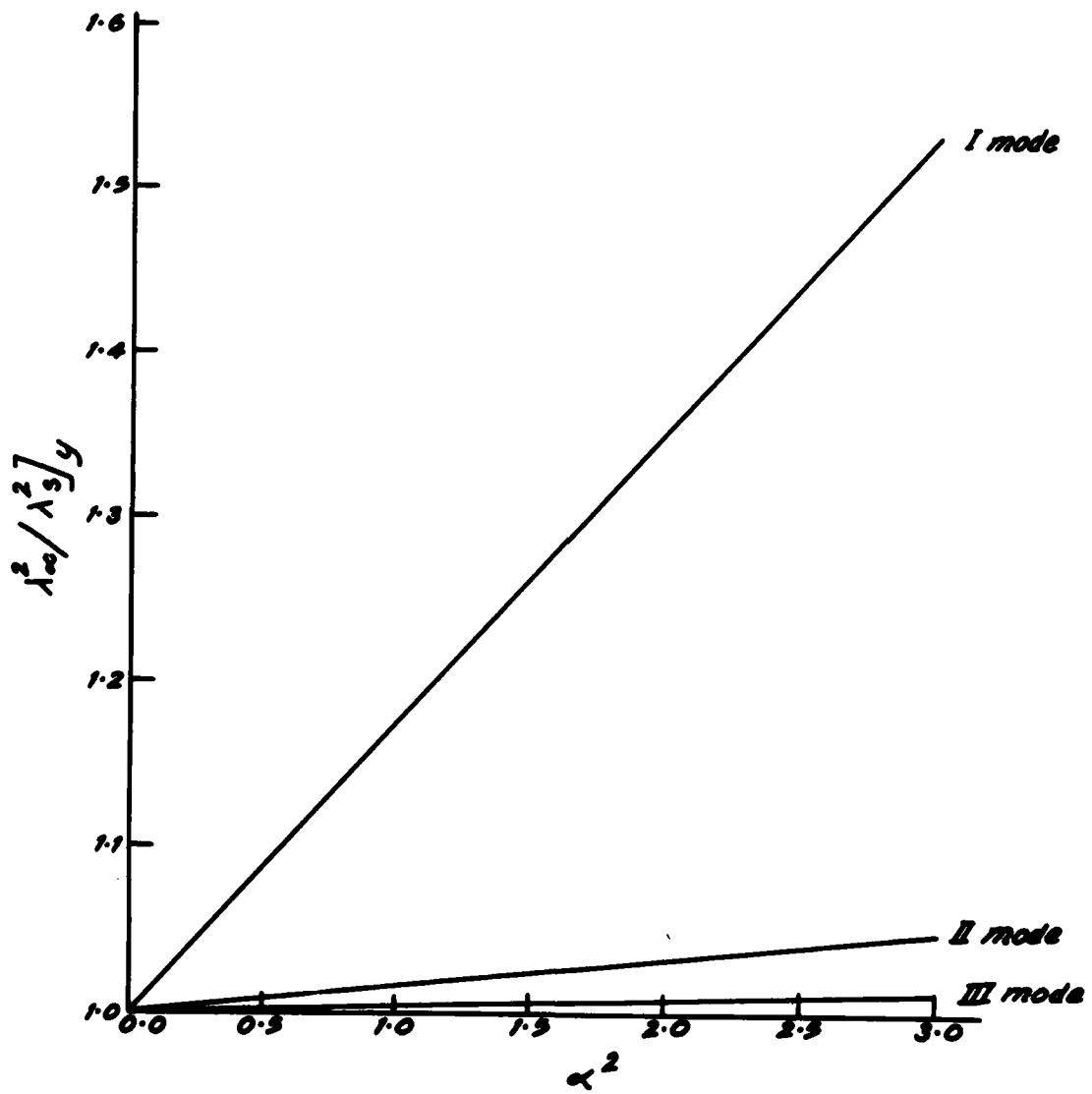

Fig.1: Effect of speed of rotation on frequency parameter ratio in flapwise bending
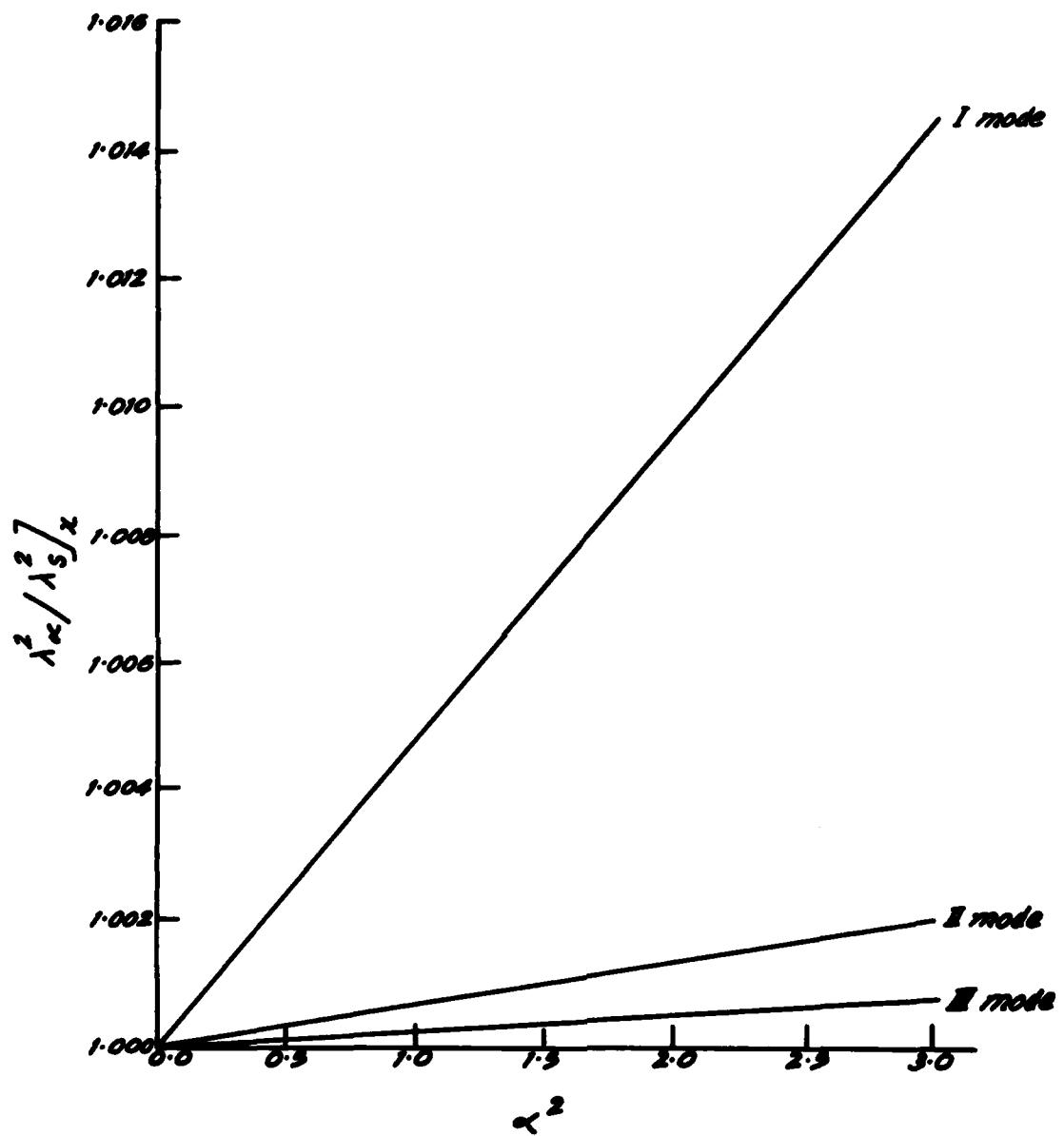
Fig.2: Effect of speed of rotation on frequency parameter ratio in chordwise bending

Effect of disc radius

The effect of nondimensional disc radius $\bar{R}$ on the frequency parameter ratio $\lambda_R^2/\lambda_\kappa^2$ is plotted in Figs.2 and 3 for both the flapwise and chordwise motions and for $\kappa = 1$, 2 and 3. The effect of disc radius is predominant on the fundamental mode, again having

a larger effect on the flapwise modes. For all the modes, the frequency parameter ratio increases linearly with $\bar{R}$, with a larger slope for larger value of α^2 in a given mode.
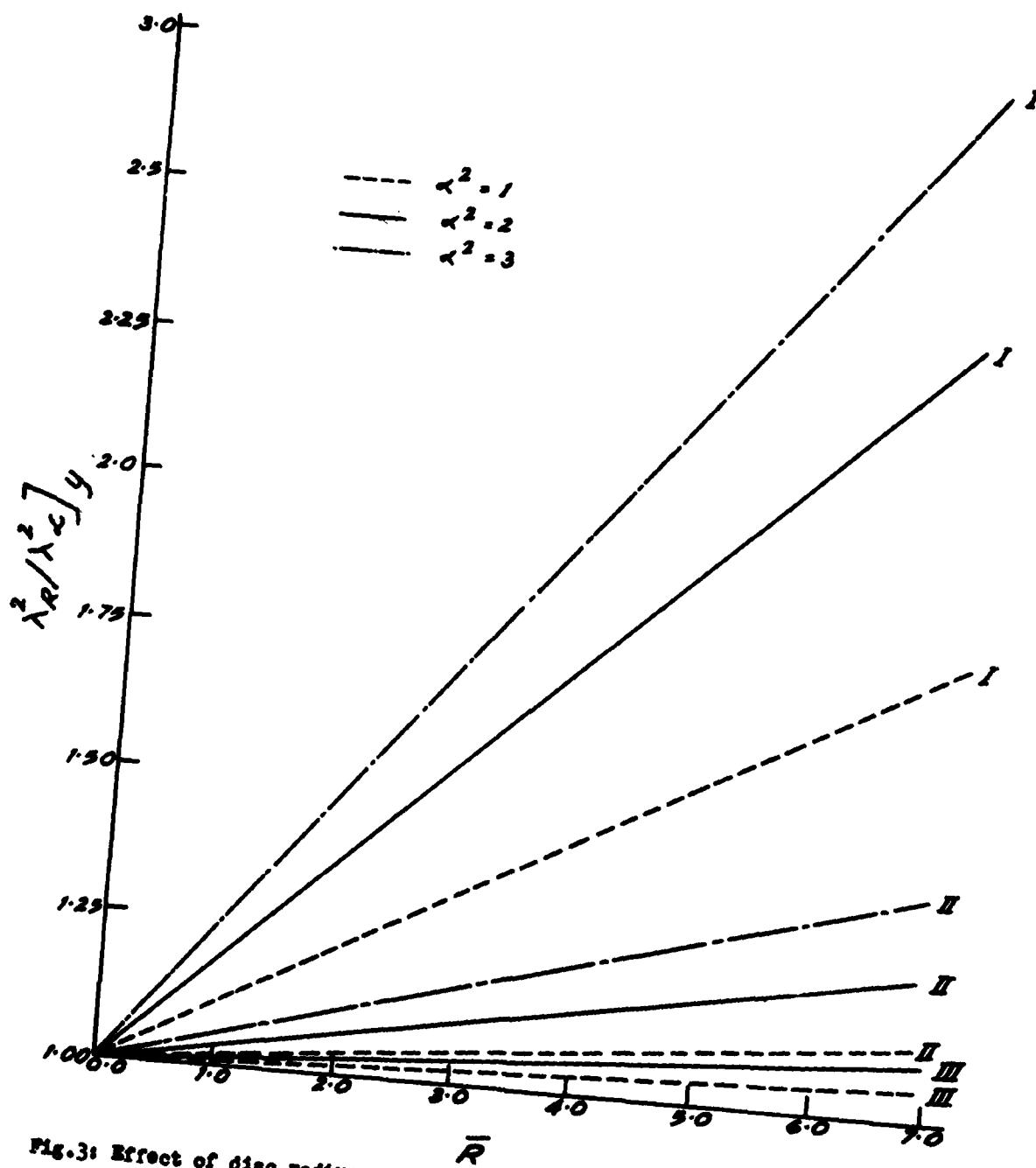
Fig.3: Effect of disc radius on frequency parameter ratio in flapwise bending.
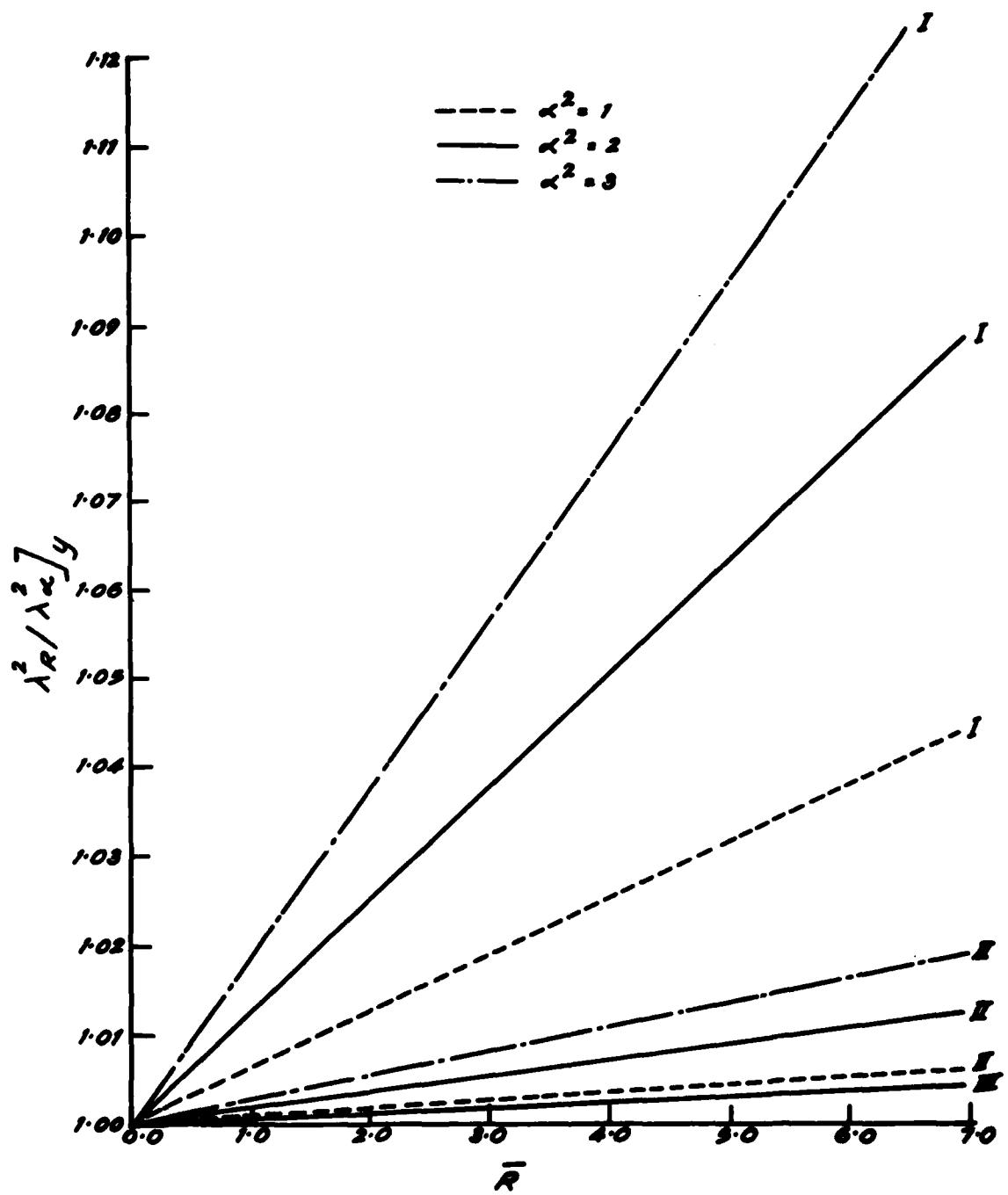
Fig.4: Effect of disc radius on frequency parameter ratio in chordwise bending.

113

Effect of pre-twist

The nondimensional frequency parameter ratio λ_y^2/λ_s^2, for the first four modes is plotted in Figs. 5 to 8 as a function of the nondimensional parameter $\bar{\hbar} = I_{yy}/I_{xx}$ for $\psi = 0.4$, 0.8 and 1.2 radians.

The effect is very small for the first mode in flapwise direction, which increases slightly as $\bar{\hbar}$ increases. This effect is more for larger pre-twists, as shown in Fig.5.

The second coupled mode is shown in Fig.6. For $\bar{\hbar}$ upto 39.3, the second coupled mode represents the first uncoupled chordwise mode, which decreases as $\bar{\hbar}$ increases, the effect
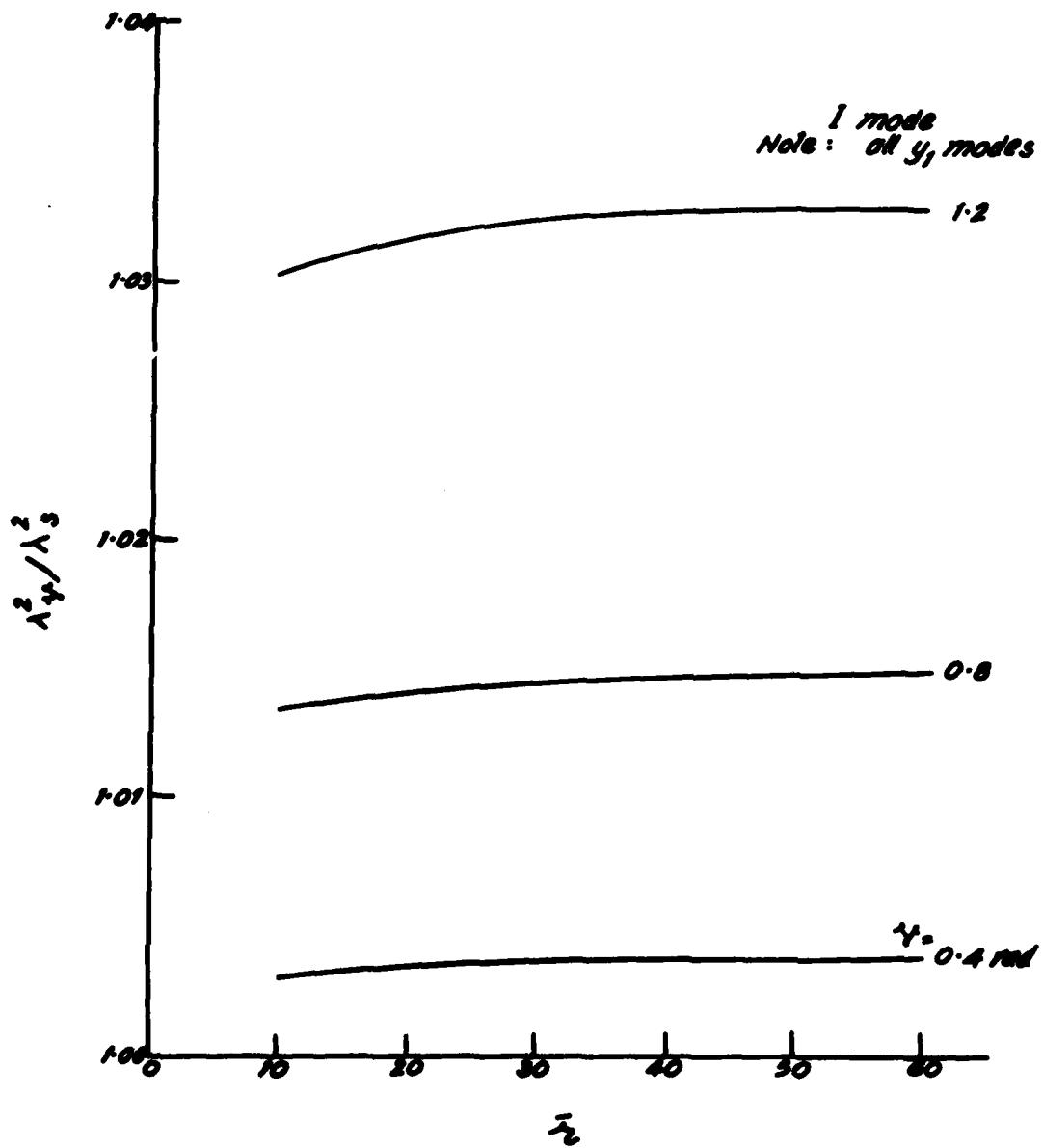
Fig.5: Effect of $\bar{\hbar}$ on frequency parameter ratio in first coupled mode for different pre-twists.

114

being more predominant for larger pre-twists. For $\hbar > 39.3$, the second coupled mode represents the uncoupled second flapwise mode and there is a small upward jump in the frequency parameter values at the transition value of $\hbar = 39.3$. In this region the coupled mode increases as $\hbar$ increases. For all $\hbar$, the second coupled mode represent- ing either first chordwise or second flapwise modes, is lesser than the corresponding uncoupled mode.

The third coupled mode is shown in Fig.7 and as before there is a transition at $\hbar = 39.3$. For $\hbar$ upto 39.3, the third coupled mode corresponds to the second uncoupled flapwise mode and
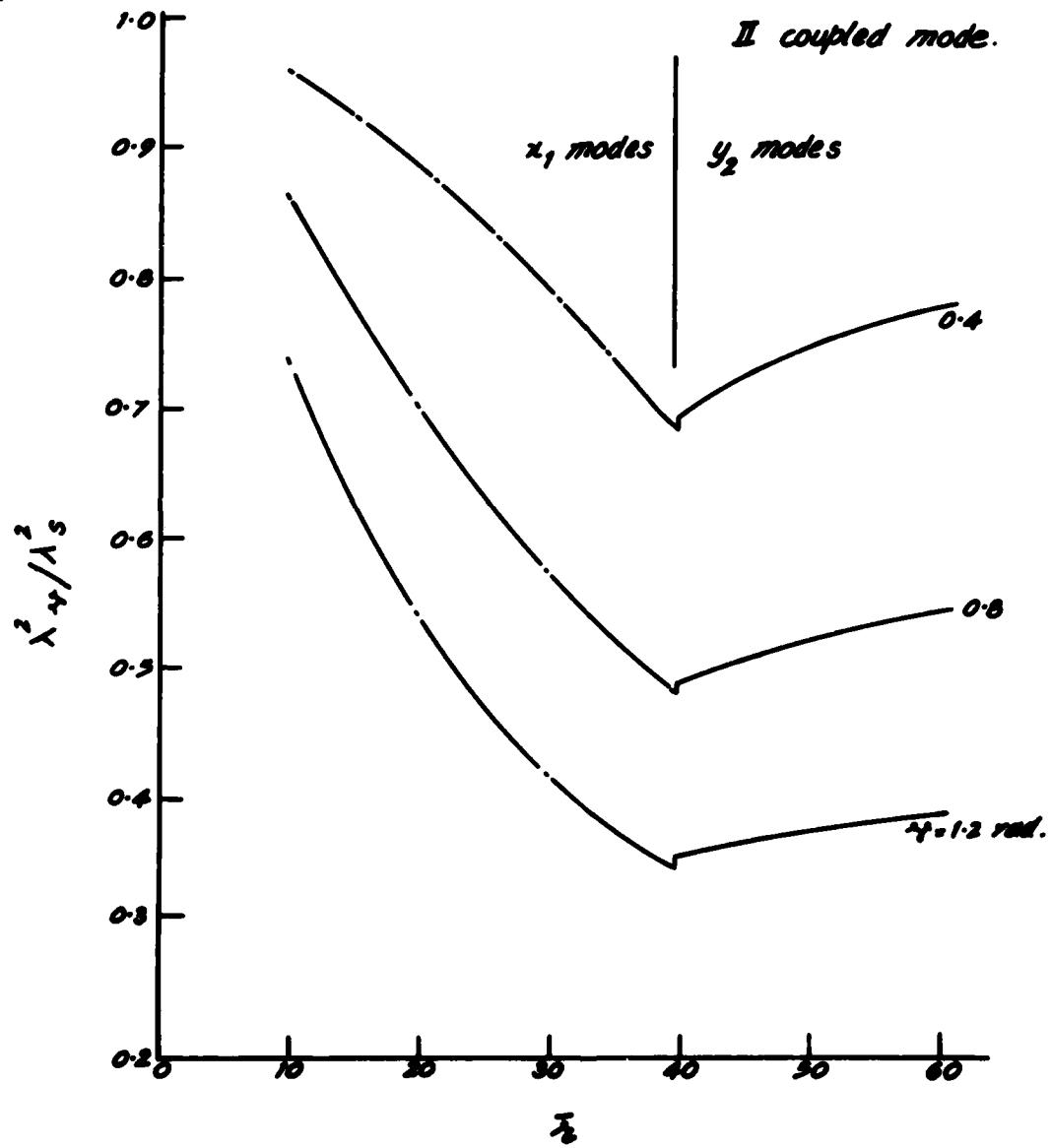
Fig.6: Effect of $\hbar$ on frequency parameter ratio in second coupled mode for different pre-twists.

increases as increases, the effect being more predominant for larger pre-twists. At the transition point, there is a small downward jump, and for $\lambda > 39.3$, this mode represents the first chordwise uncoupled mode, which
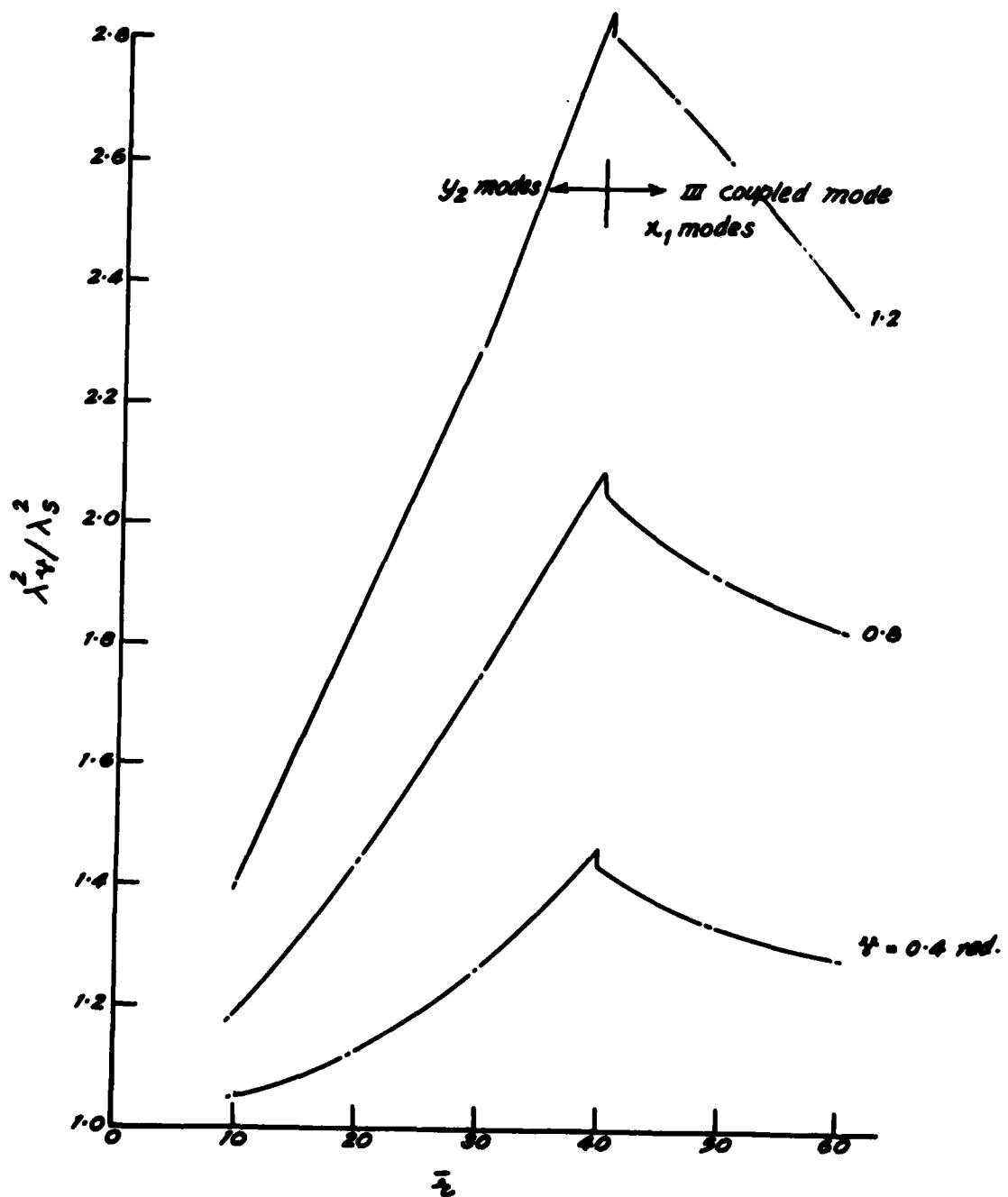
Fig.7: Effect of $\bar{n}$ on frequency parameter ratio in third coupled mode for different pre-twists.

decreases as $\bar{h}$ increases. However, for all $\bar{h}$, the third coupled mode is larger than the corresponding uncoupled modes. The transition that occurs at $\bar{h}$ =39.3 is due to the fact that the first chordwise frequency is lower than the second flapwise mode for $\bar{h}<$ 39.3, both are equal at $\bar{h}$ =39.3 and that the chordwise frequency is more than the flapwise frequency for $\bar{h}>$39.3.

The fourth coupled mode is shown in Fig.8, which for the region of $\bar{h}$ considered represents the third uncoupled flapwise mode. For $\bar{h}<$ 7.85 the fourth mode corresponds to the second chordwise mode and is not plotted in Fig.8, as in practice such small values of $\bar{h}$ do not occur. The fourth coupled mode increases as $\bar{h}$ increases, but is however less than
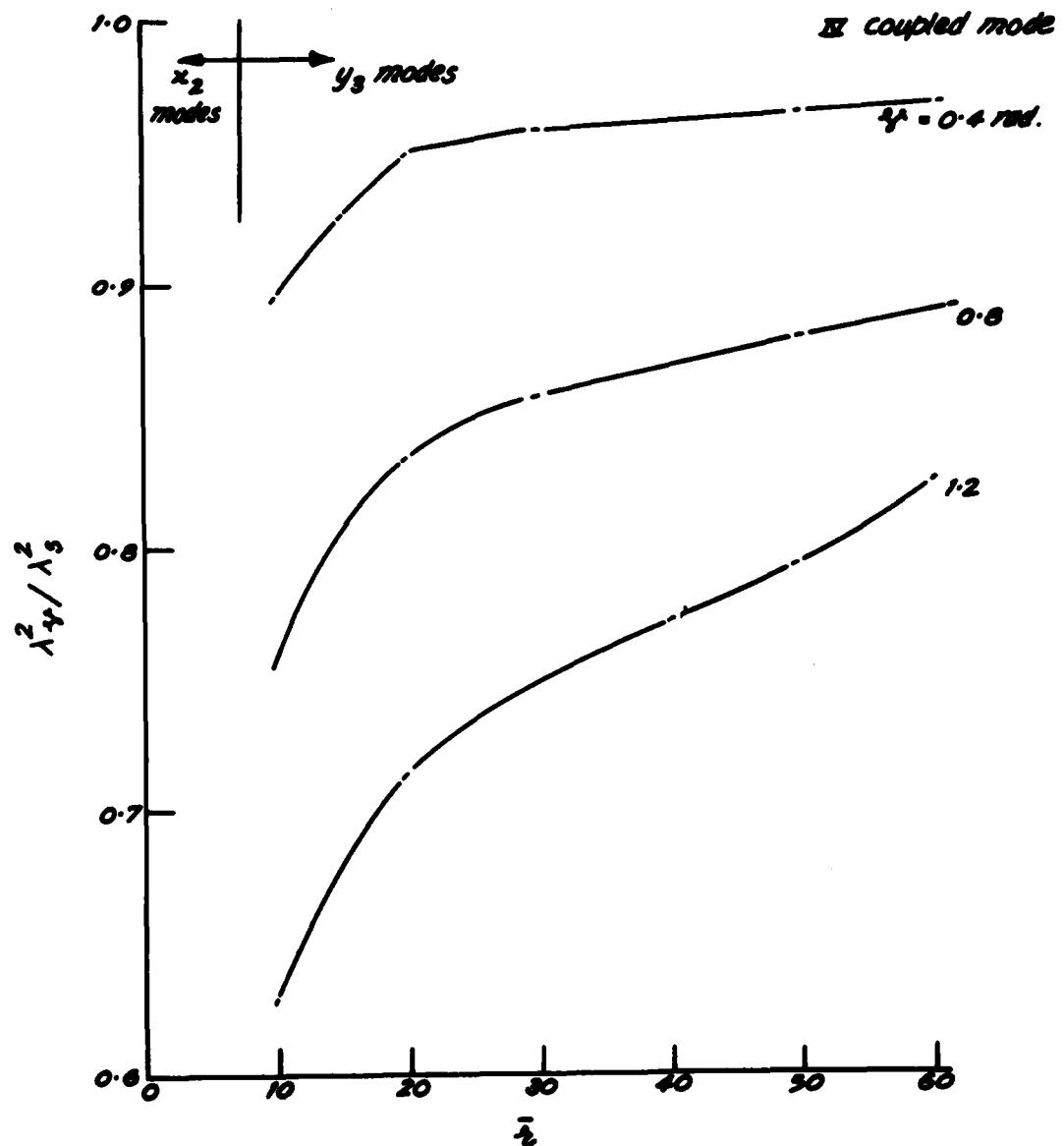
Fig.8: Effect of $\bar{h}$ on frequency parameter ratio in fourth coupled mode for different pre-twists.

the uncoupled third flapwise mode. For
a given $\bar{h}$, the frequency parameter
ratio is smaller for a larger pre-twist.
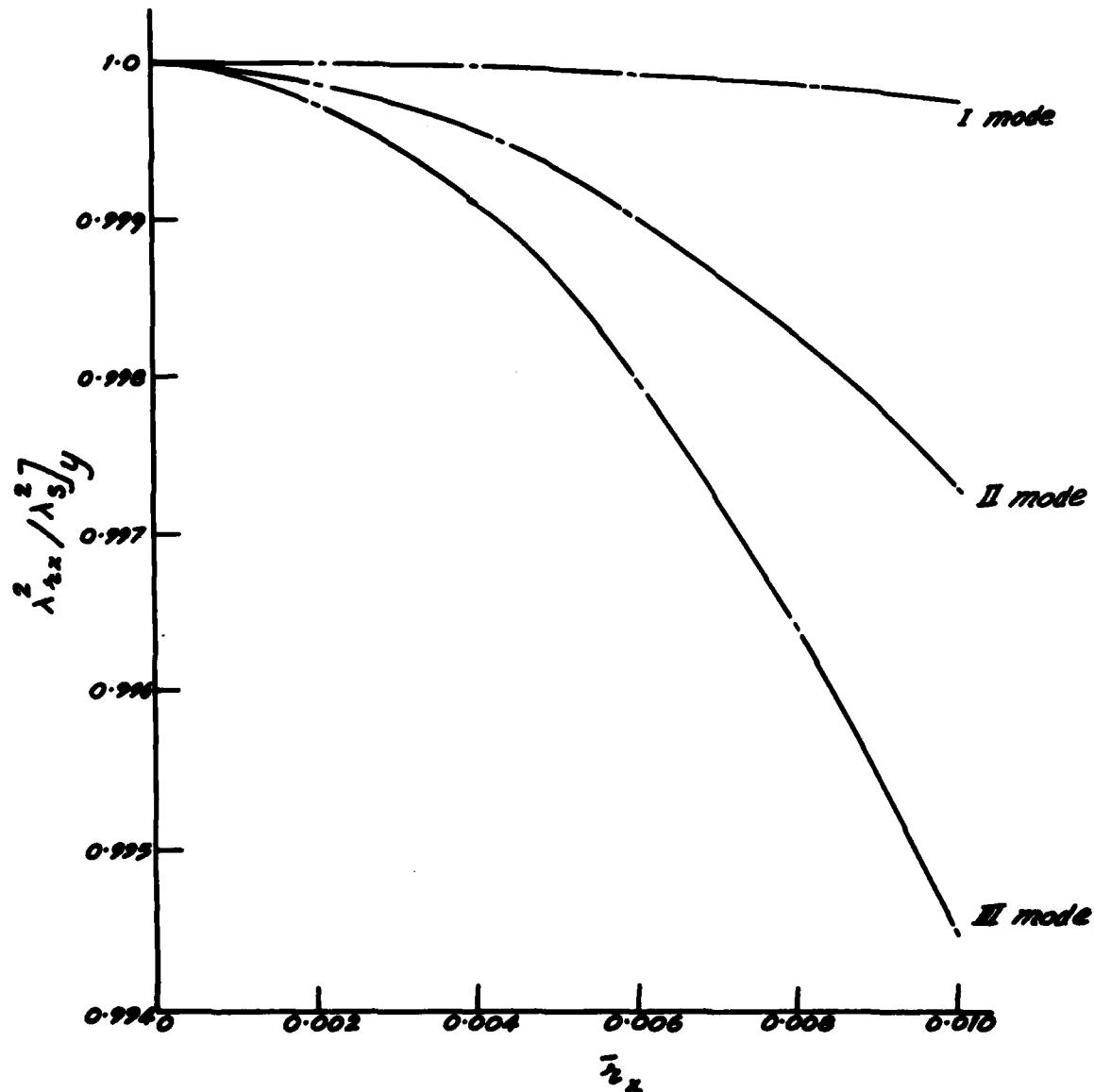
Fig.9: Effect of asymmetry $\bar{h}_x$ on frequency parameter ratio in flapwise
bending

wise bending and torsion modes is shown in Figs. 9 and 10. In Fig.9, the coupled flapwise mode shows that it decreases as $\bar{R}_x$ increases, the effect being more predominant for higher modes. The coupled torsion mode increases as $\bar{R}_x$ increases, but the effect is of the same order for all the modes and is more for the funda-mental mode. It may be noted that the frequency change is very nominal, even for a larger value of $\bar{n}_x$, the maximum percentage difference in the frequency parameter ratio is of the order of 0.5% in bending modes and 4% in torsion modes.

The effect of $\bar{n}_y$, on the coupled chordwise bending and torsion modes is shown in Figs. 11 and 12. The trend of variation of the frequency para-meter ratio is similar to that of $\bar{n}_x$ discussed above, but the effects are somewhat more predominant in this case.
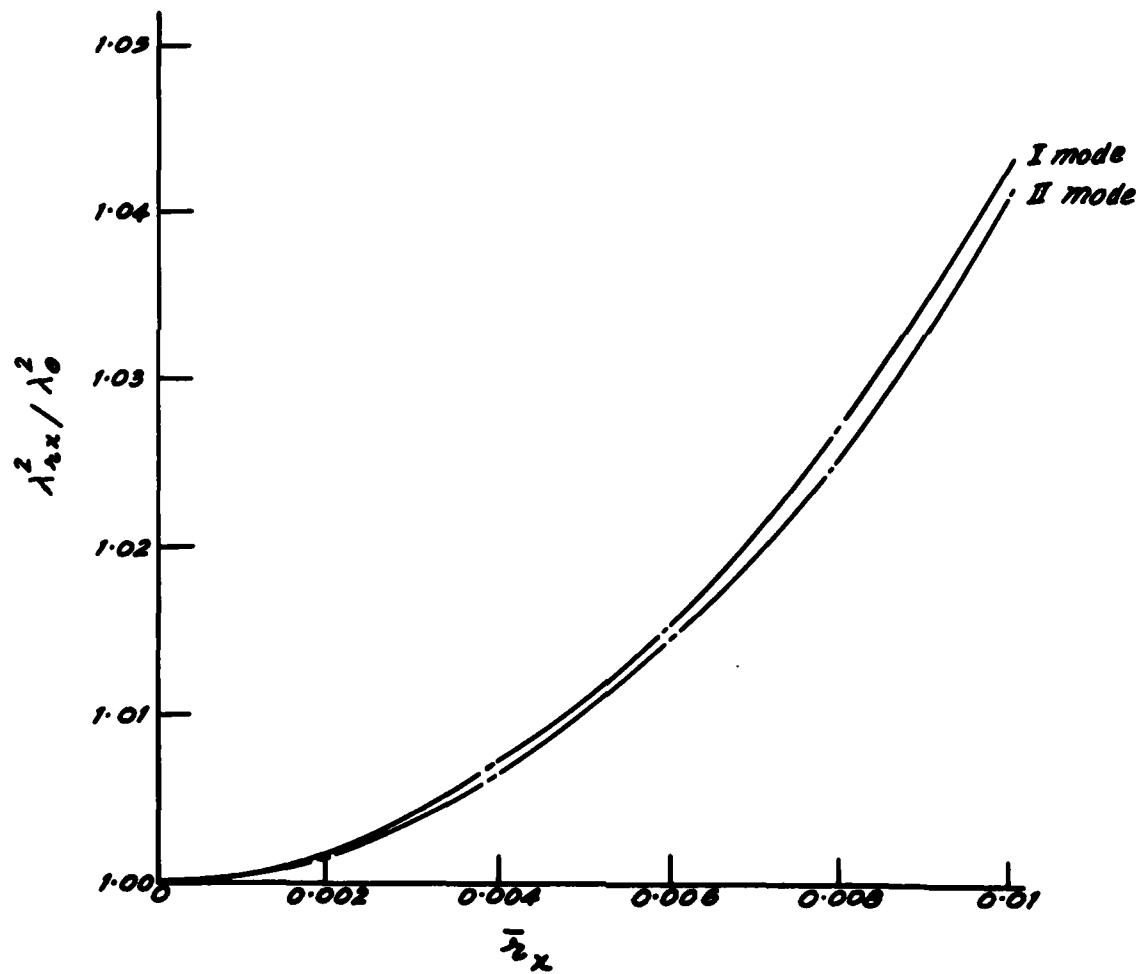
Fig.10: Effect of asymmetry $\bar{R}_x$ on frequency parameter ratio in torsion.
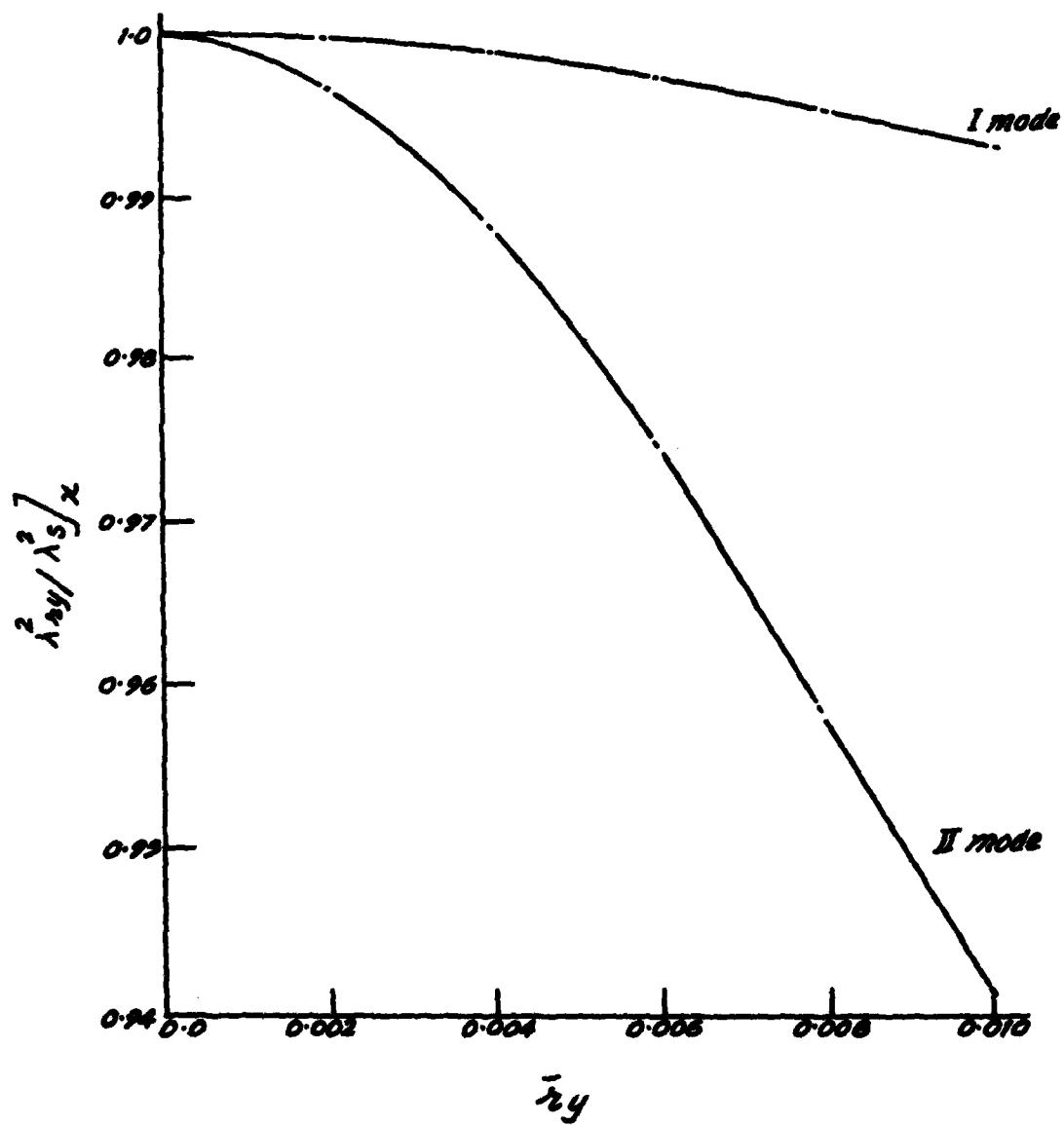
Fig.11: Effect of asymmetry $\bar{h}_y$ on frequency parameter ratio in chordwise bending.
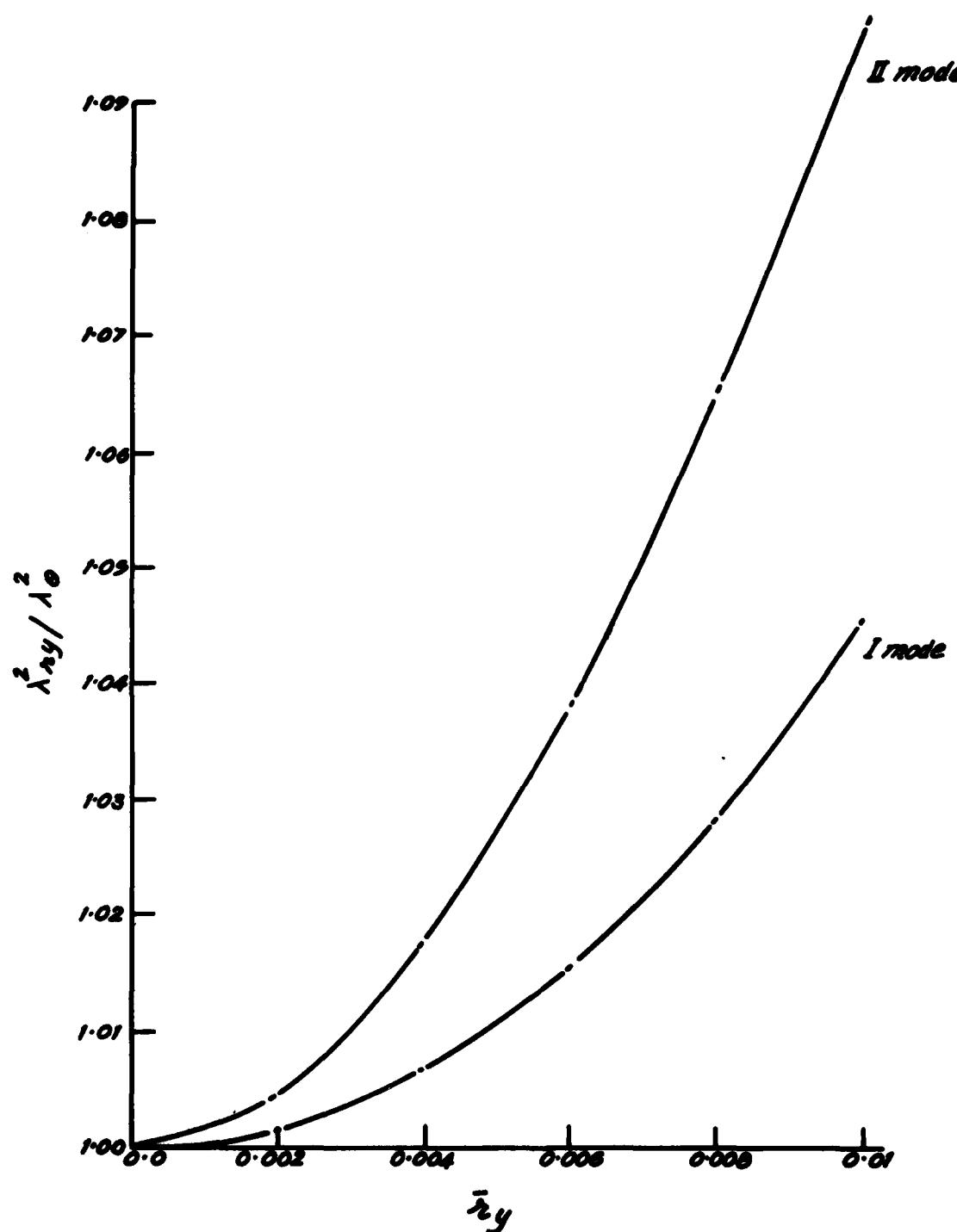
Fig.12: Effect of asymmetry $\bar{n}_y$ on frequency parameter ratio in torsion.

Effect of Stagger angle

The effect of stagger angle parameter , on the frequency parameter ratio for both flapwise and chordwise modes is given in Figs.13 and 14 respectively for α^t =1, 2 and 3. The effect of stagger angle is to decrease the natural frequency, the frequency parameter ratio decreasing linearly as $\sin\phi$ increases. The effect is more predominant on the fundamental mode, and for higher speeds of rotation. Again the chordwise modes are less effected compared to the flapwise modes.
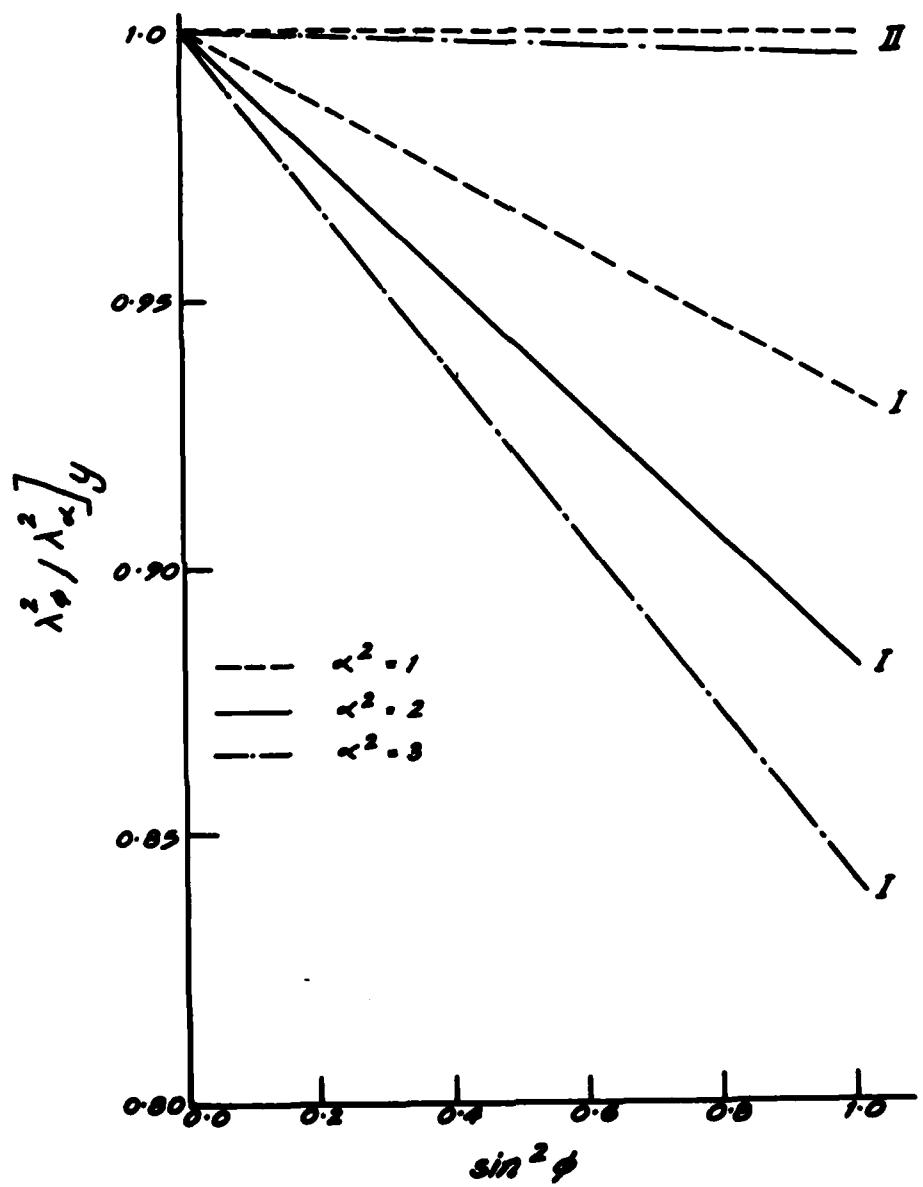

Fig.13: Effect of stagger angle on frequency parameter ratio in flapwise bending.

Since the problem is linear, the effects of different non-dimensional parameters such as pre-twist, rotation etc., considered above, on the frequency parameter ratios can be superimposed to determine the natural frequencies of a given blade. This would be of immense help in a rapid estimation of the natural frequencies of single turbomachine blades.
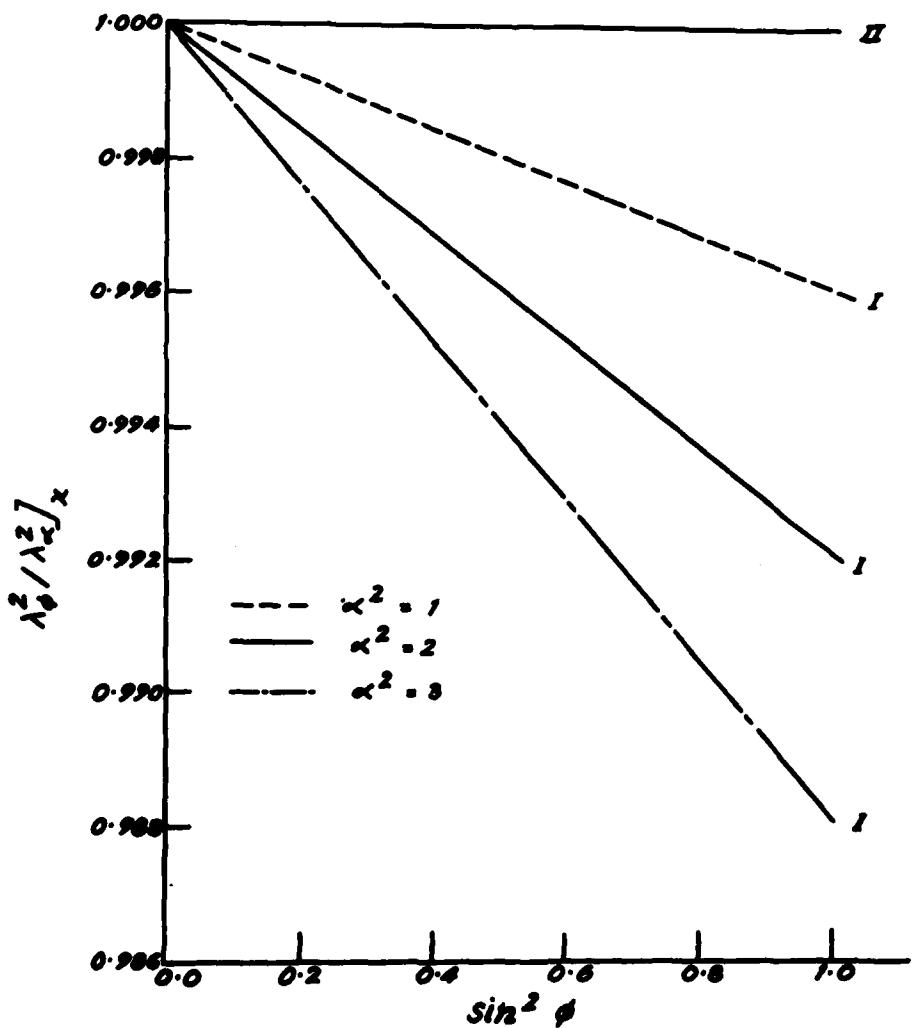

Fig.14:   Effect of stagger angle on frequency parameter ratio in chordwise bending.

CONCLUSION

The equations of motion for coupled bending-bending-torsion vibrations of rotating blades mounted on a disc at a stagger angle, are solved by the method of Galerkin, to determine the coupled natural frequencies. The results obtained are checked with available results for pre-twist, rotation, asymmetry of cross-section, disc radius and stagger angle,which show good agreement. The variation of non-dimensional parameters of the blade is presented in the form of graphical charts and will be useful in rapid estimation of coupled natural frequencies of single turbomachine blades.

Acknowledgement

References

1. J.S.Rao, Determination of natural frequencies of Turbine Blading-A Survey, Shock and Vibration Digest, v.5, No.10, p.1, 1973.

2. S.Banerji and J.S.Rao, Coupled Bending Torsion Vibrations of Rotating Blades, Paper No. ASME 76 GT 43, Gas Turbine conference, New Orleans, March 1976.

3. M.Lalanne, R. Henry and P.Trompette, Rotating Blade Analysis by the Finite Element Method, Proc. IUTAM symp. on Dynamics of Rotors, Lyngby, Denmark, p.299, 1974.

4. D. Stüwing, Zur Berechnung der Eigen Frequenzen von Schaufelpaketen axialer Turbomachinen, Maschinenbautechnik, v. 17, No.9, p.457, 1968.

5. D.J.Cottney, and D.J.Ewins, Towards the Efficient Vibration Analysis of Shrouded Bladed Disc Assemblies, Journal of Engg. for Indus, Trans. ASME, p.1054, 1974.

6. W.Carnegie, The Application of the Variational Method to derive Equations of Motion of Vibrating Cantilever Blading under Rotation, Bull Mechanical Engineering Educ., v.6, p.29, 1967.

7. D.K. Rao and J.S. Rao, Equations of Motion of Rotating Pre-twisted Blades in Bending-Bending-Torsion with effects of Warping, Shear and Rotary Inertia etc., Paper No.4.3, Proc. Silver Jubilee sessions of Aero. Society of India, 1973.

8. B. Dawson, Coupled Bending-Bending Vibrations of Pre-twisted Cantilever Blading Treated by the Rayleigh-Ritz Method,Journal of Mechanical Engg.Sci. V.10,No.5, p.381, 1968.

9. B.Dawson and W.Carnegie, Modal Curves of Pre-twisted Beams of Rectangular Cross-section, Journal of Mechanical Engg. Sci., v.11, No.1, p.1, 1969.

10. W.Carnegie, Vibration of Pre-twisted Cantilever Blading, Proc.I, Mech. E., v.173, No.12, p.343,1959.

11. W.Carnegie and B.Dawson,Vibration Characteristics of Straight Blades of Asymmetrical Aerofoil Cross-Section, Aero. Qly., v.20, p.178, 1969.

Notations:

C	Torsional stiffness	ω	weight per unit length of the blade
E	Young's modulus	x,y	Chordwise and flapwise dynamic bending deflections
G	Modulus of rigidity	κ^2	$\dfrac{\omega \omega^2 L^4}{g E I_{xx}}$
I_{cf}	Polar mass moment of inertia per unit length about the center of flexure		
I_{xx}, I_{yy}	Principal second moments of area of the cross-section of the blade.	Ψ	Pre-twist of the blade
		θ	Torsional dynamic deflection
L	Length of the blade	λ^2	$\dfrac{\omega p^2 L^4}{g E I_{xx}}$
p	Natural circular frequency	λ_s^2	Value of λ^2 for stationary straight symmetric beam
R	Disc radius	λ_c^2	Value of λ^2 considering only speed of rotation
$\bar{R}$	R/L	λ_R^2	Value of λ^2 considering only disc radius and rotation
$\bar{R}$	I_{yy}/I_{xx}	λ_p^2	Value of λ^2 considering only pre-twist
r_x, r_y	x and y coordinates of center of flexure with respect to centroid of the cross-section	λ_{nx}^2	Value of λ^2 considering only asymmetry $\bar{R}_x$
		λ_{ny}^2	Value of λ^2 considering asymmetry $\bar{R}_y$
$\bar{R}_x$	r_x/L	λ_β^2	Value of λ^2 considering stagger angle and rotation
$\bar{R}_y$	r_y/L		
		β	Stagger angle
		ω	Angular velocity of the disc

ACCELERATION THROUGH RESONANCE OF MULTI-DEGREE OF FREEDOM SYSTEMS

F. H. Wolff, A. J. Molnar, A. C. Hagg
Westinghouse Electric Corporation
Pittsburgh, Pennsylvania

Any vibration mode of a multi-degree of freedom (MDF) system is shown to be equivalent to a single degree of freedom (SDF) system, and the response of the MDF system during acceleration (or deceleration) through resonance can be readily calculated on the basis of the equivalent SDF system. Application of Q factors (magnification numbers at resonance) is given for a torsional critical speed of a synchronous motor-fan MDF system.

NOMENCLATURE

MDF = Multi-degree of freedom

SDF = Single degree of freedom

t = Time (sec)

$[I]$ = Inertia matrix

$[C]$ = Damping coefficient matrix

$[K]$ = Stiffness matrix

$\{\theta\}$ = Angular displacement vector

$\{\frac{d\theta}{dt}\}$ = Angular velocity vector

$\{\frac{d^2\theta}{dt^2}\}$ = Angular acceleration vector

$\{T(t)\}$ = Input torque vector

$\{r\}$ = Normal mode coordinate vector

$[\phi]$ = Modal matrix

ω_a, f_a = Undamped natural frequency (RPS, Hz)

ξ, ζ = Modal damping ratio

f = Instantaneous frequency of applied torque (Hz)

h = Rate of change of frequency of applied torque (Hz/sec)

Q = Quasi-resonance factor (ratio of peak dynamic displacement to the static displacement)

τ = Number of undamped free vibrations of SDF system from time 0 to time t

q = Value of τ at which $f = f_a$ (measure of rate at which system is accelerated through)

INTRODUCTION

The phenomena of accelerating and decelerating through a mechanical resonance and the large resulting vibrations which can occur has been given comprehensive treatments by F. M. Lewis [1], J. G. Baker [2], and others in terms of single degree of freedom (SDF) systems. However, most practical systems involve multi-degree of freedom (MDF) systems where the resonances are generally associated with system modes. Using the analogy between SDF systems and modes of MDF systems, the phenomena of accelerating and decelerating through resonance in MDF systems can be studied.

Q curves (peak amplifications at quasi-resonance) developed for accelerating through resonance in SDF systems are directly applicable to modes of MDF systems along with proper application of

normal mode theory. The applicable normal mode theory is presented and an example of decelerating through a torsional resonance in a MDF system is given.

The usefulness of the Q curves in analyzing MDF systems is predicated on the equivalence between a SDF system and a particular mode of a multi mode system. The classical normal mode theory uncouples the original system equations of motion formulating a set of uncoupled second order differential equations which are directly analogous to the SDF equation of motion.

ANALYSIS

A MDF torsional system can be described by a matrix set which represents the equations of motion

$$[I]\left\{\frac{d^2\theta}{dt^2}\right\} + [C]\left\{\frac{d\theta}{dt}\right\} + [K]\{\theta\} = \{T(t)\} \tag{1}$$

Applying the familiar normal mode transformation

$$\{\theta\} = [\phi]\{r\}$$

$$\left\{\frac{d\theta}{dt}\right\} = [\phi]\left\{\frac{dr}{dt}\right\} \tag{2}$$

$$\left\{\frac{d^2\theta}{dt^2}\right\} = [\phi]\left\{\frac{d^2r}{dt^2}\right\}$$

to Eq. (1) gives

$$[\phi]^T[I][\phi]\left\{\frac{d^2r}{dt^2}\right\} + [\phi]^T[C][\phi]\left\{\frac{dr}{dt}\right\}$$

$$\tag{3}$$

$$+ [\phi]^T[K][\phi]\{r\} = [\phi]^T\{T(t)\}$$

for the diagonal matrices

generalized inertia matrix, $[\phi]^T[I][\phi] =$

$$[Igen_a = \sum_{j=1}^{N} I_j \phi_{j,a}^2 ; \ a = 1,2,\ldots,N]^*$$

generalized stiffness matrix, $[\phi]^T[K][\phi] =$

$$[Kgen_a = \omega_a^2 \ Igen_a ; \ a = 1,2,\ldots,N]^*$$

---

*For lumped parameter systems.
**Assumes proportional damping conditions.

generalized damping matrix, $[\phi]^T[C][\phi] =$

$$[Cgen_a = \alpha \ Igen_a + \beta \ Kgen_a ; \ a = 1,2,\ldots,N]^{**}$$

and

generalized torque vector, $[\phi]^T\{T(t)\} =$

$$\{Tgen_a(t) = \sum_{j=1}^{N} \phi_{j,a} T_j(t); \ a = 1,2,\ldots,N\}$$

It is assumed that damping coefficient matrix [C] satisfies basic conditions of uniformity, namely,

$$[C] = \alpha[I] + \beta[K]$$

where α and β are real constants. Slight deviations from this condition are generally acceptable especially where damping is small [3,4]. Therefore,

$$2\xi\omega_a = \frac{\alpha \ Igen_a + \beta \ Kgen_a}{Igen_a} = \alpha + \beta \ \omega_a^2 \tag{4}$$

or

$$\xi = \frac{\alpha}{2\omega_a} + \frac{\beta\omega_a}{2} \tag{5}$$

where Eq. (5) can be used to determine the modal damping ratio.

The ath modal equation from the set of normal mode Eq. (3) is

$$Igen_a \frac{d^2r_a}{dt^2} + Cgen_a \frac{dr_a}{dt} + Kgen_a r_a = Tgen_a(t) \tag{6}$$

Eq. (6) for mode (a) is analogous to the SDF system (Fig. 1) where $Igen_a$, $Cgen_a$, $Kgen_a$ and $Tgen_a(t)$ correspond respectively to inertia, damping, stiffness and the forcing function. The alternate form for Eq. (6) is

$$\frac{d^2r_a}{dt^2} + 2\xi\omega_a \frac{dr_a}{dt} + \omega_a^2 r_a = \frac{Tgen_a(t)}{Igen_a} \tag{7}$$

For an applied torque $T_j(t)$ of the form $Amp_j \sin \gamma(t)$, the generalized torque is

$$Tgen_a(t) = Tgen_a \sin(\gamma(t)),$$
(8)

$$(Tgen_a = \Sigma \phi_{j,a} Amp_j)$$

where the angle of input is

$$\gamma(t) = \pi h t^2 \quad (rad) \qquad (9)$$

for an accelerating system.

Differentiating the angle of input gives an instantaneous frequency of

$$f = \frac{1}{2\pi} \frac{d\gamma}{dt} = ht \quad (Hz) \qquad (10)$$

The static or zero frequency deflection is commonly defined as

$$r_a(static) = \frac{Tgen_a}{Kgen_a} = \frac{Tgen_a}{Igen_a \omega_a^2} \quad (11)$$

It is this definition of $r_a(static)$ and the following definition of the quasi-resonance factor

$$Q(t) = \frac{r_a(t)}{r_a(static)} \qquad (12)$$

which governs a change of dependent variable in Eq. (7) to the quasi-resonance factor.

$$\frac{d^2Q}{dt^2}(t) + 2\xi\omega_a \frac{dQ}{dt}(t) + \omega_a^2 Q(t) = \omega_a^2 \sin(\gamma(t))$$
(13)

Using the definitions

$$\tau = f_a t \quad and \quad q = \frac{f_a^2}{h} \qquad (14)$$

to change the independent variable of Eq. (13) according to

$$\frac{dQ}{dt}(t) = f_a \frac{dQ}{d\tau}(\frac{\tau}{f_a}) \quad and \quad \frac{d^2Q}{dt^2}(t) = f_a^2 \frac{d^2Q}{d\tau^2}(\frac{\tau}{f_a})$$
(15)

results in a dimensionless second order differential equation for the quasi-resonance factor.

$$\frac{d^2Q}{d\tau^2}(\frac{\tau}{f_a}) + 4\pi\xi \frac{dQ}{d\tau}(\frac{\tau}{f_a}) + 4\pi^2 Q(\frac{\tau}{f_a})$$

$$= 4\pi^2 \sin(\pi\frac{\tau^2}{q})$$
(16)

Eq. (16) was solved numerically using a fourth order Runge-Kutta integration with controlled error to generate responses similar to those illustrated in Figs. 2 and 3. The peak values of the quasi-resonance factors Q were recorded and used to generate the subsequent quasi-resonance curves for uniformly accelerating excitation frequencies - Figs. 4 and 5.

Hence, knowing the modal damping ratio (from Eq. (5)) and the measure of acceleration rate (Eq. (14)), Eq.(16) or either Fig. 4 or 5 can be used to determine the amplification factor Q. Then the peak dynamic response for a mode can be determined from Eq. (12)

$$r_a(peak) = r_a(static) \times Q \qquad (17)$$

The peak physical responses in mode (a) are determined from the mode shape $\{\phi_a\}$ by

$$\{\theta_a\} = \{\phi_a\} r_a(peak) \qquad (18)$$

From Eqs. (11), (17), and (18) the peak physical response at any lumped inertia (j) in mode (a) is then

$$\phi_{j,a}(peak) = \phi_{j,a} r_a(peak)$$
(19)
$$= \phi_{j,a} r_a(static) \times Q = \phi_{j,a} \frac{Tgen_a Q}{Kgen_a}$$

The peak stresses are a function of the peak physical responses. For example, in a torsional system such as illustrated in Fig. 6, the peak relative angular displacement between adjacent inertias (j and j+1) due to mode (a) is

$$|\theta_{j,a}(peak) - \theta_{j+1,a}(peak)|$$

$$= |\phi_{j,a} - \phi_{j+1,a}| \frac{Tgen_a Q}{Kgen_a}$$
(20)

Hence, for a solid shaft of diameter D and torsional stiffness k_θ connecting the two inertias, the peak shear stress due to mode (a) would be equal to

$$\frac{16\,k_\theta}{\pi D^3}\,|\phi_{j,a} - \phi_{j+1,a}|\,\frac{Tgen_a\,Q}{Kgen_a}$$
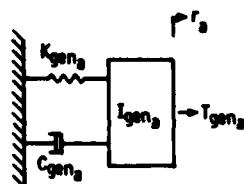
$$Igen_a\frac{d^2 r_a}{dt^2} + Cgen_a\frac{d r_a}{dt} + Kgen_a\,r_a = Tgen_a(t) \qquad \text{eq. (6)}$$

$$r_a\,(\text{static}) = \frac{Tgen_a}{Kgen_a} \qquad \text{eq. (11)}$$

$$r_a\,(\text{peak}) = r_a\,(\text{static}) \times Q = \frac{Tgen_a}{Kgen_a} \times Q \qquad \text{eq. (17)}$$

$$\theta_{j,a}\,(\text{peak}) = \theta_{j,a}\frac{Tgen_a}{Kgen_a} \times Q \qquad \text{eq. (19)}$$

Fig. 1 - Normal mode oscillator as equivalent SDF system

DISCUSSION OF QUASI-RESONANCE FACTORS

Figs. 2 and 3 illustrate the dynamic response of the quasi-resonance factors as a function of (τ/q) for a uniformly increasing acceleration (q = 100) at two different damping values ξ = 0 and ξ = .05, respectively. The peak amplitudes Q = 36.49 (for q = 100, ξ = 0) and Q = 9.3 (for q = 100, ξ = .05) both occur after the critical speed $(\tau/q = 1)$ has been reached. This apparent shift in critical speed is greater for the higher acceleration or lower q values.

The undamped response (Fig. 2) continues to oscillate with increasing frequency at an amplitude slightly less than the maximum while the damped response decays rapidly once the peak response has been reached.
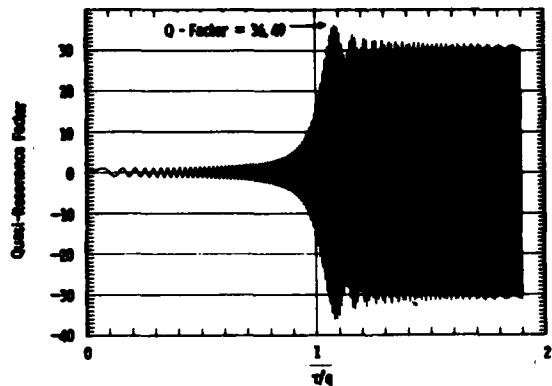
Fig. 2 - Dynamic quasi-resonance factor for SDF (q=100, ξ=0%)
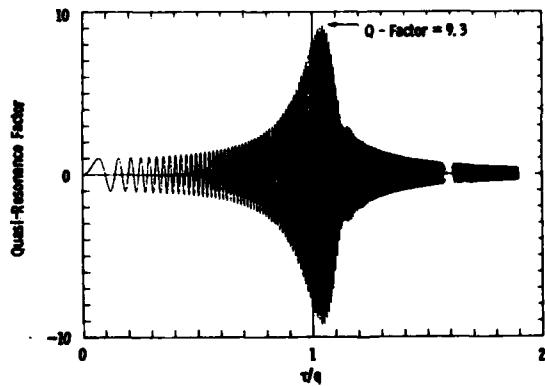
Fig. 3 - Dynamic quasi-resonance factor for SDF (q=100, ξ=5%)

The peak amplitudes are very slightly greater for deceleration cases; however, the actual differences would not be discernible on a set of design curves. Therefore, for practical purposes, the design curves of Figs. 4 and 5 can be used for both acceleration and deceleration through resonance.

An examination of the quasi-resonance curves of Fig. 4 shows the influence of the acceleration rate and damping ratio on the peak magnification factor [5]. All of the curves asymptotically approach the steady state resonance factors corresponding to the damping ratio; i.e., the slower the critical speeds are being accelerated through (large q) the more nearly the phenomena resembles the true steady state resonance - as $q \to \infty$, $Q \to 1/2\xi$.

The amplification for heavily damped systems is relatively insensitive to acceleration rate; for example, a system with 5% of critical damping would be expected to amplify the static response by a factor of $Q = 10$ for most practical accelerations. On the other hand, amplifications for lightly damped systems are sensitive to acceleration rate. For example, with .1% damping the quasi-resonance factors very from $Q = 45$ for a $q = 200$ to $Q = 110$ for a $q = 1400$. Not only is the amplification factor reduced by a high system acceleration (small q), but also the number of actual stress cycles are less which is an important fatigue consideration. Increased damping lowers the dynamic amplification; hence, the level of stress cycles are reduced.

An interesting application for these curves would concern determining what buildup could be anticipated during a frequency sweep test. Once again, if the system in question contains damping in excess of 5% of critical, a limited buildup is guaranteed ($Q \leq 10$) regardless of how slow the sweep is being performed. However, for lightly damped systems, damaging vibrations could occur during the sweep test. For example, a typical rate used during a frequency sweep test for seismic application is on the order of 2 octaves per minute [7]. This means that going from 4 Hz to 16 Hz (2 octaves when starting at 1 Hz) requires 60 seconds; therefore, an acceleration of

$$h = \frac{16 - 4}{60} = \frac{12}{60} \frac{Hz}{sec}$$

is indicated which, if a natural frequency of 10 Hz were present, would give a

$$q = \frac{f_a^2}{h} = \frac{100}{12/60} = 500$$

If the equipment had as little as 1% damping, a quasi-resonance factor of $Q = 38$ would be likely for linear behavior.
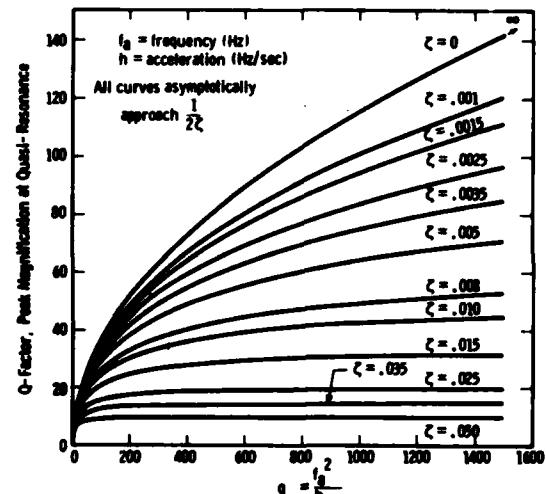

Fig. 4 - Peak magnifications vs. q for various damping ratios ξ (larger q indicates smaller accelerations)

Another way to study the buildup due to a uniformly accelerating excitation is to plot the quasi-resonance factors [6] against the percent of critical damping - Fig. 5. The Q-factors presented in this fashion give a clearer picture of the phenomena for the lower q (higher accelerations - h); i.e., the quasi-resonance curves are spread out more for the lower q values.
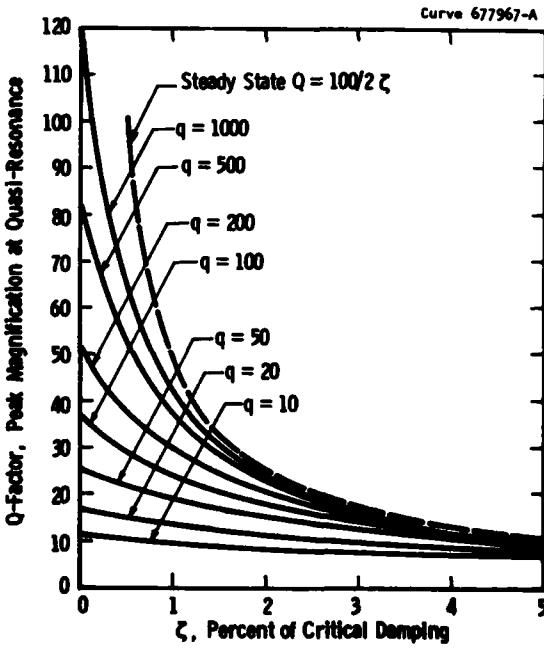
Fig. 5 - Peak magnifications vs. ξ for various q values (larger q indicates smaller accelerations)

131

EXAMPLE

A typical application for a 50 Hz supply is shown in Fig. 6 which involved a synchronous motor driven induced draft fan system which experienced shaft failures between the control wheel and motor.
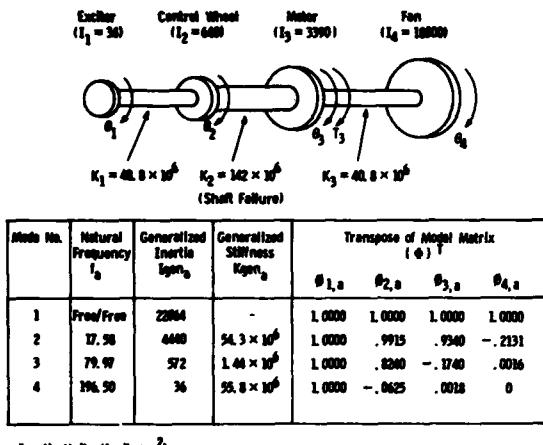

Fig. 6 - Torsional model and associated modal data of a synchronous motor-fan system

The envelope of a sample synchronous motor air gap torque is shown in Fig. 7 as a function of slip (speed, frequency, etc.). There are three main components of the air gap torque during startup of a synchronous motor:

(1) the initial component which oscillates at line frequency (ω_L) and decays rapidly;

(2) an average component which drives the system;

(3) a variable frequency component which oscillates at twice slip frequency; i.e., torque α Sin (2 x slip x ω_L t).

The magnitude of the variable frequency component is nearly constant until synchronous speed (slip=0) is reached and pull in is achieved. The twice slip frequency varies, for a 50 Hz system, from 100 Hz to 0 Hz; therefore, this air gap torque component is of main concern when considering acceleration (deceleration in terms of slip frequency) through resonances of synchronous motor driven units.

Note, from the slope of the average torque-speed curve the motor damping can be estimated. Also, the motor damping is actually negative until the knee of the torque-speed curve is reached (pull-out torque) and the curve starts downward.
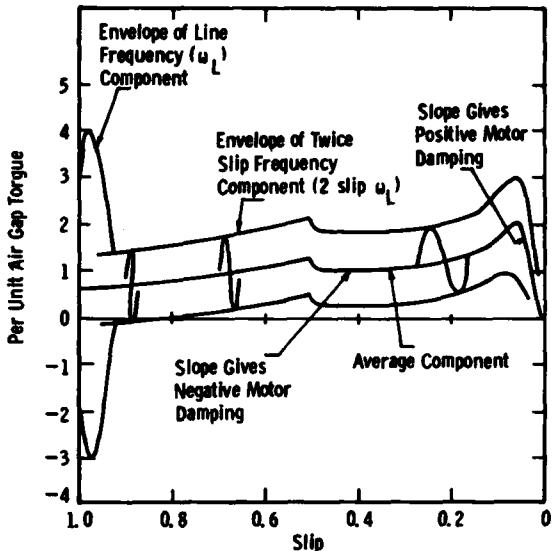

Fig. 7 - Envelope of typical synchronous motor air gap torque curve

The particular synchronous motor in this application required 11 seconds to reach running speed and generated an oscillating component of air gap starting torque that varies from 100 Hz to 30 Hz (twice slip frequency) in the 11 seconds [8]. Analytically the twice slip frequency oscillating air gap torque with uniformly decreasing frequency is defined by

$$T_3(t) = 172,000 \sin[2\pi (100 - \frac{70}{22} t)t]$$

(in-lbs)

for $0 \leq t \leq 11$.

The angular displacement

$$\gamma(t) = 2\pi(100 - \frac{70}{22} t)t \quad \text{(rad)}$$

gives the instantaneous excitation frequency of

$$f = \frac{1}{2\pi} \frac{d\gamma}{dt} = 100 - \frac{70}{11} t \quad \text{(Hz)}$$

with a deceleration rate of

$$h = \frac{1}{2\pi} \frac{d^2\gamma}{dt^2} = -\frac{70}{11}$$

(Hz/sec)

The modal data (Fig. 6) shows, in addition to the free-free mode, the presence of three torsional natural frequencies - 17.58 Hz, 79.97 Hz, 196 Hz. Because the 196 Hz is well beyond the range of excitation frequency, there is no significant forced vibration of this mode. The 17.58 Hz mode is transversed well after pull-out torque has been reached which means (for this particular motor) the oscillating component of air gap torque is at a slightly lower amplitude than initially. More importantly, both the motor and fan are supplying significant amounts of positive damping which results from the slope of the speed torque characteristics of the system. Furthermore, the measure of deceleration rate for the 17.58 Hz mode is

$$q = \frac{[f_2]^2}{h} = \frac{[17.58]^2}{70/11} = 48.5$$

which along with the large damping will result in a small magnification.

The 79.97 Hz 3rd mode is in the range of uniformly decelerating input frequency and occurs early during startup when the damping is small; accordingly, this mode was considered to be the principal source of response.

For the undamped case ($\xi = 0$), the measure of deceleration rate from Eq. (14) is

$$q = \frac{[f_3]^2}{h} = \frac{[79.97]^2}{70/11} = 1005$$

Hence, from either Fig. 4 or 5 the amplification is

$$Q = 116$$

The static response corresponding to Eq. (1) is

$$r_3(static) = \frac{Tgen_3}{Kgen_3} = \frac{\phi_{3,3} \times Amp_3}{Kgen_3}$$

$$= \frac{-.174 \times 172,000}{1.442 \times 10^6} = -.000208 \quad (rad)$$

The peak dynamic response of the third mode from Eq. (12) is

$$r_3(dynamic) = r_3(static) \times Q = .024076 \quad (rad)$$

Accordingly, the peak physical displacements of the motor-fan system due to deceleration through the 3rd mode can be found from Eq. (2) using the modal data in Fig. 6.

$$\begin{Bmatrix} \theta_1 \\ \theta_2 \\ \theta_3 \\ \theta_4 \end{Bmatrix} = \begin{Bmatrix} \phi_{1,3} \\ \phi_{2,3} \\ \phi_{3,3} \\ \phi_{4,3} \end{Bmatrix} r_3(dynamic)$$

$$= - \begin{bmatrix} 1.000 \\ .824 \\ -.174 \\ .0016 \end{bmatrix} (.024076) = \begin{bmatrix} .024076 \\ .019838 \\ -.004189 \\ .000038 \end{bmatrix}$$

The peak angle in the shaft between the control wheel and motor (where the failure occurred) is

$$\theta_2 - \theta_3 = .019838 - -.004189 = .024027 \quad (rad)$$

which compared to .02436 (rad) found from solving for a complete time history of the response of the system.

If a large value of shaft damping [9] is considered ($\xi = .01$) for a q = 1005, the amplification is

$$Q = 42.4$$

which gives a peak displacement of the control wheel-motor shaft of

$$\theta_2 - \theta_3 = (.024027) \frac{(42.4)}{(116)} = .008782 \quad (rad)$$

This compared to a peak response of .00896 (rad) via a complete transient solution.

Subsequent stress and fatigue calculations [8] using the values of ($\theta_2 - \theta_3$) corresponding to reasonable amounts of shaft damping [9,10] explained the failures.

CONCLUSIONS

For MDF systems, once a particular mode of vibration has been identified to be within the range of changing input frequency, the mechanical system can be treated as a SDF system with the aid of the generalized modal parameters. The quasi-resonance curves can then be used to determine the amount of buildup, hence the peak response, to be expected from accelerating or decelerating through the resonance.

REFERENCES

1. Lewis, F. M., "Vibration During Acceleration Through a Critical Speed", ASME, Applied Mechanics Division, APM-54-24 (1932).

2. Baker, J. G., "Mathematical Machine Determination of the Vibration of Accelerated Unbalance Rotor", Trans. ASME, 1939, pg. A-154.

3. Raleigh, Lord, "Theory of Sound", Vol. 1, Dover Publication, New York, New York, 1945.

4. Caughey, T. L., O'Kelly, M. E. F., "Classical Normal Modes In Damped Linear Dynamic Systems", Trans. ASME, 1964, (APM-31).

5. Seireg, Ali, "Mechanical Systems Analysis", pg. 589, International Textbook Co., Scranton, Pennsylvania, 1969.

6. Fischer, E. G., "Sine Beat Vibration Testing Related to Earthquake Response Spectra", Shock and Vibration Bulletin, Naval Research Laboratory, No. 42, Part 2, 1-9 (January 1972).

7. IEEE Standard 344, Seismic Qualification of Class IE Equipment for Nuclear Power Generating Stations, Revision 5, 1974.

8. Molnar, A. J., Wolff, F. H. and Hagg, A. C., "Forced and Self-Excited Torsional Vibrations of a Synchronous Motor and Fan System During Start-Up", Research Report 71-7E7-VIBAP-R1, Westinghouse Research Laboratories, Pittsburgh, Pennsylvania 15235, August 6, 1971.

9. Wilson, W. K., "Practical Solution of Torsional Vibration Problems", Vol. II, pp. 625-627, John Wiley's Sons, Inc., Third Edition (1948).

10. Hurty, W. C. and Rubinstein, M. F., "Dynamics of Structures", Prentice-Hall, Im. Englewood D Cliffs, New Jersey, 1964.